Université de Montréal

Structure-function studies of class I aldolases

Exploring novel activities: mechanism, moonlighting, and inhibition

par Paul Heron

Département de Biochimie et Médecine Moléculaire

Faculté de Médecine

Thèse présentée

en vue de l'obtention du grade de *Philosophiae Doctor* (Ph.D.)

en Biochimie et Médecine Moléculaire

option Biologie Structurale

Décembre, 2016

Université de Montréal

Faculté des études supérieures et postdoctorales

Cette thèse intitulée:

Structure-function studies of class I fructose-1,6-bishosphate aldolases – exploring novel
activities: mechanism, moonlighting, and inhibition

Présentée par :

Paul Heron

a été évaluée par un jury composé des personnes suivantes :

Daniel Zenklusen, président-rapporteur

Jurgen Sygusch, directeur de recherche

Serguei Chteinberg, membre du jury

Catherine Vénien-Bryan, examinatrice externe

Marc Drolet, représentant du doyen de la FES

Thèse acceptée le
12 avril, 2017

Résumé

La fructose-1,6-bisphosphate aldolase de classe I est une enzyme glycolytique (EC 4.1.2.13) qui catalyse le clivage réversible du fructose-1,6-bisphosphate (FBP) en dihydroxyacétone phosphate (DHAP) et glycéraldéhyde-3-phosphate (G3P). Des années de recherche sur FBP aldolase ont permis d'identifier les résidus impliqués dans son mécanisme réactionnel, ont tracé en grande partie les coordonnées de la réaction, ont révélé de nouvelles fonctions dites « moonlighting », et ont validé l'aldolase comme une cible attrayante pour des applications anti-glycolytiques tel que le cancer. Il existe néanmoins des questions en suspens relatives à ces activités que nous avons étudiées.

Tout d'abord, la trajectoire détaillée de l'aldéhyde relatif à sa liaison au site actif allant jusqu'à la formation du lien carbone-carbone par condensation aldolique est indéfini. Pour élucider les détails moléculaires liés à ces événements, nous avons déterminé des structures cristallographiques à hautes résolution de l'aldolase de classe I chez *Toxoplasma gondii*, qui porte une identité de séquence élevée avec l'aldolase humaine (57%), en complexe avec l'intermédiaire ternaire de pré-condensation. Le complexe ternaire révèle un mode de liaison non-productive inhabituel pour G3P dans une configuration *cis* qui permet l'alignement de l'aldéhyde à proximité du nucléophile naissant. La configuration compétente pour la condensation aldolique provient d'une transposition *cis-trans* de l'aldéhyde qui produit une liaison hydrogène courte permettant la polarisation de l'aldéhyde et le transfert de proton au niveau de Glu-189. Nos résultats informent les chimistes synthétiques qui cherchent à développer l'aldolase comme biocatalyseur pour des réactions stéréo-contrôlées.

Le rôle présumé de l'aldolase dans la production du méthyglyoxal (MGO), un métabolite dicarbonyle hautement réactif qui génère des « advanced glycation end products » (AGES) a également été étudié structurellement et enzymatiquement. Une enquête structurelle cristallographique de MGO générée par décomposition enzymatique chez l'aldolase de classe I a révélé que, contrairement aux indications préliminaires, l'apparition hypothétique de MGO et de phosphate inorganique (Pi) résultant de la décomposition enzymatique de DHAP dans le site actif de l'aldolase est mieux interprétée par une population mixte de DHAP et de molécules d'eau. Une étude enzymatique a révélé que la décomposition spontannée des trioses-phosphate

est une source majeure de la production de MGO, alors qu'une production catalysée par l'aldolase est peu concluante. L'identification des sources de production de MGO continue d'être une priorité afin de développer des stratégies pour atténuer les manifestations cliniques de pathologies associées au MGO.

La FBP aldolase est également reconnu pour ses activités « moonlighting » - du fait qu'elle effectue plus d'une activité sans rapport avec sa fonction glycolytique. Divers partenaires de l'aldolase sont rapportés dans la littérature, y compris les adhésines de surface cellulaire chez les parasites apicomplexes, dans lequel l'aldolase exécute une fonction d'échafaudage entre le complexe actomyosine et les adhésines - une interaction qui est décisive pour la motilité et l'invasion des cellules hôte. Le mode de liaison de cette interaction a été étudié et nos résultats sont compatibles avec une liaison au site actif. Les détails précis de cette interaction ont des implications thérapeutiques, étant donné que le ciblage de celui-ci réduit l'invasion des cellules hôte par les parasites.

Enfin, l'aldolase de classe I est de plus en plus reconnu pour son potentiel comme cible anti-glycolytique dans les cellules qui sont fortement tributaires du flux glycolytique, comme les cellules cancéreuses et les parasites protozoaires. Le développement de nouveaux inhibiteurs de haute affinité est donc non seulement avantageux pour des études mécanistiques, mais représente un potentiel pharmacologique sans fin. Nous avons développé une nouvelle classe d'inhibiteurs de haute affinité de type inhibition lente et avons déterminé la base moléculaire de leur inhibition grâce à des structures cristallographiques à haute résolution et par un profilage enzymatique.

Cette étude, qui combine plusieurs disciplines, y compris la cristallographie, enzymologie et chimie organique, souligne l'intérêt et l'importance d'une approche multidisciplinaire.

Mots-clés : aldolase de classe I, condensation aldolique, mécanisme catalytique, stéréosélectivité, méthylglyoxal, métabolite toxique, *Toxoplasma gondii*, adhésine, conception rationnelle d'inhibiteur, cristallographie aux rayons X.

Abstract

Class I Fructose-1,6-bisphosphate aldolases are glycolytic enzymes (EC 4.1.2.13) that catalyze the reversible cleavage of fructose-1,6-bisphosphate (FBP) to dihydroxyacetone phosphate (DHAP) and glyceraldehyde-3-phosphate (G3P). Years of research on FBP aldolases has identified residues implicated in the reaction mechanism, mapped the greater part of the reaction coordinates, and revealed novel moonlighting functions. Further, FBP aldolase is recognized as an attractive target for anti-glycolytic applications such as cancer. There are nevertheless outstanding questions related to these activities that were investigated in this thesis.

First, the detailed trajectory of the reaction mechanism from aldehyde binding in the active site to carbon-carbon bond formation by aldol condensation is undefined. To elucidate the molecular details related to these events, we solved high-resolution crystallographic structures of native class I aldolase from *Toxoplasma gondii*, which has a high sequence identity with human aldolase (57 %), in complex with the pre-condensation ternary intermediate. The ternary complex reveals a condensation-incompetent binding mode for G3P in a *cis*-configuration that aligns the aldehyde alongside the nascent nucleophile. The productive aldol-competent configuration arises from a *cis-trans* rearrangement of the aldehyde that produces a short hydrogen bond required for polarization of the aldehyde and coincident proton transfer at Glu-189. Our results inform synthetic chemists seeking to develop aldolases for stereo-controlled reactions in biosynthetic applications.

The suspected role of aldolase in methylglyoxal (MGO) production, a highly reactive dicarbonyl metabolite that produces advanced glycation end-products (AGES) was also probed structurally and enzymatically. A crystallographic structural investigation of MGO generated by enzymatic decomposition in class I aldolase revealed that, contrary to preliminary indications, the appearance of MGO and inorganic phosphate (P_i) resulting from enzymatic decomposition of DHAP in the active site of aldolase is more appropriately modeled by a mixed population of DHAP and water molecules. Enzymatic investigation revealed triose-phosphate decomposition to be a major source of MGO production, whereas production by aldolase did not exceed assay background levels. Identifying the main sources of MGO production continues to be a priority for mitigating the clinical manifestations of MGO-derived pathologies.

FBP aldolase is also recognized for its moonlighting properties – performing more than one activity unrelated to the glycolytic function. Diverse aldolase partners are reported, including cell surface adhesins in apicomplexan parasites, in which aldolase performs a bridging function between the actomyosin complex and the cytoplasmic domain of the adhesins – an interaction that is crucial for motility and host-cell invasion. The binding mode of this interaction was investigated and our results are consistent with active site binding. The precise details of aldolase-adhesin binding has therapeutic implications, since targeting of the latter reduces host-cell invasion by parasites.

Finally, class I aldolase is gaining prominence as an anti-glycolytic target in cells that are highly dependent on glycolytic flux, such as cancer cells and protozoan parasites. Developing new high-affinity inhibitors for these enzymes is therefore not only advantageous for mechanistic studies, but has endless pharmacological potential. We developed a novel class of high-affinity aldolase inhibitors, bisphosphonates, and determined the molecular basis of their inhibition with high-resolution crystallographic structures and enzymatic profiling.

This study, which combined several disciplines, including crystallography, enzymology, and organic chemistry, underscores the interest and significance of a multidisciplinary approach.

Table of Contents

List of Tables

List of Supporting Tables

List of Figures

List of Supporting Figures

List of Schemes

List of Abbreviations

AGES	Advanced glycation end products
Ala	Alanine
ALDOA	Aldolase A
AMA1	Apical membrane antigen 1
Arg	Arginine
Asp	Aspartic acid
ATP	Adenosine triphosphate
C-terminal	Carboxy-terminal
cm	Centimeter
DHAP	Dihydroxyacetone phosphate
EDTA	Ethylenediaminetetraacetic acid
F-actin	Actin filaments
FBP	Fructose-1,6-bisphosphate
HTS	High throughput screen
G3P	Glyceraldehyde-3-phosphate
GDH	Glycerol 3-phosphate dehydrogenase
Glu	Glutamic acid
GLUT4	Glucose transporter 4
ITC	Isothermal titration calorimetry
K	Kelvin
k	rate constant
K_a	Association constant
k_{cat}	Turnover number
K_D	Dissociation constant
kDa	Kilo Dalton
K_i	Inhibition constant
Lys	Lysine
mg	Milligram
M	Molar

mM	Millimolar
μM	Micromolar
ηM	Nanomolar
MGO	Methylglyoxal
MGS	Methylglyoxal synthase
MIC2	Microneme protein 2
NADH	Nicotinamide adenine dinucleotide
NASEP	Naphthol AS-E phosphate
N-terminal	Amino-terminal
ηm	Nanometer
NMR	Nuclear Magnetic Resonance
PDB	Protein Data Bank
RNA	Ribonucleic acid
ROS	Reactive oxygen species
Ser	Serine
SUMO	Small ubiquitin-like modifier
TgALD	*Toxoplasma gondii* aldolase
TIM	Triosephosphate isomerase
Trp	Tryptophan
Tyr	Tyrosine
WASP	Wiskott-Aldrich syndrome protein

To my family, friends, and dearest of all, my wife.

"To him be the glory" – Romans 11:36

Acknowledgments

First I would like express my great appreciation to Dr. Jurgen Sygusch for his patient guidance, enthusiastic encouragement and useful critiques during my thesis. I would also like to acknowledge the members of my thesis committee, Dr. Pascale Legault and Dr. Joelle Pelletier, for their advice and assistance in keeping my progress on schedule. My special thanks are also extended to the members of my jury for accepting to correct my thesis.

There are countless people at the University who have supported my work in one way or another, including the support staff in Biochemistry who have been helpful with the administrative aspects of my thesis. I would also like to extend my thanks to the dedicated staff at the MS platform in Chemistry (Alexandra F) and the crystallography platform (Michel S). A special acknowledgement goes to Marie P in Bioinformatics for giving me the opportunity to teach undergrads for so many years. I am also grateful to Jim O for entrusting me his undergraduate crystallography lecture. I would be remiss if I didn't acknowledge the friendly and helpful staff at BNL.

Many colleagues I have worked alongside in my laboratory have made this journey endurable and I would like to acknowledge the following for the many smiles we have shared (in chronological order): Mathieu C, Em F, Clotilde LK, Arnold DP, Octavian T, Jaan, Livia O, Joyce W, Loic, Maher, Mara, Jérémie R, Ghiles, Viridiana, Rux - and finally, the last two deserve a mention for the special comradery we have shared, Benoit J and Amira Y. Members of several other labs have been a pleasure to work alongside, including colleagues in the Baron lab, Omichinski lab, Legault lab, Ferbeyre lab and Brisson lab.

This acknowledgment would be incomplete without singling out the following colleagues with whom I've developed a special friendship and have shared memorable experiences: Bastien C et Julie B, Normand C, Thomas M, Mathieu V and their significant others.

My time at UdeM would not have been the same without my weekly injection of sports, including squash with TM, running with the RadicauxLibres, and soccer with my fellow biochemists – I hope to have left a lasting impression on my colleagues in regard to the importance of physical health.

My parents, grandparents, brothers, sisters, and friends are to be thanked for their continued support through prayer and encouragement.

Finally, my wife and best friend, Marissa – you bring the most joy of anyone to my life. Thank you for sharing so many adventures with me and being so supportive of me. You now have a Ph.T. (Putting Hubby Through) diploma.

Chapter 1

Introduction

1.1 Fructose-1,6-bisphosphate aldolase

1.1.1 General aspects

Proteins are complex molecules necessary for the chemical processes that occur in living organisms. As the chief actors within the cell, their mechanisms of action, regulation, structure, and interaction are the subject of intense scrutiny by a great number of researchers. One such protein that has been rigorously dissected for several decades is the glycolytic enzyme, aldolase. Nevertheless, sustained research on this 'old dog' continues to reveal the remarkable complexity of this understated enzyme. The goal of this thesis is to continue this tradition, and bring to light some of the lesser known facets of class I aldolases, including aspects related to its mechanism, inhibition, and moonlighting functions. The following introduction will provide a universal portrait of class I aldolases that is generally applicable to each of the subsequent chapters.

1.1.2 Historical perspective

The chemistry of life requires a bewildering array of biochemical reactions that occur simultaneously in a living cell, the sum of which is called metabolism. These reactions function coherently together to maintain fundamental processes such as tissue development, waste disposal, reproduction, and conversion of food to energy – processes that we refer to as life. One of the hallmarks of life is that these reactions do not occur randomly and spontaneously. They are tightly regulated and made possible by a phenomenon known as enzymatic catalysis, which provides the necessary acceleration that is required for an otherwise slow and un-controlled reaction. The early study of enzymes (enzymology), tightly woven with the discipline of biochemistry, evolved largely from the investigation of fermentation in the nineteenth century.

In 1860, Louis Pasteur observed that fermentation occurs in microorganisms. The inability to isolate and reproduce biochemical reactions outside living cells reinforced the largely held assumption that living cells were endowed with "vital forces" governed by special laws that enabled them to perform biochemical transformations (Kresge et al., 2005; Manchester, 1995). This theory was dispelled by a major breakthrough in 1897 when Eduard Buchner discovered that cell-free extracts that could carry out fermentation, marking the inception of biochemistry

(Buchner, 1897; Nobelprize.org). This enabled the systematic dissection of cell extracts, which led to breakthroughs in 1905 by Arthur Harden and William Young who discovered that heat-labile fractions called "zymase' (mixture of enzymes) and "cozymase" (co-factors such as NAD^+, ATP, ADP and metal ions) were both necessary for fermentation. Emil Fischer's discovery in 1894 that glycolytic enzymes display specific activity towards stereoisomeric sugars gave birth to the notion of "lock and key mechanism" between an enzyme and its substrate – a concept still used in classrooms today when teaching enzymology (Fischer, 1894).

It took several decades and the effort of many investigators to piece together the complex puzzle of glycolysis (Figure 1-1). By 1940, all components were elucidated and the pathway was formally termed the Embden-Meyerhof-Parnas pathway for the major contributions made by Gustav Embden, Otto Meyerhof, and Jacob Parnas. These early investigators pioneered many of the fundamental biochemical techniques of isolation and purification of intermediates that animated many other later discoveries. The short-lived nature of the intermediates of glycolysis and their sheer number proved to be the utmost challenge.

Otto Meyerhof, whose primary interest was to understand how energy is transformed during chemical reactions in the cell, was particularly instrumental in the discovery of the zymohexase (fructose-1,6-bisphosphate aldolase (FBPA)), the enzyme responsible the reversible cleavage of the hexose diphosphate (known as fructose-1,6-bisphosphate (FBP)) into two triose phosphate isomers, dihydroxyacetone phosphate (DHAP) and glyceraldehyde-3-phosphate (G3P) (Meyerhof and Junowicz-Kocholaty, 1943; Meyerhof and Lohmann, 1934).

The advent of new techniques such as chromatography, X-ray crystallography, NMR spectroscopy, mass spectrometry, and electron microscopy, has accelerated the discovery and detailed understanding of many metabolic pathways in cells. FBP aldolase has been no exception, and decades of investigation into this model enzyme have revealed intricacies regarding its activity in different species, its specificity for a variety of substrates, and its three-dimensional structure.
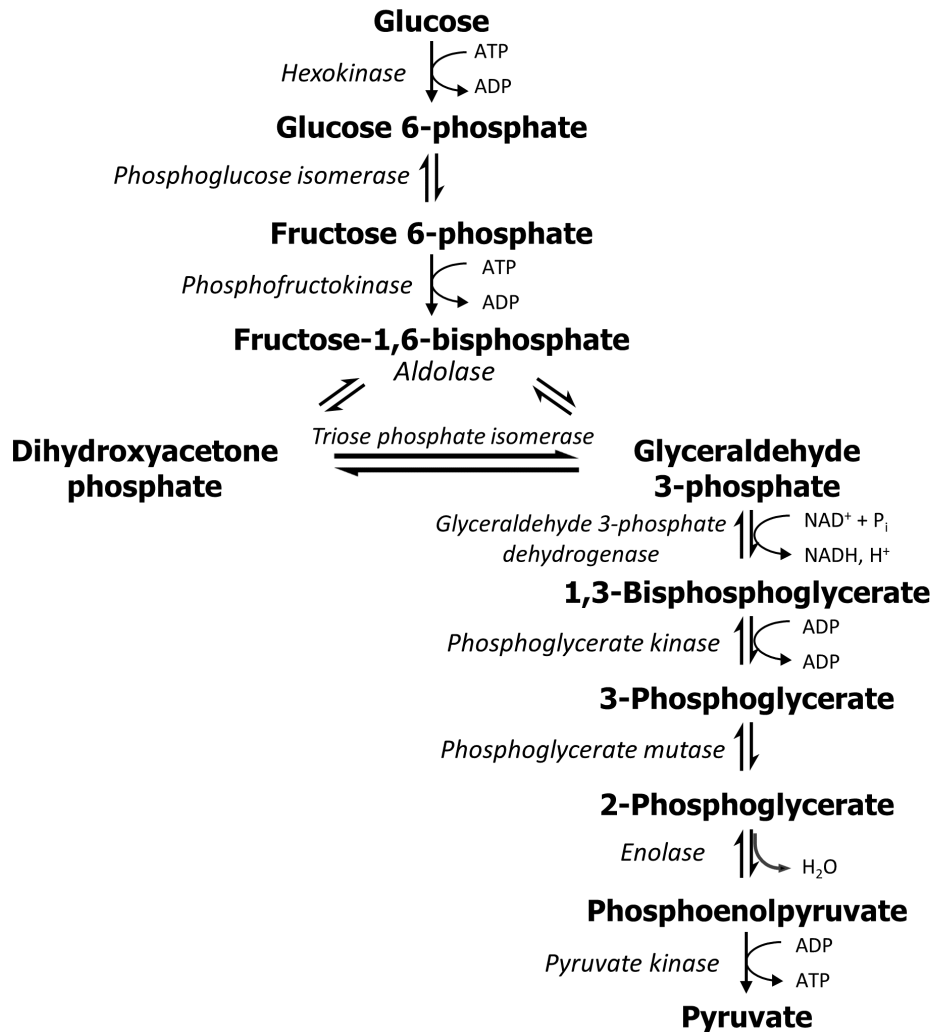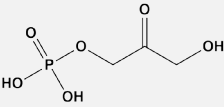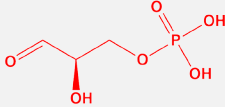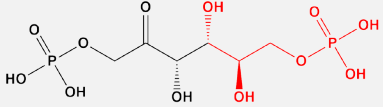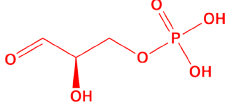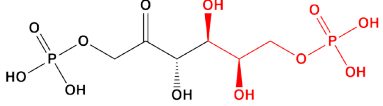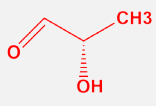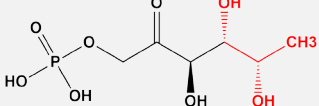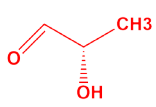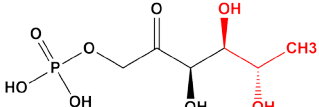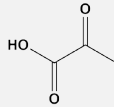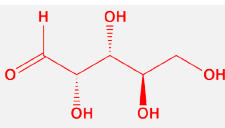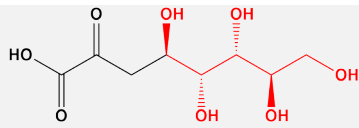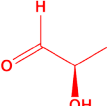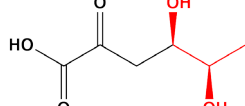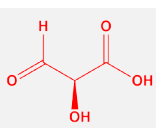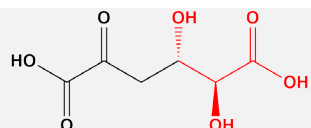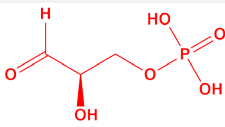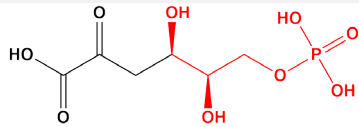
Figure 1-1. Glycolysis pathway.

Schematic representation of the enzymes and chemical intermediates of glycolysis. One molecule of glucose will generate a net of 2 pyruvates, 2 ATP, and 2 NADH. Pyruvate is a substrate for several metabolic pathways, including the citric acid cycle, fatty acid biosynthesis, amino acid biosynthesis, and gluconeogenesis.

1.1.3 Classification

FBP aldolases are lyases (Enzyme Commission number: EC **4**), capable of cleaving bonds by means other than hydrolysis or oxidation. In the subclass of enzymes capable of carbon-carbon bond cleavage (EC **4.1**), the aldehyde-lyases catalyze the reversal of an aldol condensation (EC **4.1.2**) and are hence termed, aldolases. The members of the aldolase class of enzymes can be distinguished by the stereospecific aldol condensation of a donor (nucleophile) to an acceptor (aldehyde) in the aldol condensation reaction. For example, as with FBP aldolase, fuculose-1-phosphate aldolase uses DHAP as a donor but the acceptor is lactaldehyde, producing fuculose-1-phosphate. Further, depending on the stereochemistry of the reaction, the same donor and acceptor can generate different products around the carbon-carbon bond. FBP aldolase produces a 3(*S*)-4(*R*) configuration in FBP because the attack of the nucleophilic donor occurs on the *si*-face of G3P. Conversely, tagatose-bisphosphate aldolase (TBPA) orients the *re*-face of G3P to the donor DHAP affording a 3(*S*)-4(*S*) stereochemistry around the C3-C4 bond, producing tagatose-bisphosphate (TBP). Table I highlights a number of aldolases that are grouped according to their donors and acceptors. Although not exhaustive, Table I demonstrates that several aldolases share common donors (other donors include phosphoenolpyruvate and acetaldehyde (Pricer and Horecker, 1960; Ray and Benedict, 1980; Weissbach and Hurwitz, 1959)).

Table I. Aldolases[1]

Donor	Acceptor	Aldolase [a]	Product
DHAP		**FBP-aldolase**	
		TBP-aldolase[1]	
		Fuc-1-P-aldolase[2]	
		Rha-1-P-aldolase[3]	
Pyruvate		**KDO-aldolase[4]**	
		KDF-aldolase[5]	
		KDG-aldolase[5]	
		KDGP-aldolase[5]	

[a] Abbreviations: FBP, D-frutcose1,6-bisphospahte; TBP, tagatose-1,6-bisphosphate; Fuc-1-P, L-fuculose-1-phosphate; Rha-1-P, L-rhamnulose-1-phosphate; KDO, 3-deoxy-D-mannooctulosonate; KDF, 2-keto-3-deoxy-D-fuconate; KDG, 2-keto-3-deoxy-D-glucarate; KDGP, 2-keto-3-deoxy-6-phosphogluconate.

FBP aldolase (EC **4.1.2.13**) specifically catalyzes the retro-aldol condensation of FBP into the triose-phosphates DHAP and G3P (Figure 1-2) which occurs in the catabolic direction of glucose metabolism (glycolysis). In the reverse direction (gluconeogenesis), FBP aldolase performs the aldol condensation of the aldehyde, G3P, with the ketone, DHAP, to form FBP.

D-Fructose-1,6-bisphosphate
(FBP)

FBP aldolase

D-Glyceraldehyde-3-phosphate
(G3P)

+

Dihydroxyacetone phosphate
(DHAP)
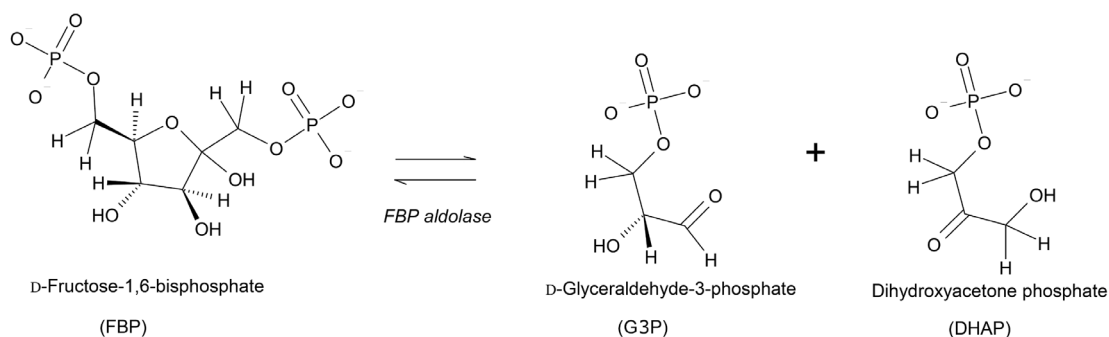
Figure 1-2. FBP aldolase reaction.

Nevertheless, aldolases are not classified according to the nucleophilic donor, but are instead classified by their mechanism of action. Decades of investigation of aldolases from different sources and organisms revealed that two classes of aldolases could be distinguished by the mechanism that is used to stabilize the negative charge that develops on the reaction intermediates (Richards and Rutter, 1961; Rutter, 1964). The first mechanism, used by Class I aldolases, involves the formation of a covalent intermediate between the ε-amino group of a lysine and the ketone of the incoming substrate (FBP or DHAP) (Grazi et al., 1962b). The resulting covalent intermediate is an iminium (commonly referred to as a Schiff base). The iminium creates an electron sink at the C2 carbon of the substrate that stabilizes the formation of the nascent enolate intermediate (enamine). In contrast, Class II aldolases stabilize the negative charge on the enolate intermediate (enediolate) with a divalent metal cation – generally Zn^{2+}, bypassing the need for a covalent intermediate. This polarizes the carbonyl group at C2, creating the electron sink required for cleavage of the carbon-carbon bond. Both strategies ultimately increase the electrophilic nature of the C2 carbon, which enables abstraction of the proton on the O4 hydroxyl group, leading to cleavage of the C3-C4 bond and formation of the enolate intermediates (Figure 1-3).
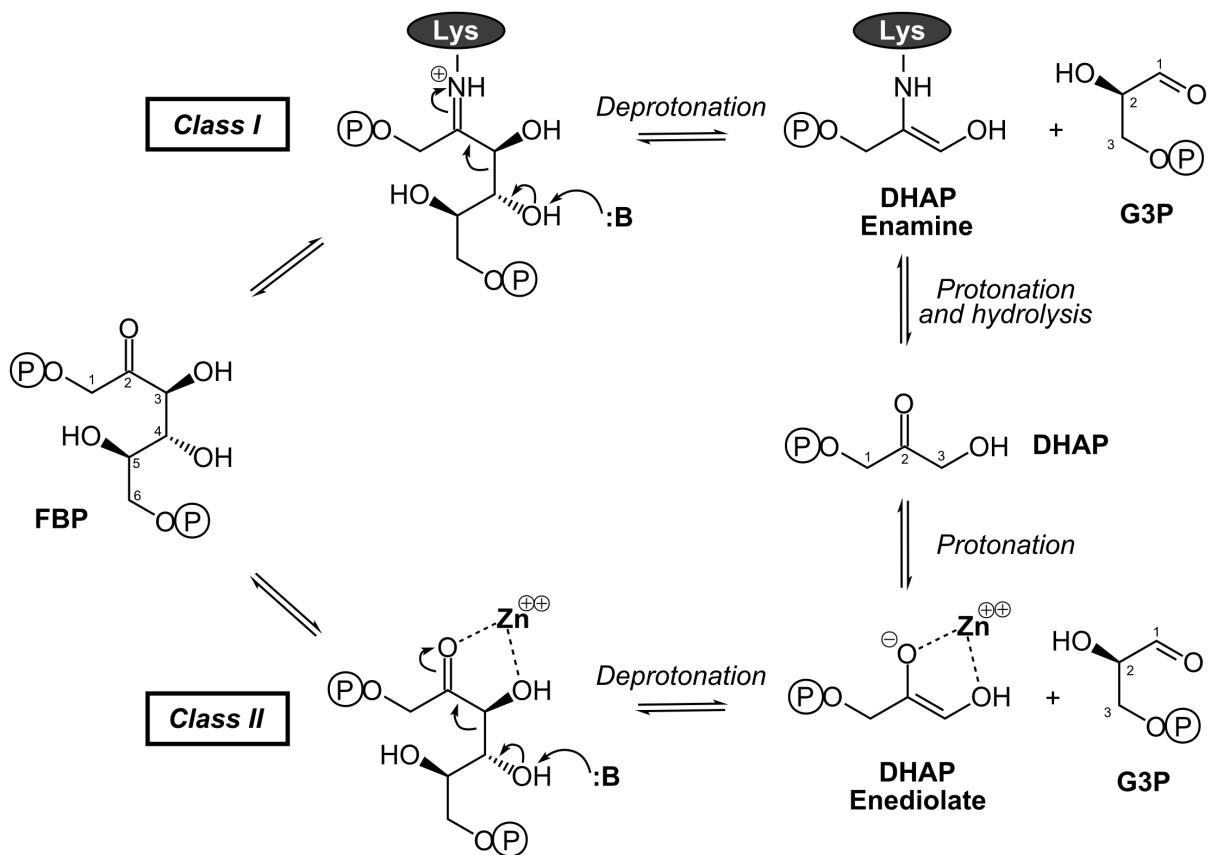
Figure 1-3. Mechanism of FBP cleavage in Class I and II aldolases.

(adapted from St-Jean (St-Jean, 2008))

The distinction between the two classes was first reported after the observation that aldolases were differentially inhibited by chelating agents such as ethylenediaminetetraacetic acid (EDTA), whereby Class II aldolases (first shown in yeast aldolase) were strongly inhibited because of their essential dependence on divalent metal ions (Richards and Rutter, 1961). Conversely, Class I aldolases (typified by the rabbit muscle aldolase) were found to be sensitive to sodium borohydride ($NaBH_4$) treatment, which reduces the Schiff base intermediate to a secondary amine and stabilizes the irreversible complex in the active site (Grazi et al., 1962a). This distinction meant aldolases could readily be classified based on their reactivity to either EDTA (Class II) or $NaBH_4$ (Class I) but early investigators quickly realized that their distribution among different organisms wasn't so apparent.

1.1.4 Distribution of aldolases

The different classes of FBP aldolases show a complex and peculiar distribution in the biosphere. Since FBP aldolase occupies a central role in sugar metabolism, it is ubiquitous in all three major kingdoms of life – archaea, bacteria, and eukaryotes. It was originally assumed that Class I aldolases were restricted to higher forms of life, including animals, plants, protozoans and green algae (Rutter and Groves, 1964) and that Class II aldolases were relegated to lower forms of life such as bacteria, fungi and blue-green algae (Lebherz and Rutter, 1969; Rutter, 1964). The distribution of aldolases in select organisms is illustrated in Figure 1-4. The striking distinction in mechanism together with other structural and functional differences led Rutter (Rutter, 1964) to postulate a convergent evolution of unrelated ancestral molecules.

Eukaryotic organisms were then discovered that produce both Class I and Class II aldolases, as first shown in *Euglena* (Rutter, 1964) and *Clamydomonas* (Russell and Gibbs, 1967). This occurrence is now equally described in prokaryotic organisms – notably *Escherichia coli* (*E.coli*) (Baldwin and Perham, 1978; Stribling and Perham, 1973; Thomson et al., 1998), and *Lactobacillus casei* (London, 1974). Upon observation in *E. coli* that both classes of aldolase were produced when grown on a gluconeogenic carbon source (pyruvate or lactate), but that only Class II was expressed on a glycolytic carbon source (glucose), it was suggested that in these organisms, Class I is better suited for gluconeogenesis while the Class II enzyme is constitutively expressed (Baldwin and Perham, 1978). In general however, most organisms produce only one class of aldolase. Both classes of aldolase are thus represented in each of the three primary kingdoms. Further, certain prokaryotes exclusively contain Class I aldolases, as first discovered in *Micrococcus aerogenes* (Lebherz and Rutter, 1973) and subsequently in *Mycobacterium smegmatis* (Bai et al., 1982, 1975) *Staphylococcus aureus* (Götz et al., 1980) and others. The isolation and characterization of Class I aldolases from a variety of sources have revealed distinguishing features. Eukaryotic Class I aldolases are invariably tetrameric with a subunit molecular mass of approximately 40 *k*Da. Sequence comparisons of the latter suggest a high degree of conservation, particularly in active site residues (Freemont et al., 1988; Kelley and Tolan, 1986). Conversely, prokaryotic Class I aldolases appear to be more diverse than their eukaryotic counterparts. Their oligomeric states range from monomeric to decameric and their subunits range in size from 27 – 40 *k*Da. Further, they are insensitive to carboxypeptidase
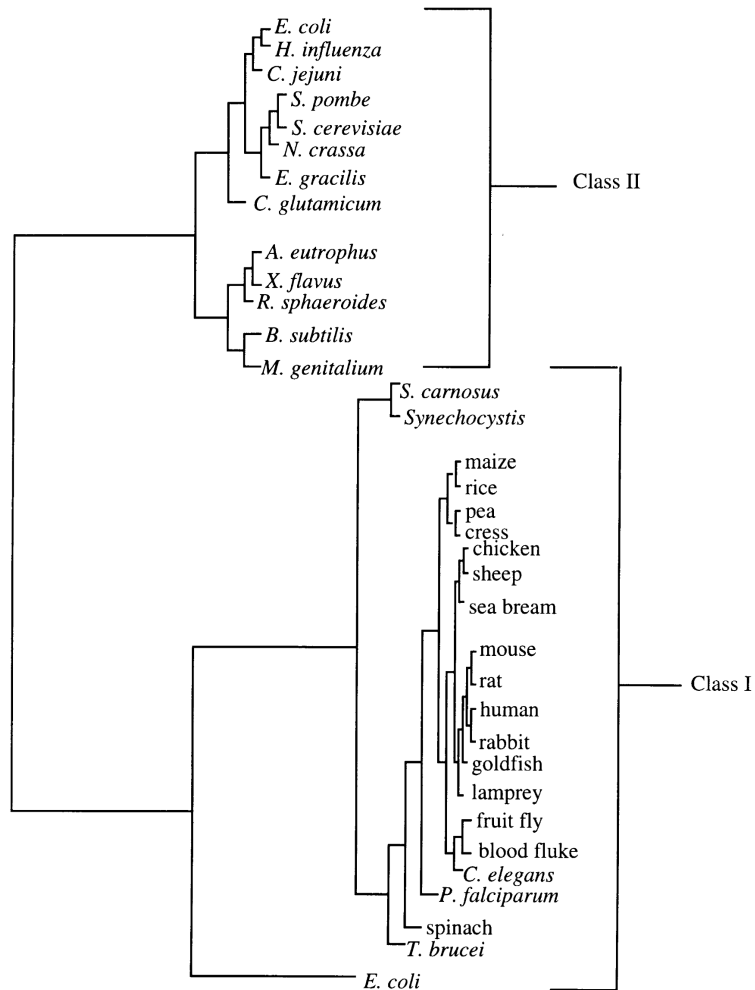
Figure 1-4. Phylogenetic tree of Class I and Class II FBP aldolases.
(taken from Thomson et al., 1998)

treatment, suggesting an alternative to the functional and highly conserved carboxy-terminal tyrosine residue, which is characteristic of eukaryotic Class I aldolases.

Adding to the elaborate puzzle, another sub-class of aldolases, an archaeal type Class I aldolase (Class IA aldolase) was recently identified and characterized in a hyperthermophilic organism (Siebers et al., 2001). Despite functional similarity with classical Class I aldolase in their use of a Schiff-base mechanism, this new family shows no significant sequence similarity with the latter.

These findings demanded a revision of the simplistic phylogenetic proposal by Rutter (Rutter, 1964). The low sequence similarity between Class I and Class II aldolases continues to suggest a convergence of function. However, the discovery of organisms expressing both types suggests the existence of a hypothetical progenote capable of produce both types. Subsequent loss of one of the classes could be explained by the functional redundancy of aldolases (Marsh and Lebherz, 1992). Notwithstanding our speculative understanding of its origins, more recent structural studies on various aldolases have shown that despite having a low sequence similarity, the different classes display a common tertiary fold: the $(\beta\alpha)_8$-(TIM)-barrel fold (TIM – triosephosphate isomerase).

1.1.5   General properties of aldolase

All FBP aldolases, regardless of their low sequence identity (~20%) (Marsh and Lebherz, 1992), adopt the TIM-barrel fold. This architectural type is the most frequently occurring protein fold (known as superfold) in the SCOP database (Structural Classification of Proteins)[2] which categorizes protein structures in the Protein Data Bank (PDB) (Gerstein and Levitt, 1997). It was first observed in triosephosphate isomerase (Figure 1-5B) and consists of eight α-helices on the outside and eight parallel β-strands on the inside that alternate along the peptide backbone (Wierenga, 2001) (Figure 1-5A). Members of the superfold are nearly always enzymes and are most often involved in molecular or energy metabolism in the cell (Nagano et al., 2002). The TIM-barrel fold contains 33 superfamilies, including the aldolase superfamily in which we find the Class I and Class II FBP aldolase families. Notwithstanding the diversity of their catalytic reactions, TIM-barrel proteins share common features including the following:

1. active site residues are always found at the C-terminal end of the β-strands in the barrel and the eight loops following the β-strands (βα-loops), implying that the geometry of the active sites is dictated by composition of the βα-loops (Brändén, 1991);
2. electrostatic calculations demonstrate the existence of a positive potential at the C-terminal end of the barrel, consistent with the preference of TIM-barrel folds to bind negatively charged substrates (Copley and Bork, 2000; Raychaudhuri et al., 1997) ;

---

[2] SCOP database - version 1.75: http://scop.mrc-lmb.cam.ac.uk/scop/

3. active sites frequently contain either phosphate-binding sites (~50% of members) or metal-ion binding sites (~66% of members) – features that are found in FBP aldolases (Nagano et al., 2002; Wierenga, 2001).

Although they ultimately perform the same reaction, Class I and Class II aldolases have distinct active site architectures. The active site of Class I aldolase is deep within the barrel involving several β-strand residues and a mobile, catalytic C-terminal helix that covers the active site (Figure 1-5C), while the active site in Class II aldolases is at the opening of the barrel and involves a catalytic loop (Figure 1-5E) (Sygusch et al., 1987).

The quaternary organization of eukaryotic Class I aldolases is invariably tetrameric with a total molecular mass of 160 kDa (Figure 1-6) (Kawahara and Tanford, 1966). Prokaryotic Class I aldolases are not regular and range in size from 27 – 40 kDa, and assemble into a variety of oligomeric states from monomers to decamers. On the other hand, Class II aldolases are generally dimeric, having a total molecular mass of 80 kDa (Figure 1-7).

As the focus of my studies have been on Class I aldolases, the following sections will be primarily concerned with Class I aldolases. The next section will provide a detailed exposition of the reaction mechanism in Class I aldolase, which will help gain a fuller appreciation of the complexities within an ostensibly simple biochemical reaction.

A
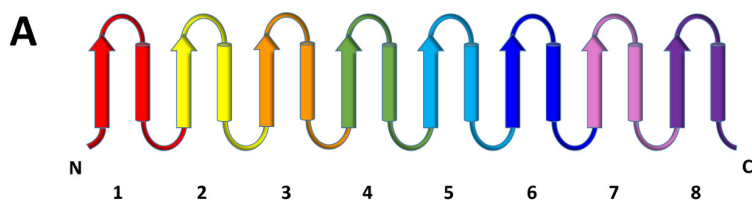
Schematic representation of the secondary structure for the archetype $(\beta\alpha)_8$-TIM-barrel fold – shown here for triosephosphate isomerase.

B
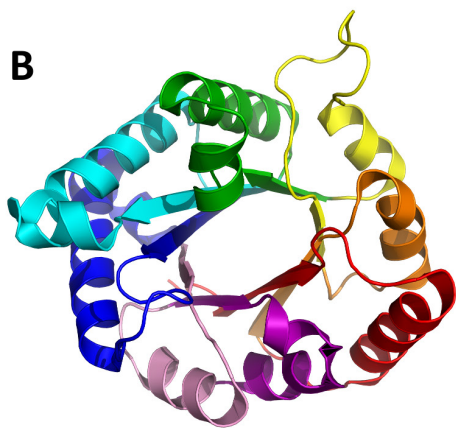
Triosephosphate isomerase (TIM) from *Gallus gallus* (PDB: 1TIM)

C

Class I FBP aldolase from *Oryctolagus cuniculus* (PDB: 1ZAH)

D
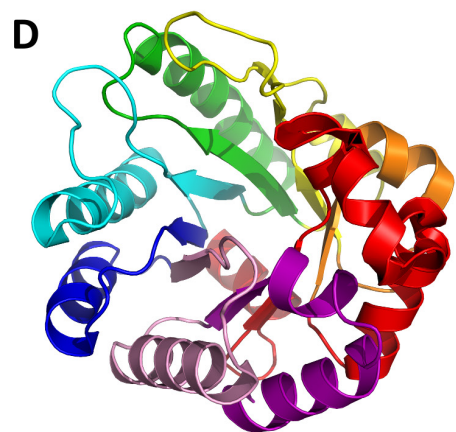
Class IA FBP aldolase from *Thermoproteus tenax* (PDB: 1OJX)

E
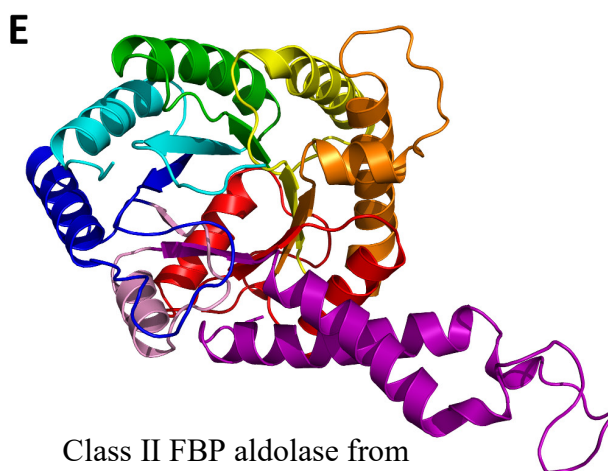
Class II FBP aldolase from *Escherichia coli* (PDB: 1B57)

Figure 1-5. The tertiary structure of various FBP aldolases compared with TIM.

(5A) Representation of the secondary structure (β-sheets: *arrows*; α-helices: *cylinders*) of an archetypal TIM-barrel fold. The repeating (βα) motifs are colored individually and numbered 1-8. (5B-5E) The tertiary fold of TIM monomer and FBP aldolases monomers from each class.
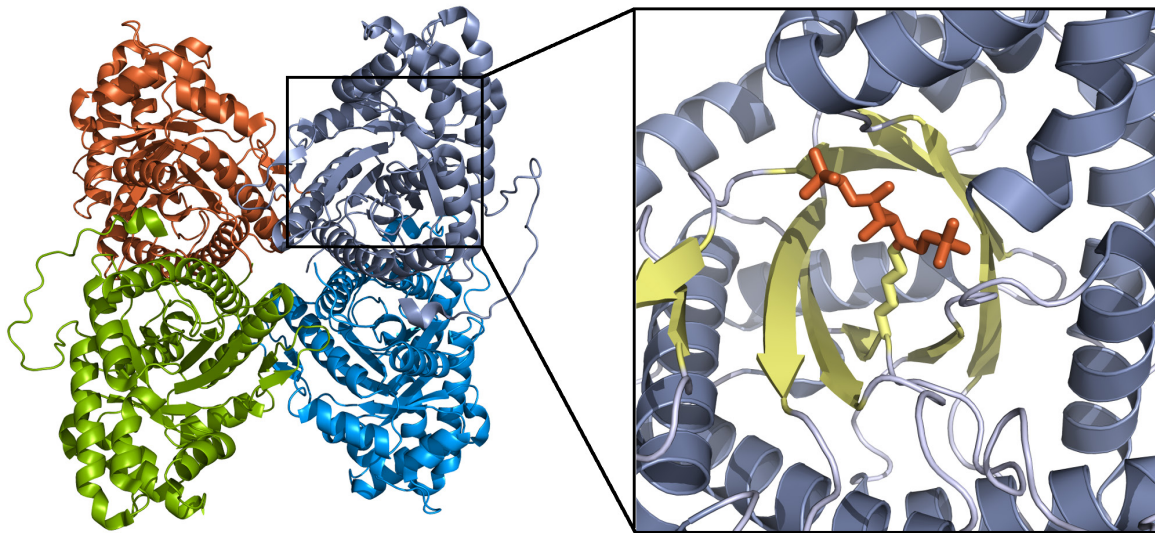
Figure 1-6. Tetrameric quaternary structure of Class I aldolase and view of active site.

The structure depicts a typical Class I aldolase, here an FBP aldolase from rabbit muscle (PDB: 1ZAI) (St-Jean, 2005). The inset on the right reveals a close-up of the active site where FBP (*orange*) is covalently bound to the catalytic lysine. The active site is deep in the β-barrel (*yellow*), surrounding by the helices (*grey*) of the TIM-barrel fold.
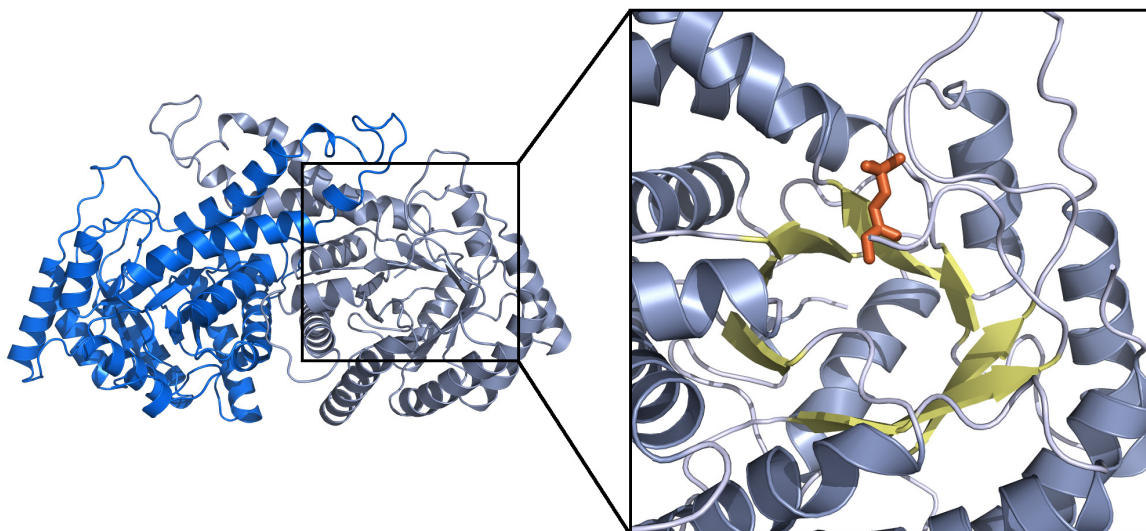
Figure 1-7. Dimeric structure of Class II aldolase and view of active site.

The dimer of a Class II aldolase from *E. coli* is presented (PDB: 1B57) (Hall et al., 1999). On the right, the active site and an inhibitor (phosphoglycolohydroxamate – a DHAP analogue) bound at the substrate binding site. Note the position of the binding site at the cusp of the barrel.

1.2 Reaction catalyzed by Class I aldolase

1.2.1 Rabbit muscle aldolase – a model aldolase

Class I FBP aldolase has received much attention since the attribution of its function by Meyerhof (Meyerhof and Lohmann, 1934). Limited by the technical purification and isolation practices of his generation, early investigators required large amounts of sample in order to conduct experiments. Aldolase from rabbit muscle proved to be an ideal source because of its natural abundance, representing as much as 5% of the protein weight of rabbit muscle (Herbert et al., 1940; Maughan et al., 2005; Taylor et al., 1948). Its abundance and ease of isolation were the reasons that aldolase from rabbit muscle became the model enzyme for Class I aldolases. For several decades, this required the sacrificing of animals to perform isolation of pure enzyme but the advent of molecular cloning techniques and recombinant enzyme expression from bacterial hosts were eventually applied to rabbit muscle aldolase and led to significant yields that have been used since (Morris and Tolan, 1993).

Rabbit muscle expresses one of three known mammalian isoforms – aldolase A (ALDOA). Two other distinct aldolases were detected in mammals – aldolase B (ALDOB) and C (ALDOC) (Peanasky and Lardy, 1958; Penhoet et al., 1966; Warburg and Christian, 1943). They were first identified from observed differences in catalytic properties of aldolase isolated from different tissues. ALDOA is found in muscle and red blood cells; ALDOB is the predominant form in the liver; and ALDOC is found in the brain. Although hybrid tetramers can be formed, the substrate specificity of each isoform in the hybrid is conserved (Penhoet et al., 1967). The substrate specificity of each isoform concurs with the recognized metabolic role of its corresponding tissue. Specifically, the distinction can be made with respect to the enzyme's catalytic preference for fructose-1-phosphate (F1P) or fructose-1,6-bisphosphate (FBP). ALDOA has an FBP/F1P activity ratio of approximately 50:1; the ratio is 1:1 in ALDOB; and the ratio is 25:1 in ALDOC (Penhoet et al., 1966; Rutter, 1964). ALDOB, central to fructose metabolism, occurs almost entirely in the liver and participates in glycogen biosynthesis by hydrolyzing F1P into the triose phosphates (DHAP and G3P) which feed into gluconeogenesis. The loss of activity of ALDOB from mutations is detrimental, and leads to hereditary fructose intolerance (Ali et al., 1998; Hers

and Joassin, 1961). The three isoforms can also be distinguished by their immunological characteristics, with antibody preparations showing little to no cross-reactivity among the isoforms (Penhoet et al., 1966).

The most marked difference between the isoforms occurs at the C-terminus. It was possible to recreate the catalytic fingerprint of one isoform by swapping its C-terminal region onto the core of a different isoform (Berthiaume et al., 1993). Likewise, upon carboxypeptidase treatment (C-terminal cleavage), rabbit muscle aldolase exhibits a 20-fold fall in the rate of cleavage of FBP and cleavage of F1P remains unchanged (Drechsler et al., 1959), suggesting the specificity in ALDOA is afforded by its C-terminus. Sequence homology of the non-conserved terminal residues (~20 C-terminal residues) is sufficient for proper classification of the three isoforms. Contrariwise, sequence comparisons of several Class I aldolases indicates a high degree of homology at the active site, including the three isoforms (Fothergill-Gilmore and Michels, 1993). This suggests that the core amino acids that line the active site serve to ensure a basal activity common to the three isoforms (Kitajima et al., 1990).

For this reason, rabbit muscle aldolase continues to be the workhorse model for studies on Class I aldolase. Further, the human muscle aldolase only differs from the rabbit homolog by 6 amino acids (out of 363); the 6 substitutions are conserved (physicochemical properties) and distant from the active site. The homologs were correctly predicted to have equivalent tertiary structures (Sawyer et al., 1988). This was soon confirmed when several high-resolution structures from different sources were obtained by X-ray crystallographic studies (rabbit muscle - Sygusch et al., 1987; human muscle - Gamblin et al., 1990; and drosophila - Hester et al., 1991). Most of the mechanistic studies have been performed on rabbit muscle aldolase. Accordingly, the following mechanistic considerations are mostly related to the rabbit muscle isozyme.

1.2.2 Mechanism at a glance

Much of the early work involved the use of radiolabeling, enzymatic and isotope exchange experiments. Later studies were structure-based and involved mutational studies. The use of substrate analogues and inhibitors have also been instrumental in elucidating the reaction
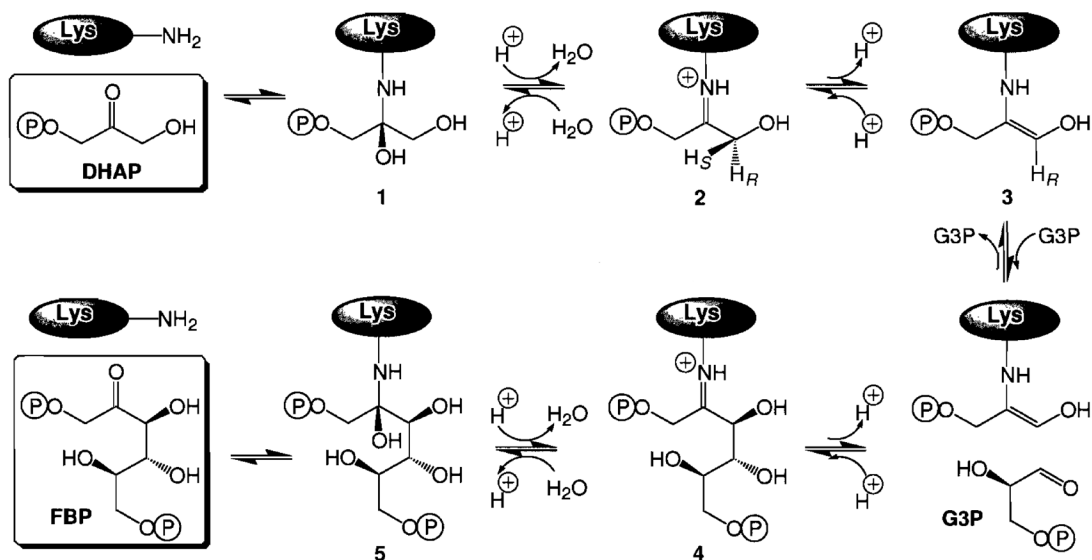
Figure 1-8. General reaction mechanism of Class I FBP aldolases.

mechanism. Here, the general reaction mechanism will be presented from a biochemical and historical perspective, and structural review of essential residues will follow.

A simplified reaction scheme for the aldol condensation reaction in aldolases, outlined in Figure 1-8, proceeds with the formation of an iminium intermediate (Schiff base) between the ε-amino group of the active site lysine (K229 in rabbit muscle) and the carbonyl group of DHAP. The neutral carbinolamine (Figure 1-8 - **species 1**) is a transition to the protonated iminium form (**species 2**). The iminium is activated by stereospecific abstraction of the pro(S) hydrogen at the C3 carbon leading to enamine formation (**species 3**), a stable resonance form of the reactive nucleophile. The following step is the condensation between the activated double bond of the enamine and the carbonyl on G3P, forming the C3-C4 bond and leading to a second iminium species (**species 4**). Hydrolysis of this iminium proceeds via another carbinolamine (**species 5**), and releases FBP. In the cleavage direction, the positive charge of the iminium on **species 4** creates the electron sink that is required for C3-C4 bond cleavage. Although this scheme summarizes the condensation (gluconeogenic) course of the reaction, it is worth noting that it is thermodynamically favoured, with an equilibrium constant of $10^4 - 10^5$ M^{-1}, favouring the formation of FBP (Connett, 1985; Lehninger et al., 1955; Veech et al., 1969). Regardless, both directions involve the intermediates that are shown in Figure 1-8. It was Rose in 1965 (Rose et

al., 1965) who first demonstrated that the reaction proceeds by an ordered sequence whereby G3P can only bind after formation of the covalent enamine intermediate with DHAP. The following sub-sections will describe the findings that exposed each of the intermediates in Figure 1-8.

i. Carbinolamine

The first step involves formation of a non-covalent Michaelis complex between the active site and DHAP. This was demonstrated in a crystal structure (PDB: 1ADO) in which DHAP is shown to adopt three mutually exclusive binding modes (Blom and Sygusch, 1997). One of the modes reveals the catalytic lysine, Lys-229, forming hydrogen bonds such that its' Nζ lone pair is aligned in an incipient conformation favourable for nucleophilic attack at the C2-carbonyl carbon of DHAP. This leads to the formation of the carbinolamine intermediate (**species 1**). The existence of this intermediate was confirmed by ^{13}C NMR (nuclear magnetic resonance) experiments with a DHAP analogue, glycolaldehyde-phosphate (Ray et al., 1983). Subsequent protonation and dehydration at the C2 carbon leads to iminium formation.

ii. Iminium

Treatment of aldolase with NaBH$_4$ after reacting the enzyme with radiolabeled DHAP (^{32}P or ^{14}C) inactivates the enzyme via conversion to a stable secondary amine. Degradation of the enzyme to its components reveals the covalent adduct with the incorporated radiolabel, *N^6-β-glyceryl-lysine* (Grazi et al., 1962a, 1962b), evidence of iminium (**species 2**) formation between DHAP and an active site lysine. The existence of the iminium was also confirmed by inactivation with cyanide, which is postulated to react with the iminium (Cash and Wilson, 1966).

iii. Enamine

The enamine intermediate (**species 3**) is produced upon proton abstraction at DHAP C3 carbon. In reality, the enamine species (neutral) is the more stable resonance form of the incipient carbanion that forms on C3 carbon after proton abstraction. Several lines of evidence demonstrate the presence of this intermediate. First, isotopic exchange experiments with deuterium suggested that a proton is exchanged with DHAP after iminium formation (Bloom

and Topper, 1956; Rose and Rieder, 1955; Rutter and Ling, 1958) and it was next demonstrated that only the pro(*S*) proton at position 3 is exchanged (Rose and Rieder, 1958). Moreover, the presence of the carbanion has been demonstrated with oxidation-reduction indicators such as potassium ferricyanide $[Fe(CN)_6]^{3-}$ and tetranitromethane which oxidize the intermediary complex to hydroxypyruvaldehyde-phosphate (Christen and Riordan, 1968; Healy and Christen, 1973). Additionally, the enamine formation was suggested from spectrophotometric data in which spectral changes were observed at 240 ηm (corresponding to enamine) after addition of DHAP to aldolase (Mehler and Bloom, 1963; Topper et al., 1957). Acid denaturation experiments in equilibrium conditions allowed trapping of intermediates and revealed that 60% of DHAP-bound complex is made up of the enamine form, while 20-24% is in the iminium/carbinolamine form, with the difference being composed of the non-covalent Michaelis complex (Kuo and Rose, 1985).

iv. Aldol condensation and iminium

The ensuing aldol condensation can occur once G3P enters the active site and is positioned appropriately. The proximity of the G3P carbonyl oxygen to an acidic residue, a conserved protonated glutamate, creates the necessary polarization at the G3P carbonyl-carbon to facilitate aldol condensation and form the C3-C4 bond. The result is another iminium intermediate (**species 4**) which has also been validated by NaBH$_4$ reduction, producing glucitol-lysine after protein degradation (Avigad and Englard, 1972). The stereospecificity of this reaction was confirmed when it was observed that only one epimer is formed upon reduction (Di Iasio et al., 1977), meaning the aldol attack forming the C3-C4 bond only occurs on the *si*-face of the carbonyl. The precise reason for this specificity remains elusive and will be the subject of chapter 2. In the cleavage direction, the reversibility of the iminium was confirmed by $^{16}O/^{18}O$ exchange between the carbonyl oxygen of FBP and water molecules (Model et al., 1968). Liberation of FBP occurs by hydration at the iminium. The addition of the water molecule occurs on the *re*-face of the iminium, as it was shown that the active site ε-amino-lysyl group attacks the *si*-face of the C2 carbonyl on FBP to produce the 2(*R*)-carbinolamine (**species 5**) (Di Iasio et al., 1977).

v. Cleavage direction

Prior to iminium formation in the cleavage direction, FBP must first undergo ring opening to expose the free carbonyl in the acyclic form. However, in solution, FBP exists in equilibrium between three forms: the cyclic α-anomer (~20%), the cyclic β-anomer (~80%), and the acyclic form (~2%) (Benkovic et al., 1972; Gray, 1971; Gray and Barker, 1970; Koerner et al., 1973; Swenson and Barker, 1971). Pre-steady state kinetics demonstrated that Schiff-base intermediate formation is faster than the rate of ring-opening, which itself is well documented (Midelfort et al., 1976), suggesting that aldolase preferentially binds the β-anomer and catalyzes ring-opening (Choi and Tolan, 2004). This was confirmed in a crystal structure of aldolase from *Thermoproteus tenax* (PDB: 1W8S) in which the cyclic β-anomer is bound at the active site (Lorentzen et al., 2005). A highly coordinated catalytic water was identified as the potential proton donor to the O5 oxygen on the furanose in the ring-opening mechanism.

1.2.3 Catalytic residues – from structure to function

Much of our understanding of the specific roles of active site residues in catalysis has been either confirmed or discovered in crystal structures of aldolases, which have been deposited in the Protein Data Bank (PDB). More recently, high resolution structures from St-Jean (St-Jean et al., 2005; St-Jean and Sygusch, 2007) have been instrumental in providing a full portrait of the mechanistic roles of active site residues. The role of each conserved residue, illustrated in Figure 1-9 is described below.

i. Lysine

The catalytic lysine responsible for iminium formation with either DHAP or FBP was identified by early investigators as 229 (Lai et al., 1965). Until the first crystal structures, this was the only residue whose role was unambiguous (see Figure 1-10 – panel **A**). A second lysine, Lys-107, was identified in the active site by inactivation with pyridoxal-phosphate, with which it forms an iminium (Anai et al., 1973; Shapiro et al., 1968). Protection experiments with FBP and other substrates indicated that Lys-107 must be located in the active site, and likely
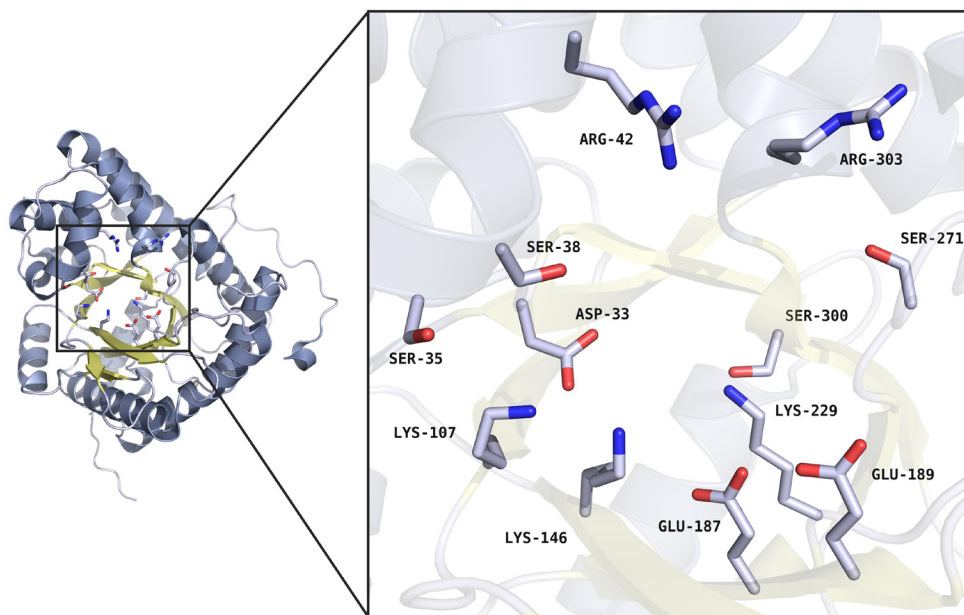
Figure 1-9. Active site of rabbit muscle aldolase (PDB: 1ZAH).

contributes to the binding of the P6 phosphate group in FBP. This would correspond to one of the two binding loci that were identified for inorganic phosphate (Ginsburg and Mehler, 1966), which are now ascribed to a high affinity site – the P1-phosphate site, and a lower affinity site – the P6-phosphate site. Likewise, a third lysine, Lys-146, was revealed in the active site after it was shown to react covalently with a substrate analogue, *N*-bromoacetylethanolamine-phosphate (Hartman and Brown, 1976). Protection with DHAP against inhibition by the analogue suggested it contributed to the binding near the P1-phosphate locus. Subsequent modification of Lys-146 by site-directed mutagenesis (K146A, K146Q, K146L, and K146H) demonstrated the importance of this residue as activity was significantly compromised (Morris and Tolan, 1994).

The linear alignment of the three lysines in the active site raised an interesting question regarding their ionisation states, as proximity of charged groups often results in electrostatic modification of pK_a values. Lys-229 must maintain its' nucleophilic character over a broad range of pHs since the enzyme preserves activity between pH 4 – 11, with a peak between 6 – 9. Structural data supports the hypothesis that Lys-229 is activated by a nearby Glu-187 during iminium formation (Maurady et al., 2002). Further, titration of the pyridoxal-phosphate inactivation suggested a pK_a near 8.0 for Lys-107 (Dax et al., 2005). Likewise, a pK_a between

6.5 and 8.5 was suggested for Lys-146 after titration experiments with *N*-bromoacetylethanolamine-phosphate (Hartman and Brown, 1976). Structural data suggests that Lys-146 remains protonated in order to stabilize the developing negative charge on the C4 hydroxyl that occurs after proton transfer to Glu-187 prior to C3-C4 bond cleavage (St-Jean et al., 2005). Further, Lys-146 also plays a key mechanistic role in facilitating another proton transfer. Activation of the DHAP enamine in the condensation direction requires abstraction of the DHAP C3-pro(*S*) proton, which has been shown to implicate the C-terminal Tyr-363 (St-Jean and Sygusch, 2007). Lys-146 stabilizes the developing negative charge on the phenolate ion during proton abstraction. Moreover, Lys-146 hydrogen-bonds the substrate C4-hydroxyl and assists substrate cleavage by stabilizing the developing negative charge on the C4-hydroxyl during this proton abstraction. The significant inhibition of enamine formation from the iminium as well as cleavage activity in Lys-146 varints (K146M) corroborates this assignment of function (St-Jean and Sygusch, 2007).

ii. Arginine

The implication of arginines in the active site was first shown by inactivation with α-dicarbonyl reagents specific for arginines (Yankeelov et al., 1968). Protection experiments revealed the likely contribution of an arginine to binding at the P1-phosphate site. Structural data showed that the side-chain of Arg-303 exhibits a significant conformational move into the active site cleft that is triggered by substrate binding at the P1-phosphate locus. The Arg-303 guanidinium group forms a salt bridge with the P1-phosphate of all incoming substrates (Choi et al., 2001). This key function is corroborated by mutagenesis of Arg-303 to alanine (R303A) which exhibits a reduced specific activity and a notable increase in the K_m (lower binding affinity) (Choi et al., 1999). The same study demonstrated the importance of two other arginines (by mutagenesis to alanine), Arg-42 and Arg-148, albeit with less impact on substrate binding than the R303A mutant. Arg-148 is implicated in P6-phosphate binding.

iii. Aspartic acid

Several key acidic residues are involved in the reaction mechanism, including Glu-187, Glu-189, and Asp-33. A critical role for Asp-33 in the catalytic mechanism was first proposed from mutational and structural studies (Morris and Tolan, 1993). Site-directed mutagenesis of Asp-

33 mutants (D33A, D33S, D33E) led to drastic loss of activity, specifically relating to enamine formation, whereas the FBP iminium still formed. It was therefore suggested that Asp-33 was responsible for proton abstraction from the C4 hydroxyl during cleavage, a role now ascribed to Glu-187. A subsequent structure showing the Asp-33 carboxylate group in proximity to the C3-proton of DHAP led to a proposed role for Asp-33 in abstraction of the C3-pro(*S*) proton (Choi et al., 2001). However, this is now ascribed to the C-terminal Tyr-363, whose hydroxyl was shown, from structural data, to be within 3Å of the C3 carbon in the iminium in an orientation consistent with incipient proton transfer (see Figure 1-11) (St-Jean and Sygusch, 2007). Nonetheless, the proximity of Asp-33 between Lys-146 and Lys-107 suggests it is involved in stabilizing the cation form of the lysines. This interaction coordinates Lys-146, placing it near O4-hydroxyl. Also, hydrogen-bonding of Asp-33 with C3-hydroxyl in the DHAP enamine intermediate helps maintain co-planarity of the DHAP O3 with respect to the C2 and C3 carbons that is requisite for resonance stabilization of the enamine form. Finally, Asp-33 could serve as a stereoselectivity filter for the substrate skeleton.

iv. Glutamic acid

A combination of mutagenesis and structural studies were also instrumental in highlighting the role of glutamates in the reaction mechanism. Glu-187 mutants (E187Q and E187A) displayed reduced cleavage activity and global pH profiles of the enzyme reaction indicate an acidic inflection point at 5.1, consistent with general base catalysis involving a glutamate (Maurady et al., 2002). Structural data has supported a role for Glu-187 in proton abstraction on the C4-hydroxyl which initiates C3-C4 bond cleavage. Furthermore, multiple roles have been ascribed to Glu-187 as a result of these crystal structures including: a) activation of Lys-229 prior to iminium formation; b) hydrogen-bonding of the FBP C2-carbonyl and C4-hydroxyl, thereby aligning the FBP for nucleophilic attack by Lys-229; c) and a proton transfer role in the conversion of the carbinolamine intermediate to the iminium (St-Jean et al., 2005). The latter role is supported by structural characterization of the enzyme with a competitive inhibitor, D-mannitol-bisphosphate (MBP), which only differs from FBP in the replacement of the 2-keto function by a hydroxyl group in the (*R*)-configuration, mimicking the carbinolamine intermediate (Figure 1-10 – panel **B**). The O2-hydroxyl of MBP hydrogen-bonds intimately with Glu-187, supporting the proton transfer role with respect to the carbinolamine (St-Jean et al.,
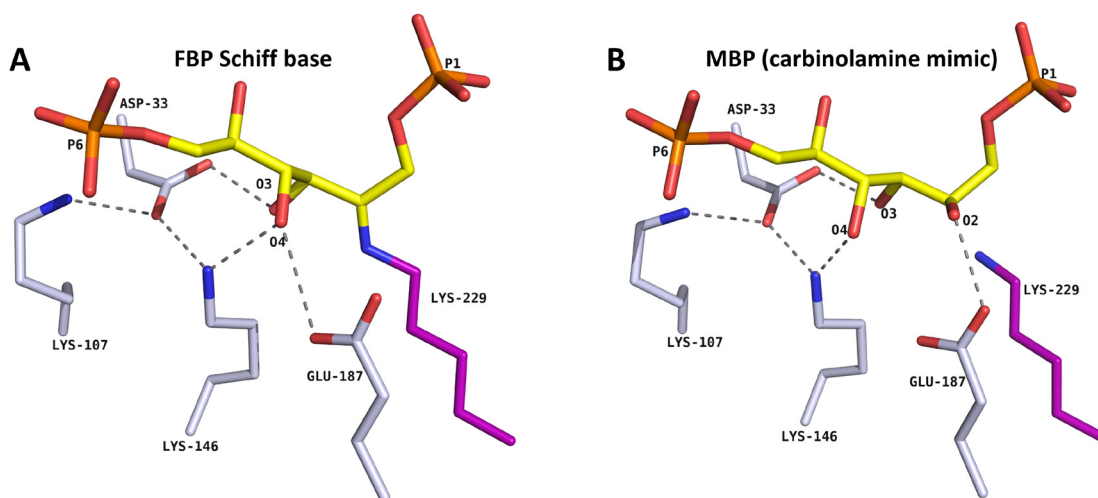
Figure 1-10. Snapshots of catalysis in FBP aldolase showing key intermediates.
Panel **A** shows selected conserved active site residues (discussed in the text) that participate in the reaction mechanism. FBP is covalently bound to Lys-229 via the iminium intermediate (PDB: 1ZAI). Hydrogen-bonding interactions are highlighted (see text for description). Panel **B** shows the binding mode of a substrate analogue, MBP, a carbinolamine mimic (PDB: 1ZAJ). Note the distinctive hydrogen-bond formed between Glu-187 and the O2-hydroxyl of MBP.

2005). A second glutamate, Glu-189, is postulated to intervene in a proton relay system to the active site periphery, but is less critical, as demonstrated by the negligible impact of mutants (E189A) (Maurady et al., 2002).

v. C-terminus and other residues

The importance of the C-terminus is discussed in previous sections. Essentially, the involvement of the C-terminus was discovered early when carboxypeptidase-treated aldolase was found to be significantly less active (Drechsler et al., 1959). The crystallographic structure of a Lys146Met variant from our laboratory, which is defective in deprotonation at the C3 iminium, is consistent with the conserved Tyr-363 facilitating the *re*-face stereospecific pro(*S*) proton exchange with respect to the DHAP C3 carbon atom in the iminium and enamine intermediates of rabbit muscle aldolase (St-Jean and Sygusch, 2007). This corroborates the initial interpretation of biochemical data by Rose et al. (1965) that proton exchange at this step becomes rate-limiting after carboxypeptidase treatment.
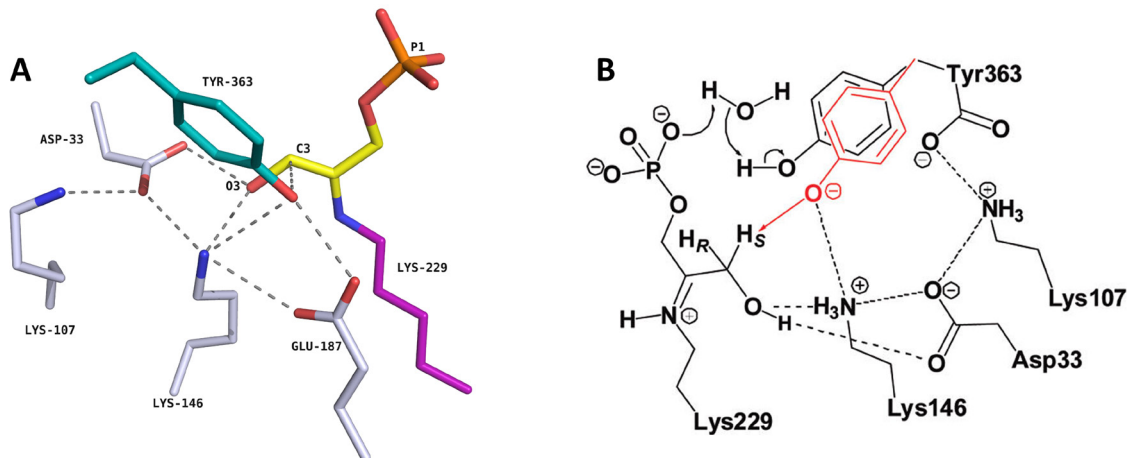
Figure 1-11. Mechanism for stereospecific proton transfer mediated by C-terminus.

The proton transfer mechanism implicates prior activation of the Tyr-363 hydroxyl via the phosphate oxyanion and a water molecule to yield the phenolate, which then abstracts the DHAP C3-pro(S) proton. Panel **A** reveals the crystal structure which helped elucidate this pathway (PDB: 2QUU). Note that Tyr-363 in panel A is not from wild-type FBP aldolase but from the superposed variant K146M (PDB: 2QUT). Panel **B** shows the precise reaction pathway resulting from interpretation of the structural data shown on the left. Stabilization of intermediates is procured by the Lys-107/Asp-33/Lys-146 triad. (panel B taken from St-Jean et al., 2009).

There remaining conserved residues in the active site (see Figure 1-9) include serine residues that mediate hydrogen-binding at the phosphate-binding sites. Ser-271 forms an unusually short hydrogen-bond with the phosphate oxyanion at the P1-phosphate site, indicating a strong active site attachment by the P1-phosphate oxyanion (Blom and Sygusch, 1997). The P6-phosphate binding is ensured by hydrogen-bonds formed with Ser-35 and Ser-38 (and Lys-146).

Figure 1-12 recapitulates the catalytic mechanism, integrating the complete enzymology and crystallography data discussed above and describing FBP condensation in class I FPBAs.
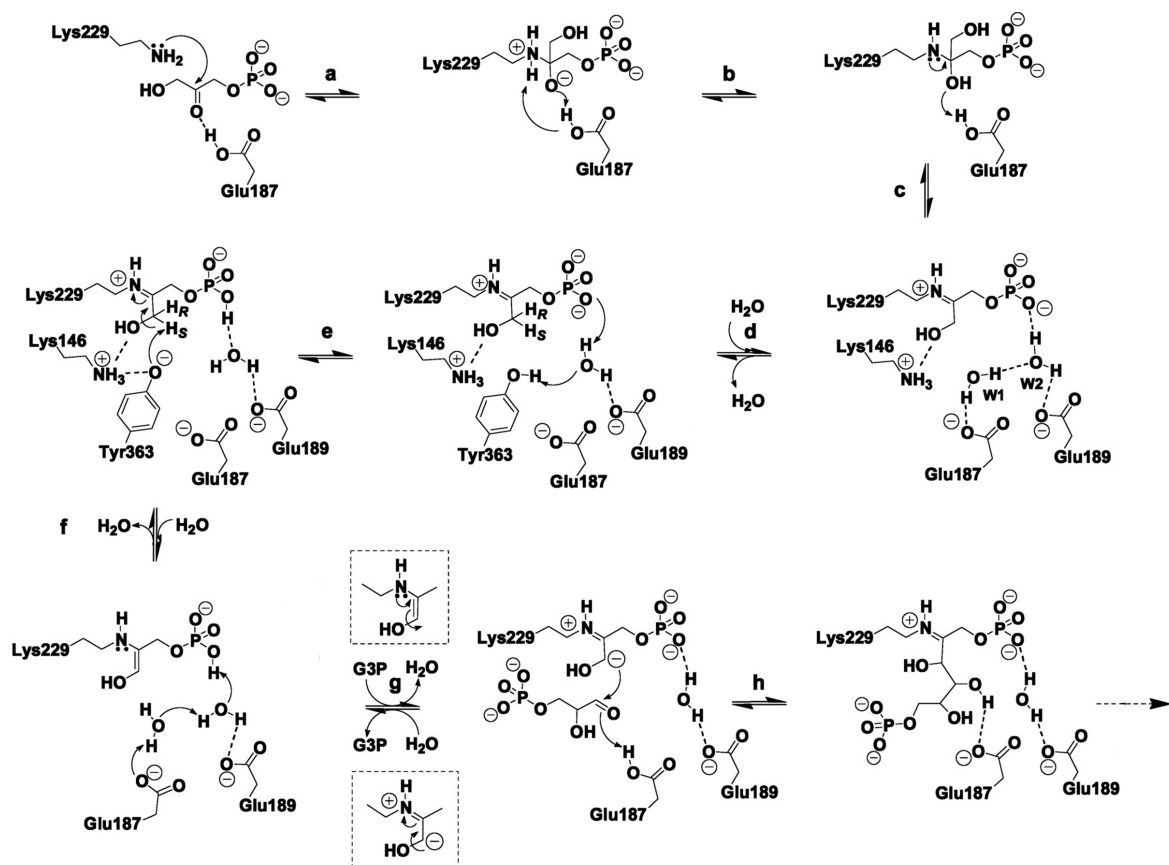
Figure 1-12. FBP condensation in Class I FBP aldolase.

The catalytic cycle begins with DHAP attachment and narrowing of the active site cleft. Glu-187 polarizes the C2-carbonyl and catalyzes iminium formation (reactions *a-c*). The ensuing reactions (*d-e*) involve activation of the Tyr-363 hydroxyl, whose developing charge is stabilized by its proximity to Lys-146. The proton transfer of the C3-pro(*S*) proton is ensured by the phenolate ion (reaction *f*), yielding the nucleophilic enamine intermediate. Glu-189 performs a proton relay to reprotonate Glu-187 (reaction *g*), which is then ready to polarize the carbonyl of the incoming aldehyde, G3P. The C3-carbanion of DHAP attacks the C1-carbonyl of G3P, which becomes protonated by Glu-187, and aldol condensation is completed (reaction *h*). The hydrolysis of FBP is not shown but can be envisaged as the reverse of reactions *a-d*. (adapted from St-Jean and Sygusch, 2007).

1.2.4 Substrates

Experimentation with substrates and analogues has contributed immensely to our understanding of catalysis in aldolases. Structural, enzymological, and other biophysical data can provide a great deal of information regarding active site architecture and mechanism. The interest in studying aldolases stems not only from a mechanistic perspective but also from an organic synthesis perspective. Aldolase is a synthetically useful catalyst for the stereoselective aldol condensation owing to the favourable reaction equilibrium (10^4 M^{-1}) towards the condensation side. Aldolase, although specific for DHAP, can accept aldehydes having a range of structures in addition to its natural substrate, G3P (Bednarski et al., 1989). A noticeable feature inferred from these results is the importance of minimizing bulky groups on the aldehyde. Likewise, DHAP analogs helped identify minimal features required for donor substrates in the condensation reaction. The most salient feature is based on the observation that no reaction occurs if a substitution is made at position 3 in DHAP. This points to the importance of the C3-hydroxyl group of DHAP (Richards and Rutter, 1961). Structural data demonstrates the importance of the hydroxyl group in forming a key hydrogen-bond with Asp-33, stabilizing the proper orientation of the C3-pro(*S*) proton.

The promiscuity towards aldehyde acceptors suggests that aldolase should cleave sugars other than FBP. Indeed, this has been observed for several FBP analogs, including D-xylulose-1,5-bisphosphate (XBP) (Mehler and Cusic, 1967), L-sorbose-1,6-bisphosphate (L-SBP) (Richards and Rutter, 1961; Tung et al., 1954), and D-sedoheptulose-1,7-bisphosphate (SedBP) (B L Horecker and Mehler, 1955). Conversely, other analogs such as D-ribulose-1,5-bisphosphate (RBP) (Rose and Warms, 1985) or D-tagatose-1,6-bisphosphate (TBP) (Hartman and Barker, 1965) are not substrates for the aldolase cleavage reaction but can readily bind the active site, acting as potent competitive inhibitors. The determining feature seems to be the stereochemistry at the C3 and C4 chiral centers where cleavage occurs. Aldolase discriminates against analogs that do not have the 3(*S*)-4(*R*) configuration, such as RBP [3(*R*)-4(*R*)] and TBP [3(*S*)-4(*S*)] (Figure 1-13).
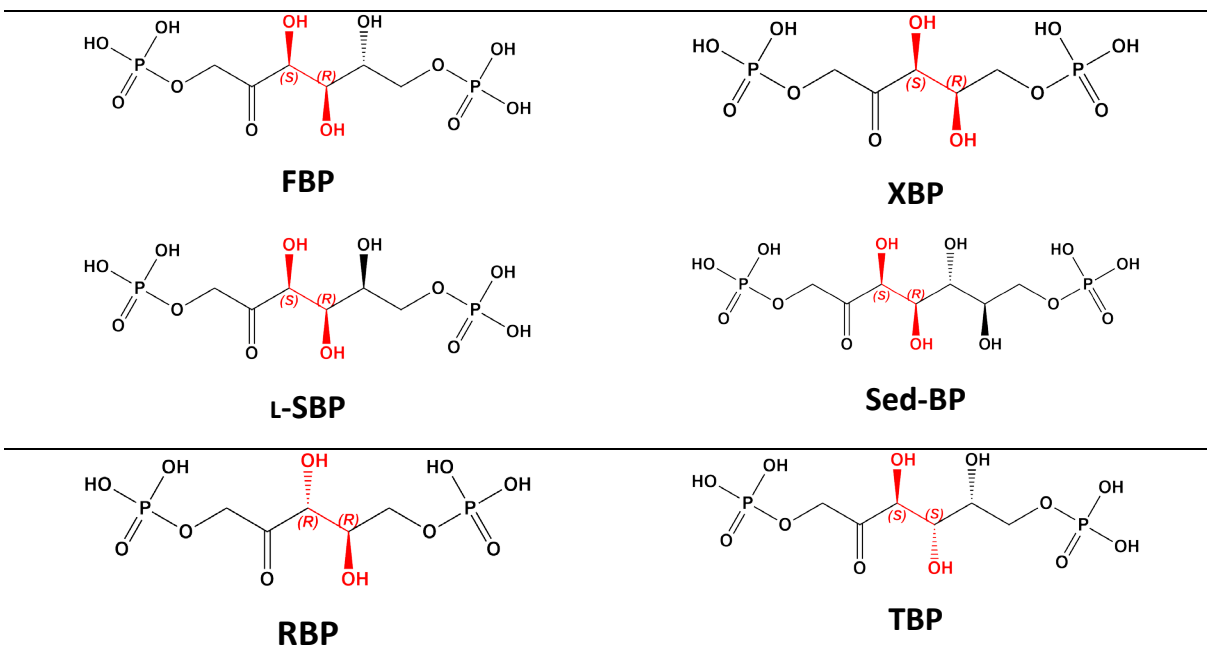
Figure 1-13. FBP analogs: substrates (FBP, XBP, SBP, and SedBP) and inhibitors (RBP and TBP).

The phosphorylation of substrates and analogs, preferably bisphosphorylated, is considered essential. This was recognized by early investigators who observed that bisphosphate analog inhibitors were on average 100 times more effective as inhibitors than their monophosphorylated counterparts. This agrees with K_m values for mono- vs. bisphosphorylated substrates (i.e. FBP vs F1P) (Richards and Rutter, 1961). Minimal binding requires phosphorylation at the P1-phosphate site, as DHAP stripped of its phosphate does not bind to aldolase. Also, substitution of the phosphate on DHAP for a sulfate is insufficient as its weaker basicity cannot promote the activation of Tyr-363 to the phenolate (Grazi et al., 1973). The low affinity of binding for fructose-6-phosphate compared to fructose-1-phosphate indicates the binding at the P6-phosphate site is cooperative but is not necessary whereas the P1-phosphate site is indispensable. The difference is now understood from crystal structures which show the P1-phosphate participating in five hydrogen-bonds compared to three hydrogen-bonds at the P6-phosphate site (St-Jean et al., 2005).

Studies on the selectivity have explored variable stereochemistry of substrate analogs at every position, including the C5 position of FBP. This is of particular interest because of conflicting reports on the discrimination of diastereomers at the C5 position. This relates specifically to the reported inactivation of aldolase by selected aldehydes, notably L-isomer of G3P, L-G3P. The first reports suggested that aldolase performs the aldol condensation of DHAP and L-G3P, producing L-sorbose-1,6-bisphosphate (SBP) (Richards and Rutter, 1961; Tung et al., 1954), albeit at a much slower rate than with incorporation of the D-isomer. Likewise, the cleavage of SBP was reported, although recorded reaction rates were much slower than with FBP. However, later experiments questioned these findings when it was shown by fluorescence quenching (Rose and O'Connell, 1969) and labeling studies (Lai et al., 1968) that aldolase is inactivated by L-G3P. Interestingly, aldolase inactivated by L-G3P is no longer a substrate for carboxypeptidase (Adelman et al., 1968) suggesting an interaction between the C-terminus and the aldehyde bound at the active site. The discrepancies noted for L-G3P and the lower specific activity in the cleavage direction for SBP remain elusive. Recent structural data by our group has provided insight to support the inactivation mechanism of L-G3P and will be the focus of chapter 2.

1.2.5 Methylglyoxal origins and glycolysis

FBP aldolase has been the subject of scrutiny for its suspected role in the production of inorganic phosphate (P_i) and methylglyoxal (MGO). MGO is a highly reactive dicarbonyl metabolite that glycates biological macromolecules, forming advanced glycation end products (AGEs). MGO was initially identified as a key intermediate of glucose metabolism, thought to be in the main stream of glycolysis leading to lactate formation in animals, plants and microorganisms (Dakin and Dudley, 1913; Neuberg, 1913). Cook et al. later observed MGO accumulation in muscle and described the first quantification technique from biological preparations (Case and Cook, 1931; Clift and Cook, 1932). The deleterious effects of MGO and other reactive aldehydes was disseminated by Thornalley and his collaborators after a succession of papers correlated MGO levels with the development of diabetic complications (McLellan et al., 1994; McLellan and Thornalley, 1989; Thornalley, 1990, 1988; Thornalley et al., 1989). This brought MGO interest back into focus and thereafter, several groups reported an association between MGO plasma levels and the vascular complications that arise in diabetic patients (Brownlee, 2005, 2001; Chan et al., 2007; Nakayama et al., 2008; Odani et al., 1999).

Since, MGO-derived AGEs have been shown to underscore several other pathologies including hypertension (Chang and Wu, 2006), atherosclerosis (Baynes and Thorpe, 2000), and neurodegenerative diseases (Dukic-Stefanovic et al., 2001; Kuhla et al., 2005; Reddy et al., 2002; Yu, 2001). Further, there is evidence suggesting that MGO may induce an increase in ROS species, contributing to cellular senescence and aging (Desai et al., 2010). Cells are nevertheless equipped with a detoxification system, the ubiquitous glyoxalase system, which comprises two enzymes, glyoxalase I and II (Figure 1-14) (Thornalley, 1993). These enzymes convert MGO to D-lactate in a conjugation reaction with a catalytic amount of reduced glutathione. However, the system lacks infallibility as the GSH/GSSG ratio can be affected by other redox couples, notably $NADPH/NADP_+$ and thioredoxin$_{red/ox}$ (Wu et al., 2004). The biological consequences of MGO is a vast subject that continues to receive significant attention, but is beyond the scope of the present overview. Here, we are more interested in evaluating the role of aldolase in enzymatically producing MGO.
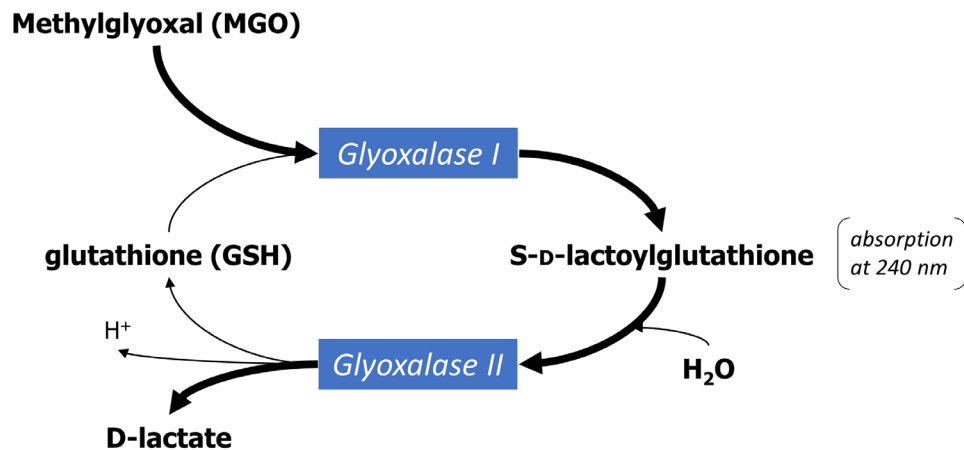
Figure 1-14. The glyoxalase system.

The ubiquitous glyoxalase system involves two enzymes, glyoxalase I (Glo1) and glyoxalase II (Glo2). MGO couples non-enzymatically with reduced glutathione (GSH) to form a hemithioacetal that is recognized by Glo1 and transformed to S-D-lactoylglutathione, which absorbs at 240 nm. Glo2 catalyzes its conversion to D-lactate and regenerates GSH.

Although many sources of MGO have been reported and reviewed (Kalapos, 2008, 1999; Thornalley, 1993), glycolysis appears to be the most important source of MGO. Glycolytic flux appears to be a major determinant of the MGO production (Beisswenger et al., 2001; Liu et al., 2012a; Nemet et al., 2005). The participation of aldolase in MGO release stems from the chemical identification of an intermediate of the aldolase reaction, the pyruvaledyde-aldolase-orthophosphate complex, that is in equilibrium with the enamine intermediate (Grazi and Trombetta, 1978). This complex decomposes slowly with the release of free pyruvaldehyde (MGO) + P_i and is significantly accelerated at acidic pH. It was subsequently proposed from isotope exchange experiments that abstraction of the O3-proton on the enamine intermediate leads to an irreversible β-1,4-elimination that cleaves the ester bond between the C1 and O1, releasing P_i (R Iyengar and Rose, 1981). Subsequent hydrolysis releases free MGO.

However, the relevance of these findings is questionable since P_i release and MGO production from aldolase appears to be influenced by acidification, the technique used to quench the enzyme activity (Kuo and Rose, 1985). Further, MGO release can be suppressed by protection with an aldehyde acceptor (G3P) (Rae et al., 1992). Work in our laboratory using

non-acidic conditions has also shown the importance of Ser-271 in binding the P1-phosphate and minimizing P_i release. A Ser-271 variant to alanine (S271A) exhibits higher P_i release than the wild-type enzyme (Munger, 2002), which is explained by a loss of the conserved strong hydrogen-bond that forms between Ser-271 and the P1-phosphate. In the MGO pathway, P_i is a better leaving group in the S271A mutant. Hence, the biological significance of aldolase with respect to MGO remains conjectural. A recent study investigated the role of aldolase with respect to MGO formation in different cell types. It was found that MGO formation in insulin-sensitive cells is different than that in insulin-insensitive cells. Insulin up-regulates aldolase A and enhances MGO formation in cultured 3T3-L1 adipocytes (Liu et al., 2012a). However, aldolase B appears to be the primary enzyme responsible for MGO overproduction in high glucose-treated insulin-insensitive vascular smooth muscle cells (VSMCs) and endothelial cells (ECs) (Liu et al., 2012b, 2011). In VSMCs and ECs, fructose up-regulates aldolase B expression while high glucose is converted into fructose, which results in MGO formation, presumably by the downstream spontaneous decomposition of triose-phosphates. Likewise, glucose-induced expression of aldolase A in adipocytes presumably contributes to MGO formation by increasing the triose-phosphate pool. Work from our group will be presented in a later chapter that will enrich the discussion surrounding aldolase and its relation to MGO. The issue remains as to whether aldolase contributes to MGO formation by a promiscuous active site reaction or by increasing the triose-phosphate pool which decomposes non-enzymatically to MGO.

In addition to aldolase, it is relevant to briefly consider other reported sources of MGO. MGO is produced in the course of carbohydrate, lipid and amino acid metabolisms, and involves both enzyme-catalyzed and non-enzymatic reactions. The main routes of enzyme-catalyzed MGO formation are well documented and have been reviewed in several papers (Cooper, 1984; Kalapos, 2013, 1999; Leoncini, 1979; Thornalley, 1993). They include MGO synthase (MGS – see below), triosephosphate isomerase (TIM – see below), cytochrome P450 2E1 (CYP 2E1) (Gonzalez, 1988), and semicarbazide-sensitive amine oxidase (SSAO) (Yu et al., 2003). A two-step reaction catalyzed by the cytochrome enzymes, acetone and acetol monooxygenase, is responsible for the conversion of acetone to MGO during fatty acid oxidation (Casazza et al., 1984). Adding to this pathway is the spontaneous conversion of ketone bodies (acetoacetic acid and β-hydroxybutyric acid) to acetone (Beisswenger, 2005). Protein catabolism also contributes
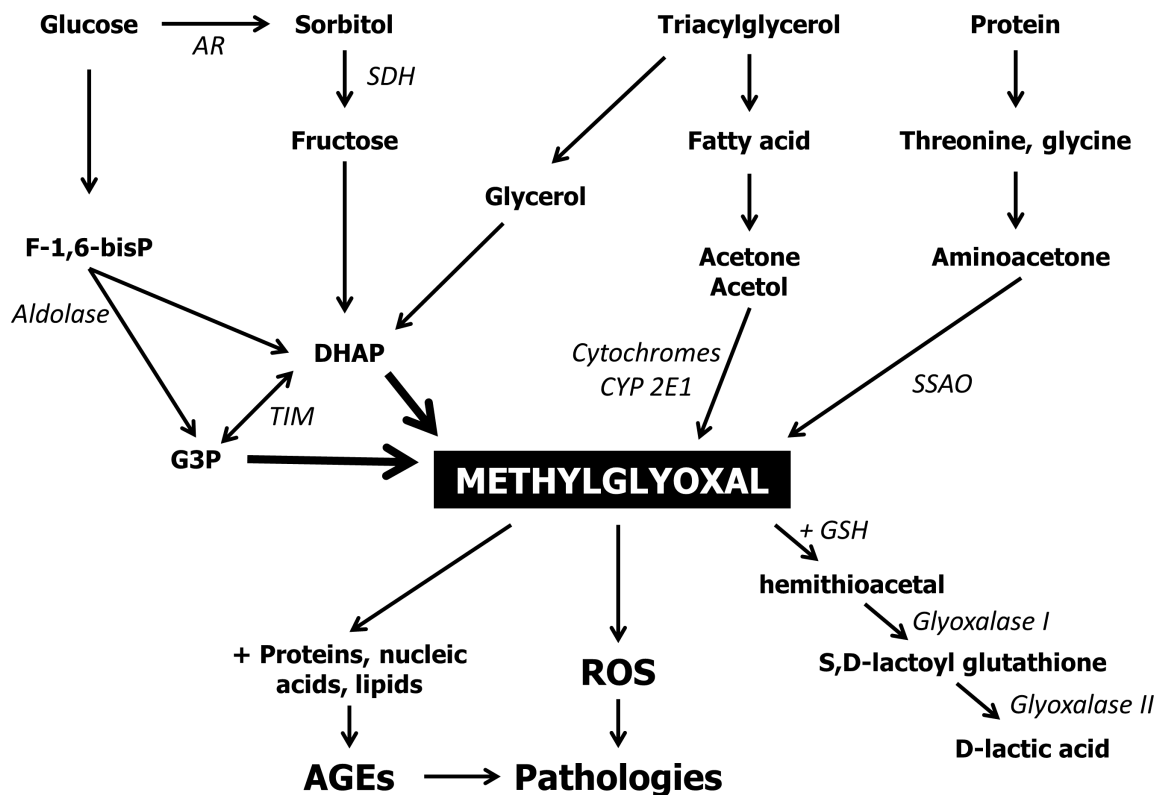
Figure 1-15. Pathways of methylglyoxal metabolism.

Abbreviations: AR, aldolase reductase; SDH, sorbitol dehydrogenase; F-1,6-bisP, fructose-1,6-bisphosphate; G3P, glyceraldehyde-3-phosphate; DHAP, dihydroxyacetone phosphate; TIM, triosephosphate isomerase; SSAO, semicarbazide-sensitive amine oxidase; AGEs, advanced glycation end-products; ROS, reactive oxygen species; GSH, reduced glutathione. Thick arrows represent important sources of methylglyoxal. For details, see text. (adapted from Desai et al., 2010)

to the formation of MGO. The catabolism of threonine and glycine involves their conversion to aminoacetone in the mitochondria, which is deaminated by SSAO, where MGO is a by-product of the reaction. The different sources of MGO formation are summarized in Figure 1-15.

MGO formation linked to carbohydrate metabolism depends on the generation of triose-phosphates (DHAP and G3P). Another glycolytic enzyme, triosephosphate isomerase (TIM), which catalyzes the isomerization of DHAP and G3P, is also responsible for the formation of MGO (Radha Iyengar and Rose, 1981; Richard, 1991, 1985). Studies on the non-enzymatic reactions of triose-phosphates have shown that TIM is a victim of the highly labile enediolate

phosphate intermediate (Figure 1-16), which decomposes to MGO + P_i (Richard, 1984). TIM is apparently unable to suppress the side-reaction during its interconversion of the triose-phosphates. The triose-phosphates are inherently unstable and rapidly decompose to MGO, according to the general scheme shown in Figure 1-16. Estimates for the rate of production from enzymatic and non-enzymatic generation of MGO indicate that enzymatic contribution by TIM is minor compared to the spontaneous decomposition of triose-phosphates (Phillips and Thornalley, 1993; Richard, 1993).
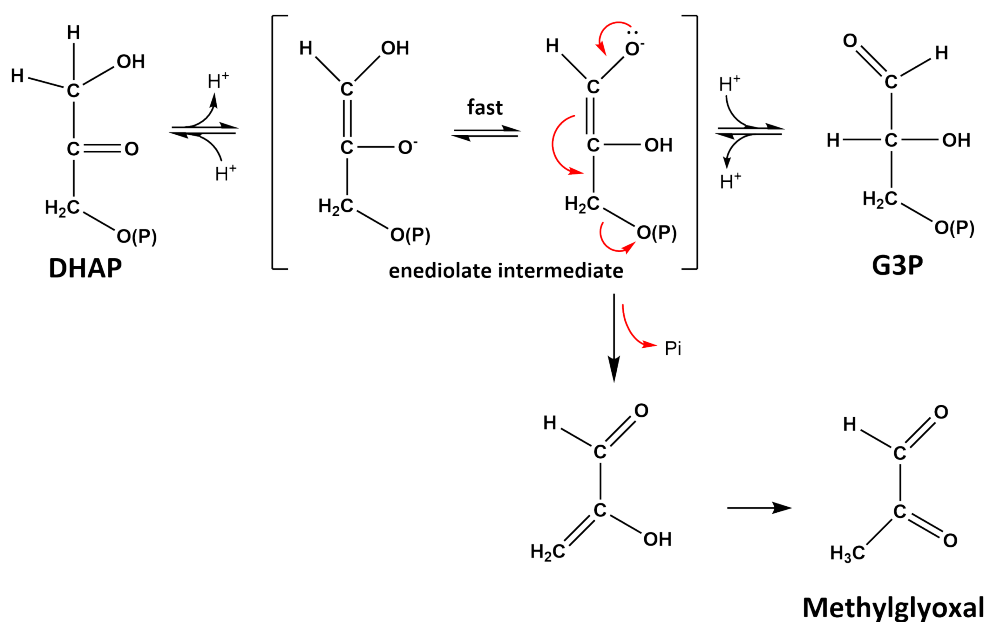
Figure 1-16. General decomposition scheme of triose-phosphates to methylglyoxal.

TIM (triosephosphate isomerase) catalyzes the isomerization between the triose-phosphates DHAP and G3P by using an enediolate intermediate (in brackets), which falls victim to decomposition by β-elimination (arrows in red), leading to P_i release and formation of MGO. This scheme also represents the general mechanism by which the triose-phosphates decompose in solution. MGS (methylglyoxal synthase) recognizes DHAP and catalyzes its conversion to MGO by the general pathway shown here. The enediolate intermediate is a shared feature in both TIM and MGS (see text for more details).

Interestingly, several organisms are equipped with MGSO, an enzyme that specifically synthesizes MGO. First identified in *E. coli* (Cooper and Anderson, 1970; Hopper and Cooper, 1971), MGS inhibition by P_i has led to the suggestion that the enzyme is regulated by P_i and in this way plays a role in the control of glycolysis depending on the availability of intracellular P_i (Cooper, 1984). Remarkably, MGS and TIM, which share neither sequence nor structural similarities, both bind DHAP converting it to a *cis*-enediolate intermediate. In both reactions, the first step involves the stereospecific abstraction of the C3-proton of DHAP to form the common enediolate intermediate. However, MGS abstract the pro(*S*) proton whereas TIM abstracts the pro(*R*) proton. TIM reprotonates the enediolate intermediate at C2 to form G3P. Conversely, MGS catalyzes the β-1,4-elmination of the phosphate from the enediolate intermediate, leading to release of the enol form of MGO (Marks et al., 2001). Limiting this side-reaction in TIM is likely the rate-limiting step of P_i release.

Over the years, many hypotheses have been provided to explain the ubiquitous nature of the glyoxalase system and the generation of MGO. The existence of MGS in some organisms suggests a role for its production in phosphate supply of operating glycolysis in conditions of phosphate deficiency (for these organisms). However, it remains unknown whether this type of regulation also exists in higher vertebrates. Altogether, a better understanding of MGO metabolism is critical for developing strategies to mitigate the clinical manifestations of MGO-derived pathologies.

1.3 Class I Aldolase as a therapeutic target

1.3.1 Targeting Aldolase – generalities

For decades, the interest in studying FBP aldolase has emerged primarily from a mechanistic perspective. Inhibition studies have provided complimentary information regarding the mechanism, dimensions, and flexibility of the active site. However, the growing understanding of aldolases' numerous roles in the cell has exposed opportunities for targeting aldolase from a clinical perspective. The abundance of aldolase in the cell, comprising as much as 5% of the soluble protein weight (Taylor et al., 1948), reveals the importance of aldolase's functions, which extend beyond its traditional role in glucose metabolism. Years of research relating to inhibition studies has provided a worthy foundation for future development of inhibitors. Gefflaut et al., (1995) provides an exhaustive compilation of the compounds and substrates that have been reported in the literature. Inhibition constants (K_i) and Michaelis constants (K_m) are reported for each compound with varying degrees of precision depending on the techniques and experimental conditions used. The multistep mechanism of aldolase lends itself well to the design of mechanism-based inhibitors. It is worth noting that inhibitors against Class II aldolases are actively developed, particularly in targeting the causative agent of tuberculosis, *Mycobacterium tuberculosis*. As this is beyond the scope of current overview, it will not be specifically addressed; refer to the following for more information: (Capodagli et al., 2013; Coinçon, 2010; Daher and Therisod, 2010). Below, the biological significance of targeting Class I aldolase will be discussed in three noteworthy contexts: 1) as a general target in cancer cells; 2) against microorganisms where glycolysis represents a unique energy source, such as parasitic protozoa; 3) and in modulating interactions with cellular partners.

i. Cancer

Glucose metabolism in cancer cells is characterized by a marked increase in both glucose uptake and aerobic glycolysis – the fermentation of glucose into lactate in the presence of oxygen, otherwise known as the "Warburg effect". This phenomenon was first proposed by German physiologist and Nobel laureate, Otto Warburg, who showed in the 1920s that tumor cells produce higher levels of lactate compared to normal tissues, even in the presence of oxygen
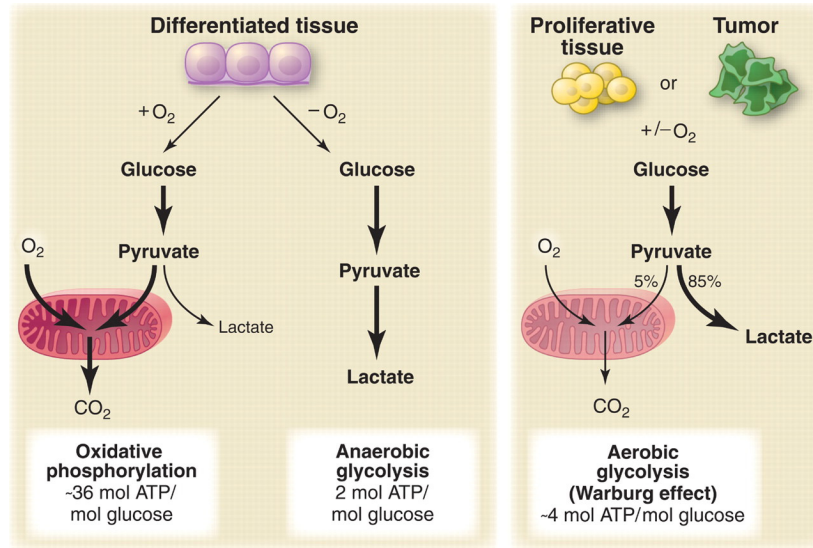
Figure 1-17. Schematic representation of the differences between oxidative phosphorylation, anaerobic glycolysis, and aerobic glycolysis (Warburg effect).

In the absence of oxygen, differentiated tissues convert glucose to lactate. Cancer cells however, follow this pathway regardless of oxygen – a process known as aerobic glycolysis (Warburg effect) (taken from Vander Heiden et al., 2009).

(Figure 1-17) (Warburg, 1956; Warburg et al., 1927). The Warburg effect has been demonstrated in different types of tumours and the concomitant increase in glucose uptake is exploited clinically for the detection of tumours using ^{18}F-fluorodeoxyglucose positron emission tomography (FDG-PET). Ongoing conceptual and empirical advances over several decades have led to the acceptance of altered metabolism as one the hallmarks of cancer, and has been extensively studied and reviewed (Hsu and Sabatini, 2008; Koppenol et al., 2011; Vander Heiden, 2011; Vander Heiden et al., 2009).

Still, the apparent contradiction that cancer cells use glycolysis to produce ATP instead of the more efficient oxidative phosphorylation remains ambiguous but several explanations have been put forward. For example, carbon from glucose is used to replicate the biomass in proliferating cells. Therefore, converting all the glucose to CO_2 to maximize ATP production via oxidative phosphorylation would be counterproductive as some of the glucose needs to be diverted to macromolecular biosynthesis. And so, a better understanding of the various components of cancer cell metabolism is paramount to identifying the potential points of

therapeutic intervention. Insofar, the most successful targets have been enzymes involved in nucleotide synthesis (Vander Heiden, 2011), but efforts to target enzymes that relate to the Warburg effect are in their infancy. A number of targets have been suggested and these include the pivotal glycolytic enzymes. Among these, aldolase was recently acknowledged as a potential target following the marked effects observed on cancer cell proliferation in an aldolase knockdown model (Lew and Tolan, 2012).

Other glycolytic enzymes have also been targeted by RNA interference (RNAi) in transformed cells, with varying degrees of effects. For example, hexokinase and phosphofructokinase knockdown induces cell cycle delay and increased apoptosis (Calvo et al., 2006; Peng et al., 2008); phosphoglucoisomerase knockdown results in reversal of the epithelial-to-mesenchymal transition (Funasaka et al., 2007); and lactate dehydrogenase interference increases sensitivity to hypoxia (Fantin et al., 2006). However, the effect on proliferation is modest (10 – 25%) in most knockdown studies. Remarkably, aldolase knockdown has the greatest effect, inhibiting cell proliferation by 90% (Lew and Tolan, 2012). This effect appears to be related to the non-glycolytic functions of aldolase, notably its role in actin filament organisation. Aldolase is known to contribute to various cellular functions related to regulation of cell shape and mobility, actin dynamics, and ATP biosynthesis (discussed in more detail in a later section). ALDOA is highly expressed in a variety of malignant cancers, including lung squamous (Du et al., 2014; Poschmann et al., 2009; Rho et al., 2009), renal cell (G et al., 1975), and hepatocellular carcinomas (Chaerkady et al., 2008). Depletion of ALDOA in lung squamous carcinoma reduces the cell motility and tumorigenesis (Du et al., 2014). Together, these findings suggest aldolase is a potential target for cancer therapy.

ii. Anaerobic parasites

The parasitic protozoa *Trypanosoma* and *Leishmania* are the causative agents of highly disabling and potentially fatal diseases including African sleeping sickness (*Trypanosoma brucei*), Chagas disease (*Trypanosoma cruzi*) and leishmaniasis (Molyneux and Ashford, 1983). They are of medical importance because they symptomatically infect humans with a reported 80 000 deaths in 2013 [10 600 (chagas) + 62 500 (leishmaniasis) + 6 900 (sleeping sickness)] down from a reported 88 000 in 1990 (Murray and al., 2015) for 65 million people at risk.

Trypanosomiasis also significantly affects human nutrition through their impact on food animals by killing 3 million cattle per year (*WHO | Trypanosomiasis, human African (sleeping sickness)*, 2016). A number of drugs have been used in the treatment of trypanosomal infections with visible improvements on the death rate.

However, currently used drugs (suramin, pentamidine, and other arsenical derivatives) often induce severe toxic side effects, and resistance against these drugs is spreading (Howells, 1985). The most recent treatment involves a combination therapy with eflornithine and nifurtimox, and appears to be equally or more effective than the individual drugs but the concern of drug resistance persists (Priotto et al., 2009). Therefore, the need for broad spectrum, inexpensive, highly efficient, and nontoxic drugs remains a priority.

Glycolysis represents a promising target for new drugs because this pathway plays an essential role in their ATP supply, glycolysis being its sole source of energy. In principle, inhibition of any step of glycolysis should lead to arrest of the glycolytic flux and concomitant death of the parasite. Unique structural features in the parasite has allowed for the design of selective compounds that can discriminate against the mammalian counterpart (Opperdoes, 1987). Several glycolytic enzymes have been inhibited, producing varying degrees of efficacy in trypanosomatids (Verlinde et al., 2001). Aldolase has been considered – selective irreversible inhibition has been reported (Dax et al., 2006) and work is ongoing.

iii. The moonlighting functions of aldolase

The abundance of aldolase in the cell has warranted suggestions that it has considerable roles outside of glycolysis and gluconeogenesis. Accordingly, several interactions with aldolase have been reported. Notably, aldolase influences cytoskeletal dynamics by interacting with actin and tubulin. This was first established through histochemical and biochemical studies showing the localization of several glycolytic enzymes within the I-band of muscle fibre (Arnold et al., 1969; Sigel and Pette, 1969). Aldolase was found strongly interacting with F-actin, promoting the cross-linking of actin filaments *in vitro* (Arnold and Pette, 1970, 1968; Clarke and Masters, 1975; Clarke and Morton, 1976; Morton et al., 1977; O'Reilly and Clarke, 1993; Wang et al., 1996). Also, binding of aldolase to α-tubulin was described (Karkhoff-Schweizer and Knull, 1987; Walsh et al., 1989) and promotes the bundling of microtubules (Volker et al., 1995;

Volker and Knull, 1997). The tetrameric arrangement of aldolase provides the multiple binding sites required for such activity. These findings, along with similar features for other glycolytic enzymes, support the notion that the cytoskeleton and microtubule network provides a scaffold that allow for the efficient delivery of substrates and products. Therefore, targeting the interface between aldolase and its binding partners has been considered for modulating cytoskeletal dynamics.

The promiscuous interaction of aldolase with other cellular partners has been described, and includes the glucose transporter GLUT4 (Kao et al., 1999), phospholipase D2 (Kim et al., 2002), light chain 8 of dynein (Navarro-Lérida et al., 2004), the erythrocyte anion exchanger Band 3 protein (Strapazon and Steck, 1976), the actin nucleator Wiskott-Aldrich Syndrome protein (WASP) (Buscaglia et al., 2006), and sortin nexin 9 (SN9) (Lundmark and Carlsson, 2004). In most cases, aldolase seems to be tethered for structural rather than catalytic purposes, often participating as a bridge between a partner and the cytoskeleton. Furthermore, all of these interactions are inhibited by the binding of the products or substrates of aldolase, indicating that they rely on free, inactive pools of the enzyme. Likewise, aldolase from apicomplexan parasites, such as *Plasmodium falciparum* (*P. falciparum*) (causative agent in malaria) and *Toxoplasma gondii* (*T. gondii*) (causative agent in toxoplasmosis), has scaffolding activity that connects the cytoplasmic tails of transmembrane adhesin molecules to the interior cystoskeleton of the parasite (Buscaglia et al., 2003; Jewett and Sibley, 2003). In the case of *T. gondii*, the coupling of the adhesin micronemal protein 2 (MIC2) to the actin filaments is achieved through the intermediary of aldolase, and promotes the antero-posterior redistribution of MIC2 molecules, which is critical for parasite motility and host cell invasion. Mutation studies involving binding-incompetent aldolase demonstrated that it is essential for efficient host cell invasion (Starnes et al., 2009). Specific disruption of this complex may allow selective prevention of cell host invasion by apicomplexan parasites. However, the limited structural data available describing this interaction is delaying any major advances on this front.

So far, a minimal aldolase binding motif was established and helped identify novel aldolase binding molecules among human proteins (Buscaglia et al., 2006). A common feature that surfaced was the presence of a short acidic sequence, often containing a sub-terminal tryptophan residue. One such motif was identified in WASP. WASP family proteins are critical regulators

of actin dynamics that bind to actin monomers and that activate the Arp2/3 complex to promote and direct actin nucleation (Yarar et al., 1999). The interaction was structurally investigated and showed the sub-terminal tryptophan sandwiched in a hydrophobic pocket created by two active site arginines (Arg-42 and Arg-303) (St-Jean et al., 2007). This confirmed the uncoupling between the structural and catalytic roles of aldolase, as Arg-303 critically binds the P1-phosphate of enzymatic substrates. Further, the acidic residues of the peptide compete with the C-terminal region of aldolase at the active site periphery in a mutually exclusive site. Finally, based on this structure, a novel naphthol phosphate-based inhibitor (NASEP) of aldolase was identified and has the potential to regulate actin dynamics (Figure 1-18) (St-Jean et al., 2007).
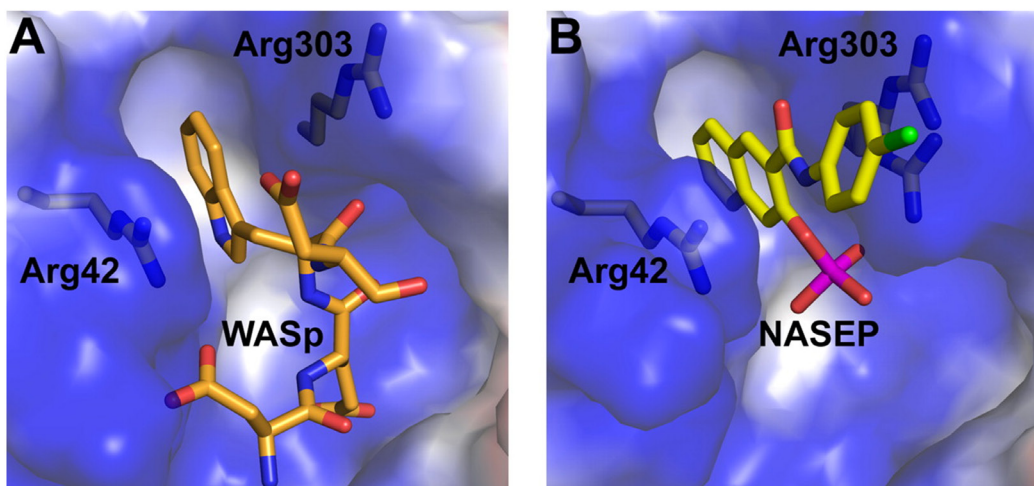
Figure 1-18. WASP and the naphthol-based inhibitor NASEP bind a unique hydrophobic pocket. (taken from St-Jean et al., 2007)

The interactions of aldolase with cellular partners offering a direct or indirect link to the cytoskeleton suggests an important role for aldolase in the regulation of this complex and dynamic cellular structure. A better understanding of the structural features that dictate these interactions would provide important clues for designing inhibitory compounds. Together, the moonlighting functions of aldolase provide therapeutic opportunities for modulating diverse pathways. The next section provides a brief overview of the numerous inhibitors that have been used against aldolase.
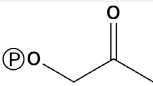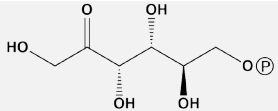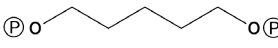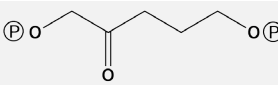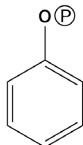
1.3.2 Classes of Inhibitors

Integrative information regarding active site mechanism and geometry can be obtained with inhibition studies. In a continuation of the above discussion on how substrates have played a role in elucidating the reaction mechanism, inhibitors have been equal in providing answers to these interrogations. Non-cleavable analogues give access to intermediate transition states that are usually inaccessible because of their high-energy nature (Hiratake, 2005). Transition-state analogues and other active site inhibitors of aldolase are therefore highly desirable, not only for their utility as mechanistic probes, but also for the aforementioned therapeutic opportunities. They have been extensively reviewed elsewhere (Gefflaut et al., 1995) and are briefly reviewed below.
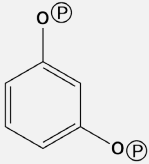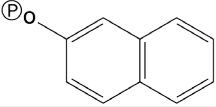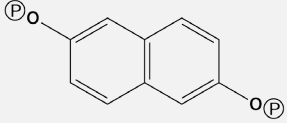
i. Competitive inhibitors

Without exception, aldolase inhibitors described in the literature possess one or more phosphate groups. Most act as competitive inhibitors, which are defined by the rapid association and dissociation from the enzyme. The following table recapitulates several representative competitive inhibitors reported in the literature (see Gefflaut et al., 1995 for a complete list).

Table II. Structures of selected competitive inhibitors

Compound		K_i (µM)	K_m FBP (µM)	K_i/K_m (FBP)	Reference
P_i	A	1300	14	93	Spolter et al., 1965
	B	6700	-	-	Rose and O'Connell, 1969
	C	1100	14	79	Spolter et al., 1965
	D	25	2.8	9	Hartman and Barker, 1965
	E	30	2.8	11	Hartman and Barker, 1965
	F	3200	10	320	Suh and Barker, 1971
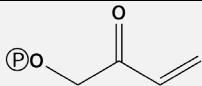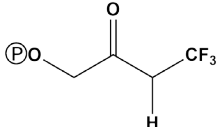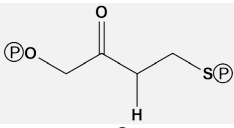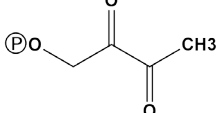
Structure	Label				Reference
	G	88	10	9	Suh and Barker, 1971
	H	490	10	49	Suh and Barker, 1971
	I	0.28	10	0.04	Suh and Barker, 1971

Analysis of the different competitive inhibitors reveals that generally, compounds deficient of an aldehyde group are competitive and reversible. Further, monophosphorylated compounds have a relatively weak affinity for the active site, with binding affinities nearing those measured for inorganic phosphate. However, the presence of a second phosphate group guarantees a tighter affinity, especially when the interatomic distance between the two phosphate groups corresponds to the distance in FBP. Hence, the improvement in affinity is weak for short chain compounds (from P_i to PP_i, or from propane-1-phosphate to propane-1,3-phosphate), but much more significant for compounds where the interatomic distance between the phosphates is close the that of FBP. This explains the 10-fold increase in affinity when adding a second phosphate to hexane-1-phosphate; likewise, the inhibition constant drops from $\sim 500\ \mu M$ to $0.4 - 2.5\ \mu M$ when a second phosphate is added to different monophosphorylated naphthols (compound **H** - Table II). The most potent inhibitors will generally satisfy the above conditions, the best affinity having been achieved with naphthalenediol-2,6-bisphosphate (NA-P$_2$) (compound **I** - Table II). Interestingly, apart from the arrangement of the phosphates, this compound shares very little with FBP, and is characterized by a rigid aromatic core. Since the equivalent aliphatic derivative has less affinity than the naphthalene derivative, it was suggested that the rigid structure imposed by the aromatic group incurs a smaller entropic loss upon binding, explaining the difference in binding affinities. However, this discrepancy has not been fully addressed and will be the subject of an upcoming chapter.

ii. Irreversible

Inhibitors that are irreversible generally involve covalent adduct formation of a reactive nucleophile in the protein (cysteine, serine, lysine, etc.) with the electrophilic center of the inhibitor. The inhibition scheme usually requires rapid and reversible initial association, followed by a time-depending irreversible inactivation. The first compounds identified as irreversible (compound **A** - Table III) result in alkylation or oxidation of cysteine residues in the protein but are less potent as they appear non-specific (Wilde et al., 1977). More interesting are the so-called 'suicide' inhibitors which form dead-end complexes in the active site (compounds **B** and **C** - Table III). These are mechanism-based inhibitors as they rely on iminium formation with an active site lysine. However, several conditions must be reunited for productive suicide inhibitors including: Michaelis complex formation in active site; iminium formation; a proton abstraction event leading to an elimination reaction of a good leaving group; and a stable compound that does not favour spontaneous elimination in solution. These conditions have proven difficult to reunite and has thus limited the success of this approach against aldolase. A more promising approach comprising time-dependent reversible inhibition has been applied with greater success to aldolase and is discussed below.

Table III. Selected irreversible inhibitors
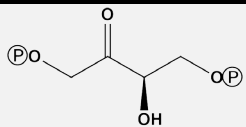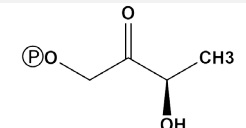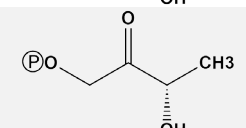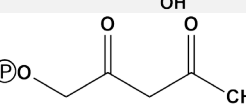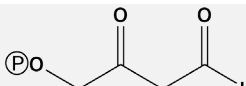
Compound		K_i (mM)	K_{inact} (s⁻¹)	Reference
	A	0.1	0.1	Wilde et al., 1977
	B	1.4	0.023	Magnien et al., 1984
	C	1.65	0.003	Riviere-Alric, 1991
	D	3.6	0.03 (min⁻¹)	(Chabot et al., 2008)
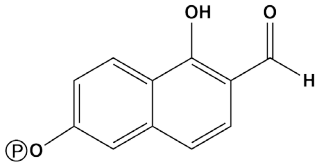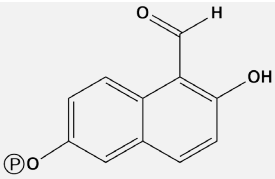
Also, irreversible inactivation was reported for both isomers of G3P (Lai et al., 1968; Rose and O'Connell, 1969). It is speculated that G3P inactivation may be at cause for the noticeable loss of activity observed when aldolase is incubated for long periods of time in the presence of FBP. The exact mechanism of inactivation by G3P is questionable and will be treated in depth in an upcoming chapter.

iii. Time-dependent reversible inhibitors (slow-binding)

Slow-binding inhibition is characterized by two equilibriums: first a rapid association which leads to formation of an enzyme-inhibitor complex – EI, followed by a reversible, time-dependent evolution of the complex to a second, often tighter, complex – EI* (Morrison and Walsh, 1988) (see annex for a complete description). The overall inhibition constant is described by K_i^*. This class of 'slow-binding' inhibitors can be as efficient as chemically reactive irreversible inhibitors, and possess a high degree of selectivity. Dr Casimir Blonski's group from *Université Paul Sabatier* has been at the forefront in the development of such inhibitors. Here are selected compounds synthesized by his group:

Table IV. Selected slow-binding inhibitors

Compound		K_i (µM)	k_{inact} (min^{-1}) k_3	k_{rev} (min^{-1}) k_4	Reference
	A	75	0.25	0.244 h^{-1}	Ferroni et al., 1991
	B	240	0.245	0.11	Blonski et al., 1995
	C	800	0.105	0.1	Blonski et al., 1995
	D	640	0.223	0.022	Gefflaut et al., 1996
	E	900	0.70	0.0033	Gefflaut et al., 1996

	F	125	0.067	1.3×10^{-5}	Dax et al., 2005
	G	$23^{[a]}$	0.39	$< 1 \times 10^{-6}$	Dax et al., 2006

[a] Inhibition constants shown for *Trypanosoma brucei* aldolase.

Compounds **D** and **E** (Table IV) are examples of slow-binding dicarbonyls that lead to formation of a conjugated enamine intermediate, which is stabilized by the enzyme. Compounds **F** and **G** (Table IV) are interesting examples of monophosphorylated naphthalene derivatives with slow-binding activity. The benzene equivalents of compounds **F** and **G** show selective slow-binding inhibition of rabbit muscle aldolase and *T. brucei* aldolase respectively (Blonski et al., 1997). The same properties, but with greater affinities, is observed for the naphthalene derivatives. It seems that an aldehyde group and an alpha-hydroxyl group combined with a phosphate group are indispensable for the slow-binding activity. The position of the aldehyde and the hydroxyl with respect to the phosphate group dictate the selectivity of the compound. Molecular dynamics simulations suggest covalent complex formation with active site lysines.

Although much information has been gathered from these studies, the design of next-generation inhibitors against aldolase can only be thoroughly envisaged with a mechanism and structure-based approach. For example, crystal structures of benzene- and naphthalene-based derivatives which remain elusive would serve as important blueprints for designing specific anti-parasitic and anti-cancerous inhibitors. These inhibitors would need to be active at low concentrations to minimize secondary effects. In the present work, structural data presented in chapter 3 will reveal the precise binding mode of several aromatic inhibitors.

1.4 Research project objectives and justification of methodology

1.4.1 General objective

This research project seeks to further our understanding, from a structural perspective, of fundamental catalytic functionalities, unresolved queries and interactions of class I aldolases. Together, as will be presented in the current thesis, a more comprehensive understanding of these activities in this enzyme is beneficial for the rational development of specific inhibitors for aldolase which have potential as therapeutic agents against cells that are highly dependent on glycolysis, such as cancer cells or parasitic protozoa. Therefore, we will attempt to answer fundamental questions regarding aldolase that remain unsettled, notwithstanding the 80 years of research that have been invested in this enzyme. As previously seen, aldolase has been extensively studied which introduces an additional challenge to anyone seeking to add value to the existing myriad of information. Thus, our reasoning and conjecturing is consistently weighed against observations made by our predecessors.

Each of the following specific aims relates to an unresolved question regarding aldolases. First, we seek to understand the determinants of selectivity in binding of the G3P isomers (D and L). Then structural data is presented to establish the importance of aldolase in contributing to cellular MGO. The following objective involves the design of class I inhibitors, which are resolved in high-resolution structures, providing important leads for improvement of affinity and specificity. Finally, we go full circle by examining the interaction of *T. gondii* aldolase with transmembrane adhesin molecules, speculating on therapeutic strategies that could be envisaged for modulating this activity.

1.4.2 Specific objectives

i. *Isomer activation controls stereospecificity of class I fructose-bisphosphate aldolases*

First, we investigated the remaining questions with regards to reaction coordinates along the Class I aldolase condensation pathway. The ternary complex is a pre-condensation state that is

fleeting and hard to capture. Knowledge of the geometry in this state is interesting, not only from the perspective of fundamental understanding, but also for developing aldolase for biosynthetic applications. The objective of this study was to probe the structure of the ternary complex in Class I aldolase and use this as a model to address unresolved queries related to stereospecificity of aldehydes.

ii. Bisphosphonate inhibitors of mammalian glycolytic aldolase

A better of understanding of the active site architecture and dynamics in Class I aldolase is critical to the rational design of selective inhibitors. The latter are desired for the targeting of cells that highly dependent on glycolysis, such as cancer cells or parasitic protozoa (ex. *Trypanosoma brucei*). Our objective in this study was to design potent, high-affinity inhibitors for aldolase, resolve their structures by crystallography, and test their efficacy as anti-glycolytics in selected cell types.

iii. Aldolase and methylglyoxal production: structural and enzymatic investigation of a promiscuous aldolase activity

Aldolase is also under investigation for its suspected role in producing a toxic metabolite, MGO. The exact mechanism is yet unknown, but preliminary evidence from our laboratory suggested the involvement of a concerted mechanism catalyzed by aldolase itself. The objective of this study was to challenge this hypothesis, which was accomplished by structural probing of aldolase crystal soaks with the substrate dihydroxyacetone phosphate, and validated by enzymatic analysis.

iv. Biophysical study of the aldolase bridging function in Toxoplasma gondii: evidence for ionic strength dependence

The final chapter of this thesis investigated the proposed role for aldolase in crosslinking the surface adhesins of apicomplexan parasites to their cytoskeleton. Specifically, in *T. gondii*, the C-terminal tails of these adhesin molecules are alleged to bind near the active site of aldolase, with a possible distal binding site. Our objective was to elucidate the crystalline structure of this interaction and determine the biophysical parameters of binding between the latter, keeping in mind the opportunities for therapeutic intervention, as apicomplexan parasites include the agents responsible for malaria and toxoplasmosis.

1.4.3 General methodology

i. *Purification and crystallization of Class I aldolases*

Any project oriented towards structural biology generally requires copious amounts of pure protein, which is usually accomplished by overexpression of recombinant protein in a bacterial system and purification by standard chromatography techniques. In our case, it was necessary to purify Class I aldolases from different sources – primarily rabbit muscle aldolase and *T. gondii* aldolase. The purification of rabbit muscle aldolase, based on ion exchange chromatography, is well documented in the literature and will only be summarized below. Subsequently, purification of *T. gondii* aldolase, based on affinity chromatography, will be elaborated.

> **Rabbit muscle aldolase**

First, rabbit muscle aldolase complementary DNA (cDNA) was cloned into a high-expression vector (pPB14) under the control of the *trc* promotor (modified *tac* promotor), as designed by Dr. Dean Tolan's group from *Boston University* (Beernink and Tolan, 1992; Morris and Tolan, 1993; Tolan et al., 1984). Overexpression of recombinant protein is accomplished in highly competent *E. coli* cells – BL21-SI (Invitrogen). The bacterial pellet is lysed by mechanical stress with aluminum oxide in a mortar and pestle. The soluble supernatant is separated by ion exchange chromatography. First, at a neutral pH (~7.5), an anion exchanger (diethylaminoethane) removes acidic bacterial contaminants, in which aldolase, by nature of its basic isoelectric point (pI ~ 8.5), passes through the column without binding. The second purification step utilizes a cation exchanger (carboxymethyl) onto which aldolase binds. Elution of the bound aldolase is done by applying a solution containing FBP. The final step involves size exclusion chromatography (Superdex200) to guarantee a homogeneous protein solution prior to crystallization. In essence, size exclusion is a polishing step that eliminates unwanted oligomers or aggregates of aldolase, which are problematic in crystallization experiments. Pure aldolase is conserved for long-term storage by precipitation (by dialysis) with 70 % ammonium sulfate and a reducing agent (dithiothreitol). Polished aldolase is used for crystallization.

> *Toxoplasma gondii* **aldolase**

On the contrary, *T. gondii* aldolase (TgALD) is purified by affinity chromatography. First, the coding sequence for TgALD [UniProt ID: Q8I8I2] was cloned into the SUMOpro Expression vector (LifeSensors[3]). The system involves fusion of the yeast SUMO protein (Smt3) at the N-terminus of a protein of interest (aldolase). The pE-SUMOpro vector (based on pET24 vector) was prepared for the expression of recombinant His_6-SUMO-TgALD (containing an N-terminal His_6 tag) in *E. coli*. Production of the fusion protein is driven through the IPTG (isopropyl β-D-1-thiogalactopyranoside)-inducible T7 RNA polymerase-promoter system, with ampicillin resistance facilitating plasmid selection and stability.

SUMO (small ubiquitin-like modifier) is a covalent modification to cellular proteins (analogous to ubiquitin modification) that regulates various cellular processes, such as nuclear transport, signal transduction, and protein stabilization. Sumoylation occurs in most eukaryotic systems, and SUMO is conserved from yeast to humans. SUMO and ubiquitin only show ~18% homology, but both possess a common three-dimensional structure characterized by a tightly packed globular fold with β-sheets wrapped around an α-helix. Fusion of SUMO with a protein of interest can dramatically enhance expression and promote solubility and correct folding of the protein. Ubiquitin fusion proteins have existed for some time but are limited by the efficiency of the protease used to remove the ubiquitin tag. Conversely, yeast SUMO protease 1 (Ulp1) recognizes the SUMO structure at the junction between SUMO and aldolase irrespective of the N-terminal sequence of aldolase (except proline). Also, SUMO Protease 1 does not cleave non-specifically within the aldolase sequence.

Like rabbit muscle aldolase, bacterial cell pellets are lysed by mechanical stress. The purification protocol implicates immobilized metal affinity chromatography (IMAC), in which Ni^{2+} is immobilized onto sepharose beads (HisTrap column[4]). The histidine-tagged SUMO construct has a strong affinity for the immobilized Ni^{2+}. Elution of the fusion protein is realized with an increasing gradient of imidazole, which competes for binding to the Ni^{2+}. The His_6-SUMO tag is removed with the SUMO protease and a second passage onto the affinity column

---

[3] https://www.lifesensors.com/; pE-SUMOpro Amp | Catalog #: 1001A
[4] GE Healthcare Life Sciences

removes the SUMO tag and the protease as both contain histidine-tags. A final polishing step using size exclusion chromatography ensures a homogeneous protein solution prior to crystallization experiments.

> **Crystallization of aldolase**

Prior to crystallization, the protein is dialyzed into a buffer with weak ionic strength (Tris 20mM pH 7.0) and concentrated to 5 – 10 *mg/m*l. Protein concentration is determined spectrophotometrically using the extinction coefficient, which for rabbit muscle aldolase was determined experimentally at 0.91 g^{-1}*L*cm^{-1} (Baranowski and Niederland, 1949). An extinction coefficient of 0.74 g^{-1}*L*cm^{-1} was determined for TgALD based on a corroborated value between the predicted coefficient (ProtParam[5]) and an experimental value (bicinchoninic acid method). The protein is then mixed with an equal volume of precipitating agent by the hanging drop vapour diffusion technique to induce crystal formation. Previously identified conditions [0.1M Na-HEPES pH 7.5, 15-20% polyethylene glycol 4000] for rabbit muscle aldolase were sufficient for obtaining thin crystal plates that diffracted to high-resolution. However, TgALD, having never been crystallized required screening through hundreds of precipitating conditions. Highly diffracting crystals with rod-like morphology were discovered in several conditions including the following: [0.1M Lithium-sulfate, 0.1M Na-Acetate pH 5.5, 2-5% polyethylene glycol 8000].

The hanging drop vapour diffusion method is a crystallization technique commonly used in protein crystallography that is centered on reducing the solubility of a protein. Small, equal volumes of protein and precipitating agent (generally consisting of salts and/or polyethylene glycols) are mixed on a cover slide which is sealed above a reservoir containing a large volume of mother liquor (precipitating solution). Because the concentration of solutes in the hanging drop is inferior to the concentration in the reservoir, water will diffuse out of the hanging drop, effectively concentrating the ingredients in the hanging drop, and reducing the solubility of the protein. As a general rule, reducing the solubility of a protein solution will result in the formation of an amorphous protein precipitate. However, if the conditions are appropriate, complementary regions on adjacent proteins will be attracted to one another. When these forces are

---

[5] SIB Bioinformatics Resource Portal

geometrically favourable, protein can self-assemble to form periodic, ordered and repeating assemblies called crystals. The principle is ideally described using a solubility phase diagram (Figure 1-19). The process of crystallization can be separated into two phases: 1) the nucleation phase; 2) and the growth phase. For nucleation to occur, a higher level of supersaturation is required than the growth phase. As the solubility is reduced in the hanging drop by vapour diffusion (trajectory of dotted line - Figure 1-19), the protein reaches a labile zone (nucleation zone), where fast growth of crystal nuclei occurs. Herein lies the chief limitation in crystallography as a whole: finding conditions that favour nucleation over precipitation. Equally challenging after conditions are identified is optimizing the time spent in the nucleation zone such as to limit excess nucleation and microcrystal formation. This is realized by modifying parameters such as protein concentration, precipitant concentration, pH, and temperature. Then, protein in solution is added to the growing nuclei until stable crystals (metastable zone) are formed (solid line - Figure 1-19).
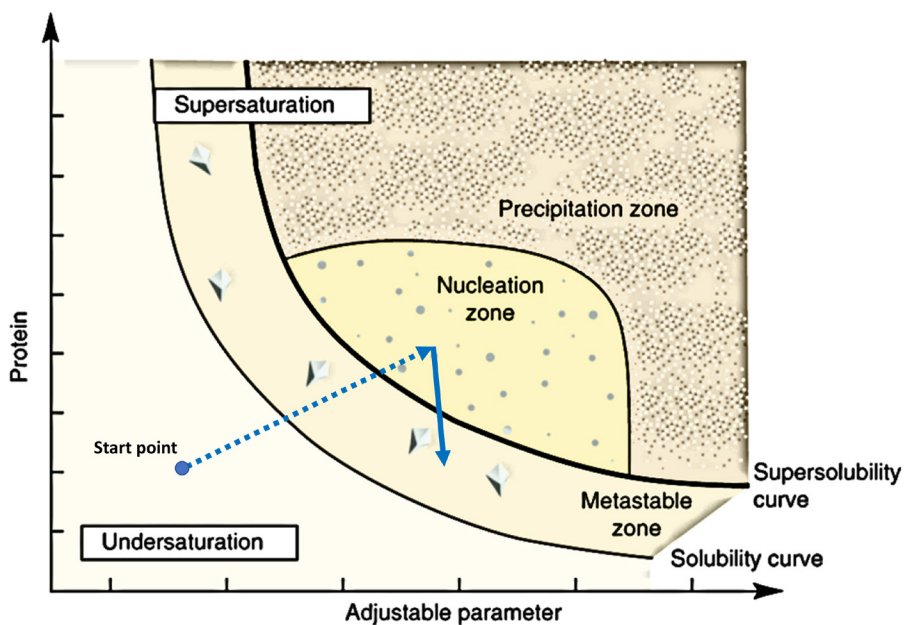
Figure 1-19. Solubility phase diagram for protein crystallization.
(adapted from Khurshid et al., 2014)

➢ **Soaking crystals**

Structures of protein – ligand complexes are prepared by soaking native crystals with a solution containing the ligand of interest (substrate or inhibitor). Crystals are porous enough that small molecules can diffuse freely within crystal channels. Less common is co-crystallization which involves mixing of protein and ligand prior to conducting crystallization experiments. All the aldolase – ligand structures presented in my thesis were prepared by the soaking method. The rate of diffusion into crystals and the affinity for the ligand governs the length of the soak that is prescribed. In rabbit muscle aldolase crystals, FBP fully occupies all the active sites in the crystal in less than a few minutes. Bulkier ligands, such as inhibitors or peptides can take hours to diffuse into the crystal. In order to trap reaction intermediates, soaked crystals are frozen and conserved in liquid nitrogen (100 K). A preliminary cryoprotection step is needed to prevent ice formation which damages crystals. Accordingly, the crystal is transferred through a solution containing a cryoprotectant such as glycol. Cryo-cooling has the added benefit of reducing radiation damage – a consequential phenomenon endured by crystals in the course of their exposure to powerful X-rays. The source of X-rays for all the data generated in my thesis was from a synchrotron, such as the *National Synchrotron Light Source* at *Brookhaven National Laboratory* in Upton (New York) or the *Canadian Light Source* at the *University of Saskatchewan* in Saskatoon.

ii. 3D structure determination by X-ray crystallography

As X-ray crystallography was the preferred approach for much of my thesis, a justification of the technique is warranted. Resolution of structural features at the atomic scale is confined to three techniques: (1) X-ray crystallography; (2) nuclear magnetic resonance spectroscopy (NMR); (3) and cryo-electron microscopy (EM). Technical and computational advances in cryo-EM have significantly closed the gap with X-ray crystallography (Callaway, 2015). Two seemingly insurmountable barriers were recently crossed: (1) the 2 Å resolution barrier and (2) solving the structure of proteins with sizes < 100 *k*Da (Merk et al., 2016). However, the embryonic state of cryo-EM with regards to high-resolution structural enzymology implied that crystallography was indeed better suited for studying atomic-scale details in aldolase. On the other hand, NMR's chief advantage over crystallography is twofold: first, data is collected on protein in solution; and NMR provides information concerning dynamics in the protein

structure. However, NMR is limited to macromolecular structures below ~50 kDa. The deconvolution of an NMR spectrum for tetrameric aldolase (~160 kDa) would be unmanageable due to signal overlaps. The clear choice for structural studies on aldolase is therefore crystallography.

Crystallography has its own limitations (primarily the growth of diffraction-quality crystals), but misconceptions continue to circulate. Crystallography is often criticized for providing a static representation of an immobilized protein in a crystal. In reality, protein crystals are composed of 40 – 60 % solvent molecules at an average concentration of ~ 600 mg/ml – protein within the crystal and thus retain some flexibility. Indeed, parts of the protein may be locked in one or more discrete conformations, but surface loops may retain flexibility if unhindered in the lattice. Increased mobility in the crystal lattice causes a drop in resolution for the sub-regions involved – consequently, electron density is occasionally not visible for surface loops.

Molecular crowding studies of the cell have shown that total macromolecular concentrations in the cytosol are between 300 – 400 mg/ml (Ellis, 2001); the environment in a crystal is therefore a reasonable approximation of the cytosol. Admittedly, proteins in a crystal are 'fixed' as opposed to the 'free' environment of the cytosol. Therefore, it opens the possibility of introducing crystalline artefacts that are the result of contacts between adjacent proteins. A careful examination of the structure is needed to avoid artefactual interpretations. For example, rabbit muscle aldolase crystals are organized in a lattice that limits access of the C-terminal region to the active site, which is needed for effective catalysis. Nevertheless, a crystal structure gives the thermal motion of each atom (the B-factor) which provides important clues regarding the mobility of certain regions.

> **Basics of X-ray diffraction**

The theory of X-ray diffraction and the steps that follow data collection are consequential but we will confine ourselves to a brief overview. Comprehensive details are readily available in several reviews and books including the textbook standard *Biomolecular Crystallography* by Bernard Rupp (Rupp, 2009).

In continuation of the above, diffraction quality crystals are selected for exposure to high-intensity X-rays that are produced at a synchrotron. A diffraction quality crystal has high

scattering power that results from the interaction of the X-rays with electrons in the crystal. The crystal is rotated around an axis during a diffraction experiment in order to collect data at all possible scattering angles. Diffraction is observable at certain angles only where constructive interference of the scattered waves occurs, determined by Bragg's law ($n \cdot \lambda = 2 \cdot d \cdot \sin \theta$). All other angles produce destructive interference, explaining the discrete nature of a diffraction pattern. The intensity of scattered waves (also called reflections) is measured on a detector and the data is processed by computers. Data reduction is undertaken with software such as HKL2000 (Otwinowski and Minor, 1997).

Data processing begins with indexing the reflections, which is the process of assigning specific coordinates for each reflection onto a three-dimensional grid system called the reciprocal lattice. Indexing also allows us to determine the organization and symmetry of the protein in the crystal lattice (known as the unit cell parameters). Data collected at all scattering angles is integrated and scaled to account for imprecisions and radiation damage that occurs during a diffraction experiment. Electron density maps are calculated from the intensity of reflections and their phases by a mathematical transformation known as the Fourier transform. However, the only information that is gathered in a diffraction experiment is the intensity of the reflections. As the scattered waves do not travel in the same direction, they have different phases when they reach the detector. The phases cannot be directly recorded during a diffraction experiment: this is known as the 'phase problem'. Initial phase estimates can be obtained in a number of ways including direct methods, anomalous scattering, multiple isomorphous replacement, and molecular replacement. The preferred method for the structures that were resolved in my thesis was molecular replacement. If a related structure is known, it can be used as a search model in molecular replacement to determine the orientation and position of the molecules within the unit cell. For example, the TgALD structure was resolved using rabbit muscle aldolase as the search model. In a sense, the phases from rabbit muscle aldolase were extracted and applied to the TgALD experimental data. This introduces a significant bias in the Fourier transform that is reflected by inaccuracies in certain electron density maps. Corrections and bias reduction are accounted for in the model building and refinement stages.

> ➢ **Model building and refinement**

Once initial phases are obtained, an initial model can be built. The following steps are carried out with structure refinement software, such as PHENIX: a software suite for the automated determination of molecular structures (Adams et al., 2002). Improvement of this model by correcting positional errors, geometry errors, bond lengths, etc., leads to better phases which in turn gives more accurate electron density maps that are used to further improve the model. The atoms in a model are classically defined by four parameters: their x, y and z positions, and their Debye-Waller factors (or B-factors, which account for the thermal motion of the atom). These are refined to fit the observed diffraction data, yielding better phases that can be used to calculate more accurate maps. A new model is fit to the new electron density map and another round of refinement is initiated. This iterative process continues until the correlation between the experimental data and the model is maximized. The agreement between the experimental data and the model is reported in the R-factor value (or R_{work}). Another criterion used to establish the fitness of the model is R_{free}, which is calculated from a subset (5 – 10 %) of reflections not included in the refinement steps. As the model improves, both R-factors decrease as the agreement between model and data is maximized. The difference between R_{work} and R_{free} allows the crystallographer to determine if the data is being over-fitted. Generally, a well-refined structure should have an R_{free} value of approximately the resolution in angstroms divided by 10; thus a 2.5 Å resolution structure would have an $R_{free} = 0.25$.

Finally, since phase bias is a common problem, primarily in structures resolved by molecular replacement, methods exist to minimize the phase bias. This is imperative for objectively determining the presence and binding location of a ligand, as was the case in several of my structures. The most common method is to calculate an omit map where electron density maps are calculated in the absence of modeled ligand. There are several omit map protocols used by crystallographers, notably the *simulated annealing omit map* (Hodel et al., 1992), which requires 'heating' and subsequent 'cooling' of the system, or the more recent *iterative-build omit map* (Terwilliger et al., 2008). Once a model of a protein structure has been finalized and validated, it is ready for deposition into a crystallographic database such as the PDB.

iii. Kinetic and Thermodynamic parameters

➢ **Kinetic parameters**

An essential component of most projects related to aldolases is the evaluation of its activity. Aldolase activity is measured spectrophotometrically with a coupled-enzyme assay involving two additional enzymes: triosephosphate isomerase (TIM) and glycerol-3-phosphate dehydrogenase (GDH) (Figure 1-20). The products of the aldolase reaction, DHAP and G3P, are the substrates of the coupled enzymes. G3P is converted to DHAP by TIM, and DHAP is subsequently converted to glycerol-3-phosphate by GDH. The GDH-catalyzed reaction utilizes NADH (transformed to NAD$^+$) as a cofactor, consuming one molecule of NADH for every molecule of DHAP. The peak absorption for NADH is 340 ηm and its consumption in the coupled-assay can be followed spectrophotometrically. The rate of oxidation of NADH to NAD$^+$, given that the coupled enzymes are in a large excess and are not rate-limiting, provides a direct measure of the rate of cleavage of FBP by aldolase.
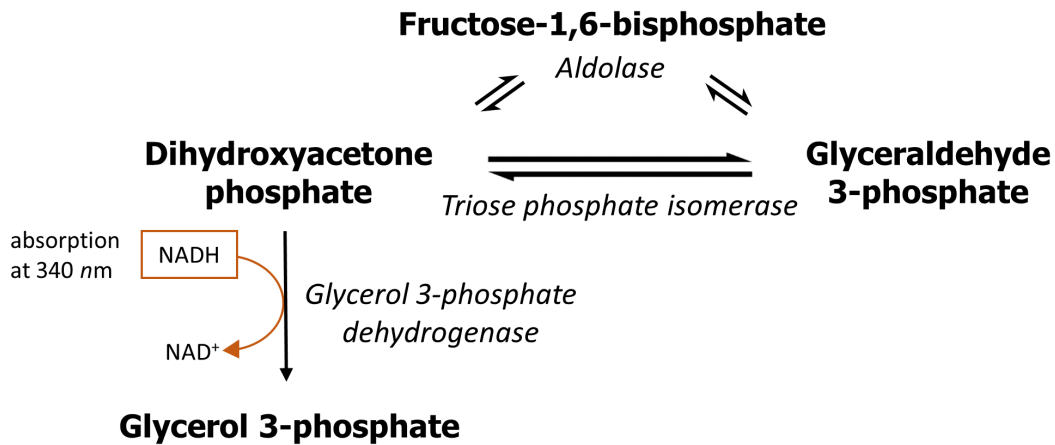
Figure 1-20. Enzyme-coupled assay for measuring Aldolase activity.

The rate, as calculated from the slope of the curve in a time-course reaction, is converted into enzyme activity units (moles of substrate converted per unit time). At a fixed enzyme concentration, we vary the substrate concentrations and inhibitor concentrations, and ultimately obtain the kinetic parameters of the reaction: V_{max} or k_{cat} and K_m. V_{max} is the specific activity of the enzyme (expressed in μmol*min^{-1}mg^{-1}) whereas k_{cat}, the turnover number, is defined as the

maximum number of chemical conversions of substrate molecules per second that a single catalytic site will execute for a given enzyme concentration. K_m is a measure of how well a substrate complexes with a given enzyme, otherwise known as its binding affinity. The kinetic parameters are obtained using a model known as Michaelis-Menton kinetics, proposed by two 20th century scientists, Leonor Michaelis and Maud Leonora Menten, to account for enzyme dynamics. Simply, the model serves to explain how an enzyme can cause kinetic rate enhancement and explains how reaction rates depend on the concentration of enzyme, substrate and inhibitor. All data pertaining to enzyme kinetics was treated with GraFit[6], which provides automated enzyme kinetic analysis.

> **Thermodynamic parameters**

Isothermal titration calorimetry (ITC) is a physical technique used to determine the thermodynamic parameters of macromolecular interactions in solution. As this technique was foundational to the project concerning the interactions between *T. gondii* aldolase and the termini of adhesin molecules, it is briefly covered here.

ITC is a titrimetric method, where aliquots of a titrant (typically a ligand at > 500 μM) are injected into a sample cell containing protein solution (~ 20 – 100 μM). The cell is composed of highly efficient thermally conducting material such as Hastelloy alloy and is contained within an adiabatic jacket. Upon titration of each aliquot, heat released or absorbed from the association between ligand and protein is measured by detecting temperature differences between the sample cell and a reference cell (containing buffer or water). The input of power required to maintain equal temperatures between the sample and reference cells is translated into a measure of heat of interaction between the binding partners. For example, an exothermic reaction increases the temperature in the sample cell, causing the feedback power to the sample cell to decrease in order to maintain an equal temperature between the two cells. A complete titration experiment produces a heat isotherm that reaches saturation of binding. Since the method is performed at constant pressure and temperature, a single ITC experiment generates data on the equilibrium association constant (K_a), the enthalpy change (ΔH), and binding stoichiometry (n).

---

[6] GraFit: Data Analysis Software by Erithacus

From these estimates, the Gibbs free energy change (ΔG) and entropy change (ΔS) can be determined using the following relationship:

$$\Delta G = -RT\ln(K_a) = \Delta H - T\Delta S$$

In addition to providing direct evidence for associations, thermodynamic data provides clues into the nature of the noncovalent forces that guide the association. Enthalpy-driven interactions tend to be polar in nature (hydrogen-bonding and ionic interactions), whereas entropy-driven interactions tend to be hydrophobic in nature (conformational changes and expulsion of water molecules). Therefore, different intereactions can exhibit comparable binding affinities but have different binding mechanisms. All data pertaining to ITC experimentation was collected and analyzed with Origin v.7[7]. In summary, ITC is advantageous because it provides a direct and complete thermodynamic characterization, is conducted in solution, and is non-destructive. The chief inconviences are a weak signal when the binding enthalpy is small, the deconvolution of complex interactions, and high sample concentration requirements.

1.4.4 Synopsis

The general introduction of this thesis touches upon universal themes that appear in each chapter. Likewise, the methodologies described in the previous section represent common elements that will reappear in the chapters that follow. The first two chapters of the results section (Chapters 2 and 3) are presented in their final edition and will be submitted for publication. The two following chapters (Chapters 4 and 5) are the results from projects in my thesis that dealt with various facets of Class I aldolases. Altogether, we hope to provoke a greater appreciation for the tremendous complexity that arises in the single, seemingly simple glycolytic enzyme, aldolase.

---

[7] Origin: Data Analysis and Graphing Software v.7

Chapter 2

Isomer activation controls stereospecificity of class I fructose-bisphosphate aldolases

Background

Aldolase occupies a key position in glycolysis, in that it guarantees the passage between the six carbon sugar and three carbon sugar. The ability of aldolase to accurately transform the hexose substrate to the triose substrate and vice-versa is therefore primordial. Nevertheless, the decades of study invested in decoding the many steps along the reaction pathway have been unproductive in capturing the elusive pre-condensation ternary complex (aldolase-enamine-g3p) in fructose-1,6-bisphosphate aldolase (FBPA).

We therefore undertook a structural study to capture the ternary complex using a model class I aldolase from *Toxoplasma gondii*, which forms stable crystals at acidic pHs, a characteristic that was required for delaying the condensation and capturing the complex. Crystals of the latter were soaked with substrate and flash-frozen for different intervals. The results obtained from this study has provided valuable insight into the precise reaction geometry of aldol addition in FBPAs. Likewise, we have been able to use these models to understand how aldolase discriminates incoming aldehydes.

The results of this study were submitted (under review) to *Journal of Biological Chemistry* with the title: *Isomer Activation Controls Stereospecificity of Class I Fructose-Bisphosphate Aldolases*. The ensemble of the work was conducted by myself, including experimentation and manuscript write-up, with critical revisions by Dr. Sygusch.

Isomer Activation Controls Stereospecificity of Class I Fructose-Bisphosphate Aldolases

Paul W. Heron[†], Jurgen Sygusch*[†]

[†]Department of Biochemistry and Molecular Medicine, Université de Montréal, Montréal H3C

3J7, Québec, Canada

*Correspondance to: Jurgen Sygusch, CP 6128, Station Centre-Ville, Montréal H3C 3J7,

Québec, Canada. Tel.: 514-343-2389; Fax: 514-343-2210; E-mail:

jurgen.sygusch@umontreal.ca

ABBREVIATIONS

FBP, fructose-1,6-bisphosphate; DHAP, dihydroxyacetone phosphate; G3P, glyceraldehyde-3-phosphate; TgALD, *Toxoplasma gondii* aldolase; RBP, D-ribulose-1,5-bisphosphate; TBP, D-tagatose-1,6-bisphosphate; SBP, L-sorbose-1,6-bisphosphate.

AUTHOR CONTRIBUTIONS

PH and JS designed the experiments, PH conducted the experiments, PH and JS analyzed the results, and PH wrote most of the paper with critical revisions by JS.

The atomic coordinates and structure factors (codes 5TJS, 5TK3, 5TKC, 5TKL, 5TKN, 5TKP) have been deposited in the Protein Data Bank, Research Collaboratory for Structural Bioinformatics, Rutgers University, NewBrunswick, NJ (http://www.rcsb.org/).

ABSTRACT

Insight into stereospecific carbon-carbon bond formation catalyzed by fructose-bisphosphate (FBP) class I aldolases was obtained from a high resolution crystallographic study analyzing substrate turnover in crystals of *Toxoplasma gondii* aldolase (TgALD) grown at acidic pH. The relatively slow diffusion by substrate FBP into TgALD crystals cryotrapped an elusive ternary enzyme complex consisting of triose-phosphate products as a dominant population in the active site. The ternary complex provided a snapshot of aldolase reaction products, dihydroxyacetone phosphate (DHAP) covalently bound to Lys-231 as an enamine/carbanion and D-glyceraldehyde-3-phosphate (D-G3P), which together delineated the essential structural features responsible for stereospecific C-C bond formation. The aldehyde product exhibited an unproductive *cis*-configuration that although mitigating aldol reaction with the enamine/carbanion enabled the cryotrapping of the ternary complex. *Cis-trans* isomerization by the D-G3P aldehyde is unhindered in the ternary complex. The D-G3P carbonyl in *trans* is competent to promote C_3-C_4 bond formation through interaction with the acid form of Glu-189 and by electrostatic interaction with Lys-146, enables efficient proton transfer to the polarized aldehyde carbonyl, and leads to stereospecific aldol addition in FBP class I aldolases. The reaction geometry demonstrates a pericyclic transition state that reflects a Bürgi-Dunitz trajectory by the attacking DHAP enamine nucleophile, and is consistent with least atomic motion during bond formation in the aldol addition reaction. The D-G3P binding loci further discriminates against the L-enantiomer of G3P by stereoelectronic repulsion. Suppression by active site geometry of enantiomeric intermediates and rotational isomers is responsible for stereospecific aldol reaction in class I FBP aldolases.
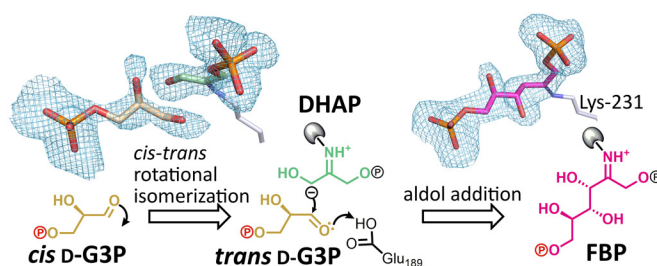
INTRODUCTION

Aldolases are central enzymes that catalyze stereospecific carbon-carbon bond formation. Their role is best known in glycolysis, where fructose-1,6-bisphosphate (FBP) aldolase (EC 4.1.2.13) reversibly cleaves FBP into the triose-phosphates, D-glyceraldehyde-3-phosphate (D-G3P) and dihydroxyacetone phosphate (DHAP). The catalytic mechanism has been extensively investigated in class I aldolases from rabbit muscle, namely for its ease of purification and high sequence identity to the human counterpart. Class I aldolases make use of a covalent mechanism implicating Schiff base formation between a lysine residue and a ketose substrate.[1]

The thermodynamically favoured aldol reaction involves a covalent intermediate with the keto triose-P (DHAP), shown as intermediate 1 in **Scheme 2-1**. Stereospecific abstraction of the pro(S) C_3 proton on DHAP ensures the development of a carbanionic character at C_3 of DHAP, which is stabilized by resonance with the enamine form (intermediate 2). The DHAP-enamine condenses with D-G3P (intermediate 3) to form the $C_3 - C_4$ bond, generating the ketimine intermediate (intermediate 4), which undergoes hydrolysis to release FBP.
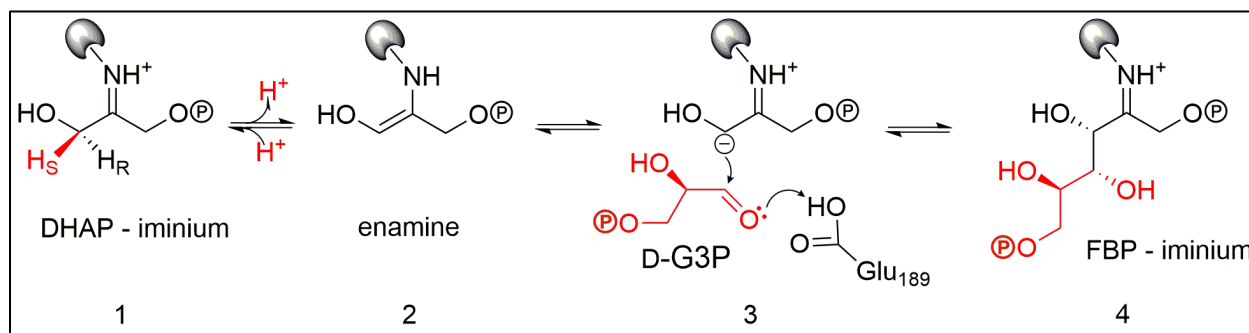
Scheme 2-1. Intermediates of the Catalytic Mechanism in Class I Aldolases

Studies with substrates and analogues has contributed immensely to our understanding of the active site architecture and catalytic mechanism in aldolases.[2–7] Class I aldolases are specific for DHAP but can accept diverse aldehydes.[6] Selectivity studies have explored the stereochemistry of substrate analogs at every position, including the C_5 position of FBP. Conflicting reports regarding the discrimination of diastereomers at the C_5 position have been reported, notably regarding the L-isomer of G3P. First reports indicated that aldolase catalyzed the condensation of DHAP and L-G3P, producing L-sorbose-1,6-bisphosphate (SBP), albeit at a much slower rate than with incorporation of the D-isomer.[8,9] Cleavage of SBP by FBP aldolase was equally

reduced compared with FBP. However, subsequent experiments by fluorescence quenching[2] and labeling studies[10] demonstrated that aldolase is rather progressively inactivated by L-G3P and that L-G3P is not a substrate for aldolase.[2]

The prototypical class I aldolase used for mechanistic studies has long been the muscle isoform from rabbit aldolase which when crystallized enabled active site trapping of a number of reaction intermediates that were determined to high resolution.[11–13] As these crystal structures involved considerable soaking times ($\geq$ 3 minutes) and high substrate concentrations (10 mM FBP) with respect to crystallized protein,[11] prior to flash-freezing, the cryogenic structures trapped only the highly populated intermediates, consistent with biochemical determination of active site populations near equilibrium.[14] This precluded the trapping of the elusive ternary enzymatic complex, aldolase-enamine-D-G3P which at neutral pH represents ~ 2% of the total bound intermediates under steady state conditions.[4,15] The small population makes it challenging to isolate an intermediate population consistent with incipient aldol addition and of sufficient active site occupancy for structural analysis. The structural constraints imposed by the active site architecture upon the enzymatic ternary complex formation ensures 3(S)-4(R) stereospecificity in C-C bond formation in FBP aldolases.

Crystals were grown class I aldolase (TgALD) crystals from *Toxoplasma gondii*, a unicellular protozoon, that shares a high level of conservation of active site residues with human muscle aldolase and that were suitable for detailed structural analysis. The acid crystallization conditions (pH 4.5 – 5.5) provided an opportunity to stabilize reaction intermediates that would otherwise be of low occupancy in human and rabbit muscle aldolase crystals typically grown at neutral pH. In class I aldolases, several rate steps of interconversions of reaction intermediates are pH dependant in the catalytic mechanism. A key proton transfer step, mediated by Glu-187, is required for both aldol and reverse aldol reaction in mammalian class I aldolases, and has a pKa of 5.2 in the muscle isozyme.[16] Acid crystallization conditions of TgALD would make this rate step limiting. Additionally, acid pH stabilizes Schiff base formation[4] rather than enamine formation, and together these considerations would argue in favor of cryotrapping intermediates with reaction geometries conducive for incipient aldolization in the direction of triose-P condensation.

Crystals for TgALD were soaked with FBP substrate for various times, and then flash frozen in LN2 to cryotrap enzymatic intermediates. The acid crystallization conditions yielded a series

of high resolution structures of enzymatic intermediates that corresponded to a series of snapshots delineating the progress of central reaction intermediates along the reaction pathway in TgALD. Notably, a ternary intermediate complex was successfully cryotrapped as a dominant population that could be shown to be consistent with incipient aldol addition. The active site configuration of the intermediate provided intimate detail of the attack geometry requisite for stereospecific aldol addition. Further analyses of these structures revealed the structural basis by which glycolytic aldolases discriminate against the L-G3P enantiomer to ensure aldehyde stereospecificity.

EXPERIMENTAL PROCEDURES

Materials. Fru(1,6)P$_2$, glycerol-3-phosphate dehydrogenase and triose-phosphate isomerase were purchased from Sigma-Aldrich. NADH was from Roche Diagnostics. All other chemicals and materials were of analytical grade and were obtained from Sigma-Aldrich, Fisher Scientific, Bioshop Canada, and GE Healthcare Life Sciences.

Purification and Crystallization. Recombinant *T. gondii* aldolase (TgALD) was cloned and prepared as previously described.[17] The TgALD gene was then subcloned into a T7-inducible pE-SUMO AMP vector available from LifeSensors Inc (SUMOpro® Gene Fusion Technology) – this was generously provided to us by Dr. David Sibley, Washington University in St. Louis. The resulting plasmid was transformed into *E. coli* BL21-Star™ (DE3) cells (Invitrogen). Overexpressing clones were identified from a mini-lysis test using a mixture of sucrose (25%), lysozyme, and Triton X-100 (0.3%) for cell lysis. The overexpressing recombinant strain grown to A$_{600}$ = 0.6 in LB medium was induced with 1mM isopropyl β-D-1-thiogalactopyranoside at 37ºC for 4 hours. Cells were harvested by centrifugation and frozen at -20ºC overnight. The bacterial pellet was lysed by mechanical disruption with type A-5 aluminum oxide using a mortar and pestle. Cells were resuspended in a lysis buffer (20 *m*M Tris-HCl pH 7.4, 0.5 M NaCl, 20 *m*M imidazole, 10mM MgCl$_2$, 0.2 *m*M PMSF) containing 1mg/g of RNAse and recombinant DNAse. The clear lysate obtained after centrifugation was dialyzed with binding buffer (20 *m*M Tris-HCl pH 7.4, 0.5 M NaCl, 20 *m*M imidazole) and was purified by affinity

purification using a HisTrap™ HP 5ml column (Ni^{2+} immobilized) connected to an ÄKTA purification system (GE Healthcare). The N-terminal 6xHis-SUMO-TgALD was eluted using elution buffer (20 mM Tris-HCl pH 7.4, 0.5 M NaCl, 0.5 M imidazole) applied on a linear gradient. The His-SUMO tag from eluted protein was cleaved by incubation for 4 hours at 30°C with SUMO protease after overnight dialysis in SUMO buffer (20 mM Tris-HCl pH 8.0, 150 mM NaCl, 10% glycerol). Prior to reinjection on the HisTrap column, samples were dialyzed with binding buffer. Fractions from the flow-through containing the protein, as determined by SDS-PAGE and enzyme activity, were pooled and precipitated overnight with precipitation buffer (100 mM Tris-HCl pH 7.6, 1 mM EDTA, 70% ammonium sulfate, 5 mM DTT). Precipitated protein was pelleted, resuspended in gel filtration buffer (20 mM Tris-HCl pH 7.4, 1 mM EDTA, 50 mM NaCl) and loaded onto a HiLoad™ 16/60 Superdex™ prep grade (GE Healthcare). TgALD eluted from the gel filtration column at an estimated molecular weight of ~160 kDa, consistent with tetramerization of TgALD. Purity was assessed by SDS-PAGE and mass spectrometry. Peak fractions were pooled, dialyzed with a minimal buffer (20 mM Tris-HCl pH 7.0), and concentrated to 5-10 $mg \cdot m$l^{-1} prior to crystallization trials.

Crystallographic Data Collection and Processing. Native TgALD crystals were identified from the Clear Strategy™ Screen I (Molecular Dimensions) and were optimized to the following conditions: 0.1 M sodium acetate pH 5.5, 0.2 M lithium sulfate, 3.5% (w/v) PEG 8000, 10% (w/v) PEG 1000. Crystals were grown at 20° C by hanging-drop vapor diffusion using a 1:1 mixture of protein:precipitant. TgALD crystals were then soaked for incremental time intervals (0.5, 1, 2, 10, and 30 minutes) with ligand buffer containing FBP (mother liquor with 1 mM FBP) or DHAP (mother liquor with 1 mM DHAP). Prior to flash-freezing in liquid nitrogen, single crystals were cryoprotected by briefly soaking them in the ligand buffer and 20% (v/v) glycerol. The data were collected at beamlines X25 and X29 of the National Synchrotron Light Source I at Brookhaven National Laboratories. The diffraction data were processed and scaled with the HKL package[18] and the final results are listed in Table 1.

Structure determination and refinement. Structures were solved by molecular replacement with PHENIX[19] Phaser-MR[20] using subunit-A from the native rabbit aldolase homotetramer structure as a reference model [Protein Data Bank (PDB) entry 1ZAH] for which there is 57.1% sequence homology[21] (*Oryctolagus cuniculus* aldolase [Uniprot ID: P00883] and *T. gondii* aldolase [Uniprot ID: Q8l8l2]). TgALD crystals have space group P $4_2 2_1 2$ with one tetrameric

TgALD subunit in the asymmetric unit. Refinement and model building were performed using the refinement module in Phenix[22] and Coot[23] respectively. Data quality was assessed and cut-off using correlation-coefficient-based criteria, $CC_{1/2}$.[24] Ligand fitting and interpretation was performed using a combination of simulated annealing $F_o - F_c$ omit maps and feature-enhanced sigma-A weighted $2F_o - F_c$ maps[25] that were calculated in the final round of refinement. All difference density maps ($F_o - F_c$) shown in the paper correspond to simulated annealed $F_o - F_c$ omit maps. Ligand coordinate and restraints were generated using Phenix eLBOW.[26] Final model statistics were calculated with MolProbity[27] and are shown in Table 1. The coordinates and structure factors have been deposited in the Protein Data Bank. All figures in the present paper were prepared using PyMOL graphics software.[28]

Active site intermediates. The identification of whether substrate and/or product species was bound in the active site for a given soaking condition (snapshot) was derived from inspection of electron density features characteristic of the ligands' chemical identities. The features included continuous electron density, extending beyond Lys-231 Nζ, indicative of formation of a stable covalent bond with the C_2 carbon. In the *1min* structure, discrimination between DHAP-enamine and DHAP-iminium intermediate is feasible by considering the geometry of the electron density observed about the C_2 carbon (**Figure S2-1A**). The planar shape observed in the *1min* structure indicates trigonal hybridization, whereas non-planar shape of the electron density about Lys-231 Nζ atom would suggest tetrahedral hybridization and is consistent with trapping of a DHAP-enamine intermediate, as was previously observed with DHAP covalently bound in rabbit muscle aldolase.[12] Another indication of DHAP-enamine trapping is the presence of an additional albeit weak hydrogen bond between Ser-301 hydroxyl and Lys-231 Nζ (3.1Å in *0.5min* structure; 3.3Å in *1min* structure) which contributes to stabilize the enamine intermediate (shown in **Figure S2-1A**). This stabilization is not possible for the DHAP carbanion, the DHAP iminium or the FBP iminium intermediates which all have formal sp^2 hybridization at Lys-231 Nζ and no longer contact the Ser-301 hydroxyl (for instance 3.7Å in the *10min* structure which has predominantly FBP covalently bound). Further, electron density developing between the DHAP C_3 and D-G3P C_1 atoms in the *2min* structure and not present in the *1min* structure suggests C-C bond formation and the presence of both the ternary complex (aldolase·enamine-D-G3P) and covalently-bound FBP intermediate in the active site (**Figure 2-1**). Indeed, nascent C-C bond formation was the clearest indication of the FBP-iminium intermediate progressively

populating the active site. The iminium geometry was consistent with similar geometries observed for previously reported aldolase and transaldolase structures where FBP was trapped in the active site.[11,29]

Active site occupancy. Occupancies of substrates in each model were determined by introducing systematic differences in their starting occupancies (eg. model 1: FBP – 0.40, triose-Ps – 0.60; model 2: FBP: - 0.60, triose-Ps – 0.40; FBP – 0.80, triose-Ps – 0.20; etc.) creating for each structure an ensemble of five models that were refined for ten cycles each with identical refinement protocols until convergence of occupancies was observed to a common value.[30] Further confirmation of model fitness affording distinction between various intermediates was accomplished by assessment of real-space correlation coefficients (CC) in Phenix.[22] Phenix performs bulk-solvent correction and scaling on the data and calculates a likelihood-weighted $2mF_o$-DF_c map. This is compared to a map calculated from the model alone, and CC for each residue are obtained. Comparison of CC values for substrate modeled at different occupancies allowed cross-validation of the convergence test performed above. Since CC scores are best interpreted as relative scores,[22] they provided a corroborative indication of the above methods for active site discernment of intermediate species. This analysis was conducted at every time point and the final models shown in **Figure 2-1C** were consistent with the highest CC scores. For example, in a pre-condensation state (*1min* structure), since there is no density between the nascent C-C bond, modeling of the FBP Schiff base complex in the *1min* structure yielded a weaker CC score (CC = 0.85) than modeling of the DHAP-enamine·D-G3P ternary complex (CC = 0.96). Discernment of DHAP-enamine from DHAP-iminium (represents a minor structural difference) yielded a higher CC for the DHAP-enamine (0.97) than for the DHAP-iminium (0.92). Likewise, slightly higher CCs were determined for *cis*-modeled D-G3P vs *trans*-modeled D-G3P in the *0.5min* (0.92 vs 0.87), *1min* (0.93 vs 0.87), and *2min* (0.92 vs 0.89) structures, corroborating the structural interpretation from omit maps, and validating the retention of *cis*-D-G3P in our models.

Activity assay. Aldolase cleavage activity was determined using a coupled assay system involving triose-phosphate isomerase and glycerol-3-phosphate dehydrogenase (TIM/GDH) by following NADH oxidation at 340 nm using a Varian Cary 300 UV-Vis spectrophotometer thermostated at 25 °C.[31]

Binding energy calculations. AutoDock 4.2.6, which considers van der Waals (vdW), H-bonding, and electrostatic energies, was used to estimate binding free energies and perform a detailed ligand intramolecular energy analysis of stereochemically-related aldehydes with aldolase.[32] The crystal structure with FBP soaked for 1 minute was used to generate atomic energy grids. Customary preparation of the protein, including addition of polar hydrogens, Kollman charges and solvation parameters were undertaken with AutoDockTools 1.5.6 (http://mgltools.scripps.edu/) which uses a modified version of Open Babel.[33] The fully refined model with D-G3P was used for the scoring function, from which Gasteiger charges and all hydrogens were computed using an input charge of -2 for D-G3P. To optimize the orientation of the O_2 hydroxyl hydrogen with respect to localized interactions in the active site, D-G3P and L-G3P were minimized using an Amber force field[34] in the Antechamber module[35] from USCF Chimera[36] for assignment of ligand parameters (bond length, charge, etc.).

PROPKA version 3.1[37,38] and H++ version 3.1 (http://biophysics.cs.vt.edu/H++)[39–41] were used to determine the pKa of active site residues. Structures for pKa calculations were prepared using the PDB2PQR server in which a PARSE force field was used to assign charges [42].

RESULTS and DISCUSSION

Ternary complex. TgALD crystallized with one tetrameric subunit in the asymmetric unit of space group $P4_22_12$, adopting the classic $(\alpha/\beta)_8$ -barrel fold, characteristic of other class I aldolases (left panel of **Figure 2-1A**). The TgALD quaternary structure corresponds to a tetramer and has 222-fold symmetry from the crystallographic packing. Data collection and refinement statistics for all crystal structures are shown in **Table 2-1**. All crystal structures were determined to high resolution (1.75 – 2.09 Å) and had comparable data collection and refinement statistics with R_{free} values close to or inferior to 20%. Flash freezing of class I TgALD crystals previously soaked in the presence of substrate for various time intervals ranging between 0 and 30 minutes trapped a series of enzymatic intermediates. The intermediates trapped included D-G3P and covalently bound DHAP, prior to the aldol reaction step leading to substrate formation (**Figure 2-1**).

Active site residues in TgALD, with respect to rabbit muscle aldolase, shown in inset of **Figure 2-1A**, are highly conserved, with only one substitution of a threonine at position 39 instead of a serine. Conservation of the subunit beta barrel fold is maintained at the structural level, even though TgALD and the rabbit isoform share only 57% sequence identity. The TgALD structure at 30-minutes (**Figure 2-1C**) corresponds to an active site fully occupied by FBP that superposes identically with the FBP bound structure of the rabbit homolog [PDB ID: 1ZAI] (r.m.s. deviation = 0.407Å based on equivalent Cα atoms). Surrounding active site residues of the same intermediates also superpose identically (r.m.s. deviation = 0.139Å based on equivalent Cα atoms of active site residues). Key active site residues, shown in **Figure 2-1A,** are shown coloured according to their biochemical properties in the homology alignment of class I aldolases from diverse species shown in **Figure 2-1B**, and underscores the high level of sequence conservation of active site residues in class I aldolases. The *blue* colour scheme emphasizes the level of similarity in residues flanking the active site. The active site similarity both in sequence and structure makes TgALD a representative candidate for studying reaction mechanisms in class I aldolases.

Table 2-1. Data collection and refinement statistics

	FBP-nat	FBP-0.5m	FBP-1m	FBP-2m	FBP-10m	FBP-30m
Data Collection						
PDB ID	5TJS	5TK3	5TKC	5TKL	5TKN	5TKP
Resolution range (Å)	38.97 - 1.78 (1.84 - 1.78) [a]	49.03 - 1.83 (1.90 - 1.83)	38.82 - 1.78 (1.84 - 1.78)	49.02 - 1.75 (1.81 - 1.75)	27.27 - 1.92 (1.99 - 1.92)	48.97 - 2.09 (2.165 - 2.09)
Space group	P 42 21 2	P 42 21 2	P 42 21 2	P 42 21 2	P 42 21 2	P 42 21 2
Unit cell a (Å), c (Å), (°)	110.2, 54.9, 90	109.8, 54.8, 90	109.8, 54.9, 90	109.6, 55.0, 90	109.1, 54.7, 90	109.12, 54.8 90
Total reflections	426298 (25526)	319675 (24753)	404145 (23443)	414630 (34281)	169255 (5154)	154210 (4866)
Unique reflections	32599 (2922)	29287 (2843)	31953 (2659)	34191 (3285)	21046 (1229)	19150 (1602)
Multiplicity	13.1 (8.9)	10.9 (8.7)	12.7 (9.0)	12.1 (7.5)	8.0 (4.3)	8.1 (3.7)
Completeness (%)	0.99 (0.89)	0.97 (0.97)	0.97 (0.82)	1.00	0.82 (0.48)	0.87 (0.67)
Average $I/\sigma(I)$	20.82 (1.48)	23.53 (2.46)	26.2 (2.7)	26.0 (1.9)	20.00 (1.42)	17.01 (1.32)
Wilson B-factor	24.57	26.18	22.63	23.92	29.64	30.45
R-merge [b]	0.085 (1.243)	0.061 (0.909)	0.059 (0.713)	0.064 (0.896)	0.067 (0.717)	0.084 (0.929)
R-meas [c]	0.089 (1.322)	0.064 (0.966)	0.062 (0.754)	0.067 (0.962)	0.071 (0.800)	0.089 (1.055)
CC1/2	1 (0.593)	1 (0.819)	1 (0.866)	1 (0.718)	1 (0.645)	0.999 (0.54)
CC*	1 (0.863)	1 (0.949)	1 (0.958)	1 (0.914)	1 (0.886)	1 (0.837)
Refinement						
R_{work} (%) [d]	0.1549 (0.2843)	0.1610 (0.2585)	0.1519 (0.2350)	0.1492 (0.2701)	0.1504 (0.3033)	0.1609 (0.2392)
R_{free} (%) [e]	0.1995 (0.3352)	0.1910 (0.3005)	0.1915 (0.2716)	0.1762 (0.2924)	0.1993 (0.3397)	0.2132 (0.2947)
CC_{work}	0.972 (0.788)	0.970 (0.872)	0.971 (0.874)	0.974 (0.823)	0.973 (0.825)	0.959 (0.734)
CC_{free}	0.952 (0.715)	0.964 (0.804)	0.960 (0.902)	0.96 (0.836)	0.956 (0.656)	0.921 (0.802)
Number of non-H atoms	2991	2972	3016	3066	2932	2882
macromolecules	2653	2656	2670	2698	2677	2657
ligands	6	25	25	38	19	19
RMSD (bond length) (Å)	0.010	0.006	0.008	0.007	0.005	0.006
RMSD (angles) (°)	1.20	0.72	0.83	0.88	0.92	0.93
Ramachandran favored	97	97	97	97	98	98
Average B-factor (Å^2)	33.91	35.09	30.16	30.66	34.86	35.90

[a] All values in parentheses are given for the highest resolution shell; [b] $R_{merge} = \sum_{hkl}\sum_i |I_i(hkl) - \bar{I}_i(hkl)| / \sum_{hkl}\sum_i I_i(hkl)$, with i running over the number of independent observations of reflection hkl; [c] $R_{meas} = \sum_{hkl}(n/(n-1))^{1/2}\sum_{i=1}^{n} |I_i(hkl) - \bar{I}_i(hkl)| / \sum_{hkl}\sum_i I_i(hkl)$, [d] $R_{work} = \sum_{hkl} ||I_o(hkl)| - |I_c(hkl)|| / \sum_{hkl} |I_o(hkl)|$; [e] $R_{free} = \sum_{hkl\epsilon T} ||I_o(hkl)| - |I_c(hkl)|| / \sum_{hkl\epsilon T} |I_o(hkl)|$, where T is a test data set randomly selected from the observed reflections prior to refinement. Test data set was not used throughout refinement and contains a minimum of 2000 unique reflections (or 5%) (smaller value is selected).
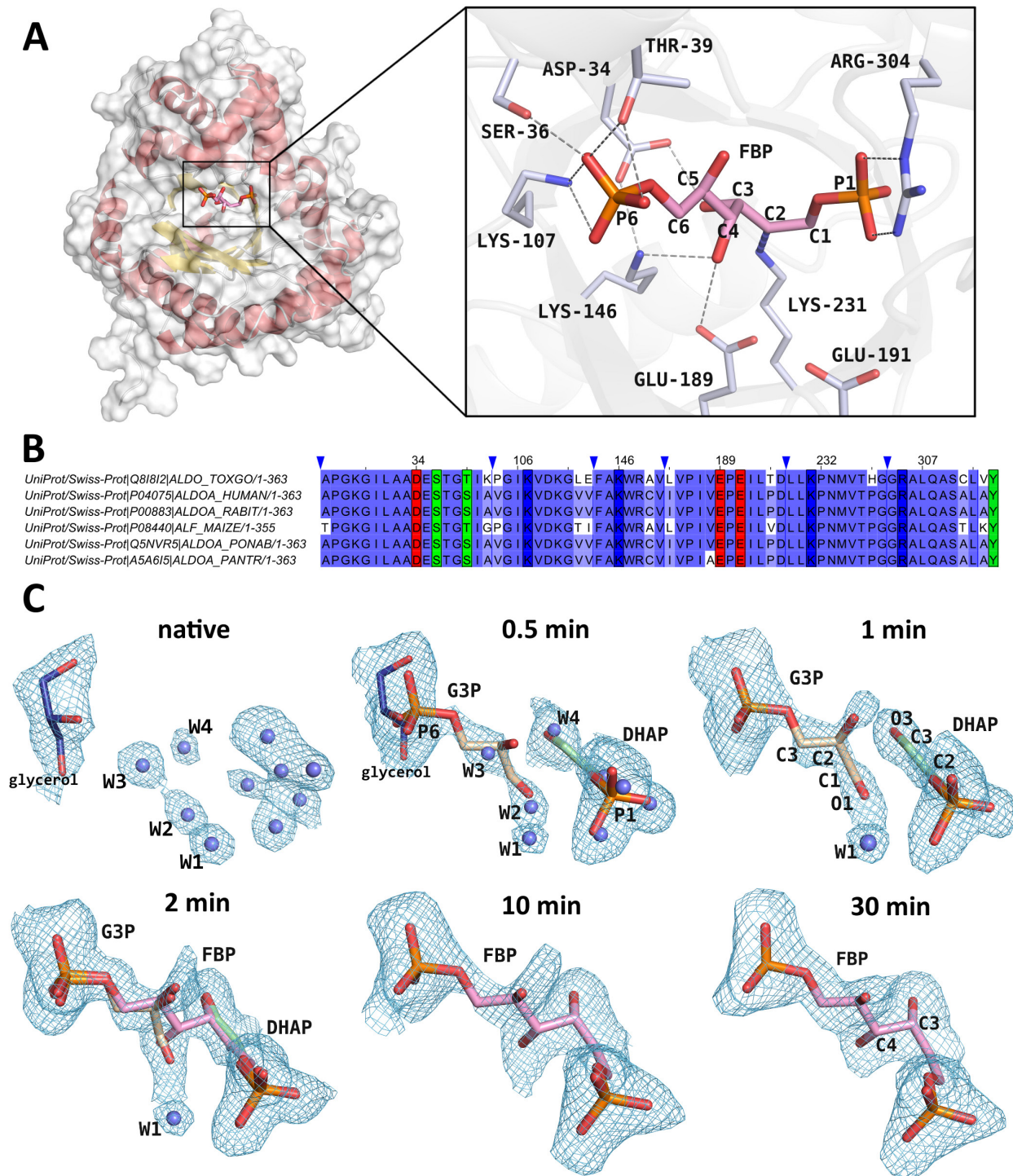
Figure 2-1. Progress of the aldol addition reaction in a class I aldolase.

(**A**) Provides an overall view of the subunit globular TIM-barrel structure (helices in *red*; sheets in *yellow*) and the active site pocket in *Tg*ALD (structure shown corresponds to *30min* soaking with FBP in crystallization buffer). In the *30min* structure, FBP is covalently bound to the Schiff base-forming Lys-231. Key active site residues that participate in hydrogen-bonding (*grey*

dashes) with substrate and in catalytic activity are depicted in the close-up (right inset). Noteworthy is the hydrogen bond made between FBP O_4 and Glu-189 and that with Lys-146. The FBP phosphates (P_1 and P_6) participate in extensive contacts with adjacent residues (some omitted). (**B**) Highlights the extensive conservation of active site residues in TgALD with respect to other class I aldolases (including rabbit muscle aldolase). The *blue* gradient illustrates the level of similarity, and the different colours correspond to key active site residues, shown in panel **A,** coloured according to their biochemical properties: *red* - acidic; *green* - polar; *blue* - basic. (**C**) Shows the crystal structures obtained corresponding to different soaking times of native TgALD crystals with FBP in the crystallization buffer and the resultant intermediates that were trapped at the incremental time points by flash-freezing soaked crystals in LN_2. Difference electron density maps were calculated from simulated annealing $F_o - F_c$ omit maps encompassing the substrate binding site and is contoured at a 2.1σ level. Where appropriate, the covalently bound intermediates, DHAP-enamine (*green*) or FBP-Schiff base (*pink*), is modeled into the active site as well as the aldehyde triose-P product D-G3P (*wheat*). Water molecules (*blue* spheres) were also modeled where appropriate. Ligands juxtaposed with water molecules at *0.5min* structure correspond to partially occupied configurations. Soaking for at least 10 minutes is required for FBP to fully populate the TgALD active site.

Aldol addition. Active site density showing potential reaction intermediates was carefully analyzed at each time point using simulated-annealing and iterative build electron density omit maps to reduce model bias and to assess the fidelity of intermediate modeling. In the native structure (**Figure 2-1C**), the active site interacts with numerous water molecules that extend to two and three hydration shells. The tightly bound water molecules in the first hydration shell of the active site (average B-factor of $35 \pm 3\text{Å}^2$ vs overall solvent B-factor of 44 ± 12 Å^2) superimpose with the ligand binding loci. Water molecules, W2 and W3, overlap with the D-G3P binding site, while W4 overlaps with DHAP O_3 atom position. The P_1-phosphate site is occupied by several water molecules while the P_6-phosphate binding site is bound by the glycerol cryo-protectant and can be seen in the *0.5min* structure, where refinement indicated indeed partial occupancies of triose-Ps, glycerol, and water molecules. Refinement using solely water molecule positions found in the active site of native TgALD was used to reveal residual electron density in difference maps, notably water molecules occurring at positions that coincided with ligand atoms when the active site was either saturated with FBP or exhibited triose-P binding. Diffusion of FBP into the crystal from the mother liquor results in an initial concentration gradient that eventually dissipates over time, however, prior to equilibration, the interior of the crystal lattice will be undersaturated with respect to the exterior substrate

concentration used for crystal soaking. To assess occupancies of the various active site entities, a linear combination of three active site populations was refined that consisted of water molecules as positioned in the native structure, FBP as found in the fully equilibrated structures, and triose-Ps as these became evident in the difference electron density map. No other active site entities were evident. Populations having partial occupancies of less than 0.1 at any given time point were excluded from further refinement. At 0.5 minutes, the occupancies of DHAP and D-G3P were 0.44 and 0.25 respectively (**Table 2-2)** while that of water molecules was 0.68 for W2, 0.72 for W3, and 0.62 for W4, yielding combined occupancies near 1.00, as expected. Upon 1 minute of soaking with FBP, the populations increased to 0.72 and 0.66 for DHAP and D-G3P, respectively. The first sign of FBP occurs at 2 minutes, with a refined occupancy of 0.46, and 0.52/0.51 for DHAP/D-G3P. 10 minutes of soaking suffices to fully populate the TgALD active site with FBP, where trace amounts of triose-Ps are rejected from the refinement. No changes were noted in the FBP population beyond 10 minutes (occupancy of 1.00 at 30 minutes). These results indicate that the crystallized TgALD conformer has demonstrable catalytic activity.

Table 2-2. Progress of populations of active site species in TgALD crystals soaked with FBP.

Structure	Refined substrate occupancy		
	DHAP	D-G3P	FBP
native	0	0	0
0.5min	0.44	0.25	0
1min	0.72	0.66	0
2min	0.52	0.51	0.46
10min	0	0	1
30min	0	0	1

Substrate diffusion into catalytically competent crystals. Surprisingly, as FBP diffused into the crystals, the first distinguishable ligands observed in the active site were the products of the aldolase forward reaction, namely the triose-Ps, DHAP and D-G3P. This would appear contrary to the thermodynamic equilibrium governing the aldolase reaction whose K_{eq} for the

cleavage reaction is ~ 10^{-4} – 10^{-5}, favouring aldol addition.[43,44] However, diffusion by FBP into the crystal lattice establishes a transient concentration gradient of FBP, prior to its equilibration, that provides an explanation for these observations. At low FBP concentrations, the thermodynamic equilibrium is not in favour of substrate formation but rather promotes triose-P formation, resulting in product formation, as is shown in **Table 2-3**. Here, the lower concentration of FBP, would correspond to the crystal interior, prior to equilibration, as FBP diffuses into the crystal, and a greater percentage of FBP would be expected to be cleaved into triose-Ps. For example, for a $K_{eq} = 10^{-4}$, at 1 uM of FBP, almost 100% of the reactant is cleaved into product. Furthermore, the triose-P products, on account of their smaller mass would diffuse more rapidly populating the crystal lattice ahead of the advancing FBP concentration front. Even at low micromolar concentrations, the K_D for DHAP of 2.4 μM[45] at pH 6.0 would favor binding and even more so if its K_D is corrected for the desolvation of DHAP ($K'_D = 1.2$ μM).[46] Binding for D-G3P is weaker ($K_D = 12.5$ μM)[2] but more favourable when the desolvated form is considered, yielding an approximate micromolar binding for the nascent D-G3P of $K'_D = 4.3$ μM.[47,48] As the local concentration of FBP increases throughout the crystal to its maximal concentration (1 mM in mother liquor), the chemical equilibrium shifts decidedly towards FBP and the population of FBP rises in the active site. The shortest time interval (*0.5min*) reflects the initial concentration gradient produced by substrate as it diffuses into the crystal lattice; DHAP and D-G3P have similar active site occupancies (**Table 2-2**) as do water molecules, W1, W2, and W3. After 1 minute, the population of the triose-Ps approaches 70% with a concomitant reduction in water occupancies. As the local concentration of FBP increases, equilibrium favours condensation with the appearance of the FBP-iminium, which becomes clearly recognizable (*2min* structure - **Figure 2-1C**) while after 10 minutes, FBP becomes the predominant species (*10min* structure - **Figure 2-1C**). Upon full equilibration with the 1 mM FBP, triose-P populations drop below 10% and are rejected by the refinement, consistent with the reported K_{eq} of 10^{-5}.

Table 2-3. Populations of the FBP cleavage product (triose-Ps) at varying local FBP concentrations in Class I aldolase.

[FBP] (μM)	Percentage of product as Triose-P [a]	
	[b] $K_{eq} = 10^{-4}$	$K_{eq} = 10^{-5}$
1	99.0	91.6
10	91.6	61.8
100	61.8	27.0
1000	27.0	9.5

[a] Theoretical populations were calculated for the K_{eq} range (10^{-4} – 10^{-5}) reported in the literature; [b] K_{eq} – equilibrium constant for the aldolase cleavage reaction.

Geometry of aldol addition. The refined reaction intermediates revealed a D-G3P- enamine ternary complex trapped in TgALD crystals with a population amenable for structural analysis (**Figure 2-1C** - *1min* and *2min* structures). A ternary complex competent for incipient aldol reaction in FBP aldolases requires that the DHAP carbanion C_3 be capable of making a *si*-face attack on the aldehyde *si*-face, generating a 3(*S*)-4(*R*) stereochemistry about the C_3-C_4 bond and thereby yielding FBP. Attack on the *re*-face of the aldehyde would result in 3(*S*)-4(*S*) stereochemistry and not FBP. Moreover, FBP aldolases are highly discriminatory towards substrates that do not have the cognate 3(*S*)-4(*R*) stereochemistry about the C_3-C_4 bond as FBP aldolases do not cleave D-ribulose-1,5-bisphosphate (RBP)[4] or D-tagatose-1,6-bisphosphate (TBP),[3] which have 3(*R*)-4(*R*) and 3(*S*)-4(*S*) configurations at the C_3-C_4 bond respectively, and which are competitive inhibitors. In the ternary complex of the *1min* structure, the orientation of the D-G3P aldehyde however is not the expected *trans*-configuration requisite for *si*-face attack, but rather the *cis*-configuration, as can be seen in **Figure 2-3A** and would result in 3(*S*)-4(*S*) chirality about the C_3-C_4 bond. Close inspection of the difference density in simulated annealing omit maps allowed for unambiguous discernment of the *cis*-configuration for the bound aldehyde (D-G3P aldehyde close-up is illustrated in **Figure 2-3A**). When the *trans*-configuration was modeled in the *0.5min*, *1min*, and *2min* structures, refinement induced rotational isomerization yielding the *cis*-configuration, which is a better fit to the data (see details in experimental procedures).

TgALD activity towards TBP was measured both at neutral pH (7.5) and acidic pH (5.5). No cleavage activity was observed at either pH indicating that TgALD exhibits the same stereospecificity as other members of the FBP aldolase family. Furthermore, the kinetic parameters determined for TgALD, shown in **Table 2-4**, were similar to the kinetic parameters cited for rabbit muscle aldolase.[13] This similarity extends to the pH activity profile for TgALD that was comparable to the previously reported profile for rabbit muscle aldolase having comparable inflections at the acidic ($pKa = 5.0 \pm 0.1$) and basic limb ($pKa = 9.4 \pm 0.2$) (**Figure 2-2**.).[16] The active site residues, which are evolutionarily conserved in both TgALD and rabbit muscle aldolase, together with activity profiles are consistent with Glu-189, which hydrogen bonds to the C4 hydroxyl of FBP in the *30min* structure shown in **Figure 2-1A** inset, as the residue responsible for proton transfer in aldol and reverse aldol reaction. In the mammalian enzyme, the homologous residue Glu-187 has been shown to be responsible for proton abstraction at the C4 hydroxyl of FBP.[11,16] Empirical pKa calculations of TgALD using Propka and H++ programs support pKa estimates ~ 5 for Glu-189.[37–41] The kinetic data implies that TgALD active site functionality is typical of class I FBP aldolases and is highly stereospecific.

Table 2-4. Kinetic parameters of the FBP cleavage reaction for recombinant native aldolases from *Toxoplasma gondii* and rabbit muscle.

enzyme	k_{cat} (s^{-1}) $\pm$ SE ^{a}	K_m (uM) $\pm$ SE	pKa_1/pKa_2
TgALD wt	7.09 $\pm$ 0.20	4.05 $\pm$ 0.80	5.0/9.4
RMA wt ^{b}	13.22	5.1 $\pm$ 1.9	5.1/~10 ^{c}

^{a} SE: standard error; ^{b} RMA: rabbit muscle aldolase; values from previous reports;[13] ^{c} pKa values reported previously[16]
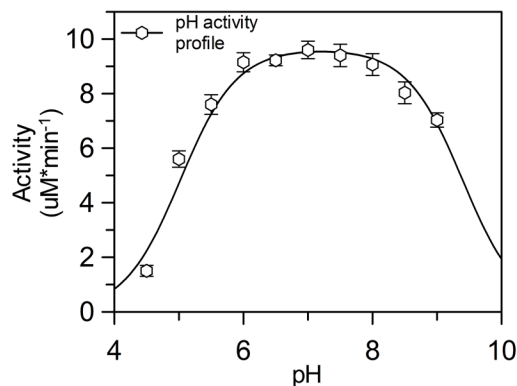
Figure 2-2. pH activity profile of the FBP cleavage reaction for TgALD.

Saturating concentrations of FBP were used to assay activity at pH 4 – 9 for every 0.5 pH unit. A double pKa curve was fitted against the kinetic data using the program GraFit (see experimental procedures). The acidic limb of the profile has a pKa of 5.0, consistent with the pKa of a glutamate residue. Error bars are shown for SE (n ≥ 3 for each point).

The preferential stabilization of the unproductive *cis*-configuration of D-G3P when only the *trans*-configuration of D-G3P is productive in C_3-C_4 bond formation is best understood in terms of rotational isomerization about the C_1-C_2 aldehyde bond. In the *1min* structure, the D-G3P carbonyl is maintained in the *cis*-configuration by hydrogen bonding to the protonated form of Glu-189 O_{E2} (2.9Å), shown in **Figure 2-3B**, and a nearby bridging water molecule, W1 (2.8Å). W1 is highly ordered (fully occupied), donating one hydrogen bond to the O_1 carbonyl and a second one to the Glu-191 while-accepting a third from the P_1-phosphate oxyanion (2.6 Å) and a fourth from a water molecule (2.8Å) in the second hydration shell. The Glu-191 carboxylate would have a pKa close to the theoretical value of 4.3, as it is solvent exposed, and is in proximity of Arg-148 that would stabilize the conjugate base form, supporting a proton acceptor role at pH 5.5 with regards to W1. Proton donation to W1 by the P_1-phosphate oxyanion is supported by an experimental pKa of 6.45 for the P_1-phosphate dianion,[49] and would be largely protonated at pH 5.5. The extensive hydrogen-bonding pattern by W1 would thus ensure trapping of the unproductive *cis*-configuration of the aldehyde phosphate in the active site.

Proton transfer would be unlikely in the *cis*-configuration as the nearest basic residue, Lys-146, is not proximal (> 4.2Å) to efficiently polarize the aldehyde carbonyl and the configuration is least favourable for in-line proton transfer as the transfer geometry bisects the *sp2* orbitals of D-G3P O_1.[50] Although the *cis*-configuration is unproductive with respect to aldol addition,

isomerization to a minor population (< 0.1 in occupancy) corresponding to the *trans*-configuration of the aldehyde, competent for proton transfer, would not be hindered in the active site ternary complex. The cryotrapping trapping of the *cis*-configuration can be attributed to the acidic pH of the crystallization buffer that has stabilized in acid form a significant fraction of Glu-189 in the crystallization buffer (pH 5.5) allowing it to participate in hydrogen-bonding interaction with the D-G3P aldehyde. At neutral pH, the acidic population of Glu-189 would be insufficient to afford detection of the *cis*-configuration of D-G3P in the active site. However, as long as generation of the low abundance population of Glu-189 is not rate limiting, *cis-trans* equilibration which has a rapid timescale would nevertheless be promoted by an acidic population of Glu-189. Stabilization of the *cis*-configuration by W1 interaction would persist as a sizable fraction of the DHAP monobasic phosphate anion remains protonated at pH 7 and thus competent to hydrogen bond with W1.

Binding of the *cis*-D-G3P configuration is also consistent with computational and experimental studies on the solution stability of its glycoaldehyde analogue.[51] The most stable aldehyde complexes have *cis*-configurations with respect to the water molecules surrounding the oxygen atoms of the glycolaldehyde by virtue of water molecules establishing bridging hydrogen bonds through their interaction with the hydroxyl and carbonyl groups in the glycoaldehyde. This suggests that D-G3P engaged in the aldolase active site would possess a predominant *cis*-configuration upon binding.

D-G3P interacts extensively via its P_6-phosphate site with residues Lys-107, Ser-36 and Thr-39 (5 hydrogen bonds) and ordered water molecules (6 hydrogen bonds), some of which interact with active site residues, thereby firmly anchoring D-G3P phosphate in the active site. However, there are fewer structural restraints that would reduce the rotational degrees of freedom of the aldehyde moiety (2 hydrogen bonds by ordered water molecules interacting with the O_1 hydroxyl and O_2 carbonyl respectively), allowing for considerable configurational rearrangement and not inconsistent with the observations that aldolase can accept structurally diverse aldehydes.[6] The competent reaction geometry for incipient C_3-C_4 bond formation by the bound D-G3P in the observed *cis*-configuration entails rotation of ~155° about the D-G3P C_1-C_2 bond by the carbonyl O_1 and a slight torsion rearrangement about the C_2-C_3 bond (~18°), placing the carbonyl oxygen within 2.5Å of the Glu-189 carboxylate and parallel to the enamine plane (**Figure 2-3C** - *trans*-configuration). Furthermore, the D-G3P carbonyl O_1 is able to make a
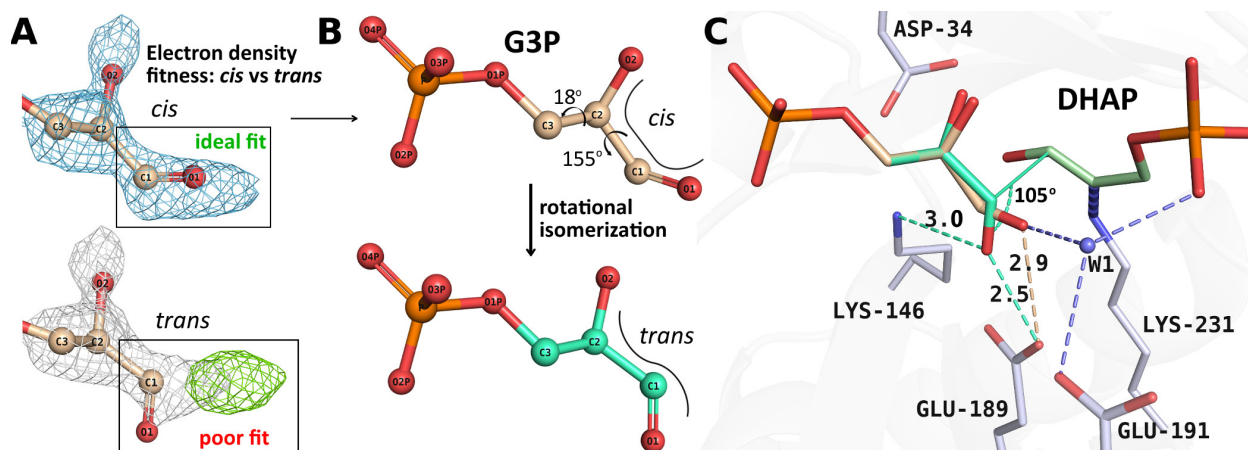
Figure 2-3. Reaction geometry associated with aldol addition implicating putative *cis-trans* rotational isomerization.

(**A**) Active site difference density calculated from a simulated annealing $F_o - F_c$ omit map is illustrated encompassing the substrate binding site surrounding the *cis*-D-G3P aldehyde group in the *1min* structure and contoured at a 2.1σ level. Unambiguous modeling of the *cis*-configuration was possible. Refinement with the *trans*-configuration afforded a poor fit, as shown by the residual difference density (*green*) calculated from a $F_o - F_c$ map (contour at 2.1σ). The corresponding $2F_o - F_c$ (contour at 1σ) encompassing the trans-configuration is colored *grey*. Refinement with the *trans*-configuration modeled into the *0.5min*, *1min*, and *2min* structures, reverted back to the *cis*-form in all cases (see experimental procedures for more details). (**B**) The *1min* structure is shown with D-G3P bound in the unproductive *cis*-form (*wheat*). The 3(*S*)-4(*R*) stereochemistry of the condensation product, FBP, requires prior rotational isomerization about the D-G3P C_1-C_2 bond yielding a putative D-G3P *trans*-configuration (*cyan*). The position of *trans* D-G3P in the active site was energy minimized using geometric restraints generated by refmac5.[52] (**C**) Superposition of the reported D-G3P configurations shows a hydrogen bond with Glu-189 (*dotted cyan line*) in the *trans*-configuration, and together with Lys-146 orients the carbonyl O_1 to promote efficient proton transfer to the polarized D-G3P carbonyl that would otherwise be unproductive in the *cis*-form.

charged interaction with the Lys-146, thereby polarizing the D-G3P carbonyl. Subsequent proton transfer from Glu-189 then initiates aldol addition. A similar configurational rearrangement has also been observed for Schiff base formation in transaldolases.[29]

In the *trans*-configuration model, the plane comprising the D-G3P-carbonyl defined by atoms C_2, C_1, and O_1 would indicate that the DHAP C_3 follows an approach angle of 105° during aldol reaction that is consistent with the geometry of incipient aldol addition adhering to the Bürgi-Dunitz angle of $105 \pm 5°$.[53,54] In enzyme catalysis, adherence to the Bürgi-Dunitz trajectory has been shown in Schiff base formation by transaldolases in case of the angle of attack by the Lys nucleophile with respect to the ketone plane of the acyclic substrate.[29] The trapping of the
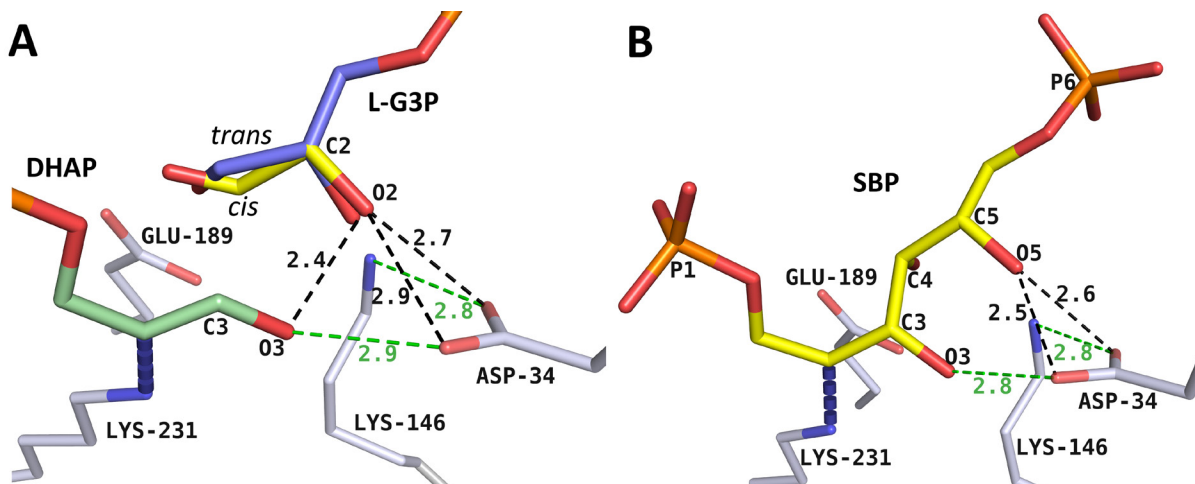
Figure 2-4. L-G3P model reveals basis for enantiomeric discrimination in class I aldolase.
(**A**) The L-enantiomer of the bound D-G3P (*yellow*) was superimposed on the D-G3P geometry from the *1min* structure. Favourable linear *syn* hydrogen bonds are depicted as *green dashes*. The steric repulsion resulting from proximity of L-G3P O_2 to surrounding oxygens (DHAP O3 oxygen, Asp-34 carboxylate oxygens) is depicted as *dark dashes*. The *trans*-configuration (*blue*) for L-enantiomer modeled using the *trans*-D-G3P model affords comparable repulsions as observed for the *cis*-configuration. (**B**) SBP was modeled into the active site using the FBP Schiff base complex as a guide. Clashes (*dark dashes*) and favourable hydrogen bonds (*green dashes*) are illustrated.

ternary complex in TgALD, as seen in **Figure 2-3B**, provides experimental corroboration of an aldol reaction adhering to the Brugi-Dunitz trajectory during enzyme catalyzed C-C bond formation.

Finally, the putative *trans*-geometry of the aldehyde affords a pericyclic transition state,[55,56] as was pointed out in the crystal structure of the Schiff base intermediate formed between FBP and rabbit muscle aldolase.[11] In TgALD, the atoms of Lys-231 Nζ, FBP C_2, C_3, C_4, and O_4 as well as a Glu-189 carboxylate oxygen form a near chair-like structure that mimics the spatial arrangement of reactants for a pericyclic transition state proposed in non-enzymatic aldol additions with preformed enolates. Comparison of the atomic positions in TgALD intermediate with the previously demonstrated chair-like conformation in rabbit muscle aldolase gives an r.m.s. deviation of 0.45Å. The *cis*-form of the aldehyde could not participate in such a transition state further reinforcing our interpretation of the *trans*-configuration as the catalytically productive form.

The formation of the C_3-C_4 bond between *trans*-G3P and DHAP-enamine are consistent with least atomic motion during aldol addition. The motions require a slight hinge movement of the

aldehyde carbonyl pivoting about the P_6-phosphate binding locus (**Figure S2-2**), by less than 1Å, enabling the aldehyde C_1 carbon to approach the DHAP C_2 carbon, thereby forming a hydrogen bond (2.8Å) interaction between the aldehyde O_1 with Lys-146 Nζ (shown in **Figure S2-2**).

Aldehyde stereospecificity. Notwithstanding the promiscuity of aldolase towards aldehydes,[6] not all aldehydes condense with DHAP, most notably of which is the L-enantiomer of G3P. Inactivation of aldolase by L-G3P has been reported in the literature,[10,57] while other reports have shown the putative reaction product of DHAP and L-G3P, L-sorbose-1,6-bisphosphate (SBP), to be a poor substrate for aldolase cleavage.[8,9] The active site constraints imposed on aldehyde binding for productive condensation provides a basis for understanding the enantiomeric selectivity at the aldehyde O_2 position.

The L-enantiomer of G3P when superposed upon the *cis*-form of D-G3P in the *1min* structure introduces steric clashes in the active site. In D-G3P, its C_2 hydroxyl is stabilized by hydrogen-bonding with an active site water molecule (3.0Å) that in turn is weakly coordinated to the Ala-32 backbone carbonyl oxygen (3.2Å). Altering the chirality at the C_2 carbon while maintaining a geometry competent for incipient aldol addition is destabilizing by +2.08 *k*cal/mol compared to the D-form, as per binding energy calculations performed with AutoDock4.2,[32] indicating the presence of destabilizing van der Waals interactions and hydrogen-bonding energy involving primarily the interaction of O_2 hydroxyl oxygen with Asp-34 carboxylate oxygens and contributions from clashes with DHAP O_3 oxygen. The O_2 hydroxyl group is positioned opposite the conserved Asp-34 carboxylate oxygens (2.7Å /2.9Å) and in steric clash with the DHAP O_3 oxygen (2.4Å) (**Figure 2-4A – *dark dashes***). The symmetrical positioning of the L-G3P O_2 oxygen opposite the Asp-34 carboxylate oxygens is non-ideal due to unfavourable bifurcated hydrogen-bonding (i.e. acute C=O···H angles)[58,59] and results in a repulsive interaction between oxygens, thereby disfavoring binding by the *cis*-configuration of the L-G3P. This clash cannot be relieved by hydrogen bond donation of the DHAP O_3 hydroxyl to L-G3P O_2 oxygen as it maintains a tight linear *syn* hydrogen bond with the Asp-34 carboxylate (**Figure 2-4A – *green dash***). The *trans*-configuration (*cyan*) for L-enantiomer based on the *trans*-D-G3P model, when energy minimized, exacerbates the repulsive effect, due to the close contact by the O_2 hydroxyl with the Asp-34 carboxylate oxygens and DHAP O_3. For both *cis/trans* isomers of

L-G3P, relief of the repulsive interactions would not be consistent with the productive binding mode leading to aldol addition.

The overlay of SBP onto the active site binding mode of FBP rationalizes the poor substrate specificity for the hexose SBP. Superposition results in the same unfavorable steric interaction between the C_5 hydroxyl and Asp-34 (**Figure 2-4B** – *dark dashes*) and would entail an unproductive binding mode for proton transfer between the SBP C_4 hydroxyl and Glu-189.

Racemic aldol addition products with respect to the configuration at C_4 have been noted in a number of aldolases. In both 2-keto-4-hydroxyglutarate aldolase[60] and L-fuculose-1-phosphate aldolase,[61] racemization occurs at C_4 of the condensation products, resulting from isomerization of the aldehyde during stereofacial attack,[62] and from the chemical nature of the acceptor aldehyde. In the class I TBP aldolase from *S. aureus*[63] and *S. pyogenes*,[64] configuration at both C_3 and C_4 is not retained by the reaction mechanism as aldol addition yields a mixture of sorbose-P2, psicose-P2, fructose-P2 and tagatose-P2. Although class I FBP aldolases maintain strict stereospecificity regarding the configuration at C_3 and C_4, the class I aldolase reaction mechanism in general would not appear to preclude active site binding of cognate rotamers, diastereomers, and enantiomers, nor preclude the existence of such enzymatic intermediate forms. Rather the active site geometry in glycolytic class I FBP aldolases has evolved to suppress a specific stereoisomer by disfavoring their activation to ensure strict stereospecificity in aldol addition. The ternary complex intermediate promoting the chemistry of bond formation is however promiscuous to stereoisomers as ternary complex formation does not entail strict stereospecificity in order to promote a reaction geometry competent for bond formation. Consequently, from an evolutionary perspective, different active sites may give rise to the same ternary complex, yet by stabilizing different stereoisomers would evolve different stereospecificities or their lack thereof.

SUPPORTING INFORMATION AVAILABLE

Data showing the structural discernment of enzymatic intermediates (enamine vs iminium) formed with FBP in *T. gondii* aldolase active site, intermediates (**Figure S2-1**), and structural rearrangements during aldol addition from *trans*-D-G3P to covalent Schiff base FBP (**Figure S2-2**).

REFERENCES

(1) Grazi, E., Rowley, P. T., Cheng, T., Tchola, O., and Horecker, B. L. (1962) The mechanism of action of aldolases. III. Schiff base formation with lysine. *Biochem. Biophys. Res. Commun. 9*, 38–43.

(2) Rose, I. A., and O'Connell, E. L. (1969) Studies on the Interaction of Aldolase with Substrate Analogues. *J. Biol. Chem. 244*, 126–134.

(3) Hartman, F. C., and Barker, R. (1965) An Exploration of the Active Site of Aldolase Using Structural Analogs of Fructose Diphosphate*. *Biochemistry (Mosc.) 4*, 1068–1075.

(4) Rose, I. A., and Warms, J. V. B. (1985) Complexes of muscle aldolase in equilibrium with fructose 1,6-bisphosphate. *Biochemistry (Mosc.) 24*, 3952–3957.

(5) Kuo, D. J., and Rose, I. A. (1985) Chemical trapping of complexes of dihydroxyacetone phosphate with muscle fructose-1,6-bisphosphate aldolase. *Biochemistry (Mosc.) 24*, 3947–3952.

(6) Bednarski, M. D., Simon, E. S., Bischofberger, N., Fessner, W. D., Kim, M. J., Lees, W., Saito, T., Waldmann, H., and Whitesides, G. M. (1989) Rabbit muscle aldolase as a catalyst in organic synthesis. *J. Am. Chem. Soc. 111*, 627–635.

(7) Gefflaut, T., Blonski, C., Perie, J., and Willson, M. (1995) Class I aldolases: Substrate specificity, mechanism, inhibitors and structural aspects. *Prog. Biophys. Mol. Biol. 63*, 301–340.

(8) Richards, O. C., and Rutter, W. J. (1961) Comparative Properties of Yeast and Muscle Aldolase. *J. Biol. Chem. 236*, 3185–3192.

(9) Tung, T. C., Ling, K. H., Byrne, W. L., and Lardy, H. A. (1954) Substrate specificity of muscle aldolase. *Biochim. Biophys. Acta 14*, 488–494.

(10) Lai, C. Y., Martinez-de Dretz, G., Bacila, M., Marinello, E., and Horecker, B. L. (1968) Labeling of the active site of aldolase with glyceraldehyde 3-phosphate and erythrose 4-phosphate. *Biochem. Biophys. Res. Commun. 30*, 665–672.

(11) St-Jean, M., Lafrance-Vanasse, J., Liotard, B., and Sygusch, J. (2005) High resolution reaction intermediates of rabbit muscle fructose-1,6-bisphosphate aldolase: substrate cleavage and induced fit. *J. Biol. Chem. 280*, 27262–27270.

(12) St-Jean, M., and Sygusch, J. (2007) Stereospecific Proton Transfer by a Mobile Catalyst in Mammalian Fructose-1,6-bisphosphate Aldolase. *J. Biol. Chem. 282*, 31028–31037.

(13) St-Jean, M., Blonski, C., and Sygusch, J. (2009) Charge Stabilization and Entropy Reduction of Central Lysine Residues in Fructose-Bisphosphate Aldolase. *Biochemistry (Mosc.) 48*, 4528–4537.

(14) Rose, I. A., Warms, J. V., and Kuo, D. J. (1987) Concentration and partitioning of intermediates in the fructose bisphosphate aldolase reaction. Comparison of the muscle and liver enzymes. *J. Biol. Chem. 262*, 692–701.

(15) Rose, I. A., and O'Connell, E. L. (1977) Specificity of fructose-1, 6-P2 aldolase (muscle) and partition of the enzyme among catalytic intermediates in the steady state. *J. Biol. Chem. 252*, 479–482.

(16) Maurady, A., Zdanov, A., de Moissac, D., Beaudry, D., and Sygusch, J. (2002) A Conserved Glutamate Residue Exhibits Multifunctional Catalytic Roles in D-Fructose-1,6-bisphosphate Aldolases. *J. Biol. Chem. 277*, 9474–9483.

(17) Jewett, T. J., and Sibley, L. D. (2003) Aldolase forms a bridge between cell surface adhesins and the actin cytoskeleton in apicomplexan parasites. *Mol. Cell 11*, 885–894.

(18) Otwinowski, Z., and Minor, W. (1997) [20] Processing of X-ray diffraction data collected in oscillation mode, in *Methods in Enzymology* (Charles W. Carter, J., Ed.), pp 307–326. Academic Press.

(19) Adams, P. D., Grosse-Kunstleve, R. W., Hung, L.-W., Ioerger, T. R., McCoy, A. J., Moriarty, N. W., Read, R. J., Sacchettini, J. C., Sauter, N. K., and Terwilliger, T. C. (2002) *PHENIX*: building new software for automated crystallographic structure determination. *Acta Crystallogr. D Biol. Crystallogr. 58*, 1948–1954.

(20) McCoy, A. J., Grosse-Kunstleve, R. W., Adams, P. D., Winn, M. D., Storoni, L. C., and Read, R. J. (2007) *Phaser* crystallographic software. *J. Appl. Crystallogr. 40*, 658–674.

(21) Söding, J. (2005) Protein homology detection by HMM–HMM comparison. *Bioinformatics 21*, 951–960.

(22) Afonine, P. V., Grosse-Kunstleve, R. W., Echols, N., Headd, J. J., Moriarty, N. W., Mustyakimov, M., Terwilliger, T. C., Urzhumtsev, A., Zwart, P. H., and Adams, P. D. (2012) Towards automated crystallographic structure refinement with <phenix.refine>. *Acta Crystallogr. D Biol. Crystallogr. 68*, 352–367.

(23) Emsley, P., Lohkamp, B., Scott, W. G., and Cowtan, K. (2010) Features and development of *Coot*. *Acta Crystallogr. D Biol. Crystallogr. 66*, 486–501.

(24) Karplus, P. A., and Diederichs, K. (2012) Linking Crystallographic Model and Data Quality. *Science 336*, 1030–1033.

(25) Afonine, P. V., Moriarty, N. W., Mustyakimov, M., Sobolev, O. V., Terwilliger, T. C., Turk, D., Urzhumtsev, A., and Adams, P. D. (2015) FEM: feature-enhanced map. *Acta Crystallogr. D Biol. Crystallogr. 71*, 646–666.

(26) Moriarty, N. W., Grosse-Kunstleve, R. W., and Adams, P. D. (2009) electronic Ligand Builder and Optimization Workbench (eLBOW): a tool for ligand coordinate and restraint generation. *Acta Crystallogr. D Biol. Crystallogr. 65*, 1074–1080.

(27) Chen, V. B., Arendall, W. B., Headd, J. J., Keedy, D. A., Immormino, R. M., Kapral, G. J., Murray, L. W., Richardson, J. S., and Richardson, D. C. (2010) MolProbity : all-atom structure validation for macromolecular crystallography. *Acta Crystallogr. D Biol. Crystallogr. 66*, 12–21.

(28) The PyMol Molecular Graphics System, Version 1.7.4, Schrodinger, LLC.

(29) Light, S. H., Minasov, G., Duban, M.-E., and Anderson, W. F. (2014) Adherence to Bürgi–Dunitz stereochemical principles requires significant structural rearrangements in Schiff-base formation: insights from transaldolase complexes. *Acta Crystallogr. D Biol. Crystallogr. 70*, 544–552.

(30) Terwilliger, T. C., Grosse-Kunstleve, R. W., Afonine, P. V., Adams, P. D., Moriarty, N. W., Zwart, P., Read, R. J., Turk, D., and Hung, L.-W. (2007) Interpretation of ensembles created by multiple iterative rebuilding of macromolecular models. *Acta Crystallogr. D Biol. Crystallogr. 63*, 597–610.

(31) Racker, E. (1947) Spectrophotometric measurement of hexokinase and phosphohexokinase activity. *J. Biol. Chem. 167*, 843–854.

(32) Morris, G. M., Huey, R., Lindstrom, W., Sanner, M. F., Belew, R. K., Goodsell, D. S., and Olson, A. J. (2009) AutoDock4 and AutoDockTools4: Automated Docking with Selective Receptor Flexibility. *J. Comput. Chem. 30*, 2785–2791.

(33) O'Boyle, N. M., Banck, M., James, C. A., Morley, C., Vandermeersch, T., and Hutchison, G. R. (2011) Open Babel: An open chemical toolbox. *J. Cheminformatics 3*, 33.

(34) Wang, J., Wolf, R. M., Caldwell, J. W., Kollman, P. A., and Case, D. A. (2004) Development and testing of a general amber force field. *J. Comput. Chem. 25*, 1157–1174.

(35) Wang, J., Wang, W., Kollman, P. A., and Case, D. A. (2006) Automatic atom type and bond type perception in molecular mechanical calculations. *J. Mol. Graph. Model. 25*, 247–260.

(36) Pettersen, E. F., Goddard, T. D., Huang, C. C., Couch, G. S., Greenblatt, D. M., Meng, E. C., and Ferrin, T. E. (2004) UCSF Chimera—A visualization system for exploratory research and analysis. *J. Comput. Chem. 25*, 1605–1612.

(37) Søndergaard, C. R., Olsson, M. H. M., Rostkowski, M., and Jensen, J. H. (2011) Improved Treatment of Ligands and Coupling Effects in Empirical Calculation and Rationalization of pKa Values. *J. Chem. Theory Comput. 7*, 2284–2295.

(38) Olsson, M. H. M., Søndergaard, C. R., Rostkowski, M., and Jensen, J. H. (2011) PROPKA3: Consistent Treatment of Internal and Surface Residues in Empirical pKa Predictions. *J. Chem. Theory Comput. 7*, 525–537.

(39) Anandakrishnan, R., Aguilar, B., and Onufriev, A. V. (2012) H++ 3.0: automating pK prediction and the preparation of biomolecular structures for atomistic molecular modeling and simulations. *Nucleic Acids Res. 40*, W537–W541.

(40) Myers, J., Grothaus, G., Narayanan, S., and Onufriev, A. (2006) A simple clustering algorithm can be accurate enough for use in calculations of pKs in macromolecules. *Proteins Struct. Funct. Bioinforma. 63*, 928–938.

(41) Gordon, J. C., Myers, J. B., Folta, T., Shoja, V., Heath, L. S., and Onufriev, A. (2005) H++: a server for estimating pKas and adding missing hydrogens to macromolecules. *Nucleic Acids Res. 33*, W368–W371.

(42) Dolinsky, T. J., Nielsen, J. E., McCammon, J. A., and Baker, N. A. (2004) PDB2PQR: an automated pipeline for the setup of Poisson–Boltzmann electrostatics calculations. *Nucleic Acids Res. 32*, W665–W667.

(43) Connett, R. J. (1985) In vivo glycolytic equilibria in dog gracilis muscle. *J. Biol. Chem. 260*, 3314–3320.

(44) Veech, R. L., Raijman, L., Dalziel, K., and Krebs, H. A. (1969) Disequilibrium in the triose phosphate isomerase system in rat liver. *Biochem. J. 115*, 837–842.

(45) Grazi, E., Sivieri-Pecorari, C., Gagliano, R., and Trombetta, G. (1973) Complexes of fructose diphosphate aldolase with dihydroxyacetone phosphate and dihydroxyacetone sulfate. *Biochemistry (Mosc.) 12*, 2583–2590.

(46) Reynolds, S. J., Yates, D. W., and Pogson, C. I. (1971) Dihydroxyacetone phosphate. Its structure and reactivity with α-glycerophosphate dehydrogenase, aldolase and triose phosphate isomerase and some possible metabolic implications. *Biochem. J. 122*, 285–297.

(47) Trentham, D. R., McMurray, C. H., and Pogson, C. I. (1969) The active chemical state of d-glyceraldehyde 3-phosphate in its reactions with d-glyceraldehyde 3-phosphate dehydrogenase, aldolase and triose phosphate isomerase. *Biochem. J. 114*, 19–24.

(48) Peczon, B. D., and Spivey, H. O. (1972) Catalytic sites in rabbit muscle glyceraldehyde-3-phosphate dehydrogenase. Their number and their kinetic and spectral properties. *Biochemistry (Mosc.) 11*, 2209–2217.

(49) Grazi, E. (1974) Quantitative evaluation of the carbanion intermediate in the aldolase reaction. *Biochem. Biophys. Res. Commun. 56*, 106–111.

(50) Duan, X., and Scheiner, S. (1992) Energetics, proton transfer rates, and kinetic isotope effects in bent hydrogen bonds. *J. Am. Chem. Soc. 114*, 5849–5856.

(51) Azofra, L. M., Quesada-Moreno, M. M., Alkorta, I., Avilés-Moreno, J. R., Elguero, J., and López-González, J. J. (2015) Understanding the Aldo-Enediolate Tautomerism of Glycolaldehyde in Basic Aqueous Solutions. *ChemPhysChem 16*, 2226–2236.

(52) Murshudov, G. N., Skubák, P., Lebedev, A. A., Pannu, N. S., Steiner, R. A., Nicholls, R. A., Winn, M. D., Long, F., and Vagin, A. A. (2011) REFMAC5 for the refinement of macromolecular crystal structures. *Acta Crystallogr. D Biol. Crystallogr. 67*, 355–367.

(53) Bürgi, H. B., Dunitz, J. D., Lehn, J. M., and Wipff, G. (1974) Stereochemistry of reaction paths at carbonyl centres. *Tetrahedron 30*, 1563–1572.

(54) Fleming, I. (2010) Molecular Orbitals and Organic Chemical Reactions: Reference Edition. John Wiley & Sons, Inc.

(55) Zimmerman, H. E., and Traxler, M. D. (1957) The stereochemistry of the Ivanov and Reformatsky reactions. I. *J. Am. Chem. Soc. 79*, 1920–1923.

(56) Dubois, J.-E., and Fort, J.-F. (1972) Dynamic stereochemistry of aldolization—XX. *Tetrahedron 28*, 1653–1663.

(57) Rose, I. A., and O'Connell, E. L. (1969) Inactivation and Labeling of Triose Phosphate Isomerase and Enolase by Glycidol Phosphate. *J. Biol. Chem. 244*, 6548–6550.

(58) McDonald, I. K., and Thornton, J. M. (1994) Satisfying Hydrogen Bonding Potential in Proteins. *J. Mol. Biol. 238*, 777–793.

(59) Görbitz, C. H., and Etter, M. C. (1992) Hydrogen bonds to carboxylate groups. The question of three-centre interactions. *J. Chem. Soc. Perkin Trans. 2* 131–135.

(60) Kobes, R. D., and Dekker, E. E. (1969) 2-Keto-4-hydroxyglutarate aldolase of bovine liver purification, criteria of purity, and general properties. *J. Biol. Chem. 244*, 1919–1925.

(61) Espelt, L., Bujons, J., Parella, T., Calveras, J., Joglar, J., Delgado, A., and Clapés, P. (2005) Aldol Additions of Dihydroxyacetone Phosphate to N-Cbz-Amino Aldehydes Catalyzed by L-Fuculose-1-Phosphate Aldolase in Emulsion Systems: Inversion of Stereoselectivity as a Function of the Acceptor Aldehyde. *Chem. – Eur. J. 11*, 1392–1401.

(62) Meloche, H. P., and Mehler, L. (1973) The stereochemistry at carbon 3 of pyruvate lyase condensation products aldolases forming condensation products racemic at carbon 4. *J. Biol. Chem. 248*, 6333–6338.

(63) Bissett, D. L., and Anderson, R. L. (1980) Lactose and D-galactose metabolism in Staphylococcus aureus. III. Purification and properties of D-tagatose-6-phosphate kinase. *J. Biol. Chem. 255*, 8745–8749.

(64) LowKam, C., Liotard, B., and Sygusch, J. (2010) Structure of a Class I Tagatose-1,6-bisphosphate Aldolase: investigation into an apparent loss of stereospecificity. *J. Biol. Chem. 285*, 21143–21152.

A

DHAP
enamine

B

FBP
iminium
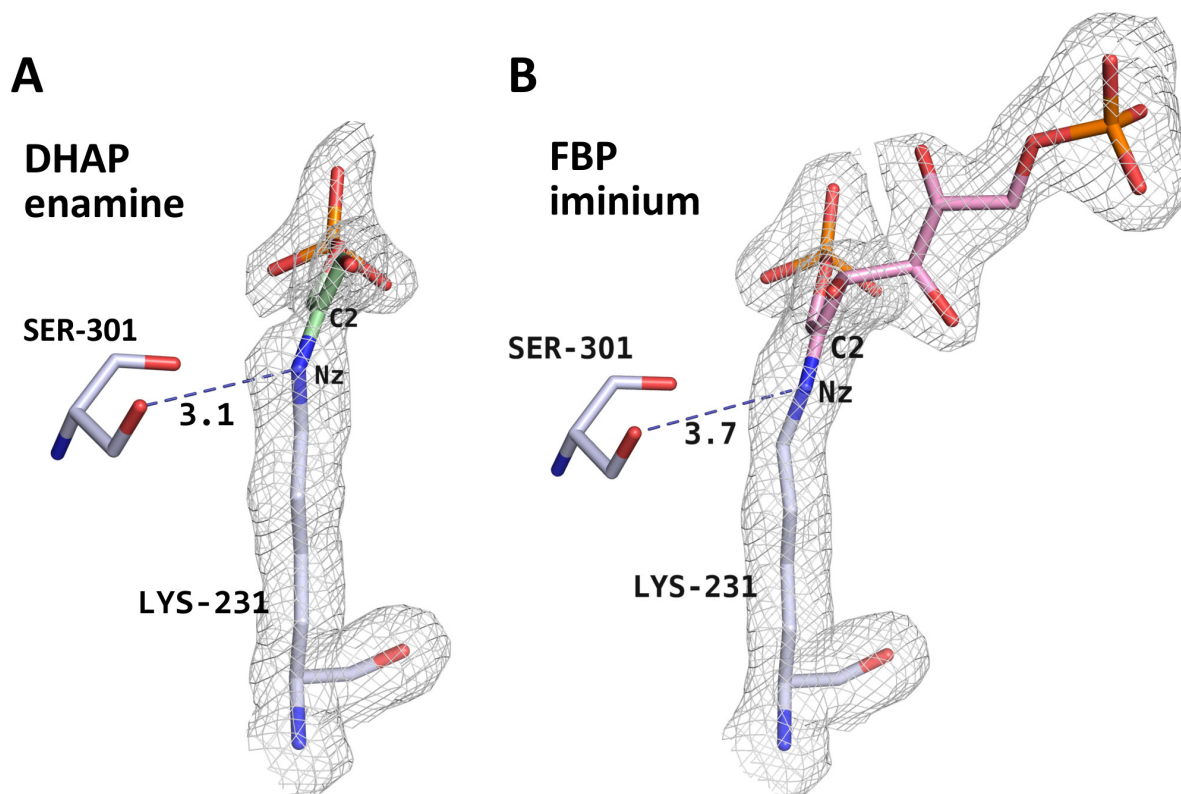
Figure S2-1. Discrimination of enzymatic intermediates formed with FBP in *T. gondii* aldolase active site.

Geometry of enzymatic intermediates was used to identify the chemical identity of the trapped intermediate-aldolase complex. (**A**) DHAP-enamine intermediate (*green*) was identified in the *0.5min*, *1min* and *2min* structures of native TgALD soaked with substrate on the basis of sp^3 hybridization of Lys-231 Nζ and hydrogen bond formation (*blue dash* – 3.1Å) between the Ser-301 hydroxyl and Lys-231 Nζ. Planar stereochemistry is observed about the C_2 atom, consistent with enamine formation. Structure shown illustrates the *1min* structure. (**B**) The iminium FBP intermediate was identified in the *10min* and *30min* structures corresponding to the Schiff base complex with FBP (*pink*). sp^2 hybridization of Lys-231 Nζ precludes hydrogen bond formation with Ser-301 (*blue dash* – 3.7Å) and is evidenced by the planarity around the Nζ atom. Structure shown illustrates the *10min* structure. Both maps depict difference electron density maps calculated from simulated annealing $F_o - F_c$ omit maps encompassing Lys-231 and bound substrate and contoured at 3σ.
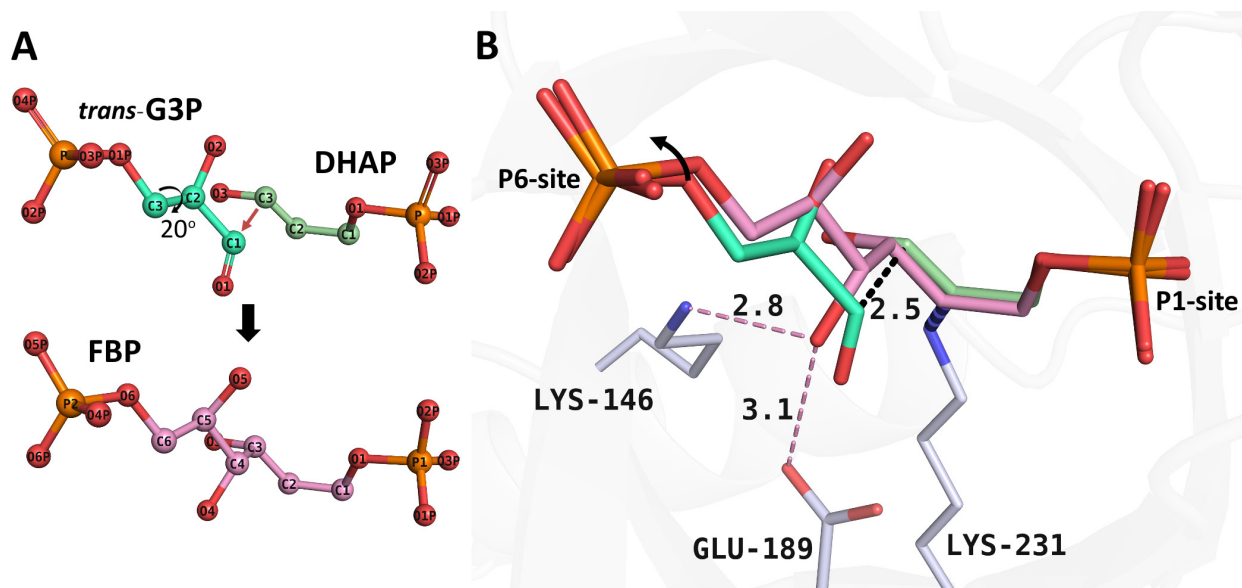
Figure S2-2. Configurational rearrangements during aldol addition.

(**A**) Panel showing nucleophilic attack on the electrophilic C1 carbonyl atom by the DHAP C3 carbanion. The modeled *trans*-configuration (*cyan*) of D-G3P is shown with the appropriate torsion angle at the C_2-C_3 bond enabling aldol addition with the DHAP-enamine to form FBP (*pink*). (**B**) The *1min* and *30min* structures were superposed (alignment of Cα atoms) to illustrate the conformational change that occurs during C_3-C_4 bond formation, and is consistent with least atomic motion. Binding by the phosphate groups of D-G3P and FBP at the P_6-site is isostructural and the trajectory requires a slight hinge rotation perpendicular to the viewing plane (~ 10°) about the D-G3P phosphate to superpose D-G3P atoms C_1, C_2, and C_3 with FBP atoms C_4, C_5, and C_6. Atoms in the DHAP enamine are essentially identically positioned as equivalent FBP atoms (r.m.s.d. = 0.202Å). The distance between DHAP C_3 and D-G3P C_1 prior to condensation is 2.5Å (*black dashes*). The nascent C_4-hydroxyl group is stabilized by a short hydrogen bend with Glu-189 and by charged hydrogen-bonding with Lys-146 (*pink dashes*).

94

Chapter 3

Bisphosphonate inhibitors of mammalian glycolytic aldolases

Background

Glycolysis has been considered a promising target in cells with a high dependence on glycolytic flux, for example cancer cells and parasite protozoa such as *Trypanosoma brucei*, the causative agent of African sleeping sickness. The location of aldolase in glycolysis, at the cusp of hexose breakdown to trioses, makes it a strategic base for anti-glycolytic agents. Hence, there is considerable interest in the development of active site-directed inhibitors for class I aldolase. Despite the large number of inhibitors that have been investigated, the precise binding modes are yet to be fully resolved.

Our laboratory has been intimately involved with development of the latter, publishing several articles advancing the cause. Nevertheless, structural data from these studies have been lacking, and is mostly limited to enzymatic and *in silico* modeling data. Here, we continue a collaborative effort with Dr. Casimir Blonski's group (Université Paul Sabatier, Toulouse), involving the conception of a novel group of inhibitors, bisphosphonates, from which we discovered an inhibitor having the highest affinity for aldolase of any known inhibitor and demonstrate its effectiveness in reducing cell viability in cancer cells.

The results of this study are to be submitted to the *Journal of Medicinal Chemistry* in an article titled: *Bisphosphonate inhibitors of mammalian glycolytic aldolases*. My involvement includes the collection and analysis of all co-crystal structures by x-ray crystallography, kinetic parameterization, and *in vivo* testing. Rachid Djilliali and Casimir Blonski performed all chemical syntheses. In addition, all figures were produced by myself including the writing of the manuscript and was subsequently revised by all parties involved, with Dr. Sygusch providing critical revisions.

**[Due to unforeseen circumstances regarding our collaborator Dr. Blonski, the chemical synthesis and purity assessment component to be included in the text and experimental section is outstanding and is indicated as such in the manuscript. Upon reception of the latter, the paper will be submitted without further delay.]

Bisphosphonate inhibitors of mammalian glycolytic aldolase

Paul W. Heron[§], Rachid Djilliali[†], Casimir Blonski[†], Jurgen Sygusch*[§]

*§ Département de biochimie et médecine moléculaire, Université de Montréal. CP 6128, Succursale Centre-Ville, Montréal, Québec, Canada H3C 3J7

† UMR 8182, ICMMO, Institut de Chimie Moléculaire et des Matériaux d'Orsay, Université Paris-Sud, Bât 420, 91405 Orsay Cedex, France

ABSTRACT

The glycolytic enzyme aldolase is an emerging drug target in diseases such as cancer and protozoan infections which are dependent on a hyperglycolytic phenotype to synthesize ATP and metabolic precursors for biomass production. To date, no structural information is available of the enzyme in complex with phosphate-derived inhibitors that would serve as a template for rational design of future pharmacological inhibitors. To address this shortcoming, we determined the crystal structure of mammalian aldolase in complex with naphthalene 2,6-bisphosphate (**1**) and then used this structure as a template for the design of bisphosphonate-based inhibitors, namely 2-phosphate-naphthalene 6-bisphosphonate (**2**), 2-naphthol 6-bisphosphonate (**3**), and 1-phosphate-benzene 4-bisphosphonate (**4**). All inhibitors targeted the active site and the most promising lead, **2**, exhibited slow-binding inhibition with an overall inhibition constant of ~38 ηM. Compound **2** inhibited proliferation of HeLa cancer cells while HEK293 cells expressing a normal phenotype were not inhibited under identical conditions. The crystal structures obtained for each bisphosphonate delineated the essential features of high-affinity phosphate-derived inhibitors and provides a template for the development of inhibitors with prophylaxis potential.
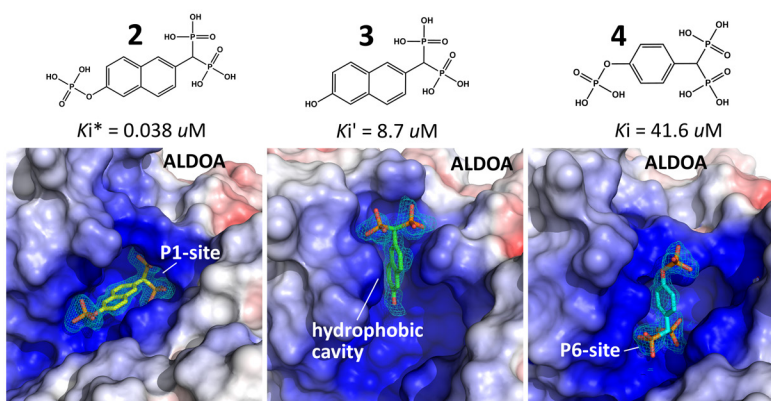
INTRODUCTION

Glucose metabolism in cancer cells is characterized by a marked increase in both glucose uptake and aerobic glycolysis, the fermentation of glucose into lactate in the presence of oxygen. Enhanced glucose uptake in cancer cells is now exploited clinically for diagnostic purposes with positron emission tomography (PET) where radiolabeled glucose (^{18}fluoro-deoxyglucose) is used as a tracer to assay for accumulation in tumors.[1] The latter effect of increased fermentation has been known for several decades, and was first proposed by German physiologist and Nobel laureate, Otto Warburg, who, in the 1920s showed that tumor cells produce higher levels of lactate compared to normal tissues, even in the presence of oxygen.[2] Hyperglycolysis not only produces ATP at a faster rate than oxidative phosphorylation, but also provides metabolic precursors for biomass production (e.g. nucleotide, amino acid, and lipid biosynthesis), aiding in the rapid proliferation of cancer cells.[3] The term "Warburg effect" was coined and ongoing conceptual and empirical advances over several decades have led to the acceptance of altered metabolism as one the hallmarks of cancer.[4] Tumor glycolysis is actively studied as a potential target for cancer therapy, however viable clinical leads have proven elusive.[5]

A leading candidate is fructose-1,6-bisphosphate (FBP) aldolase (EC 4.1.2.13), a central enzyme in glycolysis responsible for the reversible aldol reaction of fructose-1,6-bisphosphate to glyceraldehyde-3-phosphate and dihydroxyacetone phosphate. Glycolytic aldolase is a Class I enzyme, found in eukaryotes and higher plants, and characterized by the formation of a protonated imine (Schiff base) with an active site lysine. Aldolase expression levels were pronounced when investigated in several malignant cell lines such as human lung squamous carcinomas,[6–8] hepatocellular carcinomas,[9,10] pancreatic[11] and colorectal cancers.[12] Aldolase is already a target in parasitic organisms such as *Trypanosoma brucei* (causative agent for African sleeping sickness) for which glycolysis is the sole source of ATP production.[13,14] Earlier work in the literature and from our laboratory has focused on the development of class I aldolase inhibitors in such organisms.[14,15]

Among these, phosphorylated substrate analogues of fructose-1,6-bisphosphate aldolases possessing an aromatic moiety were of considerable interest due to their ability to strongly interact with the active site. First intended for their interest in probing the nature of the active site, which was assumed to be hydrophobic based on residues surrounding the reactive lysine,[16]

these aromatic derivatives were among the most powerful competitive inhibitors of the rabbit muscle aldolase-catalyzed reaction. Notably, these aromatic time-dependent reversible inhibitors (slow-binding) capable of targeting active site lysine residues, namely 2-hydroxybenzaldehyde-4-phosphate[17] and 1-hydroxy-2-napthaldehyde-6-phosphate,[18] inactivated aldolase and implicated a slow reversible Schiff base mechanism. A naphthalenic derivative, naphthalene 2,6-bisphosphate (NA-P_2) was shown to be a potent competitive inhibitor with K_i = 0.28 μM.[18] The mode of inhibition by which these phosphorylated aromatic derivatives inhibited aldolase was established by enzyme kinetics, UV/visible difference spectroscopy and site-directed mutagenesis,[17] yet these studies did not provide detailed structural insight, with the exception of computational modeling studies involving 1-hydroxy-2-napthaldehyde-6-phosphate.[18]

We sought to elucidate the interaction between several phosphorylated aromatic derivatives and the aldolase active site to serve as a template for designing potent high-affinity phosphorylated inhibitors. Here, using the previously known competitive inhibitor NA-P_2 (**1**) as template, we describe the binding of aromatic bisphosphonate substrate analogues of aldolase, namely 2-phosphate-naphthalene 6-bisphosphonate (PNAB) (**2**), 2-naphthol 6-bisphosphonate (NAB) (**3**), and 1-phosphate-benzene 4-bisphosphonate (PBB) (**4**). The mode of binding was determined by a combination of x-ray crystallography and enzyme inhibition kinetics. The high-resolution crystal structures of these phosphorylated aromatic inhibitors in complex with aldolase are described and should serve as a basis for the design of potent lead compounds.

RESULTS AND DISCUSSION

Structure of ALDOA-1 (NA-P_2) complex. To investigate the binding mode of phosphorylated aromatic compounds, rabbit muscle aldolase (ALDOA) crystals were soaked in crystallization buffer containing compound **1**. The rabbit isoform is routinely used for its ease of purification, crystallization, and is a good model candidate for the human isoform because of its exceptionally high homology.[19] The final crystal structure was determined to 1.97Å resolution (R_{work} = 12.87 %; R_{free} = 16.65 %) and shows a tetramer in the asymmetric unit of space group P2$_1$, consistent with aldolase structures previously reported for these crystallization conditions[20] (see Experimental Section for details). Data collection and refinement statistics for

all crystal structures are shown in Table 3-1. A tetramer in the asymmetric unit cell gives the opportunity to make four independent observations, and, expected from previous work, that the compound should bind in a 1:1 ratio of [inhibitor: subunit].[16]

Table 3-1. Data Collection and Refinement Statistics

Structure	ALDOA-**1**	ALDOA-**2**	ALDOA-**3**	ALDOA-**4**
Data Collection				
PDB code	5TLZ	5TLE	5TLH	5TLW
Resolution range (Å)	44.04 - 1.97	32.34 - 1.58	43.74 - 2.20	43.66 - 2.29
Space group	P 2_1	P 2_1	P 2_1	P 2_1
Unit cell a (Å), b (Å), c (Å), β	83.3 103.6 84.5	83.7 103.7 84.5	83.6 103.1 84.9	83.9 102.7 84.9
(°)	98.7	98.8	98.9	98.5
Wavelength (Å)	1.1	0.9795	0.9795	0.9795
Total / Unique reflections	277501 / 86719	541509/185199	332045 / 69202	192056 / 59193
Multiplicity	3.2	2.9 (2.4)	4.8 (4.4)	3.2 (2.6)
Completeness (%)	0.87	0.94 (0.97)	0.96 (0.92)	0.88 (0.44)
Average $I/\sigma(I)$	20.07	13.96 (1.46)	6.50 (2.88)	5.87 (1.78)
Wilson B-factor	21.83	18.22	24.98	28.71
R_{merge} [b]	0.052	0.03856 (0.71)	0.1792 (1.175)	0.1541 (0.9413)
R_{meas} [c]	-	0.0465 (0.8927)	0.1996 (1.321)	0.1823 (1.175)
CC1/2	-	0.999 (0.575)	0.986 (0.684)	0.982 (0.485)
Refinement				
R_{work} (%) [d]	0.1287 (0.2041)	0.1314 (0.2630)	0.1504 (0.2169)	0.1521 (0.2236)
R_{free} (%) [e]	0.1665 (0.2705)	0.1576 (0.2862)	0.1880 (0.2606)	0.1922 (0.2918)
Number of atoms	12322	13159	11644	11402
macromolecules	10644	10801	10662	10654
ligands	184	120	140	104
RMSD (bond length) (Å)	0.006	0.008	0.005	0.004
RMSD (angles) (°)	0.76	0.92	0.86	0.63
Ramachandran favored (%)	98	98	98	97
Ramachandran allowed (%)	2	2	2.1	2.5
Average B-factor (Å²)	29.13	26.99	32.02	37.80

[a] All values in parentheses are given for the highest resolution shell; [b] $R_{\text{merge}} = \sum_{hkl}\sum_i \left| I_i(hkl) - \bar{I}_i(hkl) \right| / \sum_{hkl}\sum_i I_i(hkl)$, with i running over the number of independent observations of reflection hkl; [c] $R_{\text{meas}} = \sum_{hkl}(n/(n-1))^{1/2}\sum_{i=1}^{n} \left| I_i(hkl) - \bar{I}_i(hkl) \right| / \sum_{hkl}\sum_i I_i(hkl)$; [d] $R_{\text{work}} = \sum_{hkl} \left\| I_o(hkl) \right| - \left| I_c(hkl) \right\| / \sum_{hkl} \left| I_o(hkl) \right|$; [e] $R_{\text{free}} = \sum_{hkl \in T} \left\| I_o(hkl) \right| - \left| I_c(hkl) \right\| / \sum_{hkl \in T} \left| I_o(hkl) \right|$, where T is a test data set randomly selected from the observed reflections prior to refinement. Test data set was not used throughout refinement and contains a minimum of 2000 unique reflections (or 5%).

Figure 3-1. Crystal structure of the ALDOA-1 complex.

(A) Electrostatic surface potentials of rabbit muscle aldolase (ALDOA) calculated using the Adaptive Poisson-Boltzmann Solver (APBS) software package with contour field of $\pm$ 5 kT/e.[12] Acidic residues are colored *red*, basic residues are colored *blue*. (B) Difference electron density calculated from a 1.97Å simulated annealing F_o - F_c omit map encompassing compound **1** and contoured at 3.0σ. *Cis-* and *trans-* conformations of **1** are shown. (C) Hydrogen-bonding network of **1** with active site residues and water molecules. Notable interactions are those formed by compound **1** phosphate moieties in the P_1- and P_6- phosphate loci of FBP (P_1: vicinal to Arg303; P_6: vicinal to Ser35).

The overall topology of the active site shown in Figure 3-1A highlights the basic electrostatic potential surface of the catalytic pocket nestled inside a TIM-barrel. The electron density surrounding the bound inhibitor (Figure 3-1B) was unambiguous and allowed for confident modeling into the active site of each tetramer subunit. The phosphate binding loci of **1** are homologous with the P_1- and P_6-phosphate binding site of the substrate FBP (shown in Figure S3-1). A feature of the FBP P_6-binding site was the electrostatic interaction implicating Lys107,

described in high-resolution structures[20] and deduced from differential protection experiments.[21] Attachment by **1** involves the same electrostatic interaction with Lys107 at the P_6-site as was found for the substrate, and is consistent with the finding that a Lys107 variant (K107M) exhibits a reduced affinity (higher K_i) for **1**.[18] The hydrogen-bonding network of this binding locus is similar to that observed in the Schiff base complex formed with FBP [PDB id: 1ZAI].[20] Notably, Lys107 interacts with two phosphate oxyanions (contacts of 3.1Å and 2.9Å) of **1** and, similarly to FBP, Ser35 and Ser38 hydroxyl groups contact the phosphate oxygens. However, the phosphate moiety of **1** is displaced with respect to the FBP P_6-phosphate by 1Å beyond the center of the active site cleft, consistent with the longer intramolecular distance between phosphate moieties of 9.8Å in **1** compared to 8.9Å in FBP. The flanking helical region (residues 34-65) undergoes a displacement upon binding by **1,** that is smaller by ~1Å compared to FBP binding, and fixes the bound phosphate at the P_6-site (Figure S3-1). Displacement by this flanking helix has been noted upon active site binding,[22,20,23] and is responsible for narrowing the active site, functioning as a clamp to bind the FBP P_6-phosphate and, more generally, capable of accommodating binding by phosphate moieties from phosphorylated analogues of varying sizes.

A surprising structural feature in the ALDOA-**1** complex was the conformational mobility at the P_1-locus shown by **1** binding, not observed with FBP or DHAP. Upon P_1-phosphate binding by aldolase substrates, FBP or DHAP, Arg303 side chain typically undergoes a conformational change which enables it to grasp and immobilize the incoming P_1-phosphate, by forming a strong bidentate hydrogen-bond. In compound **1**, an unexpected binding mode was observed consistent with two configurations of the phosphate oxyanion at the P_1-site (Figure 3-1B): a major *'trans'* configuration with respect to the orientation of the trans-annular phosphates across the aromatic core of **1**; and a minor *'cis'* configuration. Only the *cis*-configuration forms the anticipated salt bridge with Arg303. Population of the minor species corresponded to a refined occupancy of 0.35 ± 0.02 (average of four subunits) compared to the *trans*-configuration whose occupancy was 0.65 ± 0.02 (Figure 3-1C - *yellow*).

The observation of two distinct binding modes for the ALDOA-**1** complex was used as a template to design a series of novel bisphosphonate analogues, with the premise that a bisphosphonate moiety would be capable of mimicking both *cis* and *trans* phosphate positions observed in the ALDOA-**1** complex. A bisphosphonate moiety, which structurally resembles

pyrophosphate, is a compelling proposition for therapeutic applications as substitution of the central oxygen atom (pyrophosphate) for carbon (bisphosphonate) procures added stability and resistance to thermal, chemical, and enzymatic degradation.[24] Bisphosphonates are a class of drugs that are primarily used for intervention in osteoporosis.[25] Here, we sought to exploit the stability of bisphosphonates by substituting the phosphate group of **1** for a bisphosphonate, generating compound **2** (PNAB). Further, to optimize targeting to the compound **1** binding site, additional topologies were sampled. Notably compounds **3** (NAB) and **4** (PBB) were synthesized either by permutation of the central naphthalene core to a benzene core (**3**) or by elimination of the second phosphate group (**4**).

[Synthesis of the most promising compound, 2, to be shown in "Scheme 1" – to be inserted by Casimir BLONSKI]

High-resolution crystal structures of bisphosphonate analogues in complex with ALDOA. Native ALDOA crystals were soaked for 30 minutes in a solution consisting of mother liquor and a given bisphosphonate compound at final concentrations of 1 *m*M, 5 *m*M, and 20 *m*M for compounds **2**, **3,** and **4** respectively. Data collection and refinement statistics for all three structures are shown in (Table 3-1). The statistics and final resolution are indicative of the soaking conditions for each bisphosphonate: the higher concentrations used for crystal soaking with **3** and **4** to ensure adequate active site occupancy slightly impacted crystal quality, manifested by lower resolutions (2.20Å and 2.29Å respectively) and higher mosaicities of their intensity profiles, compared to the 1.58Å resolution obtained for compound **2**. A control dataset for the native crystal (not shown), diffracted to 1.63Å. All three bisphosphonates targeted the active site, yet displayed surprisingly different modes of binding.

ALDOA-2 complex structure. Electron density delineating compound **2** (Figure 3-2A) was unambiguous and allowed for confident determination of its binding mode. The average occupancy of **2** in the four subunits was 0.78 ± 0.04. Soaking times of **2** with native crystals were limited due degradation in crystal quality at longer soaking times. Comparison of the ALDOA-**2** complex with the ALDOA-**1** complex reveals an indistinguishable superposition of the inhibitors, notably at the P_1-site (shown in Figure 3-3A). In the ALDOA-**1** complex (Figure 3-1C), the phosphate forms 5 hydrogen bonds in either the *cis-* or *trans*-orientation whereas in the ALDOA-**2** complex, the bisphosphonate moiety of **2** engages in three additional hydrogen
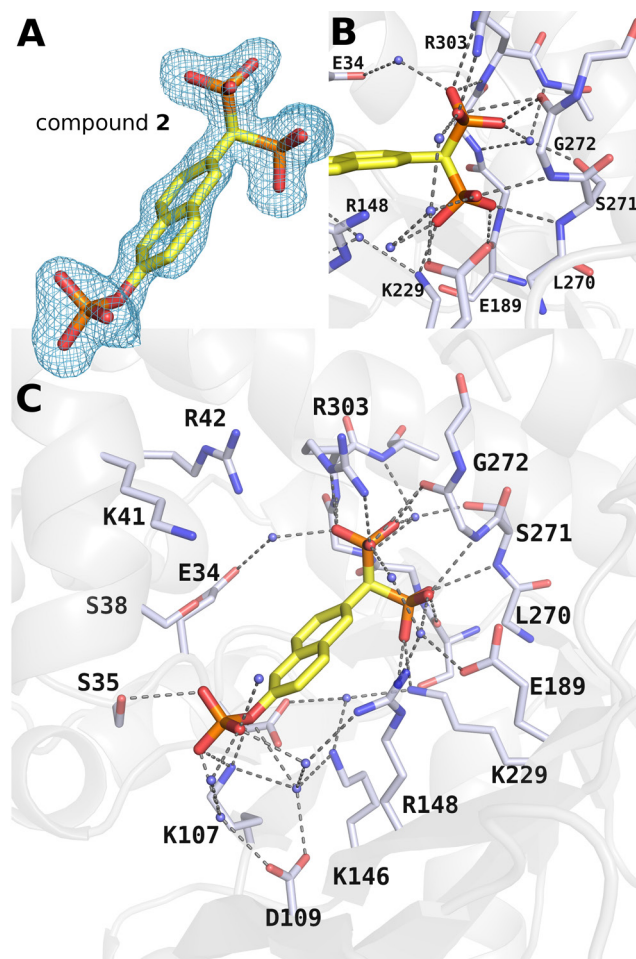
Figure 3-2. Crystal structure of the ALDOA-2 complex.

(A) Difference electron density calculated from a 1.58-Å simulated annealing F_o - F_c omit map encompassing compound **2** and contoured at 3.0σ. (B) Close-up of hydrogen-bonding contacts between bisphosphonate moiety and surrounding backbone atoms, side-chain atoms, and water molecules at the P_1-phosphate locus. (C) Extensive hydrogen-bonding network (*dashed lines*) between **2** and active site residues and water molecules is illustrated.

bonds with active site residues forming a network of 8 hydrogen bonds (Figure 3-2) (not including water molecules).

Inspection of the P_1-binding site is informative for comprehending the differences in affinity and binding kinetics in compounds **1** and **2**. Although ALDOA-**1** and ALDOA-**2** complexes appear isostructural, a notable difference was observed in the hydrogen-bonding pattern with regards to active site Ser271 (Figure 3-3A), where the residue which interacted with **1** no longer interacted directly with **2** due to active site deformation by **2**. Furthermore, attachment by both complexes enabled determination of the protonation state of the phosphate and bisphosphonate
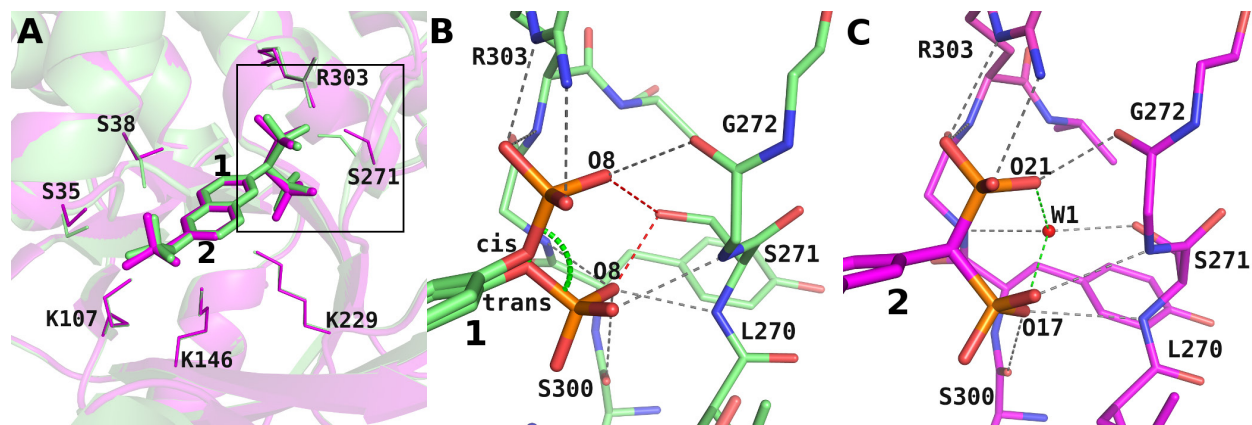
Figure 3-3. Superposition of the ALDOA-1 and ALDOA-2 complexes and interactions at the P_1-site.

(A) The structures of ALDOA complexed with **1** (*green*) and **2** (*magenta*) were superposed in PyMol to illustrate the structural similarities of their binding modes (r.m.s.d. = 0.21Å for alignment of C_α atoms in subunit A). One notable difference was observed for Ser271, shown in the inset. (B) Hydrogen-bonding network (*grey dashes*) of ALDOA-**1** complex at the P_1-binding site is illustrated for the *cis* and *trans* configurations. The *cis-trans* rotational isomerization is depicted by a *green dash*. The proximity of the Gly272 carbonyl to the phosphate O_8 of *cis*-**1** (2.89 ± 0.14Å) implies protonation of the phosphate O_8 and indicates proton donation by Ser271 O_H (*red dashes*) to O_8 (*cis*: 2.80 ± 0.08Å; *trans*: 2.65 ± 0.20Å). Further, proximity of *trans*-**1** phosphate O_8 to the Ser300 carbonyl (3.00 ± 0.10Å) is consistent with protonation of O_8. (C) In the ALDOA-**2** complex (*magenta*), the vicinal Gly272 and Ser300 backbone carbonyls also indicate protonation of the partnered oxygens on the bisphosphonate (O_{21} - 2.76 ± 0.06Å; O_{17} − 2.82 ± 0.01Å, respectively). Ser271 side-chain shifts to the rear, making room for a water molecule (W1) that donates hydrogen bonds to O_{17} (3.22 ± 0.04Å) and O_{21} (2.31 ± 0.13Å) (*green dashes*), and accepts hydrogen bonds from Ser271 side-chain O_H and Gly302 backbone N_H.

moieties for binding at the P_1 locus that was based upon their interactions with surrounding backbone and side-chain atoms. In the *cis*-configuration of the ALDOA-**1** complex (Figure 3-3B), the Gly272 backbone carbonyl engages in a hydrogen-bond with phosphate O_8 atom that is consistent with protonation of the phosphate O_8 oxyanion. Upon *cis-trans* isomerization of the phosphate, the proximity of O_8 to Ser300 carbonyl implies hydrogen bond formation and also consistent with protonation of the phosphate O_8 oxyanion in the *trans*-configuration. This hydrogen-bonding pattern implies mono-protonation of the bound P_1 phosphate oxyanion. In the ALDOA-**2** complex, Ser271 shifts to the rear of the active site (by 1.7Å compared to ALDOA-**1**) to accommodate bisphosphate binding and is replaced by W1, which donates two hydrogen bonds to the bisphosphonate moiety (Figure 3-3C – *green dashes*). W1 also accepts hydrogen bonds from surrounding active site atoms (Gly302 N_H and Ser271 O_H). For this

binding geometry, O_{17} interacts with Ser300 carbonyl while O_{21} interacts with Gly272 carbonyl indicating binding by **2** is consistent with protonation of each phosphonate moiety (i.e. dibasic bisphosphonate). Ser271 reflects active plasticity in accommodating compounds **1** and **2**.

Prior to synthesis of compound **2**, the naphthalenic derivative **1** represented the most potent reversible competitive inhibitor of the rabbit muscle aldolase-catalyzed reactions. The design of compound **1** was based on two chemical features useful for enhancing active site binding. Protection experiments had shown that the active site binding embodied two distinct phosphate binding sites: a higher affinity site – the P_1-site; and a lower affinity site – the P_6-site making binding by compounds with suitable spanning phosphate groups to both sites highly specific.[21,26] A second distinguishing feature of potent aldolase inhibitors ($0.1 – 1.0\ \mu$M range) were those possessing aromatic moieties.[16] The rigid structure imposed by the aromatic rings compared to a flexible compound such as hexanediol 1,6-bisphosphate ($K_i = 25\ \mu$M) suggests that a smaller configurational entropy loss upon active site binding by a rigid aromatic compound may underpin the observed differences in binding affinity to aldolase.[27] The additional feature of a bisphosphonate moiety in compound **2** took advantage of the cryptic phosphate binding site at the P_1 site to enhance binding affinity. Modifications were made of the bisphosphonate derivative **2** that were designed to explore additional conformational space in the aldolase active site. First, the synergy between the two phosphate loci was probed by replacing the phosphate group with a hydroxyl group (**3**), also providing an indication of the significance of the bisphosphonate moiety towards potency. Then, to assess the sufficiency of the naphthyl core in spanning the phosphate loci, a shorter aromatic core was introduced - a benzene (**4**).

ALDOA-3 complex structure. The crystal structures of ALDOA-**3** and ALDOA-**4** are shown in Figure 3-4. The binding mode of **3** and **4** are noticeably different than **2**. First, their bisphosphonate moieties do not bind at the P_1-site. The bisphosphonate in the ALDOA-**3** structure (Figure 3-4A) points towards the outside of the active site cavity and forms hydrogen bonds with the side chains of surrounding residues (Ser45, Lys311, Arg303, Arg42). Further, the naphthyl moiety of **3** is conjugated to Arg42 via a cation-π interaction, a highly stabilizing interaction.[28,29] The distance between the guanidinium group and the naphthalene ring in all four subunits is 3.48 ± 0.10Å, consistent with reported cation- π interactions for ariginine.[28,30] The interaction is further stabilized by a salt bridge that forms between Arg42 and the bisphosphonate oxygens. Also, Arg303 side-chain carbon atoms align on the distal sides of **3**,
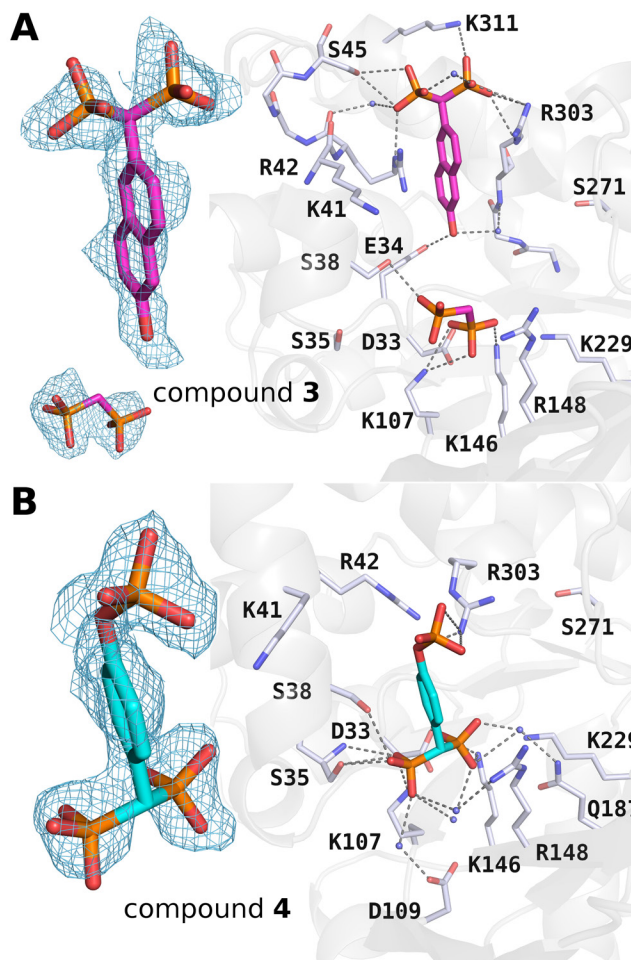
Figure 3-4. Crystal structure of ALDOA in complex with compounds 3 and 4.

(A) Difference electron density calculated from a 2.20Å $2mF_o - DF_c$ Feature Enhanced Map (FEM) showing compound **3** and contoured at 1.0σ. Noteworthy is the cation-π interaction involving Arg42 and the naphthalene moiety of compound **3** and the hydrophobic interaction with the side-chain of Arg303, shown on the right-panel. (B) Difference electron density calculated from a 2.29Å $2mF_o - DF_c$ FEM comprising compound **4** and contoured at 1.0σ. Compound **4** binding mode is different from other bisphosphonates. The hydrogen-bonding networks shows the bisphosphonate moiety contacting the P_6-phosphate binding locus involving Ser35 and Lys107.

producing a stabilizing hydrophobic environment for the naphthyl moiety. The distal O_H group of **3** is anchored by a hydrogen bond with the Glu34 carboxyl. A second binding site for **3** was identified near the P_6-locus but electron density was only visible for the bisphosphonate group (seen in Figure 3-4A), consistent with purity assessments showing no indication of free bisphosphonate, and is indicative of positional disorder of the naphthyl group at the second binding site.

The hydrophobic pocket used by **3** is a recognized binding locus for aldolase-binding partners, including the C-terminal peptide of the actin nucleation-promoting factor WASP and the LC4 domain of SNX9, a key regulator of endocytosis in cellular cargo transportation, which both intercalate a tryptophan indole ring between Arg42 and Arg303.[31,32] A novel naphthyl phosphate-based inhibitor of aldolase (NASEP) identified from the WASP study was competitive for active site binding and had a K_i of 0.1 mM. Comparison of the ALDOA-**3** complex with the ALDOA-NASEP complex (PDB id: 2OT1) (illustrated in Figure S3-2) revealed a difference of ~81° in the angle of insertion of the naphthyl group with respect to the primary axis of the NASEP naphthyl ring. The stabilizing cation-π interaction is also observed in the ALDOA-NASEP complex and appears to be a driving force for binding at this locus but is insufficient alone as native ALDOA crystals soaked in saturating tryptophan in the crystallization buffer (6 mM L-tryptophan) did not reveal evidence of tryptophan active site binding.[31] The ancillary hydrogen bonds formed between inhibitor oxygens and basic active site residues are therefore required to promote active site binding at this locus.

ALDOA-4 complex structure. The ALDOA-**4** complex (Figure 3-4B) revealed a novel mode of binding different from the previous bisphosphonate compounds. The bisphosphonate moiety of **4** is isostructural with the secondary binding site identified in the ALDOA-**3** complex. This site is located near the P_6-binding locus: one phosphonate group of **4** contacts several active site residues (Ser35, Ser38 and Lys107); the second phosphonate is stabilized by hydrogen-bonding to Lys146. The phosphate group forms an electrostatic interaction with Arg303. To accommodate the binding mode of **4** and avoid clashing with the benzene group, Arg42 folds into the hydrophobic pocket described above for **3**.

Inhibition kinetics of the bisphosphonate inhibitors. The potency of the bisphosphonate analogues **2, 3** and **4** were investigated by inhibition kinetics using previous buffer conditions (see Experimental Section). Potency of **2** was evaluated using IC50 assays, summarized in Table 3-2. Indication that **2** exhibited slow-binding behavior arose from IC50 experiments with different pre-incubation periods of the enzyme with **2** in solution. An IC50 value of 0.67 ± 0.07 μM was measured with no pre-incubation period which decreased 10-fold to an IC50 of 0.060 ± 0.008 μM with a pre-incubation of 90 minutes. To determine the nature of the slow-binding behavior by **2**, time-dependent inhibition by **2** was assessed using the method first described by Morrison and Walsh (see Experimental Section for details).[33] Briefly, in the presence of classical

competitive inhibitors, product formation remains linear prior to substrate depletion. With slow-binding inhibitors, inhibition exhibits a two phase relationship: an initial burst in product formation (v_o) corresponding to an apparent first-order loss (k_a) of activity followed by a slower steady state rate in product formation (v_s) where progress curves becomes asymptotic to the v_s. Equations 2 – 4 described in the Experimental Section were used to extract inhibition constants and are reported in Table 3-3 (direct and linearized plots are reported in Figure S3-3). An overall inhibition constant K_i^* of 38 ± 2 nM was determined. The off-rate constant of the slow-binding event (k_{-4}) was 6-fold slower than the on-rate (k_{+4}) and predicts a turnover of inhibited complex (EI*) consistent with the long pre-incubation periods required to observe full inhibition in IC50 assays. The K_i for compound **2** was 284 ± 13 nM which is virtually identical to the K_i of compound **1** of 280 ± 30 nM, coherent with the isostructural binding mode of compounds **1** and **2**. Binding of **1** and **2** at the P_6-site is quasi-isostructural, indicating that binding features at the P_1-site likely account for the difference in overall affinity. The 8 hydrogen bonds for **2** at the P_1-site with surrounding residues compared to 5 hydrogen bonds for **1** affords a greater enthalpic binding energy for **2**, yet the entropic penalty for binding of **1** is smaller due to the *cis-trans* isomerization at the P_1-site. However, binding of **2** provokes the expulsion of one additional highly ordered water molecule (W1) compared to **1** which is entropically favorable, and suggesting a higher overall affinity of **2** for aldolase.

Table 3-2. IC50 values for aldolase inhibition by 2 measured for varying pre-incubation periods.

Pre-incubation period (mins)	IC50 (pH 7.5) [a]
0	0.67 ± 0.07
10	0.17 ± 0.02
30	0.13 ± 0.01
90	0.060 ± 0.008
180	0.068 ± 0.004

[a] Measured in Tris-Acetate buffer (pH 7.5) with 10 μM FBP using activity assay described in Experimental Section.

Table 3-3. Kinetic parameters describing the slow-binding inhibition of aldolase with 2.

Parameter	Value [a]
V_m (U/mg)	11.73 ± 0.20
K_m (μM)	2.66 ± 0.27
K_i (μM)	0.284 ± 0.013
k_{-4} (min^{-1})	0.0100 ± 0.0021
k_{+4} (min^{-1})	0.0638 ± 0.0020
K_i^* (μM)	0.038 ± 0.002

[a] Values were calculated using the slow-binding model described in the Experimental Section. Direct and linearized Dixon plots are shown in Figure S3-3.

Dual competitive inhibition of aldolase by 3. Compound **3** did not show any changes in IC50 with different incubation times and was analyzed in terms of competitive inhibition as kinetic model. Given the presence of a second binding site by **3** in the active site, we applied a semi-generalized formulation for single-enzyme multiple inhibition using two reversible linear inhibitors, as previously reported and described by equation 5 (details in Experimental Section).[34] The inhibition constants for the two binding sites yielded values of 13.1 ± 3.1 μM and 8.7 ± 1.8 μM (reported in Table 3-4; inhibition kinetics are shown in Figure S3-4). Additional enthalpic contributions afforded by 3 extra hydrogen bonds in the ALDOA-**3** complex (7 hydrogen bonds) compared to ALDOA-NASEP (4 hydrogen bonds) is consistent with tighter binding of **3** compared to the similar NASEP inhibitor ($K_i = 0.1$ mM). Further, the naphthol O$_H$ group has an important role in binding affinity as it anchors the naphthalene to Glu-34 (Figure 3-4A), a contact not formed in the ALDOA-NASEP complex (Figure S3-2).

Competitive inhibition of aldolase by 4. Compound **4** showed no evidence for slow binding behavior and exhibited classical competitive inhibition consistent with the observation in the ALDOA-**4** complex showing active site tethering at the P$_6$-phosphate site. The inhibition constant has a value of 41.6 ± 4.6 μM (Table 3-4; inhibition kinetics are illustrated Figure S3-5).

Table 3-4. Inhibition mode and constants for inhibitors 1 – 4.

Inh	Mode	K_i (μM)	K_i^* (μM)
1	*Competitive* [a]	0.280 ± 0.030	-
2	*Slow-binding* [b]	0.284 ± 0.013	0.038 ± 0.002
3	Dual Compet. [c]	13.1 ± 3.1	8.7 ± 1.8
4	Competitive [d]	41.6 ± 4.6	-

[a] previously reported[18]; [b] Calculated using slow-binding inhibition described in Experimental Section; K_i^* is the overall inhibition constant; [c] Calculated using dual linear competitive inhibition described in Experimental Section; Here, K_i and K_i^* represent the inhibition constants for the two binding sites in the aldolase active site; [d] Calculated using classical competitive inhibition kinetics: direct and double-reciprocal plots are shown in Figure S3-3-Figure S3-5. Inh – Inhibitor.

Slow-binding inhibition mechanism. Compounds **1** and **2** provided an ideal opportunity to investigate the structural features responsible for their different modes of inhibition. Both compounds occupy the same binding sites yet differ in that **2** displays slow binding inhibition while **1** does not. Earlier work had shown that substitution of a phosphate group on **1** with an aldehyde (1,6-dihydroxy-2-naphthaldehyde - HNA-P) results in Schiff base formation between Lys107 and HNA-P.[18] It was suggested that the rate of covalent bond formation was responsible for the slow binding reaction. However, the slow-binding mechanism of aldolase bisphosphonate inhibitors does not entail formation of a covalent adduct. In order to identify hot spots in the structure that may explain the slow-binding origin of **2**, the ALDOA-**1** and ALDOA-**2** complexes were aligned to native ALDOA (PDB id: 1ZAH) using the ProSMART algorithm.[35] Overall global root mean square deviations (r.m.s.d. based on Cα atoms) were comparable (ALDOA-**1**-native: 0.313 ± 0.01Å; ALDOA-**2**-native: 0.231 ± 0.02Å) and localized to two main regions: 1) the active site flanking helix comprising residues 34-45; and 2) a loop comprising residues 269-275 (Figure 3-5). The conformational changes induced in the flanking helix upon FBP binding upon active site binding have not been associated with a slow binding mechanism in case of inhibitors such as the tagatose-bisphosphate diastereoisomer ($K_i = 125 \pm 16$ μM).[20] The conformational changes for the loop comprising residues 269-275 were 0.455 ± 0.02Å in ALDOA-**2** compared to ALDOA-**1** of 0.309 ± 0.01Å (r.m.s.d. for residues 268-276 from alignment of Cα atoms) with respect to the native structure ALDOA. The local r.m.s.d. of the same loop for the FBP bound structure (PDB id: 1ZAI) was 0.308 ± 0.02Å. The local r.m.s.d.
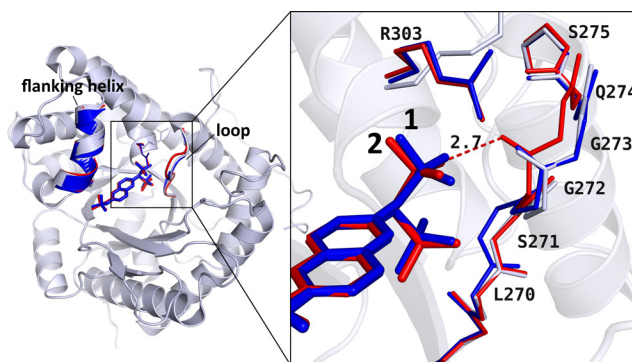
Figure 3-5. Active site dynamics upon aldolase-binding of 1 and 2.

ALDOA-**1** (*blue*), ALDOA-**2** (*red*) and native ALDOA (*grey*) (PDB id: 1ZAH) were aligned using ProSMART, identifying two regions with significant conformational differences (the flanking helix and the flexible active site loop). The inset depicts a close-up of the flexible loop, comparing the differences between all three structures. In ALDOA-**2,** the loop undergoes significant movement of residues 272-275 (r.m.s.d. of 0.657 ± 0.03Å) towards the active site cleft, affording a hydrogen bond between Gly272 and the bisphosphonate not present in ALDOA-**1**, where the loop undergoes minimal displacement with respect to ALDOA (r.m.s.d. of 0.230 ± 0.02Å). For illustration purposes, the side-chains were omitted from the loop.

becomes even greater for ALDOA-**2** using only residues 272-275 that exhibit the greatest movement (ALDOA-**2** vs native: 0.657 ± 0.03Å and ALDOA-**1** vs native: 0.230 ± 0.02Å). We speculate that movement by this loop to accommodate the bisphosphonate moiety in **2** may be the structural basis for the slow-binding inhibition. Indeed, shown in Figure 3-5, the greatest backbone movement incurred by residues 272-275 in ALDOA-**2** (Figure 3-5 – *red*) implicated the displacement of Gly272 carbonyl towards the bisphosphate moiety, producing a strong hydrogen-bond (2.76 ± 0.06Å). This movement is absent in ALDOA-**1** and where side chain displacements were limited to a single residue, Ser-271. We also considered the contribution of the protonation state of the bisphosphonate in the slow binding inhibition.

Ionization state of bisphosphonates. Bisphosphonates have four ionizable species (monobasic, pKa1=1.35; dibasic, pKa2=2.87; tribasic, pKa3=7.03; tetrabasic, pKa4=11.3).[36] The protonation state of **2** was inferred from the ALDOA-**2** complex (shown in Figure 3-3C) and corresponded to a mono-protonation state for each phosphonate group which is consistent with a dibasic species as the dominant protonated state between pH 2.87 - 7.03, according to the pKa values listed above. At pH 7.5, the conditions used for the inhibition kinetics, implies that both dibasic and tribasic species of **2** are present in solution and only the dibasic species would have the protonation state competent for binding. Binding by the dibasic species implies even

tighter binding by **2** when the pH dependence of this species is taken into account and indicating binding constants: K_i and K_i^* of ~ 140 nM and ~ 19 nM, respectively.

Minimal requirements of high-affinity binders. Fundamental to all known high-affinity aldolase binders is the inclusion of phosphate oxyanions that afford interactions with the highly basic active site, which includes 5 lysine and 3 arginine residues. The apparent promiscuity of the compound binding modes in the active site may be in part be due to this positively charged landscape making up the active site that is not very heterogeneous in terms of charge distribution (see Figure 3-1A) and hence would not enforce strongly similar binding modes on the bisphosphonate derivatives.. Comparison of the structural and kinetic data does however provide guiding principles that can be applied to the next generation of high-affinity binders. First, the weaker binding bisphosphonates compounds **3** and **4** compared to compound **2** clearly demonstrated the importance of the P_6-site for high affinity binding. Substitution of a phosphate in **2** for a hydroxyl in **3** had a dramatic effect on the binding mode and inhibition constant, consistent with the shorter span of compound **3** to simultaneously contact both P_1- and P_6-sites. This was corroborated by **4**, whose benzene core had a shorter span than the naphthalene core of **2** (~2.2Å shorter). The minimum span required to contact the P_1- and P_6-sites is ~9Å, which is possible with **2** (9.7Å) however, **4** has a span of ~7.5Å, insufficient to contact both phosphate binding loci. Attachment to not only the P_1-binding locus but also to the P_6-binding locus is synergistic and is an important consideration in the design of high affinity phosphorylated binders.

A similar trend that inhibitors capable of simultaneously satisfy binding to both phosphate binding loci exhibit tighter binding can be drawn from a study of linear bisphosphorylated inhibitors used as structural analogs of FBP for probing the active site of aldolase.[37] K_i values for propanediol-, butanediol-, pentanediol-, and hexanediol-bisphosphate inhibitors were determined to be 120, 55, 29, and 25 μM respectively. Modelling inhibitors into the active site, using the P_1- and P_6-binding locus of FBP as guides, indeed found the phosphate moieties of pentane- and hexanediol-bisphosphate could readily satisfy binding to both loci without steric collisions whereas the propanediol- and butanediol-bisphosphate are unable to span the $P_1 - P_6$ distance.[37,38]

Inhibition of aldolase *in vivo* by a bisphosphonate inhibitor. Finally, we performed *in vivo* inhibition assays in order to test cellular proliferation in the presence of the most potent

bisphosphonate inhibitor, **2**. The results of the dose response assay shown in Figure 3-6 clearly indicate that increased inhibitor concentration progressively inhibits proliferation of HeLa cells (Figure 3-6A), yet surprisingly with no effect on cellular proliferation at any tested concentration in HEK293 cells (Figure 3-6B). Furthermore, there was no growth inhibition of HeLa cells with the least potent bisphosphonate, **4**, under identical incubation conditions (Figure 3-6C). The decrease of $\sim 50\,\%$ after 72 hours of incubation by **2** at 50 μM ($p \leq 0.01$) is consistent with an EC50 ~ 50 μM for **2**. Incubation of cell growth $\sim 30\,\%$ by 72 hours ($p \leq 0.01$) at the lower concentration of 10 μM of compound **2** supports an EC50 estimate of ~ 50 μM.

The charged nature of phosphate groups greatly impedes endogenous phosphate-derivatives from escaping the cell, and renders exogenous phosphate-derivatives highly impermeable to entry across the membrane.[39] Indeed, **2** displayed *nano*-molar inhibition *in vitro*, while only exhibiting inhibition of cellular proliferation in the *micro*-molar range suggesting that the membrane permeability of **2** may be an issue given the presence of one phosphate group and two phosphonate moieties on **2**. Surprisingly, phosphorylated compounds such as FBP at high doses have been shown to display a protective effect in inflammation,[40,41] and exert their therapeutic effect by diffusion through membrane bilayers in a dose-dependent manner with no loss in cell viability and a transport efficiency of $\sim 5\%$ for 20 *m*M extracellular dose of FBP.[42] From this transport efficiency, the corrected K_i for **2** would predict an EC50 of ~ 5 μM in the dose response shown in Figure 3-6A. The presence of an additional charged phosphate moiety on **2** compared to FBP would likely further reduce transport efficiency which is not inconsistent with the observed EC50 ~ 50 μM.

Cellular targeting of glycolytic aldolase by **2** is thus not inconsistent with the proliferation data. Lessor dependence on glycolytic flux in normal phenotypes would afford selectivity as inhibition of glycolytic flux in hyperglycolytic phenotypes by **2** such as in cancer cells or protozoan infections would be detrimental to their proliferation. The fact that the dose response assay for **4,** shown in Figure 3-6C, does not reduce cell viability (Figure 3-6B), and that **4** inhibits aldolase with 150-fold lower efficacy compared to **2** indicating a very large EC50 suggests that the aldolase inhibition of cellular proliferation may have selectivity by inhibiting proliferation of cancerous phenotypes without effect on normal ones. In hyperglycolytic cells where glycolysis is the main source of energy and biomass production (Warburg effect),
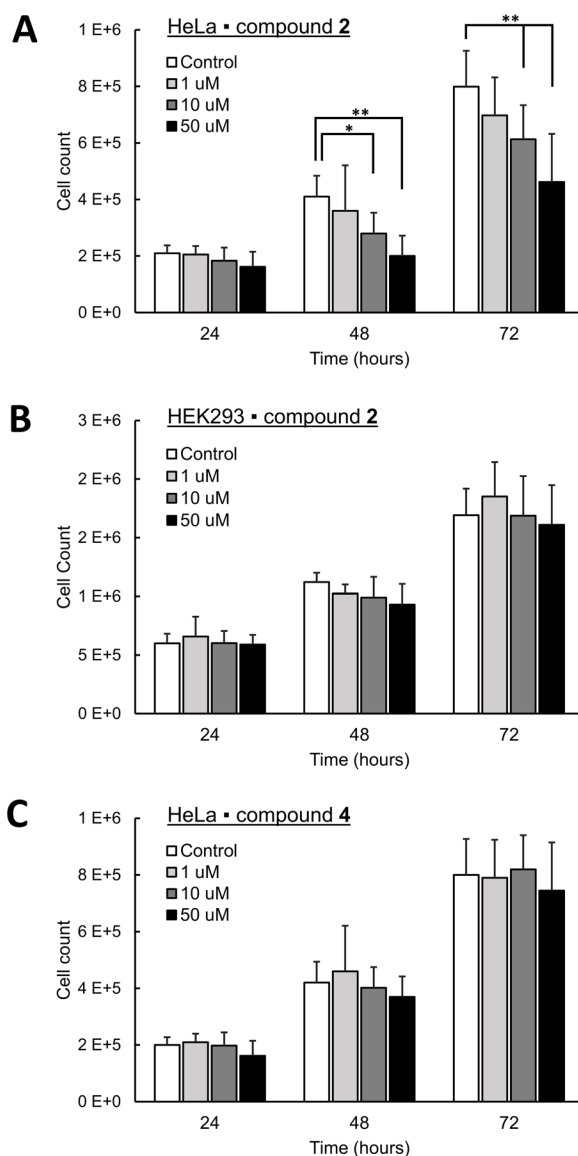
Figure 3-6. Cell growth inhibition assay.

(A) Graph shows cell count as a function of inhibitor concentration with HeLa cells. Cells were incubated for periods of 24, 48, and 72 hours with inhibitor. Cell count was determined by Trypan blue exclusion and hemocytometer. The same is shown in (B) for HEK293 cells. (C) The least potent bisphosphonate, compound **4**, served as a control treatment for HeLa cells. * $p \leq 0.05$; ** $p \leq 0.01$ (Student's two-tailed t-test). Data are from at from at least three independent experiments (standard deviations are shown as error bars).

targeting glycolysis via aldolase inhibition has been shown to be a viable strategy for inhibiting cellular proliferation.[43] Upregulation of ALDOA has recently been identified as an oncogene in a subpopulation of patients with highly metastatic pancreatic cancer[11] and an overall increase in

aldolase gene transcripts was observed for AML (acute myeloid leukemia) cells upon stromal interaction.[44]

Implications for Drug Design. From this study, functional groups, including phosphate, bisphosphonate, and naphthyl moieties of bisphosphonate inhibitors are important constituents for tight binding and represent a template for the design of future inhibitors. The highly basic nature of the aldolase active site is amenable to binding by phosphate oxyanions and drives the binding of the tested bisphosphonates to a number of different basic loci. In order to target binding to specific loci (i.e. P_1 & P_6) and afford the greatest potency, the following essential design features should be taken into consideration: 1) ability by compound phosphates to bind both P_1- and P_6-loci; and 2) retention of a rigid scaffold (naphthyl moiety) to reduce the entropic cost of binding. Using this template, we can envisage the addition of functional groups based on the proximity to surrounding residues to yield a library of high-affinity inhibitors that can serve as leads for future studies. For example, the binding locus of compound **3** at the hydrophobic pocket formed by Arg42 and Arg303 could be exploited by the addition of an aromatic group to a phosphonate moiety of **2**. To improve stability, a phosphonate moiety at the P_6-position would ensure stability against tyrosine phosphatases. The loss of a stabilizing hydrogen bond with Lys146 could be restored with a fluorine substituent on the phosphonate carbon. Also, the ionization state of the bisphosphonate should be considered to maximize biological activity at physiologically relevant pHs. Electronegative substituents on phosphonate carbons (e.g. fluorination) are known to lower the pKa of phosphonates, promoting the fully ionized form at neutral pH.[45,46] However, since **2** is competent for binding in the di-protonated bisphosphonate form, a methyl substituent may promote the dibasic bisphosphonate species at neutral pH by increasing pKa3.

The presence of phosphate groups has been problematic in drug design because of the poor ability by phosphate monoesters to penetrate cell membranes. These impediments can be circumvented by synthesizing a prodrug that masks the phosphate charges using a protecting group that can be enzymatically converted into the active phosphate monoester form once the prodrug has been internalized.[47–53] A number of approaches have been developed capable of yielding compounds with such "drug-like" properties.[39] Foremost was the modification of the phosphate group such that the inhibitor could diffuse through membranes and typically involved charge neutralization via chemical derivatives to form neutral esters(s) with the phosphorus-

derived oxygen(s). The protective groups allow permeation of the prodrug into the cells and can be efficiently removed by endogenous esterases, which restore the charge and biological activity. This approach was successfully implemented with a bisphosphonate inhibitor of inositol monophosphatase, where initially, poor membrane permeability was noted, but was rescued by using a tetrapivaloyloxy-methyl ester prodrug that retained biological activity after removal of the chemical modification by endogenous estereases.[54,55]

EXPERIMENTAL SECTION

Materials. Fru(1,6)P_2, glycerol-3-phosphate dehydrogenase and triose-phosphate isomerase were purchased from Sigma-Aldrich. NADH was from Roche Diagnostics. All other chemicals and materials were of analytical grade and were obtained from Sigma-Aldrich, Fisher Scientific, Bioshop Canada, and GE Healthcare Life Sciences.

[Chemical Synthesis and Purity. To be inserted by Casimir BLONSKI]

Purification and Crystallization. Expression and purification of recombinant native (WT) rabbit muscle aldolase was performed as described previously[20,56] using Escherichia coli strain BL21-SI for overexpression of the recombinant protein (Invitrogen). Enzyme concentration was determined using an extinction coefficient of 0.91 cm mg-1 mL at 280 ηm.[57] The native enzyme was crystallized by vapor diffusion from a 1:1 mixture of protein solution (10 mg/ml in 20 mM Tris-HCl, pH 7.0) and precipitant buffer (18% polyethylene glycol 4000 in 0.1 M Na-HEPES, pH 7.5) that was equilibrated against a reservoir of precipitant, as described previously.[20]

Crystallographic Data Collection and Processing. Aldolase crystals were soaked for either 30 min or 60 min in crystallization liquor containing one of the following ligands (**1** (NA-P$_2$), **2** (PNAB), **3** (NAB), or **4** (PBB)) at 1, 5, or 20 mM (final concentration in the mother liquor). Prior to flash-freezing in liquid nitrogen, crystals were cryoprotected by briefly soaking in a mother liquor solution containing 15% (v/v) glycerol and ligand at an appropriate concentration. Data for **1** was collected at beamlines X25 and X29 of the National Synchrotron Light Source at Brookhaven National Laboratories. The remaining datasets were collected from single crystals at beamline 08ID-1 or 08B1-1 of the Canadian Light Source, Saskatchewan, Canada. A native data set was also collected as a control. All data sets were processed with HKL2000,[58] and the data reduction results are shown in Table 3-1.

Structure determination and refinement. Crystal structures were determined by molecular replacement with PHENIX[59] Phaser-MR[60] using the native aldolase homotetramer structure as a reference model [Protein Data Bank (PDB) entry 1ZAH]. Refinement and model building were performed with phenix.refine[61] and Coot[62] respectively. Data quality and resolution cut-off was assessed using correlation-coefficient-based criteria, CC1/2.[63] Ligand fitting and interpretation was performed by a combination of simulated annealing $F_o - F_c$ omit maps and feature-enhanced sigma-A weighted $2F_o - F_c$ maps[64] that were calculated in the final round of refinement. All difference density maps ($F_o - F_c$) shown in the paper correspond to simulated annealed $F_o - F_c$ omit maps. Ligand coordinate and restraints were generated using PHENIX eLBOW.[65] Final model statistics were calculated with MolProbity[66] and are shown in Table 3-1. The coordinates and structure factors of the crystallographic structures have been deposited in the Protein Data Bank (PDB entries: 5TLE, 5TLH, 5TLW, 5TLZ). All figures were prepared using PyMOL (http://www.pymol.org).[67]

Structures requiring modeling of multiple conformations of ligand in the active site were prepared by the following sequence: occupancies of the multiple conformations were determined using a triplicate convergence test performed by setting arbitrary initial occupancies to three different values and averaging the refined occupancies.

In order to calculate electrostatic surface potentials, the Adaptive Poisson-Boltzmann Solver (APBS) software package was used.[68,69] The structure was prepared for APBS with the automated pipeline provided by PDB2PQR,[70,71] which adds any missing hydrogens, determines side-chain pK_as, and assigns force field parameters for atom charge and radius (PARSE force filed was selected by default).

Activity assays. Aldolase cleavage activity was determined using a coupled assay system involving triose-phosphate isomerase and glycerol-3-phosphate dehydrogenase (TIM/GDH) by following NADH oxidation at 340 nm using a Varian Cary 300 UV-Vis spectrophotometer thermostatted at 25 °C.[72] Activity was measured by the addition of aldolase to a solution containing substrate (FBP) made up in assay buffer (50 mM Tris-Acetate, pH 7.5, 0.3 mM NADH, and containing coupling enzymes (5 μg/mL GDH and 0.5 μg/ml TIM) to a final volume of 1 mL). All kinetic values reported comprise a minimum of three independent assays, including the inhibition studies.

Kinetic methods: (A) IC50 determinations. IC50s for aldolase inhibition by **2** were measured in activity assay conditions described above with concentrations of **2** ranging from 0.01 μM – 20 μM and a substrate (FBP) concentration of 10 μM. Aldolase was pre-incubated for 0 – 180 minutes with **2** prior to activity determination. IC50s were calculated using full 4 parameter IC50 model in GraFit Data Analysis Software.[73] For all calculations, the y-range was 5 – 6 U/*m*g, slope factors were ~1.5, and Chi^2 ~1.5 – 3.

Kinetic methods: (B) Slow-binding Inhibition. Slow-binding inhibition was analyzed according to Scheme 3-1 assuming rapid formation of an enzyme inhibitor complex (EI) complex that can undergo slow isomerization to a second enzyme inhibitor complex (EI*).[33,74] All rate steps are assumed to be fast relative to k_{+4} and k_{-4}. For this kinetic sequence, $K_i{}^*$ represents the overall inhibition constant, and K_i the dissociation constant for the Michaelis complex EI.

Scheme 3-1. General mechanism for describing slow-binding inhibition.

$$E + S \underset{k_{-1}}{\overset{k_{+1}}{\rightleftharpoons}} ES \xrightarrow{k_{+2}} E + P$$

$$+$$
$$I$$

$$k_{-3} \big\Vert k_{+3}$$

$$EI \underset{k_{-4}}{\overset{k_{+4}}{\rightleftharpoons}} EI^*$$
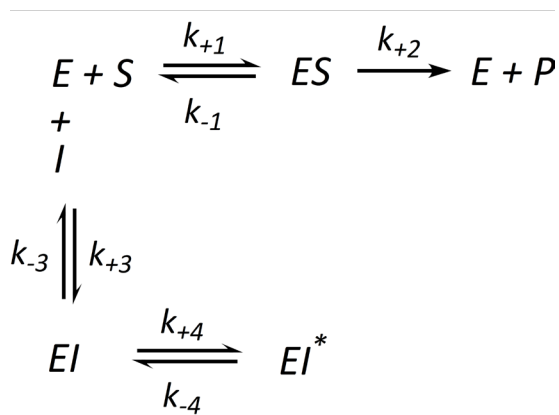
$$K_{\mathrm{m}} = \frac{V_M[S]}{K_M + [S]} \qquad K_{\mathrm{I}} = \frac{k_{-3}}{k_{+3}} \qquad K_{\mathrm{I}}^* = K_{\mathrm{I}}\,\frac{k_{-4}}{(k_{+4}+k_{-4})}$$

The slow-binding inhibition constants for inhibitor **2** were determined by non-linear regression analysis of progress curves measured in the presence of 20 – 200 μM FBP and 0.5 – 75 μM of **2**. Slow-binding inhibitors are characterized by an initial burst of reaction followed by a slower steady state where progressive curves exhibit asymptotic behavior. All progressive curves were analyzed according to Eq. 2 was fitted using GraFit Data Analysis Software v.6.0.12

yielding kinetic parameters v_o, v_s, and k_a, described by eq. 2 – 4 below. Linearized Dixon plots derived from these parameters were then used to determine K_m, K_i as well as k_{+4} and k_{-4}.

$$[P]_t = v_s t + \frac{(v_o - v_s)(1 - e^{-k_a t})}{k_a} + C \qquad (1)$$

$$v_O = \frac{V_M[S]}{K_M\left(1 + \frac{[I]}{K_I}\right) + [S]} \qquad (2)$$

$$v_S = \frac{V_M[S]}{K_M\left(1 + \frac{[I]}{K_I^*}\right) + [S]} \qquad (3)$$

$$k_a = k_{-4} + \frac{k_{+4}[I]}{K_I\left(1 + \frac{[S]}{K_M}\right) + [I]} \qquad (4)$$

Kinetic methods: (C) Competitive Inhibition. The inhibition constant (K_i) for compound **4** were determined from double-reciprocal plots of initial rates measured in the presence of 5 – 200 μM FBP and 10 - 200 μM inhibitor at constant enzyme concentration (0.01 μg/mL).

Kinetic methods: (D) Dual Competitive Inhibition. For compound **3**, inhibition kinetics were analyzed using a dual reversible linear inhibition model described previously.[34] The following equation used in the GraFit Data Analysis Software v.6.0.12 to analyze the inhibition data:

$$v = \frac{V_{max}[S]}{K_m\left(1 + \frac{[I]}{K_i} + \frac{[I]}{K_i'} + \frac{[I][I]}{K_i K_i'}\right)} \qquad (5)$$

where K_i and K_i' represent the inhibition constants for the two competitive binding sites. Assay conditions were the same as described for competitive inhibition.

Cellular growth inhibition tests. HeLa cells and HEK293 were selected for the *in vivo* growth inhibition assays. Cells were seeded into 6-well plates at densities of 2 x 10^5 cells/plate (HEK293) and 3 x 10^5 cells/plate (HeLa) (final volume 2 ml). Cells were cultured using DMEM and maintained at 37°C/ 5% CO_2 for 24, 48 or 72 hours. Treated cells received a final dose of 0.1, 1.0 or 10 μM of filter-sterilized **2**. Cells were harvested by first washing cells with pre-

warmed PBS and detached using trypsin (0.5 *m*l x (0.05% trypsin for HEK293 and 0.25% for HELA cells)). Trypsin was diluted by addition of 1.5 *m*l growth medium (DMEM). Cells were transferred to 15-*m*l conical tubes and centrifuged at 200 x g for 5 minutes. Cells were resuspended in 0.5 *m*l of pre-warmed growth medium. A 1:1 mixture of the cell suspension was mixed with Trypan Blue exclusion solution for subsequent total cell counting with a hemocytometer. The average number of cells was the result of counting three replicates in two independent experiments.

ASSOCIATED CONTENT

AUTHOR INFORMATION

Corresponding Author

*Jurgen Sygusch. E-mail: jurgen.sygusch@umontreal.ca; Tel.:514-343-2389; Fax: 514-343-6463.

 † Casimir Blonski. E-mail: casimir.blonski@u-psud.fr; Tel: 33 (0)1 69 15 47 25; Fax: 33 (0)1 69 15 72 81

Author Contributions

Funding Sources

ACKNOWLEDGMENTS

ABBREVIATIONS

FBP, Fructose-1,6-bisphosphate; NA-P$_2$, naphthalene 2,6-bisphosphate; ALDOA, aldolase A; PDB, Protein Data Bank.

REFERENCES

(1)   Som, P.; Atkins, H. L.; Bandoypadhyay, D.; Fowler, J. S.; MacGregor, R. R.; Matsui, K.; Oster, Z. H.; Sacker, D. F.; Shiue, C. Y.; Turner, H.; Wan, C.-N.; Wolf, A. P.; Zabinski, S. V. A Fluorinated Glucose Analog, 2-Fluoro-2-Deoxy-D-Glucose (F-18): Nontoxic Tracer for Rapid Tumor Detection. *J. Nucl. Med.* **1980**, *21* (7), 670–675.

(2)   Warburg, O.; Wind, F.; Negelein, E. The Metabolism of Tumors in the Body. *J. Gen. Physiol.* **1927**, *8* (6), 519–530.

(3)   Lunt, S. Y.; Heiden, M. G. V. Aerobic Glycolysis: Meeting the Metabolic Requirements of Cell Proliferation. *Annu. Rev. Cell Dev. Biol.* **2011**, *27* (1), 441–464.

(4)   Cairns, R. A.; Harris, I. S.; Mak, T. W. Regulation of Cancer Cell Metabolism. *Nat. Rev. Cancer* **2011**, *11* (2), 85–95.

(5)   Ganapathy-Kanniappan, S.; Geschwind, J.-F. H. Tumor Glycolysis as a Target for Cancer Therapy: Progress and Prospects. *Mol. Cancer* **2013**, *12* (1), 152.

(6)   Rho, J.-H.; Roehrl, M. H. A.; Wang, J. Y. Glycoproteomic Analysis of Human Lung Adenocarcinomas Using Glycoarrays and Tandem Mass Spectrometry: Differential Expression and Glycosylation Patterns of Vimentin and Fetuin A Isoforms. *Protein J.* **2009**, *28* (3–4), 148–160.

(7)   Poschmann, G.; Sitek, B.; Sipos, B.; Ulrich, A.; Wiese, S.; Stephan, C.; Warscheid, B.; Klöppel, G.; Vander Borght, A.; Ramaekers, F. C. S.; Meyer, H. E.; Stühler, K. Identification of Proteomic Differences between Squamous Cell Carcinoma of the Lung and Bronchial Epithelium. *Mol. Cell. Proteomics MCP* **2009**, *8* (5), 1105–1116.

(8)   Du, S.; Guan, Z.; Hao, L.; Song, Y.; Wang, L.; Gong, L.; Liu, L.; Qi, X.; Hou, Z.; Shao, S. Fructose-Bisphosphate Aldolase A Is a Potential Metastasis-Associated Marker of Lung Squamous Cell Carcinoma and Promotes Lung Cell Tumorigenesis and Migration. *PLoS ONE* **2014**, *9* (1), e85804.

(9)   G, P.; M, T.; Ed, W. Histological Examination of the Aldolase Monomer Composition of Cells from Human Kidney and Hypernephroid Carcinoma. *Beitr. Pathol.* **1975**, *156* (3), 266–279.

(10)   Chaerkady, R.; Harsha, H. C.; Nalli, A.; Gucek, M.; Vivekanandan, P.; Akhtar, J.; Cole, R. N.; Simmers, J.; Schulick, R. D.; Singh, S.; Torbenson, M.; Pandey, A.; Thuluvath,

P. J. A Quantitative Proteomic Approach for Identification of Potential Biomarkers in Hepatocellular Carcinoma. *J. Proteome Res.* **2008**, *7* (10), 4289–4298.

(11)   Ji, S.; Zhang, B.; Liu, J.; Qin, Y.; Liang, C.; Shi, S.; Jin, K.; Liang, D.; Xu, W.; Xu, H.; Wang, W.; Wu, C.; Liu, L.; Liu, C.; Xu, J.; Ni, Q.; Yu, X. ALDOA Functions as an Oncogene in the Highly Metastatic Pancreatic Cancer. *Cancer Lett.* **2016**, *374* (1), 127–135.

(12)   Peng, Y.; Li, X.; Wu, M.; Yang, J.; Liu, M.; Zhang, W.; Xiang, B.; Wang, X.; Li, X.; Li, G.; Shen, S. New Prognosis Biomarkers Identified by Dynamic Proteomic Analysis of Colorectal Cancer. *Mol. Biosyst.* **2012**, *8* (11), 3077–3088.

(13)   Opperdoes, F. R. Compartmentation of Carbohydrate Metabolism in Trypanosomes. *Annu. Rev. Microbiol.* **1987**, *41* (1), 127–151.

(14)   Verlinde, C. L. M. J.; Hannaert, V.; Blonski, C.; Willson, M.; Périé, J. J.; Fothergill-Gilmore, L. A.; Opperdoes, F. R.; Gelb, M. H.; Hol, W. G. J.; Michels, P. A. M. Glycolysis as a Target for the Design of New Anti-Trypanosome Drugs. *Drug Resist. Updat.* **2001**, *4* (1), 50–65.

(15)   Dax, C.; Duffieux, F.; Chabot, N.; Coincon, M.; Sygusch, J.; Michels, P. A. M.; Blonski, C. Selective Irreversible Inhibition of Fructose 1,6-Bisphosphate Aldolase from Trypanosoma Brucei. *J. Med. Chem.* **2006**, *49* (5), 1499–1502.

(16)   Suh, B.; Barker, R. Fluorescence Studies of the Binding of Alkyl and Aryl Phosphates to Rat Muscle Aldolase. *J. Biol. Chem.* **1971**, *246* (22), 7041–7050.

(17)   Blonski, C.; De Moissac, D.; Périé, J.; Sygusch, J. Inhibition of Rabbit Muscle Aldolase by Phosphorylated Aromatic Compounds. *Biochem. J.* **1997**, *323* (Pt 1), 71–77.

(18)   Dax, C.; Coinçon, M.; Sygusch, J.; Blonski, C. Hydroxynaphthaldehyde Phosphate Derivatives as Potent Covalent Schiff Base Inhibitors of Fructose-1,6-Bisphosphate Aldolase †. *Biochemistry (Mosc.)* **2005**, *44* (14), 5430–5443.

(19)   Freemont, P. S.; Dunbar, B.; Fothergill-Gilmore, L. A. The Complete Amino Acid Sequence of Human Skeletal-Muscle Fructose-Bisphosphate Aldolase. *Biochem. J.* **1988**, *249* (3), 779–788.

(20)   St-Jean, M.; Lafrance-Vanasse, J.; Liotard, B.; Sygusch, J. High Resolution Reaction Intermediates of Rabbit Muscle Fructose-1,6-Bisphosphate Aldolase: Substrate Cleavage and Induced Fit. *J. Biol. Chem.* **2005**, *280* (29), 27262–27270.

(21)   Anai, M.; Lai, C. Y.; Horecker, B. L. The Pyridoxal Phosphate-Binding Site of Rabbit Muscle Aldolase. *Arch. Biochem. Biophys.* **1973**, *156* (2), 712–719.

(22)   St-Jean, M.; Blonski, C.; Sygusch, J. Charge Stabilization and Entropy Reduction of Central Lysine Residues in Fructose-Bisphosphate Aldolase. *Biochemistry (Mosc.)* **2009**, *48* (21), 4528–4537.

(23)   St-Jean, M.; Sygusch, J. Stereospecific Proton Transfer by a Mobile Catalyst in Mammalian Fructose-1,6-Bisphosphate Aldolase. *J. Biol. Chem.* **2007**, *282* (42), 31028–31037.

(24)   Ramaswamy, B.; Shapiro, C. L. Bisphosphonates in the Prevention and Treatment of Bone Metastases. *Oncol. Williston Park N* **2003**, *17* (9), 1261-1270-1272, 1277–1278, 1280.

(25)   Reid, I. R. Short-Term and Long-Term Effects of Osteoporosis Therapies. *Nat. Rev. Endocrinol.* **2015**, *11* (7), 418–428.

(26)   Ginsburg, A.; Mehler, A. H. Specific Anion Binding to Fructose Diphosphate Aldolase from Rabbit Muscle. *Biochemistry (Mosc.)* **1966**, *5* (8), 2623–2634.

(27)   Williams, D. H.; Searle, M. S.; Mackay, J. P.; Gerhard, U.; Maplestone, R. A. Toward an Estimation of Binding Constants in Aqueous Solution: Studies of Associations of Vancomycin Group Antibiotics. *Proc. Natl. Acad. Sci.* **1993**, *90* (4), 1172–1178.

(28)   Gallivan, J. P.; Dougherty, D. A. A Computational Study of Cation−π Interactions vs Salt Bridges in Aqueous Media: Implications for Protein Engineering. *J. Am. Chem. Soc.* **2000**, *122* (5), 870–874.

(29)   Dougherty, D. A. Cation-π Interactions Involving Aromatic Amino Acids. *J. Nutr.* **2007**, *137* (6), 1504S–1508S.

(30)   Gallivan, J. P.; Dougherty, D. A. Cation-π Interactions in Structural Biology. *Proc. Natl. Acad. Sci.* **1999**, *96* (17), 9459–9464.

(31)   St-Jean, M.; Izard, T.; Sygusch, J. A Hydrophobic Pocket in the Active Site of Glycolytic Aldolase Mediates Interactions with Wiskott-Aldrich Syndrome Protein. *J. Biol. Chem.* **2007**, *282* (19), 14309–14315.

(32)   Rangarajan, E. S.; Park, H.; Fortin, E.; Sygusch, J.; Izard, T. Mechanism of Aldolase Control of Sorting Nexin 9 Function in Endocytosis. *J. Biol. Chem.* **2010**, *285* (16), 11983–11990.

(33)   Morrison, J. F.; Walsh, C. T. The Behavior and Significance of Slow-Binding Enzyme Inhibitors. In *Advances in Enzymology and Related Areas of Molecular Biology*; Meister, A., Ed.; John Wiley & Sons, Inc., 1988; pp 201–301.

(34)   MARTINEZ-IRUJO, J. J.; VILLAHERMOSA, M. L.; MERCAPIDE, J.; CABODEVILLA, J. F.; SANTIAGO, E. Analysis of the Combined Effect of Two Linear Inhibitors on a Single Enzyme. *Biochem. J.* **1998**, *329* (3), 689–698.

(35)   Nicholls, R. A.; Fischer, M.; McNicholas, S.; Murshudov, G. N. Conformation-Independent Structural Comparison of Macromolecules with ProSMART. *Acta Crystallogr. D Biol. Crystallogr.* **2014**, *70* (Pt 9), 2487–2499.

(36)   DeRuiter, J.; Clark, R. Bisphosphonates: Calcium Antiresorptive Agents. *Endocr. Module* **2002**.

(37)   Hartman, F. C.; Barker, R. An Exploration of the Active Site of Aldolase Using Structural Analogs of Fructose Diphosphate*. *Biochemistry (Mosc.)* **1965**, *4* (6), 1068–1075.

(38)   Ogata, H.; Takeo, K.; Kuwahara, A.; Suzuno, R.; Fujimoto, M.; Shimizu, J. An Exploration of the Binding Site of Aldolase Using Alkanediol Monoglycolate Bisphosphoric Esters. *Biochim. Biophys. Acta* **1983**, *742* (2), 384–390.

(39)   Elliott, T. S.; Slowey, A.; Ye, Y.; Conway, S. J. The Use of Phosphate Bioisosteres in Medicinal Chemistry and Chemical Biology. *MedChemComm* **2012**, *3* (7), 735–751.

(40)   Planas, M. E.; Sánchez, S.; González, P.; Rodrigues de Oliveira, J.; Bartrons, R. Protective Effect of Fructose 1,6-Bisphosphate against Carrageenan-Induced Inflammation. *Eur. J. Pharmacol.* **1993**, *237* (2–3), 251–255.

(41)   Veras, F. P.; Peres, R. S.; Saraiva, A. L. L.; Pinto, L. G.; Louzada-Junior, P.; Cunha, T. M.; Paschoal, J. A. R.; Cunha, F. Q.; Alves-Filho, J. C. Fructose 1,6-Bisphosphate, a High-Energy Intermediate of Glycolysis, Attenuates Experimental Arthritis by Activating Anti-Inflammatory Adenosinergic Pathway. *Sci. Rep.* **2015**, *5*, 15171.

(42)   Ehringer, W. D.; Niu, W.; Chiang, B.; Wang, O.-L.; Gordon, L.; Chien, S. Membrane Permeability of Fructose-1,6-Diphosphate in Lipid Vesicles and Endothelial Cells. *Mol. Cell. Biochem.* **2000**, *210* (1–2), 35–45.

(43)   Grandjean, G.; Jong, P. R. de; James, B. P.; Koh, M. Y.; Lemos, R.; Kingston, J.; Aleshin, A.; Bankston, L. A.; Miller, C. P.; Cho, E. J.; Edupuganti, R.; Devkota, A.;

Stancu, G.; Liddington, R. C.; Dalby, K. N.; Powis, G. Definition of a Novel Feed-Forward Mechanism for Glycolysis-HIF1α Signaling in Hypoxic Tumors Highlights Aldolase A as a Therapeutic Target. *Cancer Res.* **2016**, *76* (14), 4259–4269.

(44)   Braun, M.; Qorraj, M.; Büttner, M.; Klein, F. A.; Saul, D.; Aigner, M.; Huber, W.; Mackensen, A.; Jitschin, R.; Mougiakakos, D. CXCL12 Promotes Glycolytic Reprogramming in Acute Myeloid Leukemia Cells via the CXCR4/mTOR Axis. *Leukemia* **2016**, *30* (8), 1788–1792.

(45)   Caplan, N. A.; Pogson, C. I.; Hayes, D. J.; Blackburn, G. M. Novel Bisphosphonate Inhibitors of Phosphoglycerate Kinase. *Bioorg. Med. Chem. Lett.* **1998**, *8* (5), 515–520.

(46)   Kim, C. U.; Luh, B. Y.; Misco, P. F.; Bronson, J. J.; Hitchcock, M. J. M.; Ghazzouli, I.; Martin, J. C. Acyclic Purine Phosphonate Analogs as Antiviral Agents. Synthesis and Structure-Activity Relationships. *J. Med. Chem.* **1990**, *33* (4), 1207–1213.

(47)   Périgaud, C.; Gosselin, G.; Lefebvre, I.; Girardet, J.-L.; Benzaria, S.; Barber, I.; Imbach, J.-L. Rational Design for Cytosolic Delivery of Nucleoside Monphosphates : "SATE" and "DTE" as Enzyme-Labile Transient Phosphate Protecting Groups. *Bioorg. Med. Chem. Lett.* **1993**, *3* (12), 2521–2526.

(48)   Farquhar, D.; Khan, S.; Srivastva, D. N.; Saunders, P. P. Synthesis and Antitumor Evaluation of Bis[(pivaloyloxy)methyl] 2'-deoxy-5-Fluorouridine 5'-monophosphate (FdUMP): A Strategy to Introduce Nucleotides into Cells. *J. Med. Chem.* **1994**, *37* (23), 3902–3909.

(49)   Schultz, C. Prodrugs of Biologically Active Phosphate Esters. *Bioorg. Med. Chem.* **2003**, *11* (6), 885–898.

(50)   Mentel, M.; Laketa, V.; Subramanian, D.; Gillandt, H.; Schultz, C. Photoactivatable and Cell-Membrane-Permeable Phosphatidylinositol 3,4,5-Trisphosphate. *Angew. Chem. Int. Ed.* **2011**, *50* (16), 3811–3814.

(51)   Subramanian, D.; Laketa, V.; Müller, R.; Tischer, C.; Zarbakhsh, S.; Pepperkok, R.; Schultz, C. Activation of Membrane-Permeant Caged PtdIns(3)P Induces Endosomal Fusion in Cells. *Nat. Chem. Biol.* **2010**, *6* (5), 324–326.

(52)   Conway, S. J.; Thuring, J. W.; Andreu, S.; Kvinlaug, B. T.; Roderick, H. L.; Bootman, M. D.; Holmes, A. B. The Synthesis of Membrane Permeant Derivatives of Myo-Inositol 1,4,5-Trisphosphate. *Aust. J. Chem.* **2006**, *59* (12), 887–893.

(53)   Li, W.; Schultz, C.; Llopis, J.; Tsien, R. Y. Membrane-Permeant Esters of Inositol Polyphosphates, Chemical Syntheses and Biological Applications. *Tetrahedron* **1997**, *53* (35), 12017–12040.

(54)   Atack, J. R.; Cook, S. M.; Watt, A. P.; Fletcher, S. R.; Ragan, C. I. In Vitro and In Vivo Inhibition of Inositol Monophosphatase by the Bisphosphonate L-690,330. *J. Neurochem.* **1993**, *60* (2), 652–658.

(55)   Atack, J. R.; Prior, A. M.; Fletcher, S. R.; Quirk, K.; McKernan, R.; Ragan, C. I. Effects of L-690,488, a Prodrug of the Bisphosphonate Inositol Monophosphatase Inhibitor L-690,330, on Phosphatidylinositol Cycle Markers. *J. Pharmacol. Exp. Ther.* **1994**, *270* (1), 70–76.

(56)   Morris, A. J.; Tolan, D. R. Site-Directed Mutagenesis Identifies Aspartate 33 as a Previously Unidentified Critical Residue in the Catalytic Mechanism of Rabbit Aldolase A. *J. Biol. Chem.* **1993**, *268* (2), 1095–1100.

(57)   Baranowski, T.; Niederland, T. R. Aldolase Activity of Myogen A. *J. Biol. Chem.* **1949**, *180* (2), 543–551.

(58)   Otwinowski, Z.; Minor, W. [20] Processing of X-Ray Diffraction Data Collected in Oscillation Mode. In *Methods in Enzymology*; Charles W. Carter, J., Ed.; Macromolecular Crystallography Part A; Academic Press, 1997; Vol. 276, pp 307–326.

(59)   Adams, P. D.; Grosse-Kunstleve, R. W.; Hung, L.-W.; Ioerger, T. R.; McCoy, A. J.; Moriarty, N. W.; Read, R. J.; Sacchettini, J. C.; Sauter, N. K.; Terwilliger, T. C. *PHENIX* : Building New Software for Automated Crystallographic Structure Determination. *Acta Crystallogr. D Biol. Crystallogr.* **2002**, *58* (11), 1948–1954.

(60)   McCoy, A. J.; Grosse-Kunstleve, R. W.; Adams, P. D.; Winn, M. D.; Storoni, L. C.; Read, R. J. *Phaser* Crystallographic Software. *J. Appl. Crystallogr.* **2007**, *40* (4), 658–674.

(61)   Afonine, P. V.; Grosse-Kunstleve, R. W.; Echols, N.; Headd, J. J.; Moriarty, N. W.; Mustyakimov, M.; Terwilliger, T. C.; Urzhumtsev, A.; Zwart, P. H.; Adams, P. D. Towards Automated Crystallographic Structure Refinement with <phenix.refine>. *Acta Crystallogr. D Biol. Crystallogr.* **2012**, *68* (4), 352–367.

(62)   Emsley, P.; Lohkamp, B.; Scott, W. G.; Cowtan, K. Features and Development of *Coot*. *Acta Crystallogr. D Biol. Crystallogr.* **2010**, *66* (4), 486–501.

(63)   Karplus, P. A.; Diederichs, K. Linking Crystallographic Model and Data Quality. *Science* **2012**, *336* (6084), 1030–1033.

(64)   Afonine, P. V.; Moriarty, N. W.; Mustyakimov, M.; Sobolev, O. V.; Terwilliger, T. C.; Turk, D.; Urzhumtsev, A.; Adams, P. D. FEM: Feature-Enhanced Map. *Acta Crystallogr. D Biol. Crystallogr.* **2015**, *71* (3), 646–666.

(65)   Moriarty, N. W.; Grosse-Kunstleve, R. W.; Adams, P. D. Electronic Ligand Builder and Optimization Workbench (eLBOW): A Tool for Ligand Coordinate and Restraint Generation. *Acta Crystallogr. D Biol. Crystallogr.* **2009**, *65* (10), 1074–1080.

(66)   Chen, V. B.; Arendall, W. B.; Headd, J. J.; Keedy, D. A.; Immormino, R. M.; Kapral, G. J.; Murray, L. W.; Richardson, J. S.; Richardson, D. C. MolProbity : All-Atom Structure Validation for Macromolecular Crystallography. *Acta Crystallogr. D Biol. Crystallogr.* **2010**, *66* (1), 12–21.

(67)   *The PyMol Molecular Graphics System, Version 1.7.4, Schrodinger, LLC*.

(68)   Holst, M. Adaptive Numerical Treatment of Elliptic Systems on Manifolds. *Adv. Comput. Math.* **2001**, *15* (1–4), 139–191.

(69)   Baker, N. A.; Sept, D.; Joseph, S.; Holst, M. J.; McCammon, J. A. Electrostatics of Nanosystems: Application to Microtubules and the Ribosome. *Proc. Natl. Acad. Sci.* **2001**, *98* (18), 10037–10041.

(70)   Dolinsky, T. J.; Nielsen, J. E.; McCammon, J. A.; Baker, N. A. PDB2PQR: An Automated Pipeline for the Setup of Poisson–Boltzmann Electrostatics Calculations. *Nucleic Acids Res.* **2004**, *32* (suppl 2), W665–W667.

(71)   Dolinsky, T. J.; Czodrowski, P.; Li, H.; Nielsen, J. E.; Jensen, J. H.; Klebe, G.; Baker, N. A. PDB2PQR: Expanding and Upgrading Automated Preparation of Biomolecular Structures for Molecular Simulations. *Nucleic Acids Res.* **2007**, *35* (suppl 2), W522–W525.

(72)   Racker, E. Spectrophotometric Measurement of Hexokinase and Phosphohexokinase Activity. *J. Biol. Chem.* **1947**, *167* (3), 843–854.

(73)   Leatherbarrow, R. J. *GraFit Version 7*; Erithacus Software Ltd: Horley, U.K., 2009.

(74)   Goliĉnik, M.; Stojan, J. Slow-Binding Inhibition: A Theoretical and Practical Course for Students. *Biochem. Mol. Biol. Educ.* **2004**, *32* (4), 228–235.
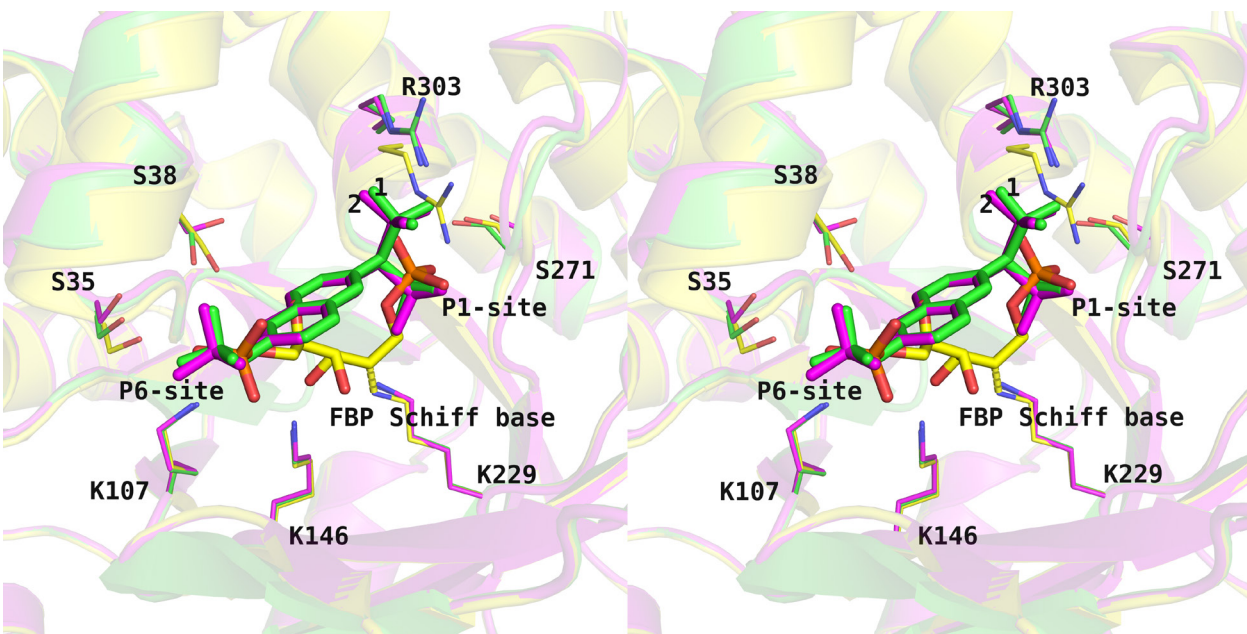
Figure S3-1. Active site comparison of ALDOA-1, ALDOA-2 and ALDOA-FBP Schiff base complex.

Stereo view of superposition between ALDOA-**1** complex (*green*), ALDOA-**2** complex (*magenta*) and Schiff base FBP complex subunit (*yellow*) (PDB id: 1ZAI) by PyMol (ALDOA-1 alignment of C_α atoms to 1ZAI, r.m.s.d = 0.17Å; ALDOA-2 alignment to 1ZAI, r.m.s.d. = 0.15Å). The phosphate moieties of **1** and **2** superpose closely with the P_1- and P_6-sites in the FBP intermediate complex (r.m.s.d. < 1Å). The major binding configuration (*trans*) of **1** coincides well with the P_1-site of FBP; conversely, the phosphate group of the minor configuration (*cis*) is ~2.5Å above the P_1-site. In the *cis* configuration, Arg303 is shifted by ~2.5Å in the ALDOA-**1** complex in comparison to the FBP-complex. The larger bisphosphonate of **2** affords the same shift in Arg303 as seen with **1**. In the ALDOA-**1** and ALDOA-**2** complexes, the entrance to the active site is slightly larger, creating a wider cavity; this is a consequence of the longer transverse interatomic P_1-P_6 distance with the naphthalene derivatives (9.8Å) compared to FBP (8.9Å) that results in a ~1Å shift of the flanking helical region (residues 34-65).
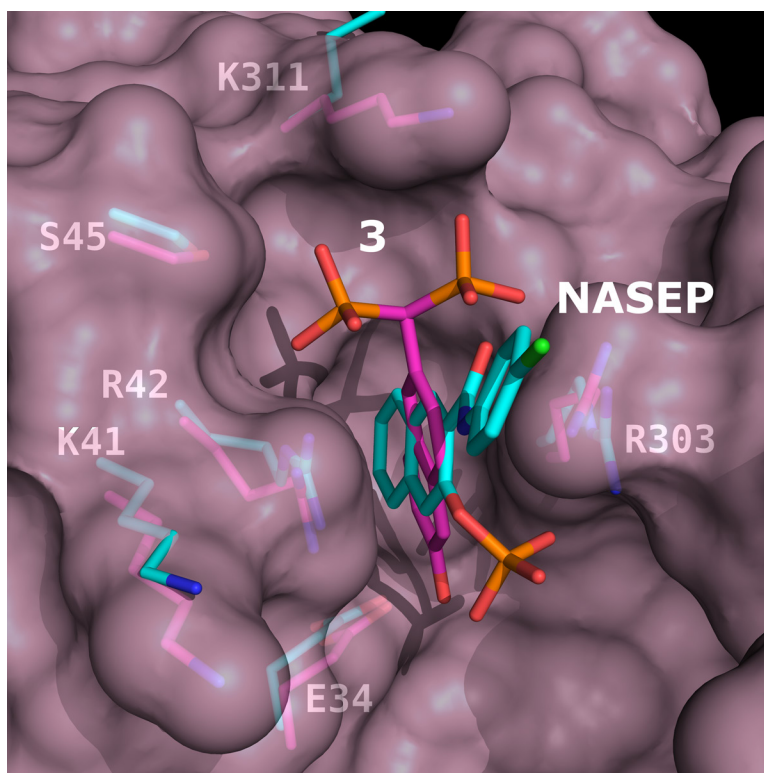
Figure S3-2. Superposition of 3 and NASEP in ALDOA active site.

The hydrophobic naphthalene moiety of **3** (*magenta*) superposes with the moiety in NASEP (*cyan*) from a previous structure (PDB id: 2OT1). Key active site residues are illustrated for both structures (ALDOA-**3**, *magenta*; ALDOA-NASEP, *cyan*). Both compounds intercalate between the active site arginines, Arg42 and Arg303, to form hydrophobic contacts in the pocket. A strong cation-π interaction is formed between Arg42 Nε and the naphthalene ring of both inhibitors. The NASEP phosphate interacts with the Arg303 guanidinium group, forming a total of 4 hydrogen bonds. The ALDOA-**3** complex comprises a total of 7 hydrogen bonds.
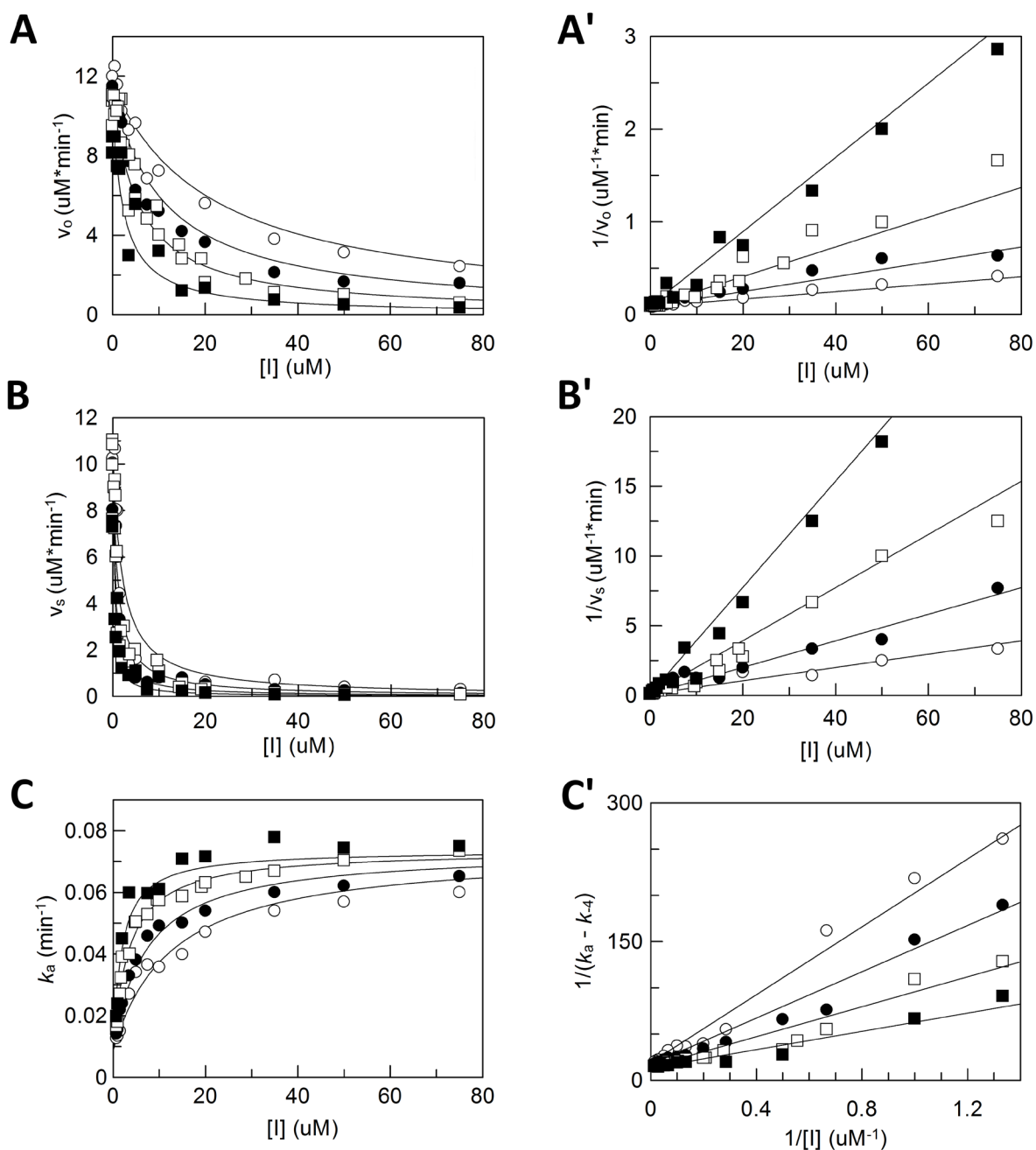
Figure S3-3. Slow-binding inhibition of aldolase by inhibitor 2.

Direct and linearized plots of the effect of inhibitor **2** on v_o (**A, A'**), v_s (**B, B'**), and k_a (**C, C'**) for the FBP cleavage activity of rabbit muscle aldolase at various substrate concentrations. FBP concentrations: (■) 20 μM, (□) 50 μM, (●) 100 μM, (○) 200 μM.
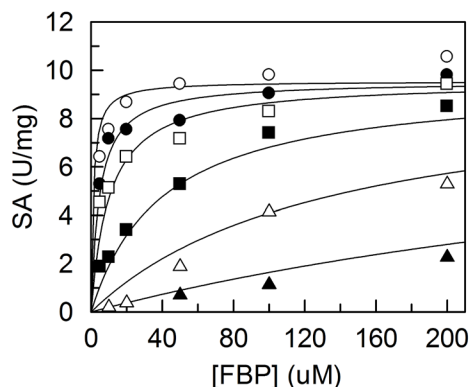
Figure S3-4. Dual competitive inhibition of aldolase by inhibitor 3.

Inhibition of aldolase activity in presence of inhibitor **3** and measured by the rate of FBP cleavage by rabbit muscle aldolase expressed in terms of specific activity (U/mg) for inhibitor **3** concentrations of: (○) 0 μM, (●) 10 μM, (□) 20 μM, (■) 50 μM, (△) 100 μM, (▲) 200 μM.
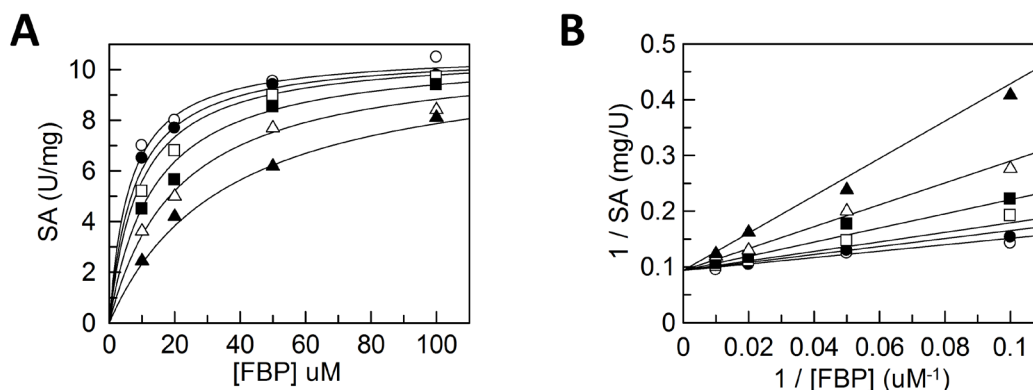
Figure S3-5. Competitive inhibition of ALDOA activity by inhibitor 4.

(A) Inhibition of aldolase activity in presence of inhibitor **4** and measured by the rate of FBP cleavage by rabbit muscle aldolase for different inhibitor concentration and expressed in terms of specific activity (U/mg). (B) Double reciprocal plot of inhibition data shown on panel **A** showing reciprocal reaction velocity (1/SA in mg/unit) plotted against reciprocal substrate concentration (1/[FBP] in μM^{-1}) for inhibitor **4** concentrations: (○) 0 μM, (●) 10 μM, (□) 20 μM, (■) 50 μM, (△) 100 μM, (▲) 200 μM.

Chapter 4

Aldolase and methylglyoxal production: structural and enzymatic investigation of a promiscuous aldolase activity

Background

Indirectly related to the catalytic mechanism is the purported production of methylglyoxal (MGO) by aldolase A, a toxic metabolite observed by our laboratory in preliminary experiments involving aldolase in the presence of dihydroxyacetone phosphate (DHAP). The pathological consequences of MGO accumulation is well recognized, but several questions remain regarding the importance of different reported sources.

The initial focus of my doctoral studies was on determining the origins of this metabolite with respect to aldolase in addition to understanding its physiological scope. This was intended as a continuation of preliminary findings by our group (conducted by a previous student, Miguel St-Jean) showing *in vitro* production of MGO by aldolase incubated with the substrate DHAP. This was corroborated by crystallographic structures of aldolase soaked with DHAP purporting to show evidence of MGO generation in the active site. This preliminary structure emanating from previous studies on the reaction mechanism of class I aldolases (St-Jean, 2005) will be shown in the following chapter, and served as the basis for our hypothesis implicating a significant role for aldolase as an MGO source.

However, during the course of experimentation, we noted that a role for aldolase in MGO production was not as important as previously stated. In this chapter, a thorough investigation of the *in vitro* production of MGO by aldolase was undertaken and comprises structural and biochemical data. The data collected and ensuing in-depth analysis ultimately supported a null hypothesis and addresses the longstanding duality between enzyme-generated and spontaneously-generated MGO from triose-phosphates.

Aldolase and methylglyoxal production: structural and enzymatic investigation of a promiscuous aldolase activity

Paul W. Heron, Jurgen Sygusch

KEYWORDS: methylglyoxal, aldolase, β-elimination, dihydroxyacetone phosphate, fructose-1,6-bisphosphate

ABSTRACT

Methylglyoxal (MGO) is a highly reactive dicarbonyl metabolite, generated primarily as a side-product of glycolysis via the decomposition of the triose-phosphates, dihydroxyacetone phosphate (DHAP) and glyceraldehyde-3-phosphate (G3P). Preliminary structural work suggested the decomposition of DHAP to MGO and inorganic phosphate (P_i) in the aldolase active site. An in-depth crystallographic structural investigation of MGO production in class I aldolase revealed a more appropriate model to account for the apparent P_i cleavage in DHAP-soaked crystals – that is, a mixture of non-decomposed DHAP and water molecules. The contribution of MGO production and P_i expulsion by aldolase was evaluated by enzymatic assays. P_i levels were shown to increase as a function of time when aldolase was incubated with fructose-1,6-bisphosphate. We evaluated the contribution of triose-phosphates towards P_i production. The coinciding levels of P_i measured in DHAP-only samples compared to DHAP-aldolase samples demonstrated that P_i production originates primarily from spontaneous decomposition of triose-phosphates. Therefore, the biological significance of the MGO synthase pathway in aldolase is resolved. Altogether, a better understanding of MGO metabolism is critical for developing strategies to mitigate the clinical manifestations of MGO-derived pathologies.

ABBREVIATIONS

MGO, methylglyoxal; P_i, inorganic phosphate; FBP, fructose-1,6-bisphosphate; DHAP, dihydroxyacetone phosphate; G3P, glyceraldehyde-3-phosphate; TIM, triosephosphate isomerase; GDH, glycerol-3-phosphate dehydrogenase; GAPDH, glyceraldehyde-3-phosphate deyhydrogenase.

INTRODUCTION

Fructose-1,6-bisphosphate (FBP) aldolase has been associated with the production of inorganic phosphate (P_i) and methylglyoxal (MGO) in several conditions. There is considerable interest in understanding MGO metabolism since it is a highly reactive dicarbonyl metabolite that glycates biological macromolecules, forming advanced glycation end products (AGEs), which have been shown to underscore several pathologies including diabetes (1), hypertension (2), atherosclerosis (3), and neurodegenerative diseases (4–7). Further, there is evidence suggesting that MGO may induce an increase in ROS species, contributing to cellular senescence and aging (8). Fortunately, cells are equipped with a detoxification system, the ubiquitous glyoxalase system, which comprises two enzymes, glyoxalase I and II (9). These enzymes convert MGO to D-lactate in a conjugation reaction with a catalytic amount of reduced glutathione. However, the system is not entirely robust as the GSH/GSSG ratio can be affected by other redox couples, notably $NADPH/NADP^+$ and thioredoxin$_{red/ox}$ (10).

MGO production is known to have a variety of origins, arising in carbohydrate metabolism, lipid catabolism, and protein catabolism. Both enzyme-catalyzed and non-enzymatic reactions take part in its formation (for reviews, see 9,11–14). For example, cytochrome P-450 enzymes (CYP2E1) catalyze the conversion of acetone to MGO during fatty acid catabolism (15). Also, catabolism of threonine and glycine produces aminoacetone, which is converted to MGO by an amine oxidase (SSAO) (16). However, carbohydrate metabolism appears to be the most important source of MGO as glycolytic flux appears to be a major determinant of MGO production (17–19). Glycolysis-linked MGO production depends strongly on the formation of triose-phosphates, which decompose either enzymatically or non-enzymatically to MGO. FBP aldolase catalyzes the cleavage of FBP to the triose-phosphates, glyceraldehyde-3-phosphate (G3P) and dihydroxyacetone phosphate (DHAP). After the interconversion of DHAP and G3P catalyzed by triosephosphate isomerase (TIM), G3P serves as a substrate for the downstream enzyme glyceraldehyde-3-phosphate dehydrogenase (GAPDH). TIM has been shown to release MGO (20–22). Studies on the non-enzymatic reactions of triose-phosphates have shown that TIM is responsible for the generation of the highly labile enediolate phosphate intermediate (Scheme 4-1), which decomposes to MGO + P_i (23). The triose-phosphates are inherently unstable and rapidly decompose to MGO, as per Scheme 4-1. Estimates for the rate of
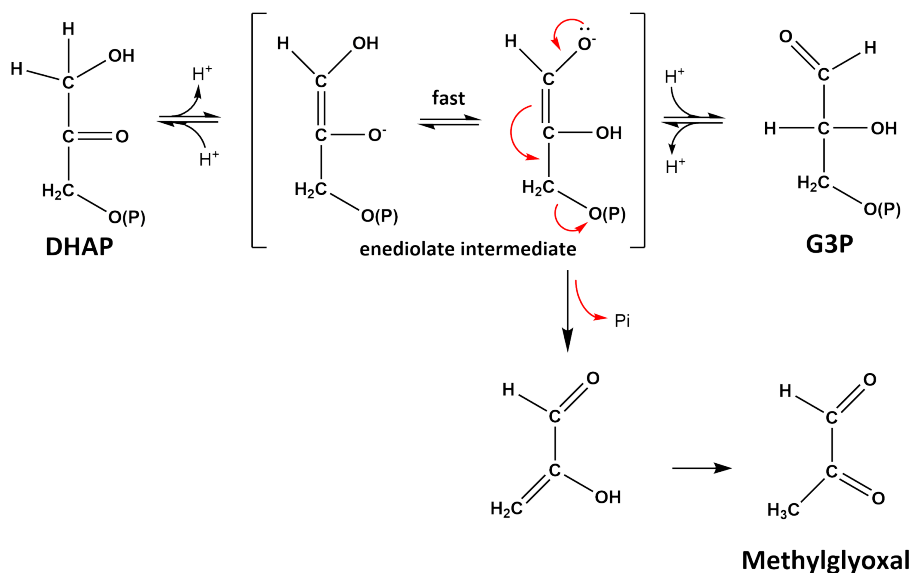
Scheme 4-1. Decomposition of the triose-phosphates to methylglyoxal.

TIM (triosephosphate isomerase) catalyzes the isomerization between the triose-phosphates DHAP and G3P by way of an enediolate intermediate (*in brackets*), which undergoes β-elimination (*arrows in red*), leading to Pi release and formation of MGO. This scheme also represents the general mechanism by which the triose-phosphates decompose in solution, and is accelerated in alkaline conditions.

production from enzymatic and non-enzymatic generation of MGO indicate that enzymatic contribution by TIM is minor compared to the spontaneous decomposition of triose-phosphates (24,25).

The participation of aldolase in MGO release was derived from the chemical identification of an intermediate of the aldolase reaction, the pyruvaledyde-aldolase-orthophosphate complex, that is in equilibrium with the enamine intermediate (26). This complex decomposes with the slow release of MGO and P_i. It was subsequently proposed from isotope exchange experiments that abstraction of the O3 proton on the enamine intermediate leads to an irreversible β-1,4-elimination that cleaves the ester bond between the C1 and O1, releasing P_i (as shown in Scheme 4-2) (27). Subsequent hydrolysis releases MGO. The biological significance of the MGO pathway in aldolase was questioned when it was shown that the pathway is accelerated by the acidification process used to quench the reaction (20).
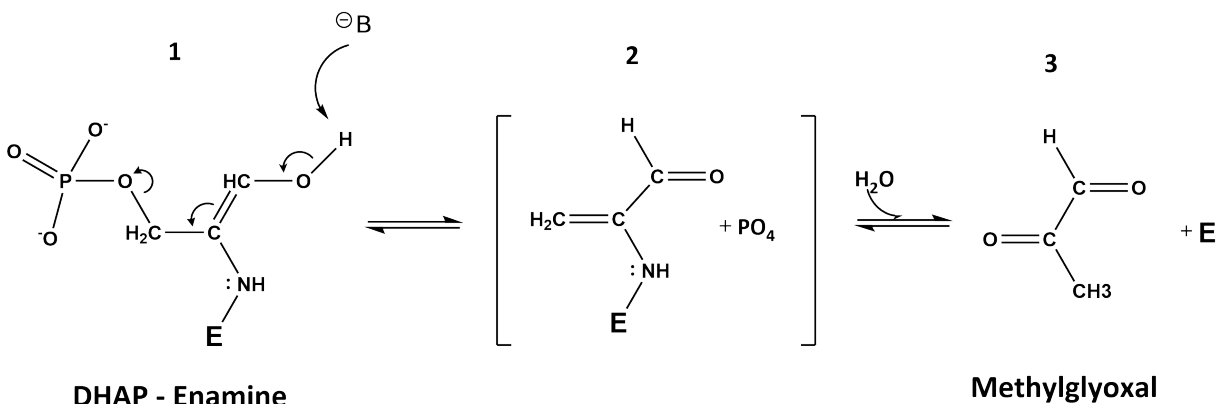
Scheme 4-2. Aldolase-catalyzed β-elimination reaction of the enamine intermediate.

The enamine intermediate (**1**) in the aldolase mechanism is vulnerable to abstraction of the O3 hydroxyl proton, leading to β-elimination of the phosphate oxyanion. Hydration of the residual covalent adduct (**2**) releases the dicarbonyl metabolite, methylglyoxal (**3**).

The function of MGO production in the metabolic machinery is still unknown but the identification of methylglyoxal synthase (MGS) in some prokaryotes suggests a role in regulating the phosphate supply of some organisms in conditions of phosphate deficiency (28,29). Whether this kind of regulation exists in higher vertebrates is unknown. Altogether, a better understanding of MGO metabolism is critical for developing strategies to mitigate the clinical manifestations of MGO-derived pathologies.

Here, the role of aldolase in contributing to the MGO pool was probed both structurally and enzymatically. Preliminary structural and biochemical data from our laboratory led to our hypothesizing an important role for aldolase in MGO formation. Early structure enzymological work with aldolase crystals soaked in the substrate DHAP provided the first signs of DHAP decomposition in the active site (see **Figure 4-1A-B**). This was initially construed as spurious density but additional structures continued to support the decomposition hypothesis – consequently, a detailed investigation was propsoed. Of concern in the purported structure is the disappearance of density at the phosphoester bond of DHAP ((**Figure 4-1B**; *green density*). The density that remains was interpreted as the elimination of the phosphate from the enamine intermediate by the mechanism described in Scheme 4-2. Modeling of DHAP into the simulated annealing omit map ((**Figure 4-1C, D**) was problematic since the DHAP C3 hydroxyl is 1.2Å from Lys-146 Nζ atom. Comparison of the conformation of Lys-146 in a previously reported
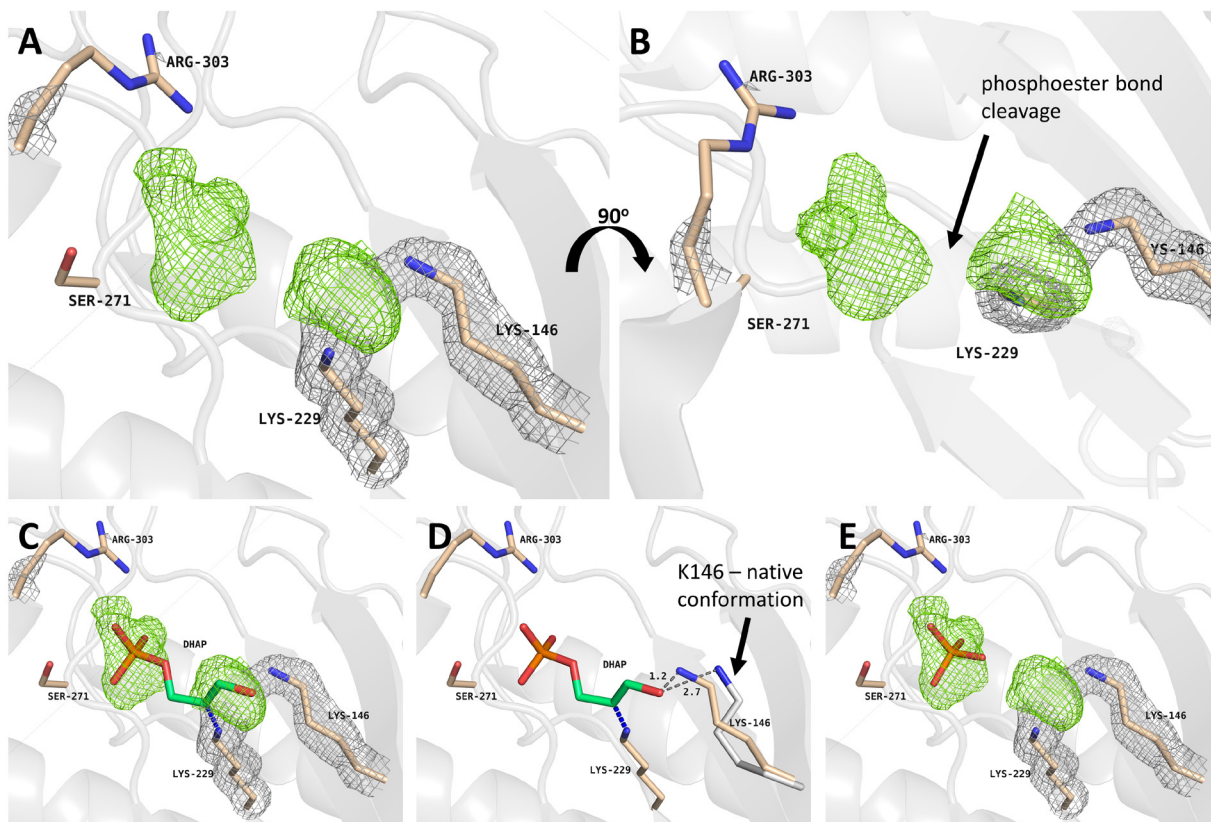
Figure 4-1. Aldolase crystal structure (DHAP-frac) showing evidence of phosphate elimination.

Rabbit muscle aldolase crystals were soaked in a solution containing 1 *m*M of DHAP for 10 minutes. All *green* densities show simulated annealing (SA) $F_o - F_c$ omit maps contoured at 3σ. Densities colored *grey* represent $2F_o - F_c$ difference maps contoured at 1.5σ. Panels (**A**) and (**B**) illustrate side and top views of the active site. (**C**) DHAP is modeled into the omit map as the enamine intermediate. (**D**) The conformation of Lys-146 is markedly altered in comparison to the native conformation where Lys-146 is shown in *light grey*. In the aldolase structure complexed with DHAP (PDB id: 2QUT), the distance between Lys-146 Nζ atom and the DHAP hydroxyl group is 2.7Å (*grey dash*). However, a movement of 1.7Å of Lys-146 brings the Nζ atom to within 1.2Å of the hydroxyl group (*grey dash*). (**E**) Phosphate oxyanion is modeled at the P1-phosphate site, with unexplained electron density between Lys-229 and Lys-146.

aldolase structure in complex with DHAP showed that Lys-146 is usually at a distance appropriate for hydrogen bonding (2.7Å) (**Figure 4-1D**). These structures therefore revealed an important movement of Lys-146 (1.7Å) towards the DHAP hydroxyl. The steric clash between Lys-146 and DHAP precluded the modeling of DHAP into the active site. Alternatively, the phosphate oxyanion was readily modeled at the P1 locus, however, the density between Lys-229 and Lys-146 remained unidentified, and was the subject of this study. Ser-271 mutations

have shown the importance of this residue in anchoring the P1-phosphate (30), which could explain why the phosphate oxyanion does not readily dissociate from the active site following elimination. Also, it is known that MGO can modify active site residues in aldolase by an unknown mechanism (31) – we thus speculated the possibility of an additional promiscuous reaction following β-elimination of the phosphate.

Furthermore, biochemical data was reported in our laboratory by Munger (Master's thesis) which purported to observe, by NMR spectroscopy, phosphate elimination from DHAP in the presence of aldolase (30). Those experiments supported an early hypothesis suggesting aldolase is inactivated by MGO after its formation (31).

In light of the above findings, we sought to conclusively demonstrate the β-elimination of phosphate in aldolase by collecting additional structural data on rabbit muscle aldolase crystals soaked with DHAP for incremental time intervals. Also, we measured the *in vitro* production of MGO by aldolase in similar conditions. Together, we showed that aldolase-produced MGO is not as significant as previously reported and a better description of the fragments first observed in the active site resulted from proper refinement of water and DHAP occupancies. Triose-phosphate decomposition appears to be a significantly greater source of MGO production than enzymatically produced MGO.

EXPERIMENTAL SECTION

Materials. FBP, DHAP, G3P, glycerol-3-phosphate dehydrogenase (GDH), triose-phosphate isomerase (TIM), methylglyoxal (40 % v/v solution), glyoxalase I, and S-D-lactoylglutathione were purchased from Sigma-Aldrich. NADH was from Roche Diagnostics. All other chemicals and materials were of analytical grade and were obtained from Sigma-Aldrich, Fisher Scientific, Bioshop Canada, and GE Healthcare Life Sciences.

Purification and Crystallization. Expression and purification of recombinant native (WT) rabbit muscle aldolase was performed as previously described (32–34) using *E. coli* strain BL21-SI for overexpression of the recombinant protein (Invitrogen) (see Chapter 1 of thesis – Methodology). The aldolase concentration was determined using an extinction coefficient of 0.91 cm $mg^{-1} \cdot mL$ and 280 *n*m (35). WT aldolase was crystallized by vapor diffusion from a 1:1 mixture of protein solution (10 $mg \cdot ml^{-1}$ in 20 *m*M Tris-HCl, pH 7.0) and precipitant buffer (18% polyethylene glycol 4000 in 0.1 M Na-HEPES, pH 7.5) that was equilibrated against a reservoir of precipitant, as previously reported (33).

Activity assays. Aldolase cleavage activity was determined using a coupled assay system involving triose-phosphate isomerase and glycerol-3-phosphate dehydrogenase (TIM/GDH) by following NADH oxidation at 340 *n*m using a Varian Cary 300 UV-Vis spectrophotometer thermostatted at 25 °C (36).

Formation of MGO from FBP and triose-phosphates in the presence of aldolase. 1 – 10 μg of rabbit muscle aldolase was incubated in the presence of 1, 10, or 100 *m*M of FBP, DHAP or G3P. In order to determine the pH dependence of MGO generation from aldolase, the incubation of aldolase with FBP was conducted in 50 *m*M of the following buffers: Na-Acetate pH 4 – 5; MES pH 5.5 – 6.5; TRIS pH 7 – 8.5; CHES pH 9 – 9.5; CAPS pH 10 – 11. For incubations in Tris, pH was adjusted with acetate or HCl. Different incubation times were tested by withdrawing samples at 5, 10, 15, 30 and 90 minutes and assaying for MGO in the sample by the methods described below.

In order to quench the incubation reaction, methods tested involved either one or a combination of the following: 1) heating the sample at 95 ºC for 1 minute; 2) acid quenching with 5 – 10 % perchloric acid or tetrachloroacetic acid; 3) removal of anions by treatment with Dowex 1x4-200 (Sigma); 4) centrifugation of sample at 10,000 rpm for 10 minutes. Dowex 1x4

– 200 is an anion exchange resin that was prepared by washing sequentially with 1 M NaOH, deionized water, 4 M acetic acid, deionized water and sterile 50 mM Tris-HCl, pH 7.4, and stored as a 50 % slurry at 4 $^{\circ}$C until ready for use.

MGO measurement. MGO was measured using two different approaches. The first method involved the glyoxalase enzyme assay system, which has been previously applied to MGO measurements (37). Enzymatically or non-enzymatically generated MGO couples spontaneously with reduced glutathione (GSH) to form a hemithioacetal that is a substrate for glyoxalase I. The hemithioacetal is converted to S-D-lactoylglutathione which has an absorption maximum at 240 nm (extinction coefficient = 3.37 mM$^{-1} \cdot cm^{-1}$) (38). The conversion of the hemithioacetal to S-D-lactoylglutathione was assayed spectrophotometrically in a quartz cuvette and provided a direct measure of MGO in a sample of interest. The assay was performed in 100 mM KH$_2$PO$_4$, pH 6.6 at 25 $^{\circ}$C (optimal pH for glyoxalase I activity). Reduced glutathione (prepared as 2 % w/v in H$_2$O – pH adjusted to 6.6 with solid sodium bicarbonate) was added in the final mixture to a final concentration of 0.033 % w/v. Up to 30 minutes of incubation was provided to complete the spontaneous coupling of MGO and GSH to the hemithioacetal – a baseline was established at 240 nm. Glyoxalase I (final concentration of 0.017 U/ml) was added to convert the hemithioacetal to S-D-lactoylglutathione and the change in OD at 240 nm gave the total concentration of S-D-lactoylglutathione in the sample, which relates directly to the concentration of MGO in the sample. A standard curve was prepared using a stock solution of MGO (Sigma) at 40 % v/v, equivalent to 5.55 M. MGO determination was conducted in both UV-transparent 96-well plates (Corning) and in quartz cuvettes. UV-transparent plates exhibited < 10 % absorbance at the lower end of the UV spectrum ($\sim$ 230 nm). Also, bovine serum albumin (BSA) (50 μg) was added per assay to reduce non-specific binding.

The EnzCheck® Phosphate Assay kit (Molecular Probes Inc.) was also used for indirect quantification of MGO. Since MGO formation by aldolase predicts inorganic phosphate (P$_i$) release, quantification of the latter is suitable. The EnzCheck phosphate assay is based on a method developed by Webb (39) in which free P$_i$ reacts with the substrate 2-amino-6-mercapto-7-methylpurine riboside (MESG) in a reaction catalyzed by purine nucleoside phosphorylase (PNP) to produce ribose-1-phosphate and 2-amino-6-mercapto-7-methylpurine. Enzymatic conversion of MESG results in a spectrophotometric shift in maximum absorbance from 330

*n*m for the substrate to 360 *n*m for the product. Experiments were conducted as per the specifications in the kit.

Crystallographic Data Collection and Processing. Native aldolase crystals were soaked in a solution containing 1 or 10 *m*M of DHAP (final concentration in the mother liquor) and flash-frozen in liquid nitrogen at the following time intervals (minutes): 1, 2, 10, 60, and 200. Prior to flash-freezing, crystals were cryoprotected by briefly soaking them in a cryo-buffer solution (DHAP at 1 or 10 *m*M/ mother liquor/ 15 % (v/v) glycerol). Data was collected at beamlines X25 and X29 of the National Synchrotron Light Source at Brookhaven National Laboratories. The remaining datasets were collected from single crystals at beamline 08ID-1 or 08B1-1 of the Canadian Light Source, Saskatchewan, Canada, using a Rayonix MX300 CCD X-ray detector. A native data set was also collected as a control. All data sets were processed with HKL2000 (40), and the final results are summarized in Table 4-1.

Structure determination and refinement. Structures were solved by molecular replacement with PHENIX (41) Phaser-MR (42) using the native aldolase homotetramer structure as a reference model [Protein Data Bank (PDB) entry 1ZAH]. Refinement and model building were performed using phenix.refine (43) and Coot (44) respectively. Data quality was assessed and cut-off using correlation-coefficient-based criteria, CC1/2 (45). Ligand fitting and interpretation was performed using a combination of simulated annealing $F_o - F_c$ omit maps and feature-enhanced sigma-A weighted $2F_o - F_c$ maps (46) that were calculated in the final round of refinement. All difference density maps ($F_o - F_c$) shown in the paper correspond to simulated annealed $F_o - F_c$ omit maps. Ligand coordinate and restraints were generated using PHENIX eLBOW (47). Final model statistics were calculated with MolProbity (48) and are shown in Table 4-1. All figures in the present paper were prepared using PyMOL graphics software (http://www.pymol.org) (49).

The occupancies of DHAP and active site water molecules in each model (corresponding to different soaking times with DHAP) was determined by introducing random differences in their starting occupancies, creating an ensemble of five models for each structure that were refined for ten cycles with identical refinement protocols until convergence was observed, similar to what has previously been recommended (50).

RESULTS

Structural Characterization of Phosphate Release and MGO formation in Aldolase Crystals. In an effort to clarify the postulated role of class I aldolase in the promiscuous formation of MGO in the active site, rabbit muscle aldolase crystals were soaked in a solution containing the mother liquor and DHAP at 1 mM. Systematically, after set periods of time (1, 10, 60, and 200 minutes), crystals were removed, cryoprotected with 15% v/v glycerol and frozen in liquid nitrogen to trap intermediate states. Data collection and refinement statistics for all crystal structures are shown in Table 4-1. All structures were determined to higher than 2Å resolution (between 1.7 – 1.99Å) and had comparable collection and refinement statistics (R_{free} ≤ 0.2). The differential soaking period had no effect on crystal quality as resolution and R-scores are constant for all structures. This allowed us to make meaningful comparisons across the different structures. A control dataset (not shown) was also collected and consisted of a non-soaked native aldolase structure. Collection and refinement statistics are also available for the preliminary structure showing the suspected adduct formation from MGO (see supporting Table S4-1). This structure was prepared using native aldolase crystals that were soaked in 1 mM DHAP for 10 minutes before flash-freezing. Data was collected up to 1.6Å and refined to an R_{free}/R_{work} of 17.3/15.1 and is comparable to the data collected in the time-course experiment. In all cases, aldolase maintains its tetrameric quaternary structure in the asymmetric unit of a P 2_1 space group, consistent with aldolase structures previously reported for these conditions (33).

Table 4-1. Data collection and refinement statistics.

	DHAP-1min	DHAP-10mins	DHAP-60mins	DHAP-200mins
Data Collection				
Resolution range (Å)	43.88 - 1.999	14.06 - 1.696	43.97 - 1.8	21.34 - 1.7
	(2.07 - 1.999) [a]	(1.757 - 1.696)	(1.864 - 1.8)	(1.761 - 1.7)
Space group	P 1 21 1	P 1 21 1	P 1 21 1	P 1 21 1
Unit cell a (Å), b (Å), c (Å)	83.2 103.1 84.6	82.4 100.9 84.5	83.4 103.4 84.5	82.4 100.8 84.5
α (°), β (°), γ (°)	90 98.6 90	90 98.2 90	90 98.8 90	90 98.3 90
Wavelength (Å)	1.1	1.1	1.1	1.1
Total reflections	351229	493178	491894	302576
Unique reflections	94086 (9055)	146946 (13835)	130939 (12866)	123645 (4762)
Multiplicity	3.7	3.4	3.8	2.4
Completeness (%)	0.89	0.90	0.93	0.78
Average $I/\sigma(I)$	8.44 (1.0)	18.3 (2.1)	13.3 (1.17)	24.8 (1.94)
Wilson B-factor	17.16	16.04	15.85	21.28
R_{merge} [b]	0.155 (0.989)	0.066 (0.601)	0.106 (0.985)	0.041 (0.225)
Refinement				
Reflections used for refine	85049 (6762)	136737 (10939)	121449 (9954)	117430 (4153)
Reflections used for R_{free}	1817 (150)	1865 (154)	1887 (159)	1889 (64)
R_{work} [c]	0.1690 (0.3164)	0.1396 (0.2432)	0.1450 (0.3050)	0.1428 (0.2236)
R_{free} [d]	0.2092 (0.3300)	0.1693 (0.2719)	0.1751 (0.3174)	0.1774 (0.2568)
Number of non-hydrogen	12143	12272	12528	12050
macromolecules	10767	10799	10799	10767
ligands	36	66	36	36
Protein residues	1413	1413	1413	1413
RMSD (bond length) (Å)	0.003	0.008	0.005	0.005
RMSD (angles) (°)	0.56	0.90	0.70	0.75
Ramachandran favored (%)	97	97	98	97
Ramachandran allowed (%)	2.7	2.2	2.1	2.4
Ramachandran outliers (%)	0.5	0.57	0.29	0.43
Rotamer outliers (%)	1.3	1.7	1	1.8
Clashscore	1.52	1.47	0.74	1.48
Average B-factor (Å^2)	28.67	26.96	24.93	32.67
macromolecules	28.07	26.06	23.64	32.06
ligands	23.70	21.20	20.32	24.47
solvent	33.61	34.16	33.27	38.17
Number of TLS groups	13	13	12	15

[a] All values in parentheses are given for the highest resolution shell.

[b] $R_{\mathrm{merge}} = \sum_{hkl}\sum_i \left| I_i(hkl) - \bar{I}_i(hkl) \right| / \sum_{hkl}\sum_i I_i(hkl)$, with i running over the number of independent observations of reflection hkl.

[c] $R_{\mathrm{work}} = \sum_{hkl} \left\| I_o(hkl) \right| - \left| I_c(hkl) \right\| / \sum_{hkl} \left| I_o(hkl) \right|$.

[d] $R_{\mathrm{free}} = \sum_{hkl \in T} \left\| I_o(hkl) \right| - \left| I_c(hkl) \right\| / \sum_{hkl \in T} \left| I_o(hkl) \right|$, where T is a test data set randomly selected from the observed reflections prior to refinement. Test data set was not used throughout refinement and contains a minimum of 2000 unique reflections (or 5%) (the smaller value is selected).
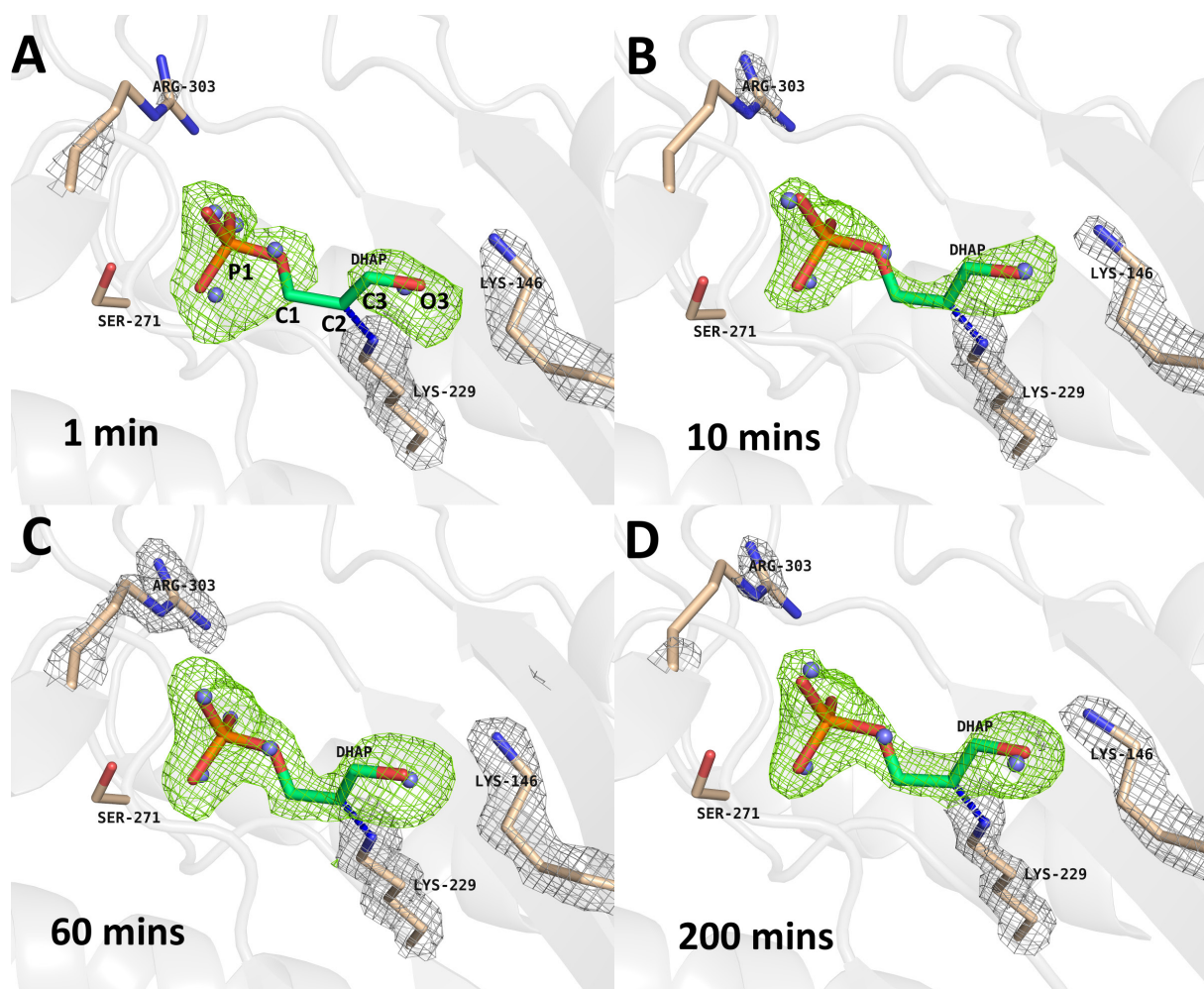
Figure 4-2. Difference density maps of aldolase soaked with DHAP for increasing time periods.

DHAP-soaked aldolase crystals were flash-frozen after incremental time intervals, trapping intermediate states, shown in **A-D**. The *green* density depicts active site simulated annealing (SA) $F_o - F_c$ omit maps contoured at 3σ. Densities colored *grey* illustrate $2F_o - F_c$ maps of critical active site residues (Lys-229, Lys146, and Arg-303) and is contoured at 1.5σ. DHAP was modeled as a covalent enamine intermediate bound to Lys-229 (*blue dashes*). To account for incomplete densities of DHAP in the active site, water molecules (*blue spheres*) were modeled at positions coinciding with the oxygen atoms of the DHAP and partial occupancies were refined in Phenix. Refined DHAP accounts for 40% of the density in the active site after 1 minute (**A**) and close to 80% after 60 minutes (**C**). All structures were refined using the same refinement protocol.

Once the structures were fully refined, simulated annealing omit maps were calculated as a way of reducing phase bias prior to ligand fitting and interpretation. Continuous electron density, extending beyond Lys-229 Nζ in each subunit, seen plainly in **Figure 4-2C**, indicates formation of a stable covalent bond with the DHAP C2 carbon. The tetrameric nature of aldolase affords the opportunity to make 4 independent observations. Subunit D is selected for illustration purposes (**Figure 4-2**) as the observations are most striking in this particular subunit. The planar shape of the electron density observed about the DHAP C2 carbon indicates trigonal hybridization, whereas non-planar shape of the electron density about Lys-229 Nζ atom suggests tetrahedral hybridization and is consistent with trapping of an enamine intermediate in each aldolase subunit (51). Another indication of enamine trapping is the presence of an additional hydrogen bond between Ser-300 hydroxyl and Lys-229 Nζ which specifically stabilizes the enamine intermediate and is not possible in the carbanion or the iminium that require sp_2 hybridization at Lys-229 Nζ. Finally, conclusive discrimination was possible by comparing real-space correlation coefficients, a measure of electron density fitness, for covalently bound DHAP modeled as enamine or iminium. Phenix performs bulk-solvent correction and scaling on the data and calculates a likelihood-weighted $2F_o - F_c$ map which is compared to a map calculated from the model alone, and correlation coefficients are calculated on a residue basis. The discrimination in hybridization between the iminium and the enamine was quantified using a paired *t*-test comparing the two forms for identical subunits and the enamine was discriminatory with a $p \leq 0.05$.

The structure incubated with DHAP for 1 minute (*DHAP-1min*) (**Figure 4-2A**) reveals signs of fracturing density at the C1 atom of DHAP, similar to the preliminary structure shown in **Figure 4-1**. However, when a phosphate oxyanion is refined in the active site at the P1-phosphate locus, a positive density peak in the $F_o - F_c$ map persists at the site between the C1 and C2 atoms of DHAP, suggesting the presence of partially occupied DHAP in the active site. Likewise, if DHAP is refined at full occupancy (i.e. occupancy of 1.0), a negative peak in the $F_o - F_c$ map appears at the same position between the C1 and C2 atoms, suggesting that DHAP is not fully occupied in the active site. Moreover, we set the occupancy of DHAP at a value of 0.5 in order to evaluate whether a reduced DHAP population can alone account for the density in the active site. Although there were no difference peaks at the C1 and C2 positions in the map, positive density appeared at the P1-site, suggesting that DHAP density alone at 0.50 does

not fully explain the density observed at the P1 locus. Rather, it is suggestive of a mixture of molecules at the P1-site. The same observation as above was made for the O3 hydroxyl site (**Figure 4-2A**). We investigated the control structure consisting of non-soaked aldolase.

When the *DHAP-1min* structure is superposed with the control structure (**Figure S4-1**), we noted the presence of water molecules all within ≤ 1 Å of the oxygen atoms on the DHAP phosphate group. The four oxygens (O11 – O14 in **Figure S4-1**) of the phosphate moeity and the O3 hydroxyl oxygen are on average 0.66 ± 0.28 Å from a water molecule at the same location in the native structure. Superposition was also performed with a previously reported native aldolase structure (PDB id: 1ZAH) and a similar observation was made, supporting our mixture hypothesis. In order to test this hypothesis, water molecules were juxtaposed onto the five oxygen atoms in DHAP (**Figure 4-2** – *blue spheres*). Starting occupancies of 0.50 were ascribed to both the DHAP enamine and the water molecules in the model. Occupancies were refined in Phenix until they stabilized and no longer fluctuated. Accordingly, an increase in DHAP occupancy was observed when the density spanning the carbon atoms on the DHAP was more prominent, as shown in **Figure 4-2A-C**.

The best agreement (lowest *R*-factor scores) between the data and the model was reached by refining a mixture of DHAP and water molecules. The same method was applied for the *DHAP-10mins*, *DHAP-60mins*, and *DHAP-200mins* models. The final models and their simulated annealing omit maps are shown for subunit D (**Figure 4-2**) and for all four subunits (**Figure S4-2**). Qualititative inspection of the omit maps in the active site shows a progressive increase in the density adjoining the C1 and C2 atoms that peaks at 60 minutes with a subsequent decrease at 200 minutes. This trend was observed in all four subunits and was most apparent in subunit D. Subunit A is systematically the most populated, showing almost full occupancy at 10 minutes (**Figure S4-2**). Additionally, since DHAP-enamine is fully occupied at 60 minutes in subunit A, the juxtaposed water molecules were rejected from the refinement (i.e. 0% occupancies).

We quantified this phenomenon by examining the DHAP occupancy as a fucntion of time. Its occupancy systematically increases from 0.53 ± 0.07 (average of four subunits) in *DHAP-1min* to 0.84 ± 0.11 in *DHAP-60mins* and is significant with a $p \leq 0.01$ ** (paired Student's *t* test) (**Figure 4-3**). Subunit A exhibits the highest occupancy of DHAP in every structure, starting at 0.58 in *DHAP-1min*, and increasing to 0.84 and 1 in *DHAP-10mins* and *DHAP-60mins*
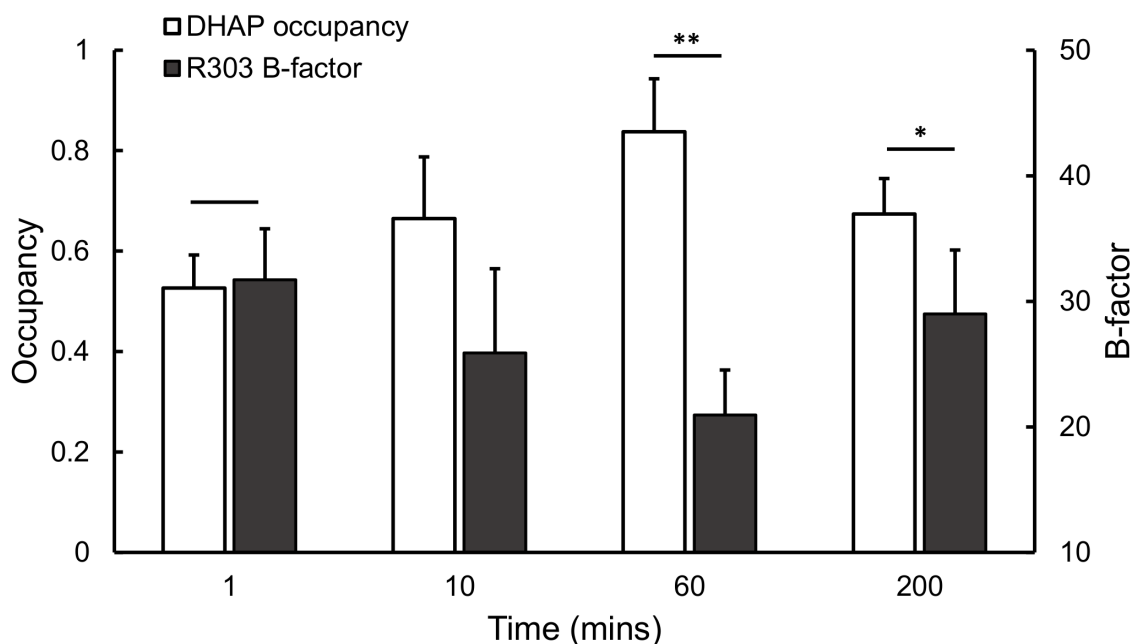
Figure 4-3. Occupancy and Temperature factor variability as a function of DHAP soak time.

Occupancy (*open bars* – left axis) of DHAP-enamine modeled in the active site of aldolase is plotted as a function of soaking time. Occupancy increases steadily from 1 minute to 60 minutes ($p \leq 0.01$ [**]) and decreases thereafter as per the 200-minute model ($p \leq 0.05$ [*]). B-factor (*dark bars* – right axis) of Arg-303 drops from 1 minute to 60 minutes ($p \leq 0.01$ [**]) but increases thereafter ($p \leq 0.01$ [**]). See text for more detail. Data bars shown as mean ± SD over the four subunits of aldolase.

respectively. The occupancies in subunit D are systematically the lowest of the four subunits, increasing slowly from 0.43 in *DHAP-1min* to 0.73 in *DHAP-60mins*. The *DHAP-200mins* model exhibits a reversal of trend as the occupancies in all four subunits drop notably to an average of 0.67 ± 0.07 from the previous 0.84 ± 0.11 average noted in *DHAP-60mins* with a *p* ≤ 0.05 [*] (**Figure 4-3**). To validate the observations in the *DHAP-60mins* and *DHAP-200mins* structures, duplicate independent datasets were collected, and the drop in occupancy was confirmed (eg. the mean occupancy in datasets 1 and 2 for 200 minutes were 0.67 ± 0.07 and 0.69 ± 0.08). The occupancy of juxtaposed water molecules is predictably inversely proportional to the DHAP occupancy, as they are mutually exclusive.

The increase in occupancy of the DHAP can also be expressed by the temperature factor (B-factor) of Arg-303, which is responsible for fixing the phosphate group at the P1-site. Previous structural data show that Arg-303 side-chain exhibits a significant conformational change into

the active site cleft that is triggered by substrate binding at the P1-site. The Arg-303 guanidinium group forms a salt bridge with the P1-phosphate of all incoming substrates. In the absence of substrate, Arg-303 has high flexibility, reflected in a B-factor and lack of electron density around the side-chain. When substrate binds, Arg-303 fixes the P1-phosphate and its B-factors drop. The Arg-303 B-factors are therefore inversely proportional to the DHAP occupancy, which is precisely observed in the four structures (**Figure 4-3** - *dark bars*). As the occupancy increases from 1 minute to 60 minutes, the average B-factor drops from 32 ± 4 Å^2 to 21 ± 4 Å^2 ($p \le 0.01$ **). Likewise, the B-factor increases to 29 ± 5 Å^2 at 200 minutes ($p \le 0.01$ **), synchronously with the decrease in the DHAP occupancy.

Enzymatic determination of MGO production by Aldolase. We also sought to characterize the enzymatic production of MGO by aldolase *in vitro.* Following the glyoxalase method for determination of MGO in solution (discovered by Racker (38) and applied by Davis and Williams (37)), aldolase was incubated with substrate for defined periods of time, the reaction was quenched, and MGO was converted to s-D-lactoylglutathione for spectrophotometric determination at 240 nm.

Experimental conditions were optimized to account for the incubation period and the concentration of substrate (**Figure S4-3** for details). Another concern was the continued production of MGO from aldolase during the glyoxalase assay – thus a quenching step was imperative to limit continued generation of MGO from aldolase during the quantification assay. Since quenching by acidification was shown to promote P$_i$ release, we chose to flash-heat samples prior to MGO quantification to inactivate aldolase. Samples were centrifuged to remove precipitated protein and MGO in the supernatant was quantified by the glyoxalase assay. The supernatant showed no activity for aldolase in samples containing 1 or 10 μg of aldolase.

The linearity and range of the detection assay was established using a 96-well set-up. The standard curve was shown to be well correlated and reproducible in the range of $10 - 500$ μM of MGO (**Figure 4-4A**). MGO concentrations below 10 μM in the 96-well plate were indistinguishable from the noise in the assay.

To identify residue(s) responsible for the β-elimination reaction, the production of MGO from aldolase was assayed across the pH spectrum (**Figure 4-4B**). The results indicate low levels of MGO production at acid pHs (4 – 5) with a sharp increase, reaching a maximum at pH 8.0, and
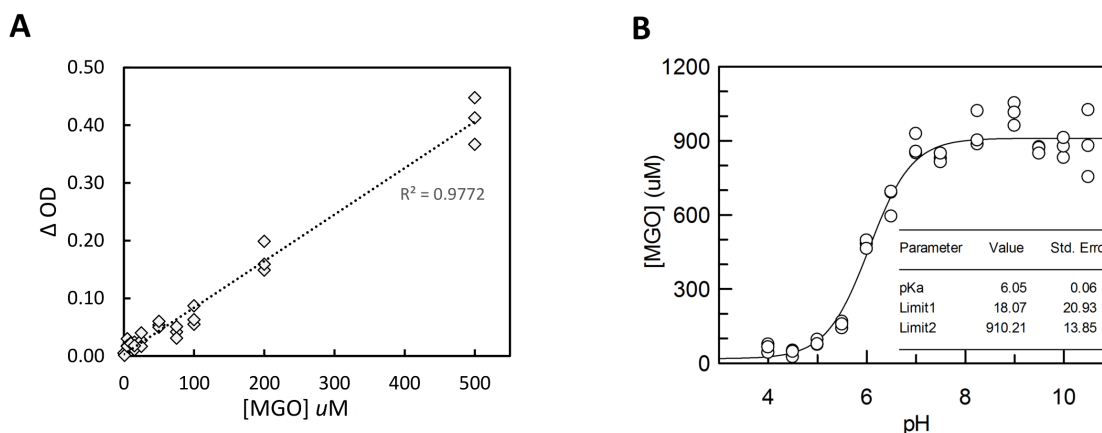
Figure 4-4. pH profile of MGO generated from FBP in the presence of aldolase.

(A) Illustrates the range of the glyoxalase enzyme assay. Known [MGO] were used to evaluate the accuracy of the assay. Values below 10 uM are at the noise limit of the assay, whereas values above 500 uM are outside the linear range. When the ΔOD remains below 0.5, the assay is linear (R^2 = 0.98), requiring dilution prior to quantification of samples for which [MGO] > 500 uM. Data for n = 3. **(B)** MGO formation in the presence of 10 ug of aldolase was determined over a broad range of pHs. The reaction was quenched by flash-heating and centrifugation. A peak [MGO] is observed at pH ~ 8.0 (Tris-HCl). Negative controls with FBP-only exhibited baseline levels of [MGO] at all pHs. Positive controls consisting of [MGO] = 200 and 1000 uM (not shown) were tested at every pH and were used to normalize data at every pH in unknown samples. Data shown for n = 3.

slightly decreasing thereafter. A pK_a 6.05 ± 0.06 was calculated using a single pK_a approximation (GraFit). As the incubation of aldolase with FBP was conducted in a variety of buffers, the experiment was repeated with pH-adjusted Tris-Acetate buffers to eliminate variable generation of MGO influenced by the use of different buffers. A pH range of 5 – 9 at 50 mM was tested and generated the same pK_a. For all subsequent experiments, we used Tris-Acetate at pH 8.0.

Triose-phosphate trapping experiments. To further our understanding of the role of aldolase in MGO production and its importance from a biological perspective, we sought to recreate the metabolic environment *in vitro*. It is primordial to discriminate between production from a catalytic activity in aldolase and triose-phosphate decomposition. If MGO produced in the presence of aldolase is primarily generated by a catalytic decomposition, then limiting the generated pool of triose-phosphates from the cleavage of FBP by aldolase should provide the
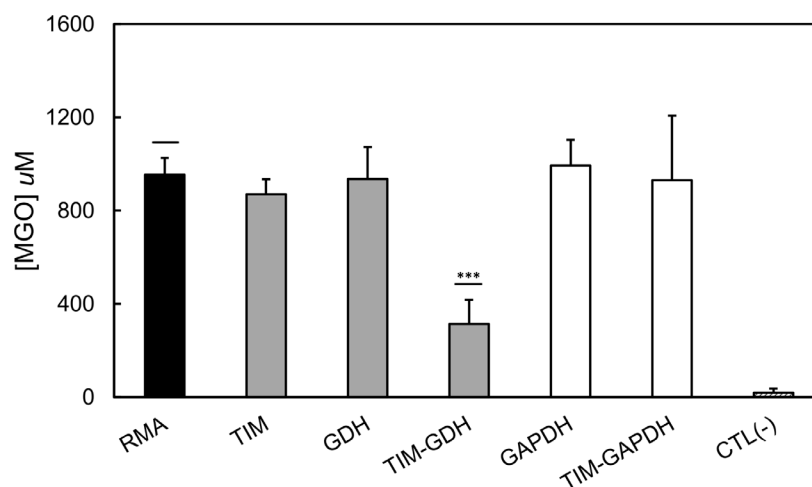
Figure 4-5. MGO generated in the presence of aldolase and associated metabolic enzymes.

FBP (4 mM) was incubated with 2 ug (0.02 U) of aldolase (*black*), or with a combination of aldolase and an excess of the auxiliary enzyme(s) shown below each bar (*grey and white*) for a period of 30 minutes prior to flash-heating and MGO determination by the glyoxalase enzyme assay. TIM is supplemented at 1 - 10 U/assay; GDH at 0.6 - 1.2 U/assay; and GAPDH at 0.1 - 0.2 U/ assay. Samples comprising GDH or GAPDH were supplemented with excess of 7 mM NADH or NAD^+ (cofactor) respectively. Also, GAPDH activity was optimized with the addition of 0.05 M sodium arsenate. The negative control [CTL (-)] consisted of an FBP-only sample. A positive control (not shown) consisted of an MGO standard that received the same treatment as the samples. The only treatment with a notable reduction consisted of aldolase mixed with TIM-GDH which produced a more than 2-fold decrease in detected MGO (p-value ≤ 0.0001 [***]) with respect to the aldolase-only sample (*black*). All other sample mixtures showed no significant differences with respect to the aldolase-only incubation. Data represent n $\geq$ 5 and are shown as mean $\pm$ SEM. Abbreviations: RMA, rabbit muscle aldolase; TIM, triosephosphate isomerase; GDH, glycerol-3-phosphate dehydrogenase; GAPDH, glyceraldehyde-3-phosphate dehydrogenase.

necessary discrimination. This was accomplished by supplementing the incubation mixture with downstream enzymes involved in the conversion of triose-phosphates. These include: glyceraldehyde-3-phosphate dehydrogenase (GAPDH) which converts G3P to 1,3-bisphosphoglycerate (BPG) (glycolysis), and glycerol-phosphate dehydrogenase (GDH) which catalyzes the conversion of DHAP to glycerol-3-phosphate (lipid biosynthesis). The result of these experiments are illustrated in **Figure 4-5** and showed a significant decrease in MGO production in the presence of TIM-GDH.

Evaluation of quenching methods. A concern from previous studies is the quenching step after the incubation period. To minimize artifacts introduced by the acidification process that promote P_i + MGO release from aldolase, heat quenching was applied to inactivate the reaction. However, additional controls revealed that flash-heating introduces significant artifacts. 1 min of flash-heating at 95 ^{o}C indeed fully inactivated the enzyme, but the triose-phosphates (DHAP and G3P) showed accelerated decomposition at these elevated temperatures. To overcome this dilemma, an anion exchange resin was employed (Dowex 1x4-200) to remove phosphate derived metabolites (FBP, DHAP, and G3P) prior to inactivation by either acid or heat quenching. Controls exhibited full removal of phosphate substrates when treated with a 50 % Dowex slurry. TCA (5 %) was tested for its ability to inactivate aldolase (2 μg). A short treatment followed by immediate centrifugation to remove precipitates was effective for inactivation of the enzyme. The supernatant was assayed for MGO. For increased sensitivity of the enzyme assay, we opted for spectrophotometric measurements using quartz cuvettes. Controls with MGO standards exhibited a clear linear response ($R^2 = 0.998$) for values of [MGO] ranging from 20 – 200 μM.

TCA treatment alone without prior removal of phosphate substrates with the anion exchanger generated quantities of MGO that were two-fold less than with heat quenching in an experiment involving 4 mM FBP mixed with 2 μg of aldolase for 30 minutes (527 ± 51 μM with heat quenching versus 197 ± 15 μM with TCA quenching) (**Figure 4-6**). This was the first indication that heat quenching might be introducing an artefact into the experiment. Because of the concerns related to triose-phosphate stability, we applied the anion exchanger as the first step to remove all phosphate derived substrates (triose-phosphates and FBP) from the mixture before quenching. Overall, we observed an average of 31 ± 6 μM MGO generated in the presence of aldolase using anion exchange/TCA quenching, and 25 ± 6 μM MGO using anion exchange/ heat quenching (**Figure 4-6**). However, there was no significant difference in both cases when compared to negative controls (22 ± 11 μM) ($p \geq 0.05$).
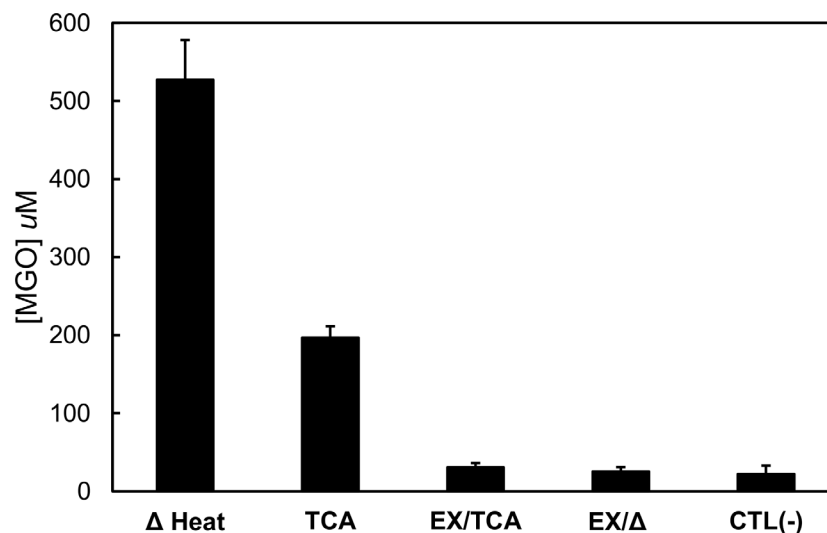
Figure 4-6. Comparison of quenching methods.

A mixture consisting of aldolase and FBP in 50 mM TRIS-acetate pH 8.0 was incubated for 30 minutes and subjected to different quenching methods including heat, 10 % tetrachloroacetic acid (TCA), or a combination of anion exchange followed by TCA (EX/TCA) or heat (EX/Δ) (see Experimental section for more details). Data for the heat and TCA treatment represents 2 ug of aldolase and 4 mM of FBP. Data for EX/TCA, EX/Δ and CTL(-) represents 5 ug of aldolase mixed with 10 mM of FBP. The negative control consisted of a sample with FBP in the absence of aldolase. Shown is for the treatment with EX/TCA. Negative controls for heat and TCA are not shown but yield comparable values. Data represent mean ± SEM for n ≥ 5.

EnzCheck phosphate detection assay. In order to address concerns related to the sensitivity of the glyoxalase assay in tested conditions, we sought an alternative method for measuring production of MGO – the EnzCheck phosphate assay, which measures inorganic phosphate (P_i) concentrations in a sample as low as 2 μM. P_i released during enzymatic or non-enzymatic MGO formation from triose-phosphates indirectly indicates the amount of MGO in the sample. Therefore, mixtures comprising aldolase and substrate were incubated and samples were withdrawn periodically to determine P_i levels. To eliminate artefacts introduced by quenching, the P_i quantification assay was performed immediately after withdrawing samples to minimize contamination of P_i produced post-incubation.

P_i levels remained constant and at baseline levels for FBP-only samples in the absence of aldolase up to 5 hours (**Figure 4-7A**). However, when aldolase was added to the mixture, P_i levels increased linearly over the 5-hour period at a rate of 27 μM/hour (**Figure 4-7A**). In order

to address the issue of spontaneous decomposition of triose-phosphates, samples comprising either DHAP or G3P were tested for phosphate production over the 5-hour period. In the absence of aldolase, DHAP exhibited a steady increase of phosphate release at a rate of 39 μM/hour (**Figure 4-7B**). The presence of aldolase in the mixture had no influence on the rate of phosphate release. Further, there appears to be a background level of Pi since at $t = 0$ mins, $[P_i] \sim 400 \, \mu$M, which represents 4 % of the initial DHAP concentration in the sample (10 mM).

Likewise, G3P was assayed for phosphate release in the presence and absence of aldolase. G3P alone exhibited a greater rate of P_i release (88 μM/hour) compared to DHAP (**Figure 4-7C**). Again, the presence of aldolase had no influence on P_i production. The initial concentration ($t = 0$ mins) of P_i is also relatively high, suggesting the presence of background P_i in the starting sample. **Figure 4-7D** summarizes the rate of increase in $[P_i]$/min for each of the samples.

As aldolase is known to bind P_i, aldolase was mixed with starting concentrations (50 and 100 μM) of a P_i standard and samples were withdrawn over 3 hours. Aldolase indiscriminately decreased the expected P_i concentration by an average of $\sim 5 \, \mu$M for all time points. Therefore, little to no influence by non-specific binding of aldolase to P_i is expected in the experimental samples. Finally, to assess the specificity of aldolase with respect to influencing phosphate release with the different substrates, each of the samples (in **Figure 4-7**) was conducted with bovine serum albumin (BSA). In each case, BSA has no influence on the progression of phosphate release when compared to the substrate-only controls (not shown).
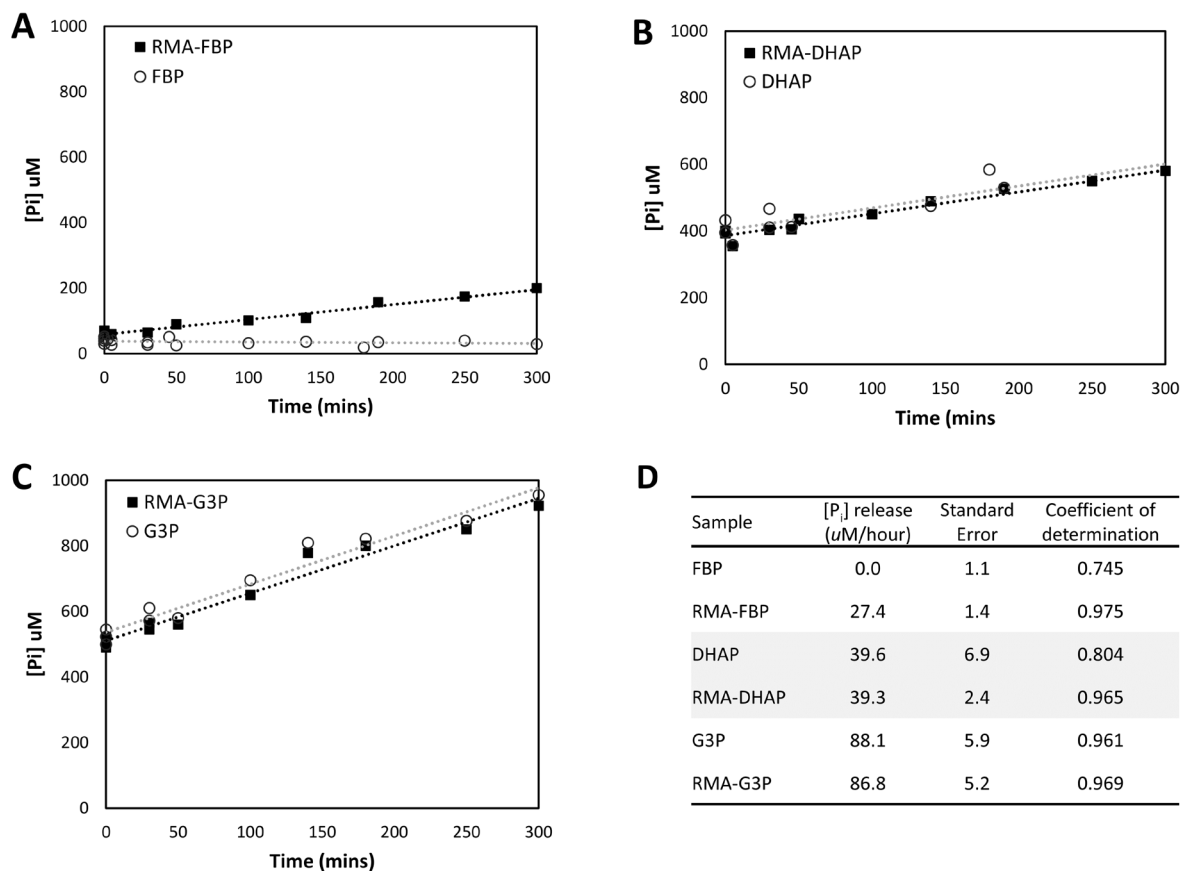
Figure 4-7. Inorganic phosphate determination from fructose-bisphosphate and triose-phosphates in the presence of aldolase.

All three graphs (**A** – **C**) illustrate measurements of P_i withdrawn from samples consisting of substrate alone (*open circles*) (negative control), or substrate in the presence of aldolase (*dark squares*). Each sample consisted of substrate at a starting concentration of 10 *m*M supplemented with 5 *u*g of aldolase. The regression analysis is shown in panel **D**. The rate of P_i release is shown in the table as the slope of the linear regression, with units of *u*M / hour (*dotted lines*). The fitness of each slope is shown in the final column of panel **D**. All data represent n ≥ 3. Abbreviations: RMA, rabbit muscle aldolase; FBP, fructose-bisphosphate; DHAP, dihydroxyacetone phosphate; G3P, glyceraldehyde-3-phosphate.

DISCUSSION

Structural investigation of MGO formation by Aldolase. In light of the preliminary findings which suggested aldolase could enzymatically generate MGO, we probed the active site with DHAP under different conditions in order to corroborate this hypothesis. This was accomplished by soaking native aldolase crystals in a solution containing DHAP and flash-freezing crystals at periodic intervals, trapping various intermediates along the secondary MGO synthase reaction pathway.

The preliminary structural data (*DHAP-frac*) indicated a possible enzymatic decomposition of DHAP, as per the evidence of phosphate oxyanion bound in the active site (**Figure 4-1**). However, the analysis of additional crystal structures in our time-course study afforded a more complete characterizaiton of the active site events. The absence of electron density contiguous with the C1-C2 atoms in the simulated annealing omit map (shown in **Figure 4-2A)** for the *DHAP-1min* structure is best described by a mixture of DHAP and five water molecules that superpose with the oxygen atoms of DHAP. The active sites become fully occupied after 60 minutes of equilibration. The length of time required to populate an active site with a substrate is dependent on a number of factors, including the affinity and the time of diffusion into the crystals. Protein crystals form by the repeat arrangment of protein molecules generating a stable lattice, often resulting in channels that allow the passage of small molecules throughout the crystal, including water, ions, and other small ligands. These crystal packing contacts are also responsible for the differential accessibility to the four subunits, accounting for the differences that are systematically observed in the four subunits (subunit A – most populated; subunit D – least populated). Visual inspection of the crystal packing interface bordering the active site in subunit A reveals an uninterupted access to the active site. The C-terminal region, involved in forming the covalent DHAP-enamine intermediate (51) binds at a secondary distal site bordering the subunit interface in the tetramer. However, in subunit D, the crystal packing contacts preclude the binding of the C-terminus at the secondary site, and the C-terminus remains folded over the active site, competing with DHAP for active site access. The accessibility in subunits B and C appears slightly greater compared to subunit A.

In light of our purported occupancy model, we can appropriately address inconsistencies with the *DHAP-frac* structure (**Figure 4-1**). Comparison of our time-course structures with the

preliminary DHAP-soaked crystal structure reveals a slight nuance with the position of Lys-146 in *DHAP-frac*. Lys-146 of *DHAP-frac* changes conformation to come within 1.2 Å of the DHAP O3 atom (seen in **Figure 4-1D**). This is noteworthy as it precludes modeling of DHAP-enamine, suggesting that the density observed between Lys-229 Nζ atoms and Lys-146 in *DHAP-frac* cannot be a mixture of DHAP and water molecules. As per **Scheme 4-2**, β-elimination of the phosphate does not result in active site release of MGO. A covalent intermediate (**2** from **Scheme 4-2**) remains bound at Lys-229, which must undergo hydrolysis before being released as MGO. Grazi et al. (1978) first proposed that the P_i derived from β-elimination remains tightly bound and is in rapid equilibrium with the enamine (**1** from **Scheme 4-2**) (26). A Ser-271 variant (S271A) that no longer tethers the P1-phosphate exhibits increased P_i release and is consistent with Grazi's proposal (30). Therefore, we envisaged the possibility that the intermediate **2** of **Scheme 4-2** is susceptible to nucleophilic attack by Lys-146, forming an unspecified bi-covalent adduct. We tested this hypothesis by modeling and refining numerous hypothetical covalent adducts that could result from an attack on the carbonyl of intermediate **2**. However, none of the tested candidates produced a stable refinement, likely because the distance between the two lysines is too short to accommodate a covalent adduct. Modeling water molecules at full occupancy near the DHAP O3 site and the P1-site is the most plausible explanation, with perhaps a residual population of DHAP.

Finally, to address the decrease in DHAP occupancy observed passed 60 minutes, two possibilities can be invoked. First, the concomitant decrease in DHAP occupancy and increase in Arg-303 B-factor in the *DHAP-200mins* structure (**Figure 4-3**) suggest a substrate turnover in the active site. Biochemical analyses revealed that DHAP populates all four active site until near full occupancy is achieved, followed by indefinite stabilization (52). Early on, we postulated that a C-terminal tyrosine (Tyr-363) performed the base-catalyzed β-elimination that releases P_i. Based on this hypothesis, we expected a higher turnover to MGO in subunit D where the C-terminus has access to the active site in the crystal packing structure. This could provide a rationale for the lower DHAP occupancy that is systematically observed in subunit D. Second, we cannot exclude the possibility that DHAP decomposition in the crystallographic solution may account for the decrease in DHAP population – but given a decomposition rate of 2% / 5h, this seems improbable. Nevertheless, the composition of the crystallographic buffer may influence DHAP stability.

Enzymatic investigation of MGO production by Aldolase. A foremost objective of this study was to demonstrate the enzymatic contribution to MGO production by aldolase. Prior to structural data, the aldolase reaction pathway was elucidated by biochemical studies that classically involved acid quenching with high concentrations of HCl or TCA and quantification of radioactively labeled substrate from the pellet or supernatant. This was pivotal in establishing the partitioning of intermediates and equilibriums in the reaction pathway. The potential for MGO synthase activity in aldolase was discovered through these studies. Yet, as P_i production appeared related to the acidification process, the relevance in physiological conditions was never explored. Acidification likely makes the phosphate oxyanion a better leaving group by disrupting the salt bridge it forms with Arg-303. We sought to address this question by testing MGO generation in a physiologically relevant context. If aldolase generates MGO as a side-product during glycolysis, it necessarily uses FBP as the substrate; therefore, aldolase was mixed with FBP and the reaction was quenched by flash-heating/cooling, followed by centrifugation to remove inactivated enzyme.

The glyoxalase enzyme assay was selected for quantification of MGO. Since P_i derived from β-elimination requires proton abstraction of the O3 hydroxyl proton, a pH profile was measured to evaluate potential candidates for proton abstraction (**Figure 4-4**). The recent discovery of the catalytic activity of C-terminal Tyr-363 in facilitating the stereospecific proton exchange at DHAP C3 atom argued in favor of Tyr-363 as the base responsible for β-elimination, as a small libration (1Å) brings the phenolate in proximity to the DHAP O3 hydroxyl (51). The neighboring Lys-146 provides electrostatic stabilization of the developing charge on the phenolate. We calculated a pK_a of 6 from the pH profile with a maximum near 8. Yet, the authors proposed a $pK_a > 9$ for the basic group involved in proton abstraction of the C3 proton. According to the pH activity profile, this would require a downshift of Tyr-363 pK_a to an acidic value that could be facilitated by its proximity to Lys-146, which has been shown to remain protonated throughout the catalytic cycle (33). However, Tyr-363 is activated by an invariant water molecule that is itself activated by the P1 phosphate dianion ($pK_a \sim 6.45$ (53)), supporting a role for the phosphate oxyanion as the conjugate base catalyzing proton transfer relayed through the invariant water molecule – explaining the observed pK_a.

Also involved in several steps of the reaction mechanism is Glu-187, which has an estimated pK_a of 5 – 6 in aldolase. However, it is not within range to induce proton abstraction of the O3

hydroxyl ($\sim 4 - 5\text{Å}$ away). Finally, Asp-33, a conserved residue in class I aldolases, hydrogen bonds the O3 hydroxyl and stabilizes the positive charge on Lys-146. It is highly acidic, and only in circumstances of acidification (i.e. acid quenching – TCA) is a proton transfer between Asp-33 and DHAP O3 hydroxyl possible. This could explain the increase in P_i expulsion observed in previous studies upon acidification of samples.

When downstream metabolic enzymes are supplemented to the aldolase-substrate mixture (**Figure 4-5**), a marked reduction in MGO production is observed in the presence of TIM and GDH. TIM interconverts the triose-phosphates. GDH uses DHAP as a substrate whereas GAPDH uses G3P. If indeed aldolase enzymatically generates MGO, the addition of downstream enzymes should have negligible effects on this production. However, if the MGO generated stems primarily from spontaneous decomposition of triose-phosphates, then trapping the latter with an excess of these enzymes would minimize this effect. Since no reduction is observed with GDH but a reduction is observed when TIM and GDH are supplemented together, it suggests that spontaneous decomposition by G3P is significant. Supplementing GAPDH should recapitulate the same effect. However, we could not confidently demonstrate this since the NAD required for GAPDH activity introduced significant background fluorescence.

The interpretation of **Figure 4-4** and **Figure 4-5** was revisited in light of the different quenching methods. It was demonstrated that flash-heating could introduce an artefact greater than acidification (**Figure 4-6**). If MGO generated in the presence of aldolase makes an important enzymatic contribution, then removing phosphate derived metabolites from the mixture prior to quenching should have little effect on the measured MGO. However, when samples are filtered with an anion exchange resin prior to quenching with either acid or heat, the quantity of MGO measured drops to baseline levels, suggesting that the bulk of MGO generated in the presence of aldolase originates from non-enzymatic triose-phosphate decomposition. It suggests that MGO observed in flash-heated samples is reflecting the *in vitro* triose-phosphate pool. We sought to corroborate this finding with an alternative detection system, the EnzCheck phosphate detection assay.

In order to directly address the decomposition of the triose-phosphates, tests were conducted to assess the solution stability of DHAP and G3P in a time-course experiment. After 5 hours at room temperature, $\sim 2\ \%$ of the starting DHAP, and $\sim 4\ \%$ of the starting G3P was shown to decompose, releasing P_i (**Figure 4-7**). On the other hand, FBP-only showed no signs of

164

decomposition. However, P_i was observed in aldolase-treated FBP samples, indicating that P_i is being produced either enzymatically or non-enzymatically from the triose-phosphates that accumulate as aldolase cleaves FBP. If aldolase generates MGO and P_i from FBP, it is presumably via the intermediary of the covalent DHAP-enamine. No difference is observed in the rate of P_i release for DHAP-only samples compared to aldolase-treated samples, suggesting that P_i produced from a mixture of FBP and aldolase originates primarily from non-enzymatic decomposition of the generated triose-phosphates.

In light of the above findings, alternate interpretations of the pH MGO production profile (**Figure 4-4**) are possible. Under conditions of optimal rabbit muscle aldolase activity (pH 7 – 9), we expect the highest turnover of FBP to triose-phosphates (54). It is therefore plausible that the MGO produced as a function of pH is sampling the triose-phosphate pool generated from triose-P decomposition to MGO, and is accelerated by the heat quenching. Another factor complicating interpretation of these results is the alkaline instability of triose-phosphates, as previously demonstrated by Rose (27).

CONCLUSION

We confirmed that enzymatic generation of MGO by aldolase is negligible compared to spontaneous decomposition of triose-phosphates. These observations are in agreement with other findings that discount the contribution of aldolase to MGO production. For example, MGO release can be suppressed by protection with an aldehyde acceptor (G3P) (55). Yet, if acidification promotes MGO production from aldolase, physiological environments that favor such conditions should be evaluated for increased MGO levels. Altogether, a better understanding of MGO metabolism is critical for developing strategies to mitigate the clinical manifestations of MGO-derived pathologies.

REFERENCES

1. Brownlee M. Biochemistry and molecular cell biology of diabetic complications. Nature. 2001 Dec 13;414(6865):813–20.

2. Chang T, Wu L. Methylglyoxal, oxidative stress, and hypertension. Can J Physiol Pharmacol. 2006 Dec 1;84(12):1229–38.

3. Baynes JW, Thorpe SR. Glycoxidation and lipoxidation in atherogenesis. Free Radic Biol Med. 2000 Jun 15;28(12):1708–16.

4. Dukic-Stefanovic S, Schinzel R, Riederer P, Münch G. AGES in brain ageing: AGE-inhibitors as neuroprotective and anti-dementia drugs? Biogerontology. 2001;2(1):19–34.

5. Kuhla B, Lüth H-J, Haferburg D, Boeck K, Arendt T, Münch G. Methylglyoxal, Glyoxal, and Their Detoxification in Alzheimer's Disease. Ann N Y Acad Sci. 2005 Jun 1;1043(1):211–6.

6. Reddy VP, Obrenovich ME, Atwood CS, Perry G, Smith MA. Involvement of maillard reactions in Alzheimer disease. Neurotox Res. 2002 Jan;4(3):191–209.

7. Yu PH. Involvement of cerebrovascular semicarbazide-sensitive amine oxidase in the pathogenesis of Alzheimer's disease and vascular dementia. Med Hypotheses. 2001 Aug;57(2):175–9.

8. Desai KM, Chang T, Wang H, Banigesh A, Dhar A, Liu J, et al. Oxidative stress and aging: Is methylglyoxal the hidden enemy? Can J Physiol Pharmacol. 2010 Mar;88(3):273–84.

9. Thornalley PJ. The glyoxalase system in health and disease. Mol Aspects Med. 1993;14(4):287–371.

10. Wu G, Fang Y-Z, Yang S, Lupton JR, Turner ND. Glutathione Metabolism and Its Implications for Health. J Nutr. 2004 Mar 1;134(3):489–92.

11. Cooper RA. Metabolism of Methylglyoxal in Microorganisms. Annu Rev Microbiol. 1984;38(1):49–68.

12. Kalapos MP. Methylglyoxal in living organisms: chemistry, biochemistry, toxicology and biological implications. Toxicol Lett. 1999 Nov 22;110(3):145–75.

13. Leoncini G. The role of alpha-ketoaldehydes in biological systems. Ital J Biochem. 1979 Aug;28(4):285–94.

14. Kalapos MP. Where does plasma methylglyoxal originate from? Diabetes Res Clin Pract. 2013 Mar;99(3):260–71.

15. Casazza JP, Felver ME, Veech RL. The metabolism of acetone in rat. J Biol Chem. 1984 Jan 10;259(1):231–6.

16. Yu PH, Wright S, Fan EH, Lun Z-R, Gubisne-Harberle D. Physiological and pathological implications of semicarbazide-sensitive amine oxidase. Biochim Biophys Acta BBA - Proteins Proteomics. 2003 Apr 11;1647(1–2):193–9.

17. Beisswenger PJ, Howell SK, O'Dell RM, Wood ME, Touchette AD, Szwergold BS. α-Dicarbonyls Increase in the Postprandial Period and Reflect the Degree of Hyperglycemia. Diabetes Care. 2001 Apr 1;24(4):726–32.

18. Liu J, Desai K, Wang R, Wu L. Up-regulation of Aldolase A and Methylglyoxal Production in Adipocytes. Br J Pharmacol. 2012;n/a–n/a.

19. Nemet I, Turk Z, Duvnjak L, Car N, Varga-Defterdarović L. Humoral methylglyoxal level reflects glycemic fluctuation. Clin Biochem. 2005 Apr;38(4):379–83.

20. Iyengar R, Rose IA. Liberation of the triosephosphate isomerase reaction intermediate and its trapping by isomerase, yeast aldolase, and methylglyoxal synthase. Biochemistry (Mosc). 1981 Mar 1;20(5):1229–35.

21. Richard JP. Kinetic parameters for the elimination reaction catalyzed by triosephosphate isomerase and an estimation of the reaction's physiological significance. Biochemistry (Mosc). 1991 May 7;30(18):4581–5.

22. Richard JP. Reaction of triose phosphate isomerase with L-glyceraldehyde 3-phosphate and triose 1,2-enediol 3-phosphate. Biochemistry (Mosc). 1985 Feb 1;24(4):949–53.

23. Richard JP. Acid-base catalysis of the elimination and isomerization reactions of triose phosphates. J Am Chem Soc. 1984 Aug 1;106(17):4926–36.

24. Phillips SA, Thornalley PJ. The formation of methylglyoxal from triose phosphates. Investigation using a specific assay for methylglyoxal. Eur J Biochem FEBS. 1993 Feb 15;212(1):101–5.

25. Richard JP. Mechanism for the formation of methylglyoxal from triosephosphates. Biochem Soc Trans. 1993 May;21(2):549–53.

26.   Grazi E, Trombetta G. A new intermediate of the aldolase reaction, the pyruvaldehyde-aldolase-orthophosphate complex. Biochem J. 1978 Nov 1;175(2):361–5.

27.   Iyengar R, Rose IA. Concentration of activated intermediates of the fructose-1,6-bisphosphate aldolase and triosephosphate isomerase reactions. Biochemistry (Mosc). 1981 Mar 3;20(5):1223–9.

28.   Cooper R a., Anderson A. The formation and catabolism of methylglyoxal during glycolysis in Escherichia coli. FEBS Lett. 1970 Dec 11;11(4):273–6.

29.   Hopper D j., Cooper R a. The regulation of Escherichia coli methylglyoxal synthase; a new control site in glycolysis? FEBS Lett. 1971 Mar 16;13(4):213–6.

30.   Munger C. Mécanisme enzymatique de la fructose 1,6-bisphosphate aldolase de muscle de lapin: Étude du rôle des sérinés 271 et 300 du site actif. [Montreal]: Université de Montréal; 2002.

31.   Leoncini G, Ronchi S, Maresca M, Bonsignore A. Studies on the interaction of fructose 1,6-P2 aldolase with methylglyoxal. Ital J Biochem. 1980 Aug;29(4):289–99.

32.   Berthiaume L, Tolan DR, Sygusch J. Differential usage of the carboxyl-terminal region among aldolase isozymes. J Biol Chem. 1993 May 25;268(15):10826–35.

33.   St-Jean M. High Resolution Reaction Intermediates of Rabbit Muscle Fructose-1,6-bisphosphate Aldolase: Substrate Cleavage and Induced Fit. J Biol Chem. 2005 Jun 2;280(29):27262–70.

34.   Morris AJ, Tolan DR. Site-directed mutagenesis identifies aspartate 33 as a previously unidentified critical residue in the catalytic mechanism of rabbit aldolase A. J Biol Chem. 1993 Jan 15;268(2):1095–100.

35.   Baranowski T, Niederland TR. Aldolase activity of myogen A. J Biol Chem. 1949 Sep;180(2):543–51.

36.   Racker E. Spectrophotometric measurement of hexokinase and phosphohexokinase activity. J Biol Chem. 1947 Mar;167(3):843–54.

37.   Davis KA, Williams GR. Glyoxaiase I, a lyase or an oxidoreductiye isomerase? Can J Biochem. 1969 May 1;47(5):553–6.

38.   Racker E. The mechanism of action of glyoxalase. J Biol Chem. 1951 Jun;190(2):685–96.

39. Webb MR. A continuous spectrophotometric assay for inorganic phosphate and for measuring phosphate release kinetics in biological systems. Proc Natl Acad Sci U S A. 1992 Jun 1;89(11):4884–7.

40. Otwinowski Z, Minor W. [20] Processing of X-ray diffraction data collected in oscillation mode. In: Charles W. Carter J, editor. Methods in Enzymology [Internet]. Academic Press; 1997 [cited 2015 Apr 1]. p. 307–26. (Macromolecular Crystallography Part A; vol. 276). Available from: http://www.sciencedirect.com/science/article/pii/S007668799776066X

41. Adams PD, Grosse-Kunstleve RW, Hung L-W, Ioerger TR, McCoy AJ, Moriarty NW, et al. *PHENIX* : building new software for automated crystallographic structure determination. Acta Crystallogr D Biol Crystallogr. 2002 Nov 1;58(11):1948–54.

42. McCoy AJ, Grosse-Kunstleve RW, Adams PD, Winn MD, Storoni LC, Read RJ. *Phaser* crystallographic software. J Appl Crystallogr. 2007 Aug 1;40(4):658–74.

43. Afonine PV, Grosse-Kunstleve RW, Echols N, Headd JJ, Moriarty NW, Mustyakimov M, et al. Towards automated crystallographic structure refinement with *phenix.refine*. Acta Crystallogr D Biol Crystallogr. 2012 Apr 1;68(4):352–67.

44. Emsley P, Lohkamp B, Scott WG, Cowtan K. Features and development of *Coot*. Acta Crystallogr D Biol Crystallogr. 2010 Apr 1;66(4):486–501.

45. Karplus PA, Diederichs K. Linking Crystallographic Model and Data Quality. Science. 2012 May 24;336(6084):1030–3.

46. Afonine PV, Moriarty NW, Mustyakimov M, Sobolev OV, Terwilliger TC, Turk D, et al. FEM: feature-enhanced map. Acta Crystallogr D Biol Crystallogr. 2015 Mar 1;71(3):646–66.

47. Moriarty NW, Grosse-Kunstleve RW, Adams PD. electronic Ligand Builder and Optimization Workbench (eLBOW): a tool for ligand coordinate and restraint generation. Acta Crystallogr D Biol Crystallogr. 2009 Sep 16;65(10):1074–80.

48. Chen VB, Arendall WB, Headd JJ, Keedy DA, Immormino RM, Kapral GJ, et al. MolProbity : all-atom structure validation for macromolecular crystallography. Acta Crystallogr D Biol Crystallogr. 2010 Jan 1;66(1):12–21.

49. The PyMol Molecular Graphics System, Version 1.7.4, Schrodinger, LLC.

50.   Terwilliger TC, Grosse-Kunstleve RW, Afonine PV, Adams PD, Moriarty NW, Zwart P, et al. Interpretation of ensembles created by multiple iterative rebuilding of macromolecular models. Acta Crystallogr D Biol Crystallogr. 2007 May 1;63(5):597–610.

51.   St-Jean M, Sygusch J. Stereospecific Proton Transfer by a Mobile Catalyst in Mammalian Fructose-1,6-bisphosphate Aldolase. J Biol Chem. 2007 Aug 15;282(42):31028–37.

52.   Kuo DJ, Rose IA. Chemical trapping of complexes of dihydroxyacetone phosphate with muscle fructose-1,6-bisphosphate aldolase. Biochemistry (Mosc). 1985 Jul 16;24(15):3947–52.

53.   Grazi E. Quantitative evaluation of the carbanion intermediate in the aldolase reaction. Biochem Biophys Res Commun. 1974 Jan 7;56(1):106–11.

54.   Maurady A. A Conserved Glutamate Residue Exhibits Multifunctional Catalytic Roles in D-Fructose-1,6-bisphosphate Aldolases. J Biol Chem. 2002 Jan 4;277(11):9474–83.

55.   Rae C, Bubb WA, Kuchel PW. Aldolase-catalyzed diketone phosphate formation from oxoaldehydes. NMR studies and metabolic significance. J Biol Chem. 1992 May 15;267(14):9713–7.

56.   Du S, Guan Z, Hao L, Song Y, Wang L, Gong L, et al. Fructose-Bisphosphate Aldolase A Is a Potential Metastasis-Associated Marker of Lung Squamous Cell Carcinoma and Promotes Lung Cell Tumorigenesis and Migration. PLoS ONE. 2014 Jan 23;9(1):e85804.

57.   Poschmann G, Sitek B, Sipos B, Ulrich A, Wiese S, Stephan C, et al. Identification of proteomic differences between squamous cell carcinoma of the lung and bronchial epithelium. Mol Cell Proteomics MCP. 2009 May;8(5):1105–16.

58.   Chaerkady R, Harsha HC, Nalli A, Gucek M, Vivekanandan P, Akhtar J, et al. A Quantitative Proteomic Approach for Identification of Potential Biomarkers in Hepatocellular Carcinoma. J Proteome Res. 2008 Oct 3;7(10):4289–98.

59.   Parks SK, Chiche J, Pouysségur J. Disrupting proton dynamics and energy metabolism for cancer therapy. Nat Rev Cancer. 2013 Sep;13(9):611–23.

60.   Antognelli C, Mezzasoma L, Fettucciari K, Talesa VN. A novel mechanism of methylglyoxal cytotoxicity in prostate cancer cells. Int J Biochem Cell Biol [Internet].

2013 [cited 2013 Feb 4]; Available from: http://www.sciencedirect.com/science/article/pii/S1357272513000137

61. Ghosh A, Bera S, Ray S, Banerjee T, Ray M. Methylglyoxal induces mitochondria-dependent apoptosis in sarcoma. Biochem Mosc. 2011 Oct 12;76(10):1164–71.

SUPPORTING INFORMATION

Table S4-1. Data collection and refinement statistics

ALDO-DHAP-frac

Data collection		Refinement	
Wavelength (Å)	0.9795	Reflections used in	168510 (13060)
Resolution range	41.8 - 1.6 (1.66 - 1.6) [a]	Reflections used for R_{free}	1883 (144)
Space group	P 1 21 1	R_{work} [d]	0.1507 (0.2427)
Unit cell a (Å), b (Å), c (Å),	82.6 100.937 84.561	R_{free} [e]	0.1728 (0.2795)
α (°), β (°), γ (°)	90 98.27 90		
Total reflections	919902 (60751)	CC(work)	0.973 (0.921)
Unique reflections	178317 (15984)	CC(free)	0.964 (0.886)
Multiplicity	5.2 (3.8)	Number of non-hydrogen	12245
Completeness (%)	0.93 (0.88)	macromolecules	10779
Average $I/\sigma(I)$	18.52 (2.21)	ligands	36
Wilson B-factor	17.28	Protein residues	1408
R-merge [b]	0.05345 (0.5077)	RMSD (bond length) (Å)	0.005
R-meas [c]	0.0594 (0.5847)	RMSD (angles) (o)	0.97
CC1/2	0.999 (0.83)	Ramachandran favored (%)	98
CC*	1 (0.953)	Ramachandran allowed (%)	1.9
		Ramachandran outliers (%)	0.36
		Rotamer outliers (%)	1.4
		Clashscore	1.66
		Average B-factor (Å^2)	28.77
		macromolecules	27.92
		ligands	32.03
		solvent	35.14
		Number of TLS groups	13

[a] All values in parentheses are given for the highest resolution shell.

[b] $R_{merge} = \sum_{hkl}\sum_i |I_i(hkl) - \bar{I}_i(hkl)| / \sum_{hkl}\sum_i I_i(hkl)$, with i running over the number of independent observations of reflection hkl.

[c] $R_{meas} = \sum_{hkl}(n/(n\text{-}1))^{1/2}\sum_{i=1}^{n} |I_i(hkl) - \bar{I}_i(hkl)| / \sum_{hkl}\sum_i I_i(hkl)$,

[d] $R_{work} = \sum_{hkl}\|I_o(hkl)| - |I_c(hkl)\| / \sum_{hkl}|I_o(hkl)|$.

[e] $R_{free} = \sum_{hkl\epsilon T}\|I_o(hkl)| - |I_c(hkl)\| / \sum_{hkl\epsilon T}|I_o(hkl)|$, where T is a test data set randomly selected from the observed reflections prior to refinement. Test data set was not used throughout refinement and contains a minimum of 2000 unique reflections (or 5 %) (the smaller value is selected).

Figure S4-1. Superposition of WT-Aldolase with DHAP soaked Aldolase.

The *DHAP-1min* structure (*green*) is shown superposed with a control structure (*blue*), which resembles a previously reported native aldolase structure (PDB id: 1ZAH). Every water molecule in the native structure (*blue spheres*) is within ≤ 1 Å of the oxygen atoms on DHAP, including the four oxygen atoms of the phosphate group (O11 – O14) and the O3 oxygen. Note also the conformational change that occurs with Arg-303 upon DHAP binding – the guanidinium folds down and forms a salt bridge with O12 and O13 of DHAP. The structures were superposed using the <align> algorithm in PyMol.
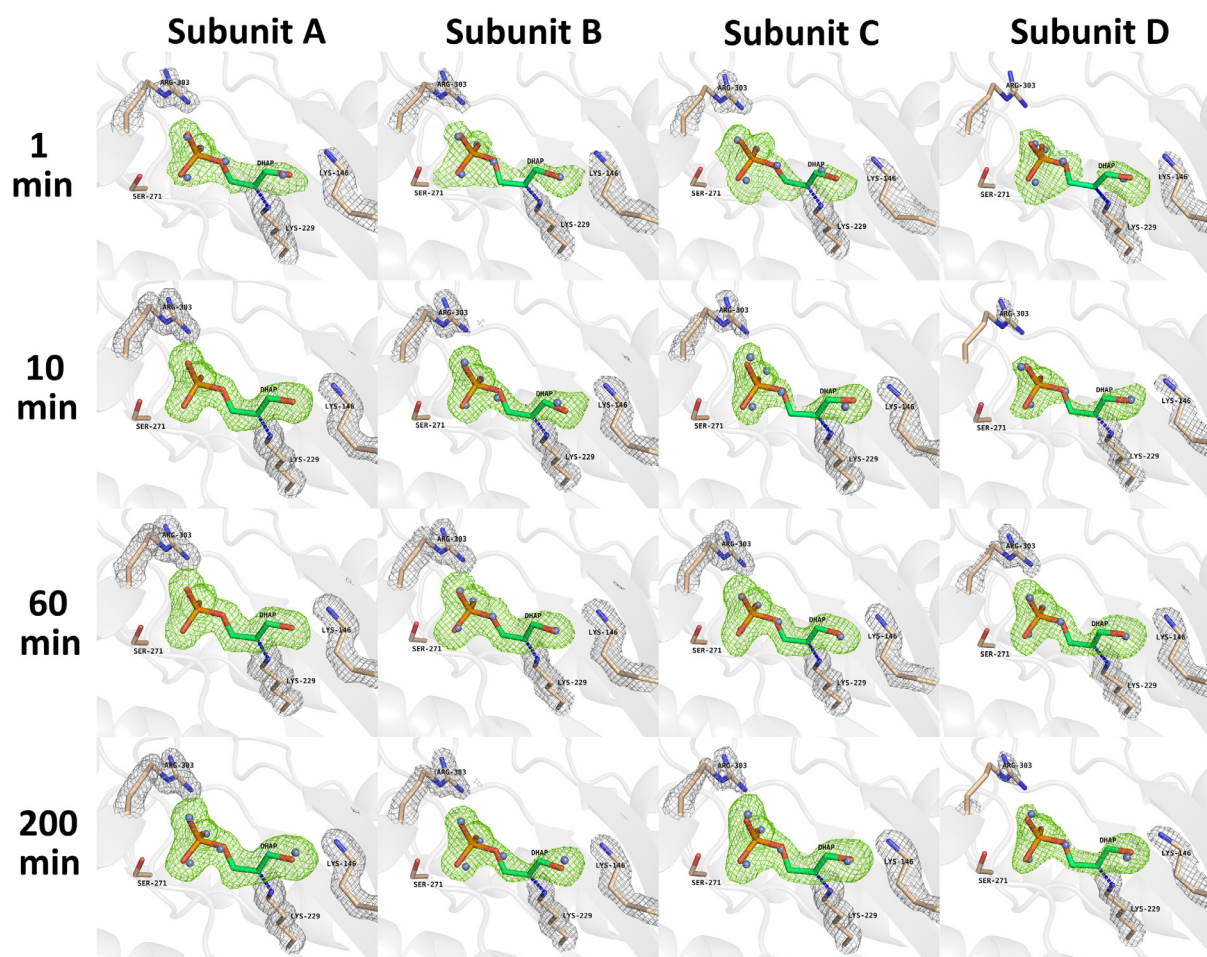
Figure S4-2. Omit maps of aldolase active sites for all soaking times.

Native rabbit muscle aldolase crystals were soaked for predetermined amount of time (1, 10, 60, and 200 minutes) and frozen to trap intermediates. The four columns represent the four aldolase subunits [A-D]. The *green* density illustrates simulated annealing $F_o - F_c$ omit maps contoured at 3σ. Densities colored *grey* represent $2F_o - F_c$ maps of critical active site residues and is contoured at 1.5σ for all structures. DHAP was modeled into each structure as the enamine intermediate. To account for weaker densities for DHAP in the active site, water molecules (*blue spheres*) were modeled at positions coinciding with the oxygen atoms of the DHAP and partial occupancies were refined in Phenix. In some cases, DHAP was refined to full (100 %) occupancy (Subunit A – 10 minutes) and in other models (Subunit D – 1 minute), DHAP only accounted for up to 40 % of the density in the active site. All structures were refined using the same refinement protocol.
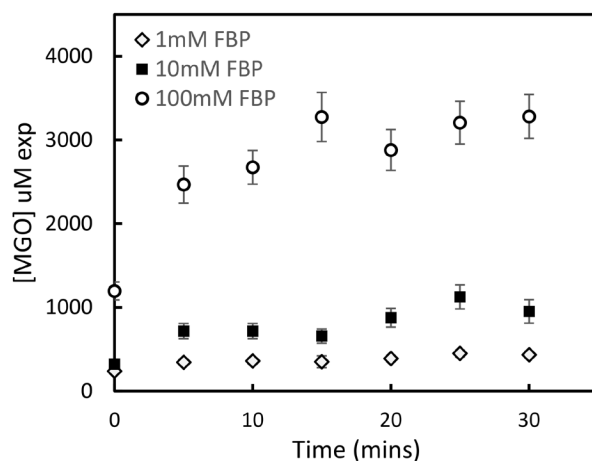
Figure S4-3. MGO production from FBP in the presence of Aldolase as a function of time.
Aldolase (10 *ug*) was incubated with 1, 10 and 100 *m*M FBP in 50 *m*M Tris-HCl, pH 8.0. Samples were withdrawn from the incubate mixture at 5 minute intervals from 0 to 30 minutes and MGO was immediately quantified by the glyoxalase enzyme assay. Here, samples were measured without quenching prior to quantification. Negative controls consisted of FBP at the three concentrations incubated in the absence of aldolase for 30 minutes and exhibited baseline levels of MGO. The positive control consisted of pre-calculated [MGO] which received the same treatment. These served as a standard curve from which [MGO] was determined experimentally for unknown samples. Data represent mean ± SD for n = 3.

As the endogenous substrate for aldolase is FBP, three concentrations were evaluated (1, 10, and 100 *m*M of FBP). For all three concentrations, incubation with aldolase yielded an inflection point in MGO generation which was observed after 5 minutes with an ensuing progressive increase in measured MGO. With 100 *m*M of FBP, it was difficult to get a precise reading for the difference in optical density, as the conversion of the hemimercaptal to S-D-lactoylglutathione never reached a plateau. The total MGO determination for 100 *m*M is therefore likely underestimated. 30 minutes of incubation with 10 *m*M of FBP produces quantifiable amounts of MGO, and was selected for subsequent experiments.

Chapter 5

Biophysical study of the aldolase bridging function in Toxoplasma gondii: evidence for ionic strength dependence

Background

Moonlighting, the performance of more than one unrelated function by a single protein, is becoming widely accepted as a common phenomenon in systems biology. Glycolytic enzymes are among the first proteins to have been recognized for their moonlighting activities. Aldolase in particular has an astonishing array of moonlighting functions that are seemingly unrelated to its glycolytic function. However, the precise role of aldolase in reported interactions is not well understood.

Our laboratory has been at the forefront in describing the precise nature of such interactions, using primarily x-ray crystallography to delineate critical binding residues. This approach has previously been applied by our group to describe the aldolase-WASP (St-Jean, 2005) and aldolase-LC4 (Rangarajan et al., 2010) interactions. Here, considerable efforts were applied to investigate the scaffolding function of aldolase in apicomplexan parasites, where it links surface adhesin molecules to the interior actomyosin complex, providing the motive force needed for host-cell invasion. A better description of this interaction has important therapeutic implications, as it represents a potential target for treatment of apicomplexan infections, such as malaria and toxoplasmosis. Therefore, our on-going interest in the development of aldolase inhibitors positioned us well for this project.

We collaborated with the laboratory of Dr. David Sibley at Washington University, St. Louis, whose research centers on the intracellular parasite, *Toxoplasma gondii*. During the course of our experimentation, his group challenged the existing crosslinking model for aldolase, suggesting its primary function is in glycolysis. *In vitro* data revealed in this chapter also questioned the relevance of this interaction, as it was abrogated in conditions of high ionic strength. The results of our biophysical investigation of the aldolase-adhesin interaction are presented in the following chapter. The constructs were provided by Dr. Sibley's group, and the rest of the work was conducted by myself.

Biophysical study of the aldolase bridging function in *Toxoplasma gondii*: evidence for ionic strength dependence

Paul W. Heron, Jurgen Sygusch

ABSTRACT

Host-cell invasion by apicomplexan parasites relies on the scaffolding activity of the glycolytic enzyme aldolase (ALD), which mediates interactions between surface adhesins and the parasite cytoskeleton. Prior studies have delineated the binding region in *Toxoplasma gondii* (Tg) adhesin members, microneme protein 2 (MIC2) and apical membrane antigen 1 (AMA1), to a cytoplasmic C-terminal domain containing conserved acidic stretches and a highly conserved tryptophan. Here, the binding mode of the TgALD interaction with adhesin tails was probed by protein crystallography and the thermodynamic binding parameters were evaulated by isothermal titration calorimetry. A large entropic contribution to the binding isotherms suggests a concomitant displacement of the flexible TgALD C-terminal region and expulsion of water molecules upon adhesin tail binding. Surprisingly, the interaction exhibits ionic strength dependence, weakening at higher values, providing a rationale for the absence of adhesin tails in co-crystal structures that were crystallized at higher ionic strength. Properly defining the interaction remains a priority for future study as gliding motility and host-cell invasion are critical for parasite survival and dissemination.

INTRODUCTION

The Apicomplexa is a large phylum of obligate intracellular parasites that contains the causative agents of toxoplasmosis (*Toxoplasma gondii*) and malaria (*Plasmodium falciparum*). A unifying characteristic is their possession of unique, apically localized secretory organelles known as micronemes and rhoptries that regulate the discharge of adhesive proteins involved in host-cell invasion, intracellular survival and parasite dissemination (1). Unlike cilia or flagella-based mechanisms, apicomplexan parasites rely on a unique gliding motility for host-cell invasion that generates force by linking the secreted adhesive proteins to an internal actomyosin network. According to the model, gliding motility is a substrate-dependent mode of locomotion that requires transmembrane adhesin proteins secreted apically from micronemes that translocate along the surface to the posterior end of the parasite in a conveyor belt motion. Further, the process is dependent on the actomyosin complex since disruption of actin in *T. gondii* inhibits motility of zooites (invasive form of the parasite) and prevents host-cell invasion (2–5). Also, disruption of myosin (TgMyoA) severely impairs invasion (6). The regulatory light chain of TgMyoA is anchored to a structural layer of flattened vesicles beneath the plasma membrane, defined as the inner membrane complex (IMC), through its interaction with the glideosome associate proteins (TgGAP40, TgGAP45, TgGAP50) (7, 8). Transmission of the motive force to the exterior of the parasite implicates micronemal transmembrane proteins that communicate with actin by their association with aldolase (ALD), an actin-binding protein (1, 9). Together these form the glideosome complex where progressive movement of F-actin–ALD–micronemal protein propels the parasite forward, as shown schematically in **Figure 5-1**. Adhesins are removed at the posterior pole by an intramembrane proteolytic event involving rhomboid-type proteases, leaving a trail of debris behind the moving parasite (8, 10).

Micronemal adhesins are essential components of the glideosome and have been investigated for their potential as prophylactic targets. One such molecule is the thrombospondin-related anonymous protein (TRAP), first discovered in *Plasmodium falciparum* sporozoites (11, 12). TRAP orthologs were subsequently found in other apicomplexans, including the *T. gondii* micronemal protein 2 (MIC2) (13) which is essential in gliding motility, adherence, and efficient host-cell invasion (14).
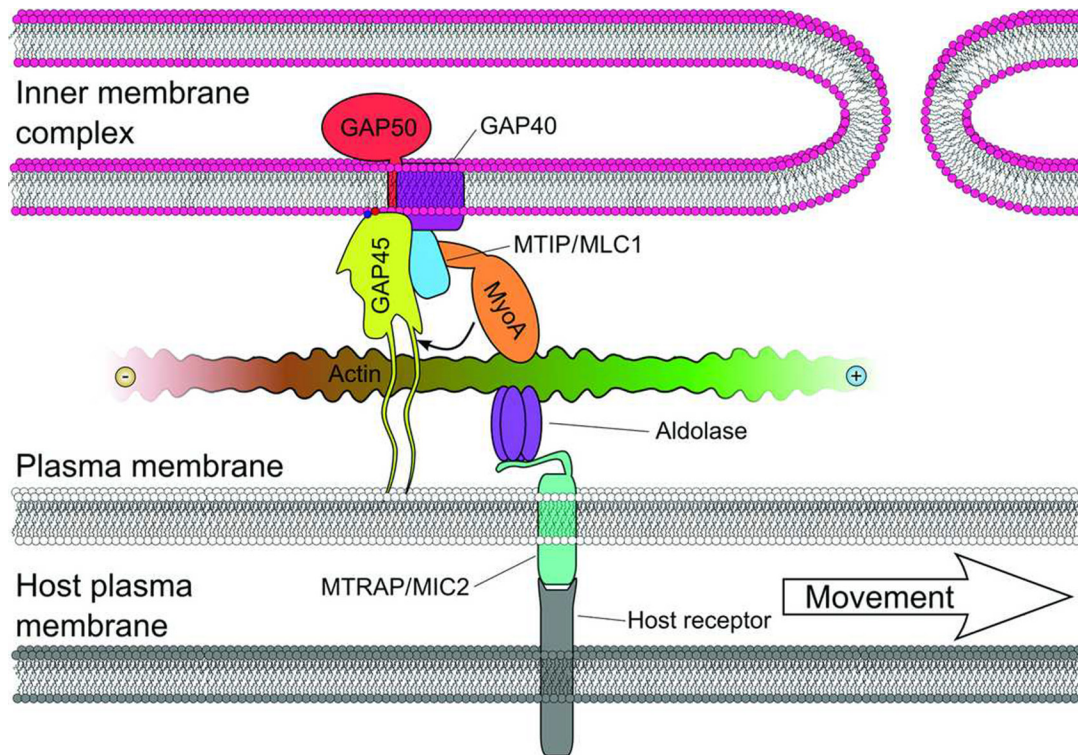
Figure 5-1. Model for gliding motility in apicomplexans.

The myosin motor complex (MyoA) produces the motive force that drives gliding motility in apicomplexans by walking towards the barbed (+) end of actin filaments, which are located between the plasma membrane and the inner membrane complex (IMC). MyoA is anchored to the IMC through association with glideosome associated proteins (GAP40, GAP45, GAP50). The glideosome structure attaches to host substrates through transmembrane adhesins, such as MIC2 (*T. gondii*) and TRAP (*P. falciparum*), that connect to actin through the scaffolding protein, aldolase. The overall effect produces a conveyor belt movement known as gliding motility that propels the parasite forward. Figure adapted from Kumpula and Kursula, 2015 (15).

TRAP family proteins contain various extracellular adhesive motifs, including epidermal growth factor-like repeats, Apple domains, thrombospondin type 1 repeats, and integrin A-like domains (15), which mediate contacts with host cells by recognizing such receptors as glycosaminoglycans and heparin-like molecules (16–18). In addition to a transmembrane region, they contain a short cytoplasmic tail (C-tail) that is rich in acidic residues and contains a sub-terminal tryptophan (Trp) residue (13). These conserved C-tail features are critical to their function, as shown in mutational studies where replacement of the Trp impairs motility in

Plasmodium sporozoites (19). Despite their low sequence similarity, the conserved function of C-tail orthologs in *Plasmodium* and *T. gondii* was demonstrated by domain swapping experiments (19). Their functionality is essential to infectivity, as shown in *T. gondii* zoites (20).

The C-tails of *Plasmodium* TRAP (TRAPt) and *T. gondii* MIC2 (MIC2t) were found to mediate binding to the cytoskeleton through a bridging molecule, the glycolytic enzyme fructose-1,6-bisphosphate aldolase (ALD) (9, 21). Coimmunoprecipitation and colocalization experiments with parasite lysates have validated this interaction. Mutational studies mapping the binding requirements for MIC2t to TgALD, indicated a positively charged cluster in ALD which accommodates the acidic tail (22). Mutations were identified that specifically abrogated C-tail binding whilst minimally perturbing enzyme activity, providing a means to separate the two functions of ALD. Further support for the direct role of ALD in bridging adhesin-cytoskeletal interactions comes from *in vivo* experiments with a conditional knockout (cKO) of TgALD which was complemented with the various delineated TgALD mutants. Parasite strains expressing a TgALD variant deficient only in MIC2t binding exhibited reduced infectivity (22). Structural work with *P. falciparium* ALD and TRAPt corroborated this mode of binding, which involves a network of hydrogen bonds between the acidic residues of the tail and positively charged residues near the ALD active site (23).

Also important for host-cell invasion are micronemal adhesins that participate in the formation a moving junction (MJ), a structure that forms between the host and parasite membranes which requires specialized adhesive Rhoptry neck proteins (RONs) that are secreted apically from rhoptry organelles. RONs are inserted into the host plasma membrane where they mediate association with transmembrane micronemal adhesins, including apical membrane antigen 1 (AMA1), which was shown to fulfill a key function in the invasion of host-cells by *T. gondii* and *Pasmodium* zoites (24–26). The extracellular domains of AMA1 associate with RONs, forming key interactions that stabilize the MJ (27–30). Like MIC2t, AMA1 C-tail (AMA1t) associates *in vitro* with ALD (31), and is disrupted when the conserved Trp is mutated to an alanine in T. gondii (W548A) and exhibited reduced invasion when tested *in vivo* (32).

Altogether, the studies suggest that ALD may play a key role during parasite invasion. Eukaryotic class I ALDs are tetrameric (33) and in the direction of glycolysis catalyze the cleavage of fructose-1,6-bisphosphate into the trioses: dihydroxyacetone phosphate and glyceralehyde-3-phosphate. The active site of each subunit is located at the center of an $(\alpha\beta)_8$

TIM-barrel fold (34). The tetrameric nature of ALD provides the ideal scaffold for cross-linking actin to stipulated partners. The actin-binding ability of ALD is well documented and experimentation with ALD mutants delineated the actin binding region to a cluster of conserved residues that overlaps the catalytic pocket (35). The association between the latter was also demonstrated *in vitro* for *T. gondii* (36). Data thus far is indicative of an important role for ALD in crosslinking the cytoskeleton to micronemal adhesins. Moonlighting functions of ALD have been previously described and include among many a role for the assembly and activity of the vacuolar H+-ATPase proton pump (37), a role for ALD in promoting adhesion of *Neisseria meningitidis* to endothelial cells *in vivo* (38), and a role in regulating actin dynamics by associating with Wiskot-Aldrich syndrome protein, an actin nucleation-promoting factor (39). Despite compelling *in vivo* and *in vitro* data showing the association between ALD and adhesins, the structural determinants of the interaction are poorly understood. Previous structural work with *Plasmodium* ALD (PfALD) produced a co-crystal with a TRAP-peptide (23), but difficulties crystallizing TgALD limited progress.

Here, we sought to characterize the interaction of MIC2t and AMA1t with TgALD using x-ray crystallography. High-resolution crystal structures were obtained for native TgALD. Yet, our efforts did not yield co-crystal structures with several forms of the adhesin tails. The interactions were confirmed by isothermal titration calorimetry but it was found that ionic strength plays a determining role in the affinity of interaction between TgALD and the adhesin tails. This suggests that previous evidences of *in vitro* interactions between ALD and adhesin tails may in fact be non-specific and is consistent with the recent finding that the TgALD–TgAMA1 interaction is not required for parasite motility or invasion; rather, according to the study, ALD is primarily important for energy metabolism but does not play an essential role in coupling adhesins to the cytoskeleton during invasion (31). Given these findings, the role of ALD in motility and invasion needs to be re-evaluated. Our approach and results complementing these findings are described in this chapter and may provide valuable insight into the binding mode of the adhesin tails to TgALD.

EXPERIMENTAL PROCEDURES

Materials. Fru(1,6)P$_2$, glycerol-3-phosphate dehydrogenase and triose-phosphate isomerase were purchased from Sigma-Aldrich. NADH was from Roche Diagnostics. All other chemicals and materials were of analytical grade and were obtained from Sigma-Aldrich, Fisher Scientific, Bioshop Canada, and GE Healthcare Life Sciences.

Purification and Crystallization of TgALD. Recombinant *T. gondii* aldolase (TgALD) was amplified and cloned as previously described (9, 22) (UniProt ID: Q8I8I2; gene accession number: AY150663). The TgALD gene was then subcloned into a T7-inducible pE-SUMO AMP vector available from LifeSensors Inc (SUMOpro® Gene Fusion Technology), which was generously provided by Dr. David Sibley, Washington University in St. Louis. The resulting plasmid was transformed into *E. coli* BL21-Star™ (DE3) cells (Invitrogen). Overexpressing clones were identified from a mini-lysis test using a mixture of sucrose (25%), lysozyme, and Triton X-100 (0.3%) for cell lysis. The overexpressing recombinant strain grown to A$_{600}$ = 0.6 in LB medium was induced with 1 *m*M isopropyl β-D-1-thiogalactopyranoside at 37° C for 4 hours. Cells were harvested by centrifugation and frozen at -20 °C overnight. The bacterial pellet was lysed by mechanical disruption with type A-5 aluminum oxide using a mortar and pestle. Cells were resuspended in a lysis buffer (20 *m*M Tris-HCl pH 7.4, 0.5 M NaCl, 20 *m*M imidazole, 10mM MgCl$_2$, 0.2 *m*M PMSF) containing 1 *m*g/g of RNAse and recombinant DNAse. The clear lysate obtained after centrifugation was dialyzed with binding buffer (20 *m*M Tris-HCl pH 7.4, 0.5 M NaCl, 20 *m*M imidazole) and was purified by affinity purification using a HisTrap™ HP 5 *m*l column (Ni^{2+} immobilized) connected to an ÄKTA purification system (GE Healthcare). The N-terminal 6xHis-SUMO-TgALD was eluted using elution buffer (20 *m*M Tris-HCl pH 7.4, 0.5 M NaCl, 0.5 M imidazole) applied on a linear gradient. The His-SUMO tag from eluted protein was cleaved by incubation for 4 hours at 30 °C with SUMO protease after overnight dialysis in SUMO buffer (20 *m*M Tris-HCl pH 8.0, 150 *m*M NaCl, 10% glycerol). Prior to reinjection on the HisTrap column, samples were dialyzed with binding buffer. Fractions from the flow-through containing the protein, as determined by SDS-PAGE and enzyme activity, were pooled and precipitated overnight with precipitation buffer (100 *m*M Tris-HCl pH 7.6, 1 *m*M EDTA, 70% ammonium sulfate, 5 *m*M DTT). Precipitated protein was pelleted, resuspended in gel filtration buffer (20 *m*M Tris-HCl pH 7.4, 1 *m*M EDTA, 50 *m*M

NaCl) and loaded onto a HiLoad^{TM} 16/60 Superdex^{TM} prep grade (GE Healthcare). Purity was assessed by SDS-PAGE and mass spectrometry. Peak fractions were pooled, dialyzed with a minimal buffer (20 *m*M Tris-HCl pH 7.0), and concentrated to 5-10 *m*g·*m*l^{-1} prior to crystallization trials.

Crystallographic Data Collection and Processing. Because of early challenges in obtaining high-quality diffracting crystals, a rational engineering strategy was undertaken to reduce the surface entropy of the protein. Surface entropy reduction (SER) seeks to replace clusters of solvent exposed, flexible residues with residues of lower conformational entropy in order to minimize the loss of conformational entropy that occurs upon crystallization. Thus, crystallization is thermodynamically favourable and crystallizability increases (40). Using the web server SERp (41), mutations were identified that were suitable for SER. These were cross-validated using crystallization propensity predictors, including OB-score (42), ParCrys (43), and XtalPred (44). A consensus was reached for numerous lysine clusters and multiple sequence alignment (ClustalO with other class I ALDs (UniProt IDs: ALF_plafa, P14223; ALDOB_human, P05062; ALDOB_rabbit, P79226; ALDOA_rabbit, P00883; ALDOA_human, P04075; ALDO_leime, Q9U5N6) was used for assignment of conserved mutations. In most cases, the crystallizability scores for native TgALD were poor but the proposed mutations had a considerable impact on the amenability of crystallization. As such, the following variants were prepared as His-SUMO fusions using the QuickChange method: K135A-K135A, K157A-K159A, and K321A-K323A. Crystallizable variants were purified as above.

Native *Tg*ALD crystals were identified from the Clear Strategy^{TM} Screen I (Molecular Dimensions) and were optimized to the following conditions: 0.1 M sodium acetate pH 5.5, 0.2 M lithium sulfate, 3.5% (w/v) PEG 8000, 10% (w/v) PEG 1000. Crystals were grown at 20 °C by hanging-drop vapor diffusion using a 1:1 mixture of protein:precipitant. Prior to flash-freezing in liquid nitrogen, single crystals were cryoprotected by brief soaking in the ligand buffer and 20% (v/v) glycerol. The data were collected at beamlines X25 and X29 of the National Synchrotron Light Source I at Brookhaven National Laboratories. The diffraction data were processed and scaled with the HKL package (45) and the final results are listed in Table 1 found in the associated content.

Structure determination and refinement. Structures were solved by molecular replacement with PHENIX (46) Phaser-MR (47) using subunit-A from the native rabbit ALD homotetramer structure as a reference model [Protein Data Bank (PDB) entry 1ZAH] for which there is 57.1% sequence homology (48) (*Oryctolagus cuniculus* ALD [Uniprot ID: P00883] and *T. gondii* ALD [Uniprot ID: Q8l8l2]). The native *Tg*ALD structure has one molecule in the asymmetric unit in the space group P 42 21 2. Refinement and model building were performed using the refinement module in Phenix (49) and Coot (50) respectively. Data quality was assessed and cut-off using correlation-coefficient-based criteria, $CC_{1/2}$ (51). Final model statistics were calculated with MolProbity (52) and are shown in Table S5-1. All figures in the present paper were prepared using PyMOL graphics software (53).

Peptide purification. The full length cytoplasmic C-terminal adhesin tails (AMA1t and MIC2t) were provided by Dr. David Sibley, Washington University in St. Louis. They were obtained from an RH strain cDNA library by PCR amplification as previously described (9, 31) and subcloned into the SUMO expression system described above, resulting in 6xHis-SUMO-AMA1t and 6xHis-SUMO-MIC2t fusions that were transformed, expressed and purified as described above for TgALD. After cleavage of the SUMO tag, the C domains for study comprised residues 510 - 569 for AMA1t (UniProt ID: B6KAM0) and residues 721 – 769 for MIC2t (UniProt ID: S8F9G8). The purity of the C-tails was assessed by ESI-MS. The full length cytoplasmic sequences are as follows: MIC2t (721 – 769) SYHYYLSSSV GSPSAEIEYE ADDGATKVVM EEEKETLVPV DDDSDMWME; AMA1t (510 - 569) LDRNKGVQAA HHEHEFQSDR GARKKRPSDL MQEAEPSFWD EAEENIEQDG ETHVMVEGDY.

Peptide synthesis. Shorter peptides employed for co-crystallography and biophysical experimentation were obtained by custom synthesis. MIC2t-25 (745 - 769) and AMA1t-25 (545 - 569) were prepared by CanPeptide Inc. at > 95% purity which was also confirmed in-house by LC-MS. A shorter MIC2t-15 (555 - 569) was obtained from GenScript at > 94% purity.

Sequence alignment. Multiple sequence alignment was performed using Jalview version 2.9 (54). Default parameters in Clustal Omega were used for all alignments.

ITC assays. Calorimetric titrations were performed in either duplicates or triplicates (as indicated in the text) on a MicroCal VP-ITC or a MircoCal ITC200 calorimeter from Malvern Instruments Ltd. All measurements were made at 25 ºC using degassed solutions. The proteins were dialyzed against 20 *m*M Tris-HCl at pH 7.4 or another buffer as indicated in the text. The

measurement cell (1.4275 mL for the VP-ITC and 0.3 mL for the ITC200) contained the 20 - 100 μM ALD solution and was titrated with 200 – 1000 μM ligand solution in the same buffer, using 40 x 7 μL injections for the VP-ITC and 15 x 2.5 μL injections for the ITC200. The stirring rate was kept at 307 rpm for all measurements with the VP-ITC and 1000 rpm for all measurements with the ITC200. Ligand was injected into buffer so as to account for the heat of dilution and mixing, and the resulting isotherm was subtracted from the enzyme data prior to analysis. Data was analyzed using the one-site model in the Origin software (version 7.0).

Activity assay. Aldolase cleavage activity was determined using a coupled assay system involving triose-phosphate isomerase and glycerol-3-phosphate dehydrogenase (TIM/GDH) by following NADH oxidation at 340 nm using a Varian Cary 300 UV-Vis spectrophotometer thermostatted at 25 °C (55).

RESULTS

Native TgALD structure determination. A parallel approach was envisaged for the crystallization of TgALD, which had not yet been solved. The surface entropy reduction (SER) strategy indicated variants with thermodynamically favourable properties (lower entropic penalty upon crystallization) rendering them amenable to crystallization. Crystal growth conditions were identified for a variant (K157A-K159A), producing highly-diffracting crystals of the variant form (1.82 Å; R_{free}/R_{work} = 0.19/0.16; structure not shown). The conditions consisted of 0.1 M sodium acetate pH 5.5, 0.2 M lithium sulfate, 3.5% (w/v) PEG 8000, 10% (w/v) PEG 1000. Highly diffracting crystals with the same rod morphology were also identified in a condition consisting of 0.1 M sodium acetate pH 5.0, 1.5 M ammonium sulfate. Both of these conditions were successfully applied to native TgALD and a high-resolution structure was determined in space group P 42 21 2 at a resolution of 1.78 Å with R_{free}/R_{work} of 0.1995/0.1549. Data collection and refinement statistics are shown in Table S5-1 (supporting information).

TgALD crystallized with one molecule in the asymmetric unit, adopting the classic $(\alpha/\beta)_8$ TIM-barrel fold of other class I ALDs. The tetrameric structure exhibits 222 crystallographic symmetry and validates the crosslinking model for ALD in apicomplexans (**Figure S5-1**). Small ligands were readily soaked into this crystal lattice, including the ALD substrates

dihydroxyacetone phosphate and fructose-1,6-bisphosphate. Soaking experiments with the adhesin tails was unsuccessful (including trials with the following peptides: MIC2t, MIC2t-15, MIC2t-25, AMA1t, and AMA1-25). Presumably, the size of the peptides limits their diffusion through the crystalline pores, as confirmed by the diameter of only ~ 8Å in the largest channels of the crystal lattice. Therefore, we undertook co-crystallization experiments with the adhesin peptides. Hundreds of screens were unproductive in generating a co-crystal structure, whilst yielding a profuse amount of native structures with no evidence of bound peptide. Closer inspection of the native structure seen in **Figure S5-1**, specifically relating to crystal lattice contacts, revealed a tight packing between symmetry mates. Several structures were solved from crystals grown in different crystallization conditions, but they consistently adopted the same P 42 21 2 symmetry with tight packing. Superposition (using PyMol align) with co-crystal structures of previously resolved ALD-peptide structures revealed that packing differences with TgALD potentially abrogates binding of peptides near the same loci used in ALD structures co-crystallized with peptides (**Figure S5-2**). The crystal contacts near the anticipated peptide binding site may sterically interfere with binding of the adhesin tails (see discussion for more detail).

In the native structure, the C-terminal region of TgALD, which is implicated in the catalytic activity (56), binds at a site distal from the catalytic cleft, resting near the interface between subunits. The three terminal residues, 361-YVY-363, are very well resolved in the structure, and have correspondingly low temperature factors. These residues also mediate several inter-molecular contacts with neighbouring subunits, promoting tight packing within the crystal that could abrogate peptide binding in the anticipated lining near the active site. Since TgALD consistently crystallizes in the tight-packing form, we sought a strategy to promote formation of crystals with alternate crystalline arrangements (different space-groups). Therefore, the flexible C-terminal region (residues 345 – 363) was truncated (TgALDΔC) as a means of encouraging crystallization in alternative space-groups.

Crystallization of TgALDΔC. TgALDΔC was purified, characterized kinetically, and crystallized. A maximal cleavage activity k_{cat} of 0.26 ± 0.01 s^{-1} (SE, n = 3), representing ~ 25 fold reduction in activity with respect to the wild-type enzyme (10.88 ± 0.31 s^{-1}). The kinetic parameters for TgALDΔC are consistent with previously reported values for carboxypeptidase-

treated (cleaved C-terminus) rabbit muscle ALD which exhibits ~ 20 fold reduction in fructose-1,6-bisphosphate cleavage activity (57). The K_m also diminishes from a value of $4.05 \pm 0.80 \ \mu$M in wild-type TgALD to $0.38 \pm 0.07 \ \mu$M in TgALDΔC and is consistent with the kinetic model where a simultaneous reduction in both V_{max} and K_m occurs if the loss of the C-terminal region only impacts the rate of DHAP dissociation from the active site (57). Structurally, the increase in affinity upon C-terminal truncation is consistent with C-terminus truncation not competing with substrate binding. To confirm that the ALD fold was unperturbed in TgALDΔC, a crystal structure was solved.

The TgALDΔC crystal structure was solved to 2.01Å and was refined to R_{free}/R_{work} of 0.185/0.152 (data not shown). TgALDΔC crystallized in a different space group (F 222) with a more unrestrained crystal packing compared to native TgALD, whilst retaining the same fold as the native structure (alignment of TgALDΔC and native TgALD in PyMOL has a root mean square deviation (RMSD) of 0.145Å). The less tightly packed configuration in the crystal is validated by respective Matthews coefficients (58, 59), which gives an estimate of the solvent content (V_s) in the crystal. TgALDΔC has a V_s of 56% (F 222 space group), whilst native TgALD has a V_s of 42% (P 42 21 2 space group)[8]. This more relaxed crystal packing is consistent with the previous suggestion that the C-terminus promotes a tighter packing and precludes co-crystal formation between TgALD and the adhesin peptides. Therefore, we pursued co-crystallization of TgALDΔC with the custom peptides (AMA1t-25 and MIC2t-25). Once more, this was unproductive. To clarify the shortcomings of the crystallography trials, the thermodynamic parameters of the interaction between the adhesin tails and TgALD was explored in solution by isothermal titration calorimetry (ITC). The results of this investigation are shown in Table 5-1 and reveal a surprising finding.

---

[8] Calculated using *MATTPROB: http://www.ruppweb.org/mattprob/default.html*

Table 5-1. Thermodynamic binding parameters between TgALD and adhesin C-tails.

Enzyme	Peptide	Standard Conditions	K_d (μM) [a]	ΔH (cal/mol)	ΔS*T (cal/mol)	χ2
TgALD	MIC2t	20mM TRIS 7.4	0.8[b]	23470	31886	1.18E+04
TgALD	MIC2t-25	20mM TRIS 7.4	11.9	14710	21426	1.84E+04
TgALD	MIC2t-15	20mM TRIS 7.4	16.1[b]	3292	9834	8.94E+02
TgALD	AMA1t	20mM TRIS 7.4	2.9[b]	12360	19906	4.72E+03
TgALD	AMA1t-25	20mM TRIS 7.4	1.5	12550	20502	5.09E+04
TgALDΔC	MIC2t	20mM TRIS 7.4	10.0	-1807	5006	385.4
TgALDΔC	MIC2t-25	20mM TRIS 7.4	5.6	-2127	5036	1.21E+03
TgALDΔC	AMA1t	20mM TRIS 7.4	2.3	-8441	-750	2.25E+04
TgALDΔC	AMA1t-25	20mM TRIS 7.4	4.5	-11220	-3903	2.40E+04
Modified experimental conditions						
TgALD	MIC2t-25	100mM NaAc 5.5, 100mM LiSO$_4$ 100mM TRIS 8.5, 100mM LiSO$_4$ 100mM HEPES 7.0, 100mM LiSO$_4$	n.b.[c]	-	-	-
TgALD	MIC2t-25	100mM TRIS 7.4	17.0	2454	8969	1.54E+04
TgALD	MIC2t-25	5mM TRIS 7.4	5.8	16230	23363	3.31E+04
TgALDΔC	AMA1t-25	100mM TRIS 7.4	n.b.	-	-	-
TgALDΔC	MIC2t-25	100mM TRIS 7.4	n.b.	-	-	-
TgALDΔC	MIC2t-25	100mM TRIS 7.1, 10mM MgCl$_2$	n.b	-	-	-
Acidic conditions						
TgALD	MIC2t-25	20mM NaAc 5.5	3.1	2182	9685	7.57E+03
TgALD	MIC2t-25	100mM NaAc 5.5	n.b.	-	-	-
TgALD	AMA1t-25	20mM NaAc 5.5	6.1	4503	11622	1.56E+04

[a] abbreviations: K_d, dissociation constant; ΔH, enthalpy change; ΔS, entropy change; T, temperature (298K); $χ^2$, chi squared. TRIS, Tris buffer; NaAc, sodium acetate; HEPES, Hepes buffer,

[b] data was collected on VP-ITC; all other isotherms collected on MicroCal-ITC200.

[c] n.b. – no binding; unable to model thermodynamic binding parameters.

ITC binding isotherms were measured for TgALD and TgALDΔC with the adhesin C-tails of MIC2 and AMA1 in conditions with various pHs and ionic strengths. The buffer conditions are indicated sequentially as <buffer, pH, salts>. The modified conditions represent the composition of crystallographic conditions for which TgALD crystals were obtained; precipitants (polyethylene glycol or high salt concentrations) were omitted as they can interfere with ITC experiments and present considerable challenges in sample preparation. A control isotherm measuring the heat generated from dilution of ligand during injection was subtracted from all test isotherms. All thermodynamic parameters were modeled using the 'one-site model' in Origin software. Raw binding isotherms and data fitting for modeled isotherms are shown in **Figure S5-3** - **Figure S5-6**. An example of data exhibiting no binding (n.b.) is shown in **Figure S5-7**. Data are representative of n ≥ 3 in standard conditions (20 mM TRIS pH 7.4) and n ≥2 in modified conditions.

Thermodynamic parameters of interaction resolved by ITC. Table 5-1 summarizes the results obtained from the ITC experiments between TgALD and the adhesin tails. Under standard low ionic strength conditions, TgALD binds full-length cytoplasmic MIC2t and AMA1t with dissociation constants in the low-micromolar range (0.8 μM and 2.9 μM respectively). With MIC2, the affinity of TgALD for the C-tail is reduced with the shorter MIC2t-25 (11.9 uM) and MIC2t-15 (16.1 uM). However, full length AMA1t (60 residues) and AMA1t-25 have similar binding affinities to TgALD (2.9 uM vs 1.5 μM). Consistently, in standard conditions and for native TgALD, the change in enthalpy (ΔH) is positive but smaller in magnitude than the entropic contribution (-T·ΔS). Comparison of the binding energetics of MIC2t variants shows that there is both greater enthalpic and entropic contributions with the longer variants. However, AMA1t and AMA1t-25 show little differences in energetics.

Binding of the C-tails to the TgALDΔC variant was also tested in order to validate whether C-terminal truncation of TgALD affects adhesin C-tail binding. Binding affinity in all cases remains in the low micro-molar range. However, the binding energetics are markedly different to binding with native TgALD, notably with respect to the negative ΔH values.

We suspected the crystallographic buffer conditions to adversely affect the binding of the C-tails to TgALD. To test this, crystallographic solutions that yielded crystal hits served as templates that were tested by ITC. Enzyme and ligand were prepared by dialysis with the identified buffers and adjuvant salts, excluding precipitants such as polyethylene glycol (PEG) which introduce complications with respect to sample preparation and ITC signal due substantial background noise. Binding of adhesin C-tails appears to be sensitive to ionic strength, as indicated by the negligible binding observed in samples prepared in higher buffer concentrations (100 mM) and comprising salts (100 mM LiSO$_4$ or 10 mM MgCl$_2$) (examples of negligible binding isotherms are shown in **Figure S5-7**). Likewise, increasing Tris buffer concentration from 5 mM to 20 mM and 100 mM changes the binding affinity of TgALD and MIC2t-25 from 5.8 μM to 11.9 μM and 17 μM respectively. The same trends were observed using the TgALDΔC variant.

The conditions producing stable TgALD crystals (pH 5 – 5.5) were also tested to assess whether acidic pH could influence binding affinity and energetics. Although there is little influence on binding affinity, the energetics were changed. The ΔH and T·ΔS both decrease at acidic pH for TgALD binding to MIC2t-25 and AMA1t-25 but their overall free energies of

binding remain relatively unchanged compared to standard conditions. At pH 7.4, TgALD binds to MIC2t-25 and AMA1t-25 with respective free energies of -6.72 *k*cal/mol and -7.55 *k*cal/mol. The respective measurements at acidic pH, as shown in Table 5-1, are -7.50 *k*cal/mol and -7.12 *k*cal/mol. Increasing the buffer concentration of sodium acetate (NaAc) to 100 *m*M abrogates binding of TgALD to MIC2t-25. The solution binding was also tested in conditions mirroring crystallographic conditions that produced a co-crystal structure of ALD-LC4 peptide (60) - 100 *m*M Tris, pH 7.1, 10 *m*M MgCl$_2$. No binding was profiled for these conditions between TgALD and MIC2t-25.

Finally, based on the latter findings, we presumed co-crystallization might succeed using low ionic strength conditions, available commercially in a high-throughput screen typically used for crystallization of monoclonal antibodies (LISS – Hampton Research). Unfortunately, hits identified from this screen (20 *m*M Tris pH8.5, 23% PEG2K MME) had the same morphology (rod-like crystals) as the native TgALD crystals from earlier but diffracted poorly. There was no evidence of peptide density near the active site in solved structures.

DISCUSSION

The functions of ALD in glycolysis and gluconeogenesis are well established, however its non-enzymatic structural function as a scaffold protein that crosslinks numerous proteins to the actin cytoskeleton has only been recently appreciated. The finding that pools of ALD interacts with a host of cellular partners (23, 35, 61–66) provides strong support for the active implication of ALD in these processes. Included among recently identified partners are the TRAP family adhesin proteins that play a critical role in productive host-cell invasion of apicomplexan parasites. Here, the binding mode of TRAP-orthologs in *T. gondii* (MIC2 and AMA1) was investigated both structurally and biophysically.

TgALD structure. The binding of MIC2 to TgALD, like several other described interactions, involves interactions mediated in part by a highly conserved C-terminal tryptophan preceded by two non-contiguous clusters of acidic residues that are critical for binding to TgALD *in vitro* (67) (see multiple sequence alignment in **Figure 5-2**). The native TgALD structure reveals a basic groove including the substrate-binding pocket that is capable of forming electrostatic

interactions with the acidic peptides, as was shown from *in vitro* and modeling studies (22). These same residues are implicated in F-actin binding (35), consistent with the hypothesis that the ALD tetramer performs crosslinking to binding partners with diametrically opposed subunits. Modeling of MIC2t with TgALD revealed that the indole ring of Trp-767 was sandwiched between the hydrophobic side chains of Arg-43 and Arg-304 while the carboxyl group of Asp-765 in the first acidic cluster makes several key hydrogen bonds with basic side groups in Arg-148, Lys-42, and Arg-43 (22). The penultimate Trp in other ALD-binding partners intercalates in the same hydrophobic pocket formed by adjacent arginines (39, 60) (**Figure S5-2**), including *Plasmodium* TRAP-tail (23). Mutation of the penultimate Trp disrupts binding to ALD (67). The proximal cluster of acidic residues preceding MIC2 Trp-767 (Asp-761, Asp-762, Asp-763, and Asp-765) is considered to be important for ALD-binding, whereas the distal cluster (Glu-751, Glu-752, Glu-753, Glu-755) is believed to be essential for parasite survival, but doesn't appear to be necessary for ALD-binding (67). However, findings from ELISA experiments (not shown) indicated that the shorter MIC2t-15 has less affinity for ALD than the longer MIC2t-25 which encompasses both acidic clusters. Consequently, both shorter and longer peptides were tested in co-crystallization experiments. Our ITC experiments confirmed the difference in binding affinity between different MIC2t length-variants: the full length MICt (49 cytoplasmic residues) binds with a K_d of 0.8 μM; MIC2t-25 with a K_d of 11.9 μM; and MIC2t-15 with a K_d of 16.1 μM, suggesting the distal acidic cluster (defined in **Figure 5-2**), which is not present in MIC2t-15, does indeed influence ALD-binding, though to a small degree. The importance of electrostatic and hydrophobic interactions in mediating interactions between TRAP family tails and ALD is thus well established.

AMA1t (residues 510 – 569) also includes a conserved Trp (Trp-548), however, unlike its TRAP family counterparts, it is not penultimate, but is located upstream from the C-terminus adjacent to a conserved phenylalanine (Phe-547). The aromatic pair (Phe-Trp) is critical to ALD-binding as alanine variants eliminates ALD-binding and block host-cell invasion (32, 68). More recently the contribution of Phe-547 to binding was however shown to be modest (31). Downstream from this pair is a cluster of acidic residues that is also important to *in vitro* ALD-binding (31) (see **Figure 5-2**). The penultimate C-terminal acidic residues Glu-566 and Asp-568 are also important for the interaction. AMA1t-25 and the full length were selected for co-crystallization experiments, since both encompass the conserved Trp and acidic residues.
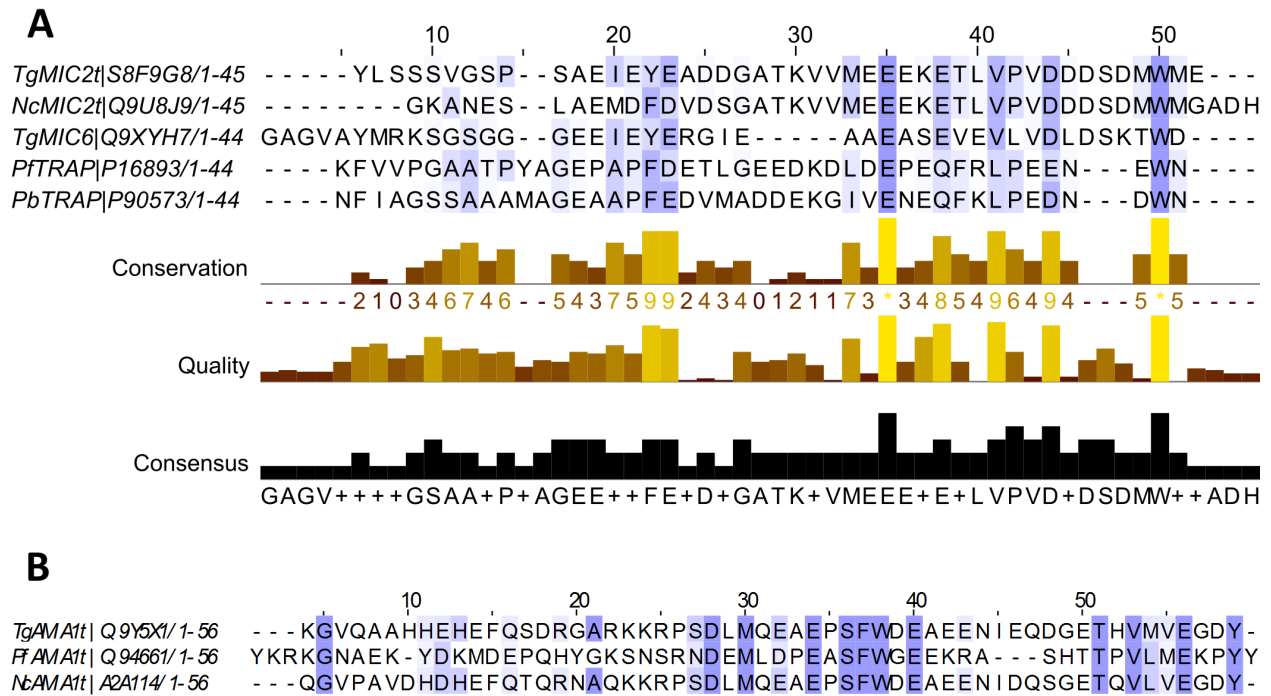
Figure 5-2. Conservation of amino acid residues within micronemal adhesin proteins.

(A) Shown is a multiple sequence alignment of the cytoplasmic tails of the TRAP family of proteins. The *blue* colour gradient indicates the level of conservation (*darker*, more conserved), which is also indexed numerically from 0-9. The corresponding confidence in the level of conservation is indicated by the Quality annotation - an ad-hoc measure of the likelihood of observing the mutations (if any) in a particular column of the alignment, and a consensus sequence is provided. Residues suspected of mediating interactions with ALD include the conserved penultimate tryptophan (TgMIC2 W567), the proximal acidic stretch consisting of aspartic acids, and the distal acidic stretch consisting of glutamic acids. The acidic patches are separated by a hydrophobic stretch. **(B)** Shown is a sequence alignment comprising the cytoplasmic C-terminal AMA1 adhesin tails. The highly conserved tryptophan (TgAMA1 W548) is located upstream from the C-terminal extremity beside a conserved tyrosine. A stretch of acidic residues (glutamic acids) follows the tryptophan. Also mediating ALD interactions are the terminal acidic residues. Abbreviations: Tg, *T. gondii*; Nc, *N. caninum*; Pf, *P. falciparum*; Pb, *P. berghei*. UniProt accession numbers are provided beside each identifier.

Despite a concerted effort, co-crystallization experiments did not yield a co-crystal structure of TgALD with either adhesin C-tail. The unencumbered crystal lattice packing of the TgALDΔC mutant ($V_s \sim 56\%$ compared to $V_s \sim 42\%$ in native TgALD) provided an opportunity to reproduce the successful co-crystallization conditions obtained for ALD-LC4 ($V_s \sim 57\%$) (60) – however none of our solved structures displayed any evidence of adhesin binding. This is consistent with results from a recent study that investigated the structural basis of *Plasmodium* ALD binding to a related ligand (reticulocyte homology ligand) – similar difficulties in resolving bound ligand were noted: their co-crystal structure only reveals movements of helices within the ALD that indirectly suggest ligand binding (69). We favor the notion that ionic strength precluded binding of ligand in their crystallographic conditions. Likewise, the PfALD-TRAP co-crystal structure determined by Bosch et al. (23) is problematic for the following reasons: 1) The crystallographic conditions (50 *m*M cacodylic acid pH 6.0, 20% PEG 2000) may have favoured non-specific interactions (low ionic strength); 2) Recalculated simulated annealing difference omit maps show little evidence of electron density for the TRAP ligand in the active site. Our ITC binding experiments in conditions of high ionic strength provide the first indications that ionic strength may play a determining role in the interaction.

Ionic strength dependence of ALD-adhesin interaction. We evaluated the thermodynamic binding parameters by ITC for TgALD and the adhesin tails. Consistent with previous reports, we demonstrated the solution binding of MIC2t and AMA1t to TgALD. A modest difference in binding affinity between AMA1t and AMA1t-25 (2.9 μM and 1.5 μM respectively) suggests little participation of distal residues to ALD-binding. Marginally stronger affinities for the longer MIC2t variants suggest the distal residues participate in binding.

The absence of ligand in our co-crystal structures prompted control binding experiments in conditions reflecting the crystallographic solution that produced TgALD crystals. These conditions of higher ionic strength (summarized in Table 5-1) indicated an ionic strength dependence of the TgALD-adhesin interaction, in which binding is weakened or eliminated when the ionic strength surpasses 0.1. Likewise, increasing the Tris buffer concentration from 5 *m*M to 100 *m*M (ionic strengths of 0.004 and 0.084 respectively), reduces the binding affinity by 3-fold. This brings into question the biological significance of ALD-adhesin binding, and is coherent with a recent controversial finding suggesting ALD is primarily important for energy

metabolism rather than interacting with micronemal adhesins (31). The authors demonstrated that ALD-depleted *T. gondii* cells were sensitive to glucose but showed normal motility and host-cell invasion when grown without glucose, suggesting that ALD does not realize an essential role in these important aspects of parasite biology.

At present, the nature of the ionic strength dependence of the ALD-adhesin interaction is unclear. One indication that MIC2t readily associates with cations comes from the nominal mass determination by mass spectrometry of the purified MIC2t peptide. In addition to the primary peak at the expected molecular weight (5536 Da), we observed several minor peaks at higher weights corresponding to integer multiples of sodium ions (70) (**Figure S5-8**). Whether these minor species represent artefacts introduced by the mass spectrometry protocol or the purification process is unclear. It nevertheless suggests that the acidic peptides can interact with multiple cations in solution. These can ultimately interfere with peptide binding to ALD and may result in the weaker interactions that were observed.

The influence of salt ions on protein-protein interactions is poorly understood, and therefore affinity modulations by salts are difficult to rationalize (71). Factors to consider include the biophysical properties of proteins and salt ions such as the net charge, surface charge density and hydrophobicity of the protein and hydration, size, polarizability and valency of salt ions (72). In general, we can anticipate that the competitive bindings of cations and anions (ionic screening) for protein surface determine the final effect on protein-peptide interactions, and is especially relevant for electrostatic interactions, which are critical to ALD-adhesin binding. The apparent discrepancy between TgALD and rabbit muscle ALD in successfully co-crystallizing acidic peptides is intriguing since their isoelectric points are comparable (p*I* = 7.6 and 8.4 respectively) and the residues forming the basic groove to which the acidic cluster interacts are conserved. The ionic strength dependency of rabbit muscle ALD binding to acidic peptides (WASP, LC4) for which co-structures are solved has not been tested. However, the ionic strength dependence of ALD and actin association, which overlaps with the adhesin binding site, was evaluated both *in vitro* and *in silico*. In general, *in vitro* studies reveal that the interaction diminishes with increasing ionic strength (73–75), showing complete disruption for some buffer conditions (76), but in others remaining appreciable at physiological ionic strength (0.1 – 0.15 M) (73). This was confirmed by a Brownian dynamics simulation approach that showed a diminish in the degree of association between F-actin and glycolytic enzymes as ionic

strength increases but remained significant at physiological ionic strengths (77). *In vitro* binding assays, such as F-actin binding assays, are often conducted in lower ionic strengths (0.01 – 0.05 M) in order to enhance potential interactions (78). Likewise, the interactions between TgALD and MIC2/AMA1 were demonstrated by GST pull-down from cell lysates resuspended in a buffer composed of 50 *m*M KCl, 20 *m*M Hepes pH 7.5, 2 *m*M $MgCl_2$ and 0.2 *m*M EDTA (9, 31, 67), with an ionic strength of 0.064 – well within the range of binding demonstrated by ITC. To gain a fuller appreciation of this phenomenon in aldolase-adhesin binding and its relevance at physiological ionic strengths, a systematic investigation is required.

Adhesin mode of binding to TgALD. The binding isotherms provide insight into the mode of binding. The driving force for the TgALD-adhesin interaction is entropic, consistent with an entropic gain from displacement of the anchored TgALD C-terminal region as well as solvation entropy from expulsion of water molecules near the active site. The positive ΔH for native TgALD binding to adhesin tails taken together with the negative ΔH observed for the same pairs with TgALDΔC confirms the displacement of the C-terminal region of ALD upon adhesin tail binding that causes unfavourable disruption of existing intramolecular interactions (hydrogen bonding) within ALD. In the TgALDΔC variant, the lack of pre-existing C-terminal attachment near the active site suggests the negative ΔH observed with TgALDΔC directly reflects the non-bonded interactions that form between TgALD and the adhesin tails. These observations are consistent with binding of the adhesin C-tails near the active site.

Perspectives. The recent finding showing the dispensability of TgALD to host-cell invasion of parasites (31) taken together with our *in vitro* binding experiments at high ionic strength force a revision of the current model. It is conceivable that the interaction occurs *in vivo* but that redundant adaptors exist which may also contribute to the bridging function, including other glycolytic enzymes such as GAPDH which is also known to interact with adhesin tails (69). Indeed, longitudinal intensity profiling by 3D immunofluorescence microscopy of the distribution of aldolase in invading *Plasmodium* merozoite shows actin and aldolase present at or immediately behind the tight junction as the parasite enters the host cell (79). It is conceivable that aldolase localizes with the junction during invasion, providing the gliding motor a direct access to energy production during invasion. Nevertheless, a more recent study in *Plasmodium*

corroborated an important role for the aldolase-TRAP interaction, complicating the model (80). It has also been recently proposed that the interaction between apical proteins and aldolase is regulated by phosphorylation/dephosphorylation events that modulate invasion of *Plasmodium* merozoites into erythrocytes, as shown with phosphorylated adhesin C-domains using biolayer interferometry (81). The recent studies indicating a role for aldolase in mediating a bridging function may be reconciled to the contesting genetic studies by considering the destabilizing consequences of high concentrations of FBP on membrane bilayers (82), as anticipated in ALD-depleted parasites. There are indications that FBP is a potent calcium and divalent ion chelator, and high FBP concentrations chelate the counterbalancing ions that interact with the phospholipid head groups of the lipid bilayer, affecting membrane stability (82). Disruption of the membrane by FBP accumulation may provoke host-cell invasion by an unknown mechanism – this needs to be considered for future study. Manifestly, defining these pathways remains a priority for future study as gliding motility and host-cell invasion are critical for parasite survival and dissemination.

REFERENCES

1. Sibley, L. D. (2004) Intracellular Parasite Invasion Strategies. *Science*. **304**, 248–253

2. Dobrowolski, J. M., and Sibley, L. D. (1996) Toxoplasma invasion of mammalian cells is powered by the actin cytoskeleton of the parasite. *Cell*. **84**, 933–939

3. Dobrowolski, J. M., Carruthers, V. B., and Sibley, L. D. (1997) Participation of myosin in gliding motility and host cell invasion by Toxoplasma gondii. *Mol. Microbiol.* **26**, 163–173

4. Wetzel, D. M., Håkansson, S., Hu, K., Roos, D., and Sibley, L. D. (2003) Actin Filament Polymerization Regulates Gliding Motility by Apicomplexan Parasites. *Mol. Biol. Cell*. **14**, 396–406

5. Drewry, L. L., and Sibley, L. D. (2015) Toxoplasma Actin Is Required for Efficient Host Cell Invasion. *mBio*. **6**, e00557-15

6. Meissner, M., Schlüter, D., and Soldati, D. (2002) Role of Toxoplasma gondii Myosin A in Powering Parasite Gliding and Host Cell Invasion. *Science*. **298**, 837–840

7. Gaskins, E., Gilk, S., DeVore, N., Mann, T., Ward, G., and Beckers, C. (2004) Identification of the membrane receptor of a class XIV myosin in Toxoplasma gondii. *J. Cell Biol.* **165**, 383–393

8. Opitz, C., and Soldati, D. (2002) "The glideosome": a dynamic complex powering gliding motion and host cell invasion by Toxoplasma gondii. *Mol. Microbiol.* **45**, 597–604

9. Jewett, T. J., and Sibley, L. D. (2003) Aldolase forms a bridge between cell surface adhesins and the actin cytoskeleton in apicomplexan parasites. *Mol. Cell*. **11**, 885–894

10. Urban, S., and Freeman, M. (2003) Substrate Specificity of Rhomboid Intramembrane Proteases Is Governed by Helix-Breaking Residues in the Substrate Transmembrane Domain. *Mol. Cell*. **11**, 1425–1434

11. Robson, K. J., Frevert, U., Reckmann, I., Cowan, G., Beier, J., Scragg, I. G., Takehara, K., Bishop, D. H., Pradel, G., and Sinden, R. (1995) Thrombospondin-related adhesive protein (TRAP) of Plasmodium falciparum: expression during sporozoite ontogeny and binding to human hepatocytes. *EMBO J.* **14**, 3883–3894

12. Robson, K. J. H., Hall, J. R. S., Jennings, M. W., Harris, T. J. R., Marsh, K., Newbold, C. I., Tate, V. E., and Weatherall, D. J. (1988) A highly conserved amino-acid sequence in thrombospondin, properdin and in proteins from sporozoites and blood stages of a human malaria parasite. *Nature*. **335**, 79–82

13. Wan, K.-L., Carruthers, V. B., Sibley, L. D., and Ajioka, J. W. (1997) Molecular characterisation of an expressed sequence tag locus of Toxoplasma gondii encoding the micronemal protein MIC2. *Mol. Biochem. Parasitol.* **84**, 203–214

14. Huynh, M.-H., and Carruthers, V. B. (2006) Toxoplasma MIC2 Is a Major Determinant of Invasion and Virulence. *PLoS Pathog.* **2**, e84

15. Soldati, D., Dubremetz, J. F., and Lebrun, M. (2001) Microneme proteins: structural and functional requirements to promote adhesion and invasion by the apicomplexan parasite Toxoplasma gondii. *Int. J. Parasitol.* **31**, 1293–1302

16. Harper, J. M., Hoff, E. F., and Carruthers, V. B. (2004) Multimerization of the Toxoplasma gondii MIC2 integrin-like A-domain is required for binding to heparin and human cells. *Mol. Biochem. Parasitol.* **134**, 201–212

17. Ménard, R. (2001) Gliding motility and cell invasion by Apicomplexa: insights from the Plasmodium sporozoite. *Cell. Microbiol.* **3**, 63–73

18. Carruthers, V. B., Giddings, O. K., and Sibley, L. D. (1999) Secretion of micronemal proteins is associated with toxoplasma invasion of host cells. *Cell. Microbiol.* **1**, 225–235

19. Kappe, S., Bruderer, T., Gantt, S., Fujioka, H., Nussenzweig, V., and Ménard, R. (1999) Conservation of a Gliding Motility and Cell Invasion Machinery in Apicomplexan Parasites. *J. Cell Biol.* **147**, 937–944

20. Jewett, T. J., and Sibley, L. D. (2004) The Toxoplasma Proteins MIC2 and M2AP Form a Hexameric Complex Necessary for Intracellular Survival. *J. Biol. Chem.* **279**, 9362–9369

21. Buscaglia, C. A., Coppens, I., Hol, W. G. J., and Nussenzweig, V. (2003) Sites of Interaction between Aldolase and Thrombospondin-related Anonymous Protein in Plasmodium. *Mol. Biol. Cell*. **14**, 4947–4957

22. Starnes, G. L., Coincon, M., Sygusch, J., and Sibley, L. D. (2009) Aldolase Is Essential for Energy Production and Bridging Adhesin-Actin Cytoskeletal Interactions during Parasite Invasion of Host Cells. *Cell Host Microbe.* **5**, 353–364

23. Bosch, J., Buscaglia, C. A., Krumm, B., Ingason, B. P., Lucas, R., Roach, C., Cardozo, T., Nussenzweig, V., and Hol, W. G. J. (2007) Aldolase provides an unusual binding site for thrombospondin-related anonymous protein in the invasion machinery of the malaria parasite. *Proc. Natl. Acad. Sci. U. S. A.* **104**, 7015–7020

24. Mital, J., Meissner, M., Soldati, D., and Ward, G. E. (2005) Conditional Expression of Toxoplasma gondii Apical Membrane Antigen-1 (TgAMA1) Demonstrates That TgAMA1 Plays a Critical Role in Host Cell Invasion. *Mol. Biol. Cell.* **16**, 4341–4349

25. Triglia, T., Healer, J., Caruana, S. R., Hodder, A. N., Anders, R. F., Crabb, B. S., and Cowman, A. F. (2000) Apical membrane antigen 1 plays a central role in erythrocyte invasion by Plasmodium species. *Mol. Microbiol.* **38**, 706–718

26. Hehl, A. B., Lekutis, C., Grigg, M. E., Bradley, P. J., Dubremetz, J.-F., Ortega-Barria, E., and Boothroyd, J. C. (2000) Toxoplasma gondii Homologue ofPlasmodium Apical Membrane Antigen 1 Is Involved in Invasion of Host Cells. *Infect. Immun.* **68**, 7078–7086

27. Alexander, D. L., Mital, J., Ward, G. E., Bradley, P., and Boothroyd, J. C. (2005) Identification of the Moving Junction Complex of Toxoplasma gondii : A Collaboration between Distinct Secretory Organelles. *PLOS Pathog.* **1**, e17

28. Lamarque, M., Besteiro, S., Papoin, J., Roques, M., Normand, B. V.-L., Morlon-Guyot, J., Dubremetz, J.-F., Fauquenoy, S., Tomavo, S., Faber, B. W., Kocken, C. H., Thomas, A. W., Boulanger, M. J., Bentley, G. A., and Lebrun, M. (2011) The RON2-AMA1 Interaction is a Critical Step in Moving Junction-Dependent Invasion by Apicomplexan Parasites. *PLOS Pathog.* **7**, e1001276

29. Tonkin, M. L., Roques, M., Lamarque, M. H., Pugnière, M., Douguet, D., Crawford, J., Lebrun, M., and Boulanger, M. J. (2011) Host Cell Invasion by Apicomplexan Parasites: Insights from the Co-Structure of AMA1 with a RON2 Peptide. *Science.* **333**, 463–467

30. Richard, D., MacRaild, C. A., Riglar, D. T., Chan, J.-A., Foley, M., Baum, J., Ralph, S. A., Norton, R. S., and Cowman, A. F. (2010) Interaction between Plasmodium falciparum Apical Membrane Antigen 1 and the Rhoptry Neck Protein Complex Defines

a Key Step in the Erythrocyte Invasion Process of Malaria Parasites. *J. Biol. Chem.* **285**, 14815–14822

31. Shen, B., and Sibley, L. D. (2014) Toxoplasma aldolase is required for metabolism but dispensable for host-cell invasion. *Proc. Natl. Acad. Sci.* 10.1073/pnas.1315156111

32. Sheiner, L., Santos, J. M., Klages, N., Parussini, F., Jemmely, N., Friedrich, N., Ward, G. E., and Soldati-Favre, D. (2010) Toxoplasma gondii transmembrane microneme proteins and their modular design. *Mol. Microbiol.* 10.1111/j.1365-2958.2010.07255.x

33. Penhoet, E., Kochman, M., Valentine, R., and Rutter, W. J. (1967) The subunit structure of mammalian fructose diphosphate aldolase. *Biochemistry (Mosc.)*. **6**, 2940–2949

34. Sygusch, J., Beaudry, D., and Allaire, M. (1987) Molecular architecture of rabbit skeletal muscle aldolase at 2.7-A resolution. *Proc. Natl. Acad. Sci. U. S. A.* **84**, 7846–7850

35. Wang, J., Morris, A. J., Tolan, D. R., and Pagliaro, L. (1996) The Molecular Nature of the F-actin Binding Activity of Aldolase Revealed with Site-directed Mutants. *J. Biol. Chem.* **271**, 6861–6865

36. Zheng, B., Yin, Z.-K., He, A., Li, Z.-Y., and Zhan, X.-M. (2011) Protein interaction between aldolase and actin of Toxoplasma gondii by GST pull-down. *Zhongguo Ji Sheng Chong Xue Yu Ji Sheng Chong Bing Za Zhi*. **29**, 363–367

37. Lu, M., Ammar, D., Ives, H., Albrecht, F., and Gluck, S. L. (2007) Physical Interaction between Aldolase and Vacuolar H+-ATPase Is Essential for the Assembly and Activity of the Proton Pump. *J. Biol. Chem.* **282**, 24495–24503

38. Tunio, S. A., Oldfield, N. J., Berry, A., Ala'Aldeen, D. A. A., Wooldridge, K. G., and Turner, D. P. J. (2010) The moonlighting protein fructose-1, 6-bisphosphate aldolase of Neisseria meningitidis: surface localization and role in host cell adhesion. *Mol. Microbiol.* **76**, 605–615

39. St-Jean, M., Izard, T., and Sygusch, J. (2007) A Hydrophobic Pocket in the Active Site of Glycolytic Aldolase Mediates Interactions with Wiskott-Aldrich Syndrome Protein. *J. Biol. Chem.* **282**, 14309–14315

40. Derewenda, Z. S., and Vekilov, P. G. (2006) Entropy and surface engineering in protein crystallization. *Acta Crystallogr. D Biol. Crystallogr.* **62**, 116–124

41. Goldschmidt, L., Cooper, D. R., Derewenda, Z. S., and Eisenberg, D. (2007) Toward rational protein crystallization: A Web server for the design of crystallizable protein variants. *Protein Sci.* **16**, 1569–1576

42. Overton, I. M., and Barton, G. J. (2006) A normalised scale for structural genomics target ranking: The OB-Score. *FEBS Lett.* **580**, 4005–4009

43. Overton, I. M., Padovani, G., Girolami, M. A., and Barton, G. J. (2008) ParCrys: a Parzen window density estimation approach to protein crystallization propensity prediction. *Bioinforma. Oxf. Engl.* **24**, 901–907

44. Slabinski, L., Jaroszewski, L., Rychlewski, L., Wilson, I. A., Lesley, S. A., and Godzik, A. (2007) XtalPred: a web server for prediction of protein crystallizability. *Bioinformatics*. **23**, 3403–3405

45. Otwinowski, Z., and Minor, W. (1997) [20] Processing of X-ray diffraction data collected in oscillation mode. in *Methods in Enzymology* (Charles W. Carter, J. ed), pp. 307–326, Macromolecular Crystallography Part A, Academic Press, **276**, 307–326

46. Adams, P. D., Grosse-Kunstleve, R. W., Hung, L.-W., Ioerger, T. R., McCoy, A. J., Moriarty, N. W., Read, R. J., Sacchettini, J. C., Sauter, N. K., and Terwilliger, T. C. (2002) *PHENIX*: building new software for automated crystallographic structure determination. *Acta Crystallogr. D Biol. Crystallogr.* **58**, 1948–1954

47. McCoy, A. J., Grosse-Kunstleve, R. W., Adams, P. D., Winn, M. D., Storoni, L. C., and Read, R. J. (2007) *Phaser* crystallographic software. *J. Appl. Crystallogr.* **40**, 658–674

48. Söding, J. (2005) Protein homology detection by HMM–HMM comparison. *Bioinformatics*. **21**, 951–960

49. Afonine, P. V., Grosse-Kunstleve, R. W., Echols, N., Headd, J. J., Moriarty, N. W., Mustyakimov, M., Terwilliger, T. C., Urzhumtsev, A., Zwart, P. H., and Adams, P. D. (2012) Towards automated crystallographic structure refinement with *phenix.refine*. *Acta Crystallogr. D Biol. Crystallogr.* **68**, 352–367

50. Emsley, P., Lohkamp, B., Scott, W. G., and Cowtan, K. (2010) Features and development of *Coot*. *Acta Crystallogr. D Biol. Crystallogr.* **66**, 486–501

51. Karplus, P. A., and Diederichs, K. (2012) Linking Crystallographic Model and Data Quality. *Science*. **336**, 1030–1033

52. Chen, V. B., Arendall, W. B., Headd, J. J., Keedy, D. A., Immormino, R. M., Kapral, G. J., Murray, L. W., Richardson, J. S., and Richardson, D. C. (2010) MolProbity : all-atom structure validation for macromolecular crystallography. *Acta Crystallogr. D Biol. Crystallogr.* **66**, 12–21

53. *The PyMol Molecular Graphics System, Version 1.7.4, Schrodinger, LLC*

54. Waterhouse, A. M., Procter, J. B., Martin, D. M. A., Clamp, M., and Barton, G. J. (2009) Jalview Version 2—a multiple sequence alignment editor and analysis workbench. *Bioinformatics*. **25**, 1189–1191

55. Racker, E. (1947) Spectrophotometric measurement of hexokinase and phosphohexokinase activity. *J. Biol. Chem.* **167**, 843–854

56. St-Jean, M., and Sygusch, J. (2007) Stereospecific Proton Transfer by a Mobile Catalyst in Mammalian Fructose-1,6-bisphosphate Aldolase. *J. Biol. Chem.* **282**, 31028–31037

57. Rose, I. A., O'Connell, E. L., and Mehler, A. H. (1965) Mechanism of the Aldolase Reaction. *J. Biol. Chem.* **240**, 1758–1765

58. Kantardjieff, K. A., and Rupp, B. (2003) Matthews coefficient probabilities: Improved estimates for unit cell contents of proteins, DNA, and protein-nucleic acid complex crystals. *Protein Sci.* **12**, 1865–1871

59. Weichenberger, C. X., and Rupp, B. (2014) Ten years of probabilistic estimates of biocrystal solvent content: new insights *via* nonparametric kernel density estimate. *Acta Crystallogr. D Biol. Crystallogr.* **70**, 1579–1588

60. Rangarajan, E. S., Park, H., Fortin, E., Sygusch, J., and Izard, T. (2010) Mechanism of Aldolase Control of Sorting Nexin 9 Function in Endocytosis. *J. Biol. Chem.* **285**, 11983–11990

61. Kusakabe, T., Motoki, K., and Hori, K. (1997) Mode of Interactions of Human Aldolase Isozymes with Cytoskeletons. *Arch. Biochem. Biophys.* **344**, 184–193

62. Volker, K. W., and Knull, H. R. (1997) A Glycolytic Enzyme Binding Domain on Tubulin. *Arch. Biochem. Biophys.* **338**, 237–243

63. Navarro-Lérida, I., Martínez Moreno, M., Roncal, F., Gavilanes, F., Albar, J. P., and Rodríguez-Crespo, I. (2004) Proteomic identification of brain proteins that interact with dynein light chain LC8. *PROTEOMICS*. **4**, 339–346

64. Strapazon, E., and Steck, T. L. (1976) Binding of rabbit muscle aldolase to band 3, the predominant polypeptide of the human erythrocyte membrane. *Biochemistry (Mosc.)*. **15**, 1421–1424

65. Kim, J. H., Lee, S., Kim, J. H., Lee, T. G., Hirata, M., Suh, P.-G., and Ryu, S. H. (2002) Phospholipase D2 Directly Interacts with Aldolase via Its PH Domain. *Biochemistry (Mosc.)*. **41**, 3414–3421

66. Kao, A. W., Noda, Y., Johnson, J. H., Pessin, J. E., and Saltiel, A. R. (1999) Aldolase mediates the association of F-actin with the insulin-responsive glucose transporter GLUT4. *J. Biol. Chem.* **274**, 17742–17747

67. Starnes, G. L., Jewett, T. J., Carruthers, V. B., and Sibley, L. D. (2006) Two Separate, Conserved Acidic Amino Acid Domains within the Toxoplasma gondii MIC2 Cytoplasmic Tail Are Required for Parasite Survival. *J. Biol. Chem.* **281**, 30745–30754

68. Srinivasan, P., Beatty, W. L., Diouf, A., Herrera, R., Ambroggio, X., Moch, J. K., Tyler, J. S., Narum, D. L., Pierce, S. K., Boothroyd, J. C., Haynes, J. D., and Miller, L. H. (2011) Binding of Plasmodium merozoite proteins RON2 and AMA1 triggers commitment to invasion. *Proc. Natl. Acad. Sci.* **108**, 13275–13280

69. Pal-Bhowmick, I., Andersen, J., Srinivasan, P., Narum, D. L., Bosch, J., and Miller, L. H. (2012) Binding of Aldolase and Glyceraldehyde-3-Phosphate Dehydrogenase to the Cytoplasmic Tails of Plasmodium falciparum Merozoite Duffy Binding-Like and Reticulocyte Homology Ligands. *mBio*. 10.1128/mBio.00292-12

70. Keller, B. O., Sui, J., Young, A. B., and Whittal, R. M. (2008) Interferences and contaminants encountered in modern mass spectrometry. *Anal. Chim. Acta*. **627**, 71–81

71. Zangi, R. (2010) Can Salting-In/Salting-Out Ions be Classified as Chaotropes/Kosmotropes? *J. Phys. Chem. B*. **114**, 643–650

72. Zhang, J. (2012) *Protein-protein interactions in salt solutions*, INTECH Open Access Publisher, [online] http://cdn.intechopen.com/pdfs/34373/InTech-Protein_protein_interactions_in_salt_solutions.pdf (Accessed August 22, 2016)

73. Lakatos, S., and Minton, A. P. (1991) Interactions between globular proteins and F-actin in isotonic saline solution. *J. Biol. Chem.* **266**, 18707–18713

74. Shearwin, K., Nanhua, C., and Masters, C. (1990) Interactions between glycolytic enzymes and cytoskeletal structure--the influence of ionic strength and molecular crowding. *Biochem. Int.* **21**, 53–60

75. Walsh, J. L., and Knull, H. R. (1988) Heteromerous interactions among glycolytic enzymes and of glycolytic enzymes with F-actin: effects of poly(ethylene glycol). *Biochim. Biophys. Acta.* **952**, 83–91

76. Bronstein, W. W., and Knull, H. R. (1981) Interaction of muscle glycolytic enzymes with thin filament proteins. *Can. J. Biochem.* **59**, 494–499

77. Forlemu, N. Y., Njabon, E. N., Carlson, K. L., Schmidt, E. S., Waingeh, V. F., and Thomasson, K. A. (2011) Ionic Strength Dependence of F-actin and Glycolytic Enzyme Associations: A Brownian Dynamics Simulations Approach. *Proteins*. **79**, 2813–2827

78. Ouporov, I. V., Knull, H. R., and Thomasson, K. A. (1999) Brownian dynamics simulations of interactions between aldolase and G- or F-actin. *Biophys. J.* **76**, 17–27

79. Riglar, D. T., Whitehead, L., Cowman, A. F., Rogers, K. L., and Baum, J. (2016) Localisation-based imaging of malarial antigens during erythrocyte entry reaffirms a role for AMA1 but not MTRAP in invasion. *J Cell Sci*. **129**, 228–242

80. Nemetski, S. M., Cardozo, T. J., Bosch, G., Weltzer, R., O'Malley, K., Ejigiri, I., Kumar, K. A., Buscaglia, C. A., Nussenzweig, V., Sinnis, P., Levitskaya, J., and Bosch, J. (2015) Inhibition by stabilization: targeting the Plasmodium falciparum aldolase–TRAP complex. *Malar. J.* 10.1186/s12936-015-0834-9

81. Diaz, S. A., Martin, S. R., Howell, S. A., Grainger, M., Moon, R. W., Green, J. L., and Holder, A. A. (2016) The Binding of Plasmodium falciparum Adhesins and Erythrocyte Invasion Proteins to Aldolase Is Enhanced by Phosphorylation. *PLoS ONE*. 10.1371/journal.pone.0161850

82. Ehringer, W. D., Su, S., Chiang, B., Stillwell, W., and Chien, S. (2002) Destabilizing effects of fructose-1,6-bisphosphate on membrane bilayers. *Lipids*. **37**, 885–892

SUPPORTING INFORMATION

Table S5-1. Data collection and refinement statistics.

Native TgALD

Data Collection		Refinement	
Wavelength (Å)	1.075	Reflections used in refine	32662 (2916)
Resolution range (Å)	38.97 - 1.78 (1.84 - 1.78)[a]	Reflections used for R_{free}	2000 (179)
Space group	P 42 21 2	R_{work} (%) [d]	0.1549 (0.2843)
Unit cell a (Å), b (Å), c (Å), (°)	110.2 110.2 54.9 90 90 90	R_{free} (%) [e]	0.1995 (0.3352)
Total reflections	426298 (25526)	CC_{work}	0.972 (0.788)
Unique reflections	32599 (2922)	CC_{free}	0.952 (0.715)
Multiplicity	13.1 (8.9)	Number of non-H atoms	2991
Completeness (%)	0.99 (0.89)	macromolecules	2653
Average $I/\sigma(I)$	20.82 (1.48)	ligands	6
Wilson B-factor	24.57	Protein residues	348
R-merge [b]	0.085 (1.243)	RMSD (bond length) (Å)	0.010
R-meas [c]	0.089 (1.322)	RMSD (angles) (°)	1.20
CC1/2	1 (0.593)	Ramachandran favored (%)	97
CC*	1 (0.863)	Ramachandran allowed (%)	2.3
		Ramachandran outliers (%)	0.29
		Rotamer outliers (%)	0.72
		Clashscore	2.24
		Average B-factor (Å^2)	33.91
		macromolecules	32.58
		ligands	63.55
		solvent	43.97
		TLS groups	1

[a] All values in parentheses are given for the highest resolution shell.
[b] $R_{merge} = \sum_{hkl}\sum_{i}|I_i(hkl) - \bar{I}_i(hkl)|/\sum_{hkl}\sum_{i}I_i(hkl)$, with i running over the number of independent observations of reflection hkl.
[c] $R_{meas} = \sum_{hkl}(n/(n-1))^{1/2}\sum_{i=1}^{n}|I_i(hkl) - \bar{I}_i(hkl)|/\sum_{hkl}\sum_{i}I_i(hkl)$,
[d] $R_{work} = \sum_{hkl}||I_o(hkl)| - |I_c(hkl)||/\sum_{hkl}|I_o(hkl)|$.
[e] $R_{free} = \sum_{hkl \in T}||I_o(hkl)| - |I_c(hkl)||/\sum_{hkl \in T}|I_o(hkl)|$, where T is a test data set randomly selected from the observed reflections prior to refinement. Test data set was not used throughout refinement and contains a minimum of 2000 unique reflections (or 5%) (the smaller value is selected).

Figure S5-1. TgALD fold.

TgALD adopts the prototypical TIM-barrel (α/β)$_8$ fold. Helices are shown in *blue* and sheets in *yellow*. The assymetric unit consists of one subunits (left panel) and the symmetry mates reveal the tetrameric nature of TgALD (right panel).
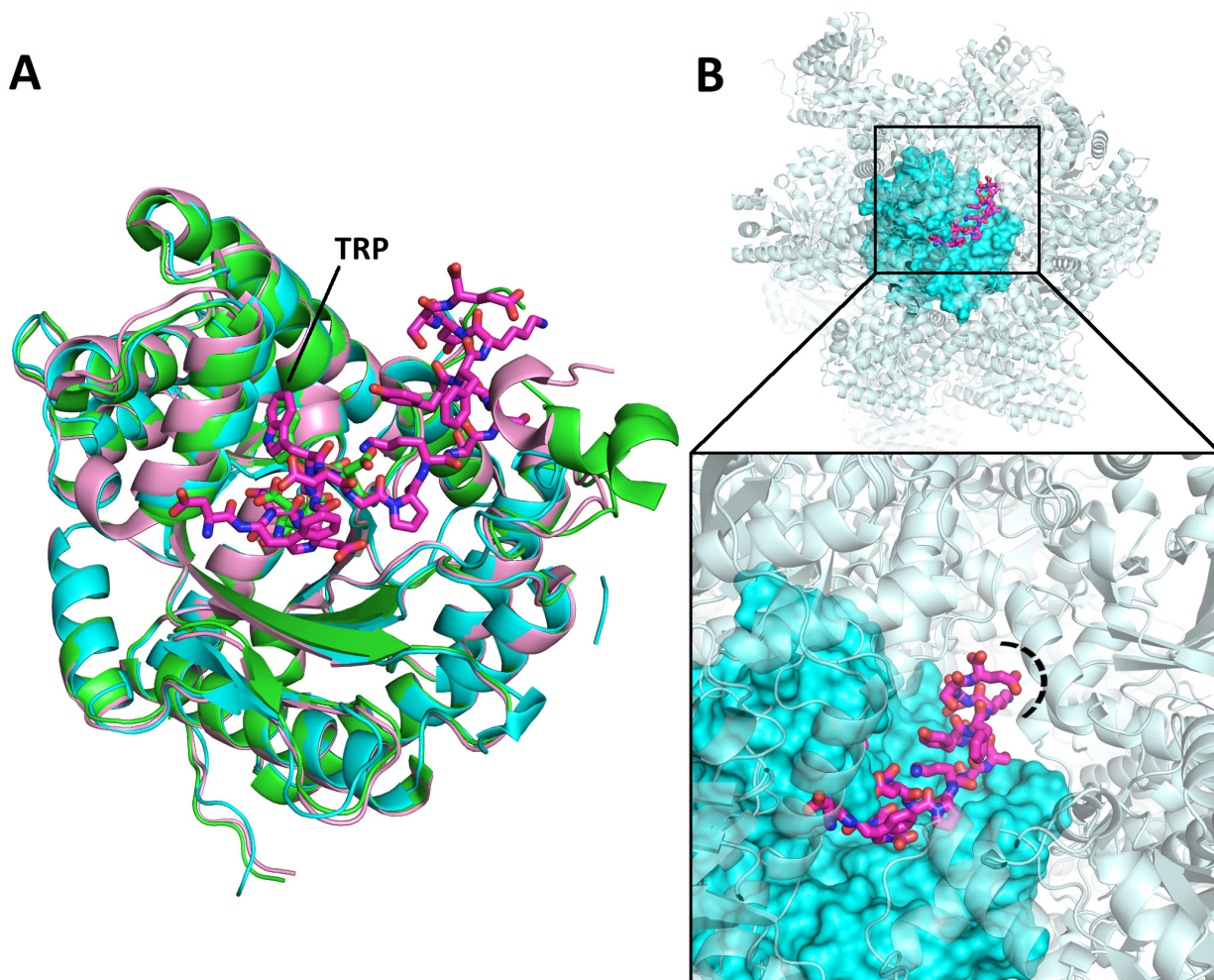
Figure S5-2. Superposition of WASP and LC4 peptides onto TgALD structure.

(A) Native TgALD (*cyan*) is superposed with previously resolved co-crystal structures of ALD-LC4 (PDB: 3LGE) (*pink*) and ALD-WASP (PDB: 2OT0) (*green*). The tertiary fold of TgALD is markedly similar to the rabbit muscle ALD fold shown in green and pink. LC4 (magenta) and WASP (*green*) peptides are shown overlapping the catalytic cleft. Of the 31 C-terminal LC4 residues co-crystallized with ALD, 19 are visible in the structure. The penultimate tryptophan (TRP) shared by TRAP family tails intercalates between two conserved arginines. The common acidic motif binds a basic lining that continuous outside the active cleft. **(B)** The higher-order structure with symmetry mates in the native TgALD structure (SG: P 42 21 2) is shown. Based on previous reports suggesting a similar mode of binding for TRAP-peptides, LC4 serves as an appropriate guide for modeling TRAP-peptide binding (LC4 modeled directly on TgALD). In its current crystalline state, the tight packing would produce a steric clash (dashed line in close-up panel) that would preclude peptide binding.

A TgALD-MIC2t

Time (min)
-10 0 10 20 30 40 50 60 70 80 90 100 110 120 130 140 150 160

Data: run1TgAwtMi_NDH
Model: OneSites
Chi^2/DoF = 886.7
N   1.52   ±0.0470 Sites
K   4.79E4 ±1.81E3 M^{-1}
∅H   7300   ±275.2 cal/mol
∅S   45.9 cal/mol/deg

B TgALD-MIC2t-25

Time (min)
0   10   20   30   40   50

Data: gALDMIC225_NDH
Model: OneSites
Chi^2/DoF = 1.846E4
N   2.01   ±0.0386 Sites
K   8.40E4 ±6.58E3 M^{-1}
ΔH   1.471E4   ±451.1 cal/mol
ΔS   71.9 cal/mol/deg

C TgALD-MIC2t-15

Time (min)
-10   0   10   20   30   40   50   60   70   80

Data: PH001_NDH
Model: OneSites
Chi^2/DoF = 894.2
N   1.01   ±0.0181 Sites
K   6.22E4 ±4.52E3 M^{-1}
∅H   3292   ±94.56 cal/mol
∅S   33.0 cal/mol/deg

Figure S5-3. ITC binding isotherms for TgALD and MIC2 C-tails.

210

A TgALD-AMA1t

Time (min)

Data: run1TgAwtAm_NDH
Model: OneSites
Chi^2/DoF = 4716
N   1.09   ±0.00870 Sites
K   3.41E5 ±1.00E4 M^{-1}
∆H   1.236E4   ±130.2 cal/mol
∆S   66.8 cal/mol/deg

B TgALD-AMA1t-25

Time (min)

Data: A25ph74run_NDH
Model: OneSites
Chi^2/DoF = 5.087E4
N   1.57   ±0.0153 Sites
K   6.76E5 ±7.59E4 M^{-1}
∆H   1.255E4   ±174.9 cal/mol
∆S   68.8 cal/mol/deg
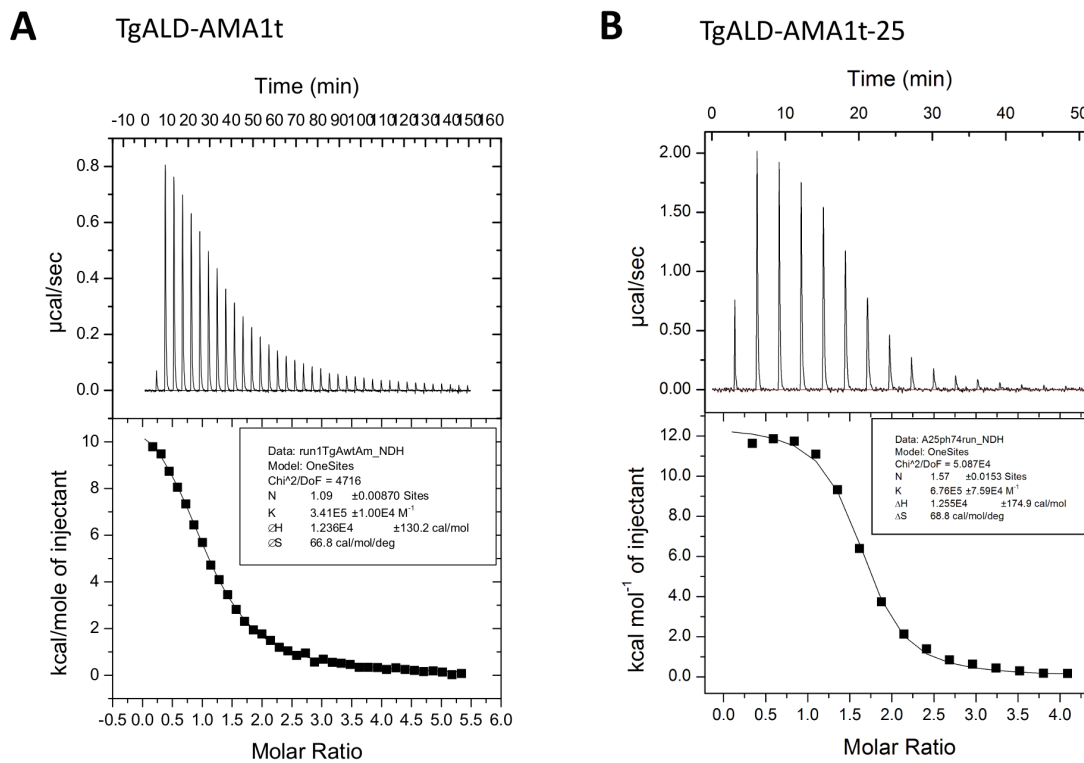
Figure S5-4. ITC binding isotherms for TgALD and AMA1 C-tails.
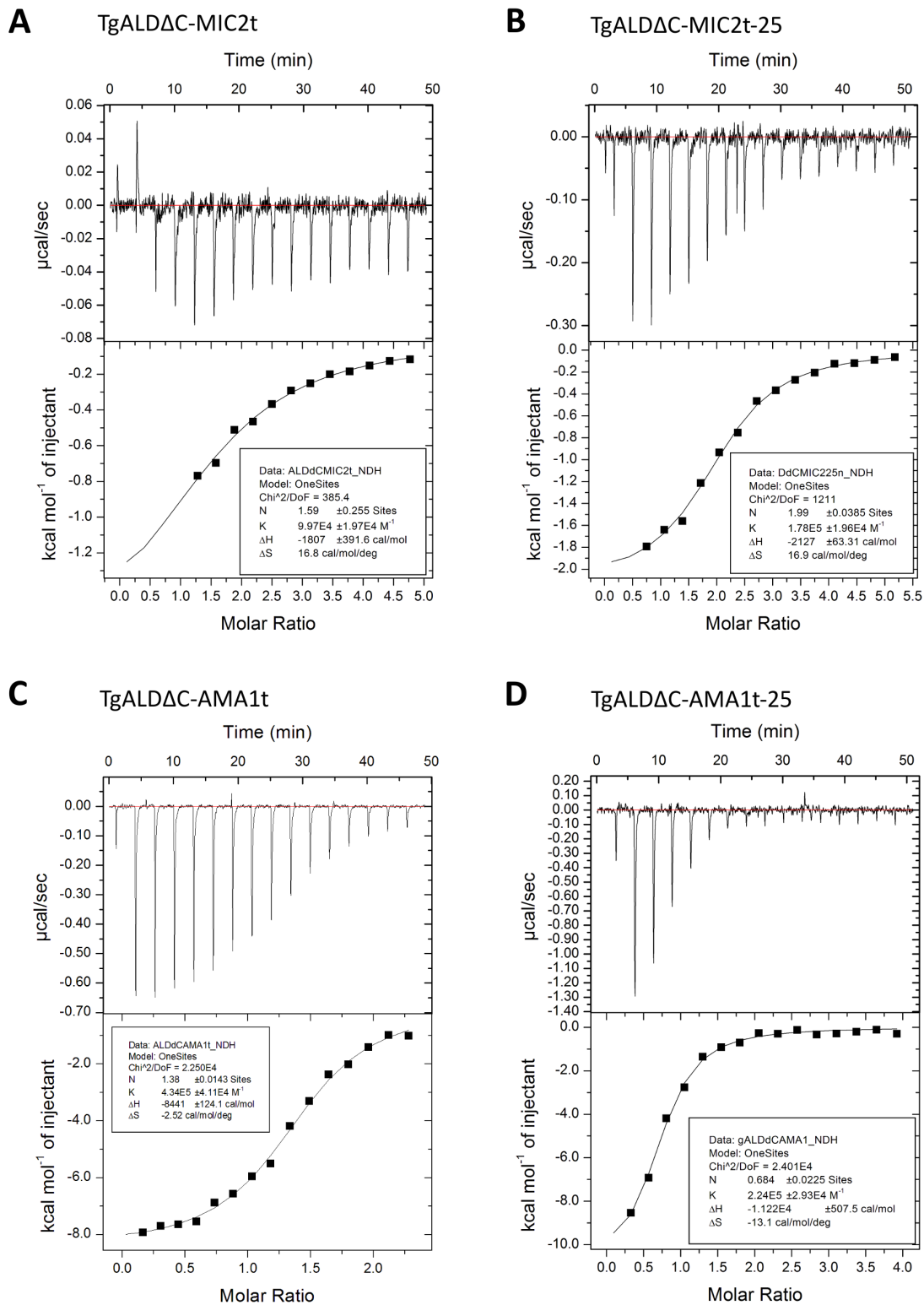
Figure S5-5. ITC binding isotherms for TgALDΔC variant and MIC2/AMA1 C-tails.

212

A TgALD-MIC2t-25
TRIS 100mM 7.4

Time (min)

Data: run5TgAMic2_NDH
Model: OneSites
Chi^2/DoF = 1.535E4
N   1.37   ±0.155 Sites
K   5.88E4 ±5.39E4 M⁻¹
ΔH   2454   ±665.1 cal/mol
ΔS   30.1 cal/mol/deg

B TgALD-MIC2t-25
TRIS 5mM 7.4

Time (min)

Data: gALDMIC225_NDH
Model: OneSites
Chi^2/DoF = 3.305E4
N   1.95   ±0.0253 Sites
K   1.71E5 ±1.21E4 M⁻¹
ΔH   1.623E4   ±313.9 cal/mol
ΔS   78.4 cal/mol/deg

C TgALD-MIC2t-25
NaAc 20mM 5.5

Time (min)

Data: A2520mMrun_NDH
Model: OneSites
Chi^2/DoF = 7574
N   2.96   ±0.0475 Sites
K   3.27E5 ±6.93E4 M⁻¹
ΔH   2182   ±50.38 cal/mol
ΔS   32.5 cal/mol/deg

D TgALD-AMA1t-25
NaAc 20mM 5.5

Time (min)

Data: A25ph55run_NDH
Model: OneSites
Chi^2/DoF = 1.556E4
N   1.53   ±0.0990 Sites
K   1.64E5 ±4.24E4 M⁻¹
ΔH   4503   ±528.9 cal/mol
ΔS   39.0 cal/mol/deg

Figure S5-6. ITC binding isotherms for TgALD adhesin C-tails in varied experimental conditions.

213

A TgALD-MIC2t-25
TRIS 100mM 8.5, LiSO4 100mM
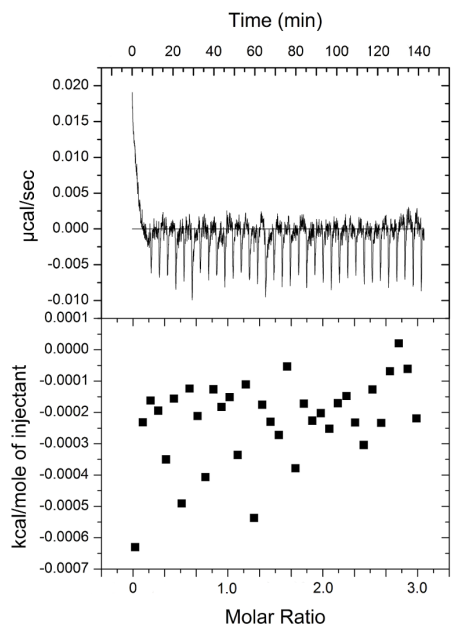
B TgALDΔC-MIC2t-25
TRIS 100mM 7.4
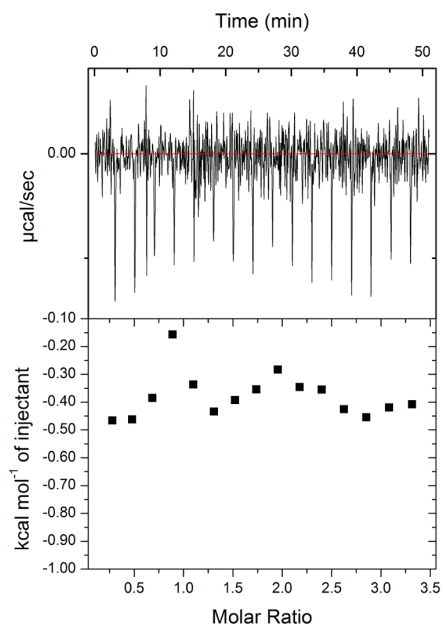
Figure S5-7. ITC binding isotherms showing no binding for TgALD and TgALDΔC with MIC2t-25 in conditions of high ionic strength.
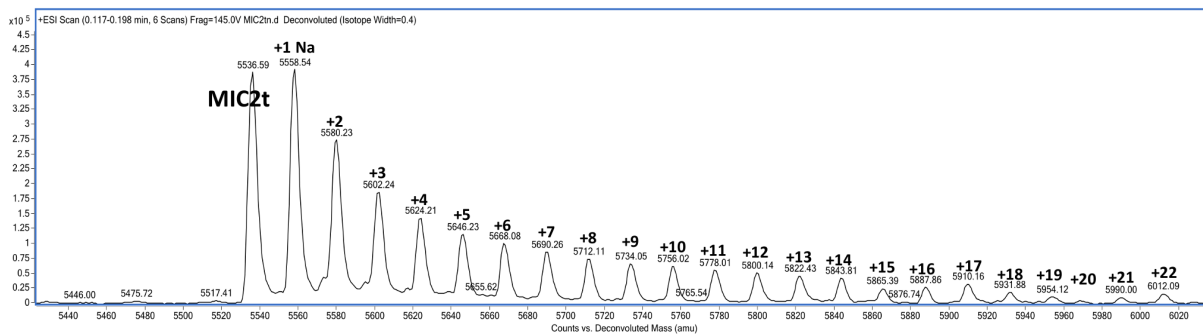
Figure S5-8. Nominal mass determination of MIC2t by ESI-MS.

Purified cytoplasmic MIC2 C-terminus (MIC2t) (Theoretical weight: 5536 Da) purity and weight was verified by mass spectrometry. Several sub-species of MIC2t were found corresponding to bound integer multiples of sodium (Na) (up to 22 Na bound).

Chapter 6

Discussion & Perspectives

Synopsis

The goal of this thesis was to explore unresolved questions related to the many activities of class I aldolases and discover ways to modulate these activities. Our studies have provided valuable insights on several fronts, including activities related to its mechanism, moonlighting functions, and strategies for disrupting these activities. Here, with the perspective of an ensemble view, the different elements of my thesis are reviewed and outstanding questions are addressed.

6.1 Investigation of novel aspects of the reaction mechanism and promiscuous catalytic activities

6.1.1 Stereoselectivity of the class I FBP aldolase addition reaction

In the first part of the thesis, we started by considering the reaction geometry of aldol addition in fructose-bisphosphate aldolases. Previous structural work in our laboratory trapped the rabbit muscle aldolase-FBP complex corresponding to the postulated Schiff-base intermediate having a reaction geometry consistent with incipient C3-C4 bond cleavage catalyzed by Glu-187, which is adjacent to the Schiff-base forming Lys-229 (St-Jean et al., 2005). From this work, it was suggested that atom arrangement about the C3-C4 bond adopts a pericyclic-like transition state occurring in nonenzymatic aldol additions. Our study sought to demonstrate this intermediate in the pre-condensation state, which we accomplished by trapping substrate in pre-equilibrium conditions using native class I aldolase crystals from *T. gondii*.

The ternary structure, aldolase-enamine-G3P, represents the first successful trapping of the elusive intermediate in class I FBP aldolases, confirming the identity of glutamate (TgALD Glu-189) as the acid responsible for proton donation to the G3P O1 carbonyl during aldol addition. Interestingly, we trapped the *cis*-aldehyde form of G3P, a condensation incompetent transition in the reaction pathway (summarized in Figure 6-1). The *cis*-configuration describes the geometry of G3P O1 and O2 respectively around the C1-C2 bond. In the *cis*-configuration, the *re*-face of the carbonyl group opposes the incoming nucleophile, the C3 carbanion of the bound

DHAP. However, aldol addition in FBP aldolases is only productive when the G3P aldehyde *si*-face is opposite the nucleophile, producing the 3*(S)*-4*(R)* stereoisomer, FBP. Condensation on the G3P *re*-face would produce tagatose-1,6-bisphosphate (TBP), the 3*(S)*-4*(S)* epimer. The non-processivity with the *re*-face was confirmed enzymatically by the absence of FBP aldolase reactivity towards TBP. TBP exhibits competitive inhibition with a K_i of 125 ± 16 μM. The ternary structure reveals the molecular basis for the stereospecific active site discrimination at the C4 substrate position.

The bound *cis*-configuration of G3P served as a guide for modeling of the addition-competent *trans*-configuration (shown in *cyan* - Figure 6-1) that presents the aldehyde *si*-face to the nascent nucleophile. The limited conformational freedom afforded by the fixation of the phosphate group at the P6-site through a network of hydrogen bonds comprising the conserved residues Ser-36, Thr-39, and Lys-107, allowed us to confidently map the *trans*-geometry. The *cis*-G3P C2 hydroxyl contacts the enzyme through a bridging water molecule (Wat-2) (3.0Å) that is coordinated (3.2Å) to Ala-32 backbone carbonyl. The *cis*-G3P aldehyde is also stabilized by an ordered water molecule (Wat-1) (2.8Å) that is coordinated with the phosphate oxyanion of the bound DHAP (2.6Å). We speculated the involvement of Wat-1 as the acid in the proton exchange reaction with G3P aldehyde prior to condensation. However, this is inconsistent with observations that FBP aldolase do not generate TBP, the result of aldol addition to the *cis*-form. TBP soaked at high concentrations in rabbit muscle aldolase crystals only shows electron density at the phosphate loci (St-Jean et al., 2005). Yet, our structures at equilibrium consist of fully occupied FBP (not TBP), suggesting that condensation cannot occur between the enamine and *cis*-G3P. Considering the above constraints and following the principle of least atomic motion, we predicted rotational freedom around the C-C bonds of G3P (C1-C2 and C2-C3). This was validated by a simple relaxation of the G3P with an Amber force field showing the fixation of the phosphate group at the P6-site (affording negligible movements) and a larger displacement at the aldehyde-extremity (> 1Å movement).

The *cis*-G3P aldehyde hydrogen bonds with the carboxylate of Glu-189 (2.9Å) (Figure 6-1). Seemingly, this distance is insufficient for proton transfers since at equilibrium (> 10 minutes of soaking time with FBP), TBP is not observed in electron density maps. Theoretical and experimental requirements for proton transfers demand the coupling of the proton
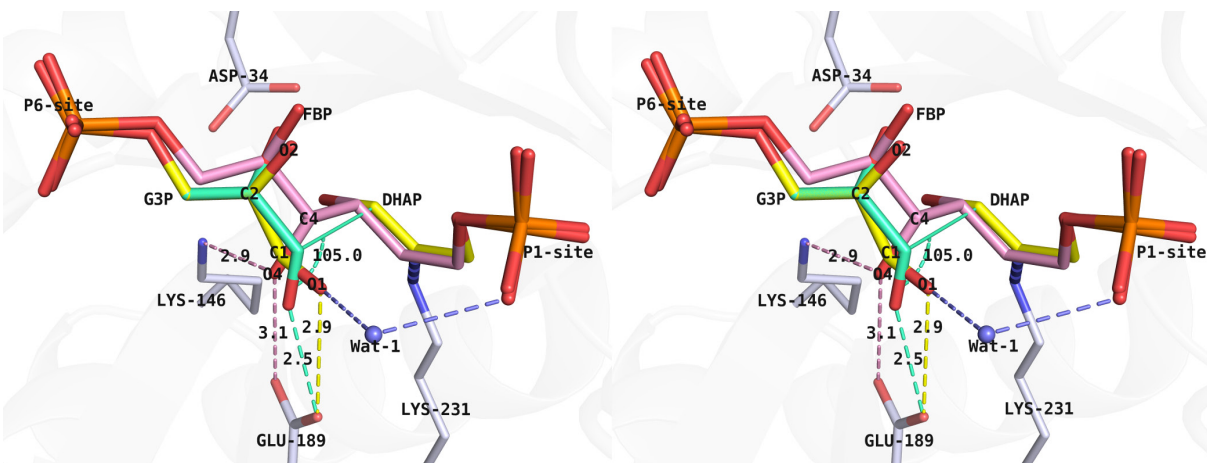
Figure 6-1. Pre-aldol addition reaction trajectory in class I FBPAs (stereo view).

In *yellow* is shown *cis*-G3P ternary structure with covalently bound DHAP in the *T. gondii* ALD active site. G3P is *cis* with respect to the O1 and O2 geometry about the C1-C2 bond. In this configuration, the interaction with Glu-189 is too short for proton transfer (*yellow dash* – 2.9Å). Wat-1 provides a structural anchor point that positions the G3P aldehyde next to the covalent enamine. Rotation of the aldehyde to the *trans* position (*cyan*), whilst mitigating steric interference from Lys-146, creates the desired short hydrogen bond with Glu-189 (*cyan dash* – 2.5Å) that polarizes the aldehyde and catalyzes aldol addition. An ideal nucleophilic approach angle of 105° (∠DHAP C2⋯G3P C1 – G3P O1), known as the Bürgi-Dunitz angle (α_{BD}), arises during nascent bond formation. The product of the aldol addition, a covalent Schiff base FBP, is illustrated in *pink* and key interactions of the O4 hydroxyl to Glu-189 and Lys-146 are shown as *pink dashes*.

donor/acceptor moieties to an length of 2.5Å – 2.6Å (Ishikita and Saito, 2014). Rotating the C2-C3 dihedral angle by 20° brings *cis*-G3P aldehyde to within ideal proton transfer distance of Glu-189, but induces a steric clash between the G3P C1 carbon and Lys-146 amino group (2.7Å). Thus, proton transfer is inaccessible in the *cis*-configuration. Likewise, Wat-1, at 2.8Å from the aldehyde is equally out of reach for proton transfer, negating production of the 4(*S*) epimer (TBP). The only conceivable conformational change that encourages proton transfer whilst mitigating steric clashes is a *cis-trans* isomerization involving the following G3P dihedrals: C1-C2, +155°; and C2-C3, -20°.

A role for Glu-189 as the general acid in the aldol addition reaction is consistent with its proximity to Lys-146, which stabilizes the developing negative charge during the proton transfer. As it is equidistant to FBP C4 hydroxyl and Glu-189 carboxylate, in the cleavage direction, Lys-146 hydrogen bonds the substrate C4 hydroxyl and assists cleavage by stabilizing

the developing negative charge on the latter; similarly, in the condensation direction, Lys-146 stabilizes the developing charge on Glu-189.

Finally, the question of whether the *cis*-ternary complex is relevant and on the reaction pathway is addressed here. Is there a need for such a complex? We know from previous studies that G3P only enters the condensation pathway after DHAP-enamine formation (Rose and Warms, 1985). The G3P binding energy is satisfied primarily by interactions at the phosphate loci, whereas the G3P carbon frame exhibits torsional freedom. Our structure reveals a mechanism used by FBP aldolases to juxtapose the aldehyde near the enamine prior to aldol addition. Wat-1 fixes the aldehyde in the *cis* position, which subsequently rotates to *trans* during condensation. The stereospecificity of the reaction is guaranteed by the spatial disposition of Glu-189 and Lys-146, which precludes condensation on the non-polarized *cis*-aldehyde. Therefore, it is reasonable to suggest that proper alignment of G3P in its binding cavity is guaranteed by the *cis*-position. These findings are complementary to mechanistic work conducted in our laboratory on a related aldolase, tagatose-bisphosphate aldolase (TBPA) from Streptococcus pyogenes, which is indiscriminate towards the four 3(*S/R*) – 4(*S/R*) stereoisomers: 3(*S*)-4(*R*)-fructose-1,6-bisphosphate (FBP), 3(*S*)-4(*S*)-tagatose-1,6-bisphosphate (TBP), and 3(*R*)-4(*S*)-sorbose-1,6-bisphosphate et 3(*R*)-4(*R*)-psicose-1,6-bisphosphate (Low-Kam, 2015).

In these studies, it was shown that TBPA produces the 3(S/R) epimers by a *cis-trans* isomerization around the C2-C3 bond of the DHAP covalent intermediate, catalyzed by a nearby catalytic water, allowing the enamine to attack from both its *re*- and *si*-face. Additionally, it was shown that a conserved glutamate, Glu-163, equivalent to TgALD Glu-189, is responsible for proton abstraction of the C4 hydroxyl leading to cleavage of the hexose substrate. TBPA indiscriminately accommodates all four diastereomers, exhibiting no steric clashes between active site residues and C3 or C4 hydroxyls in all configurations. However, modeling of the four stereoisomers in FBPA demonstrated how clashes occur with nearby residues, with the
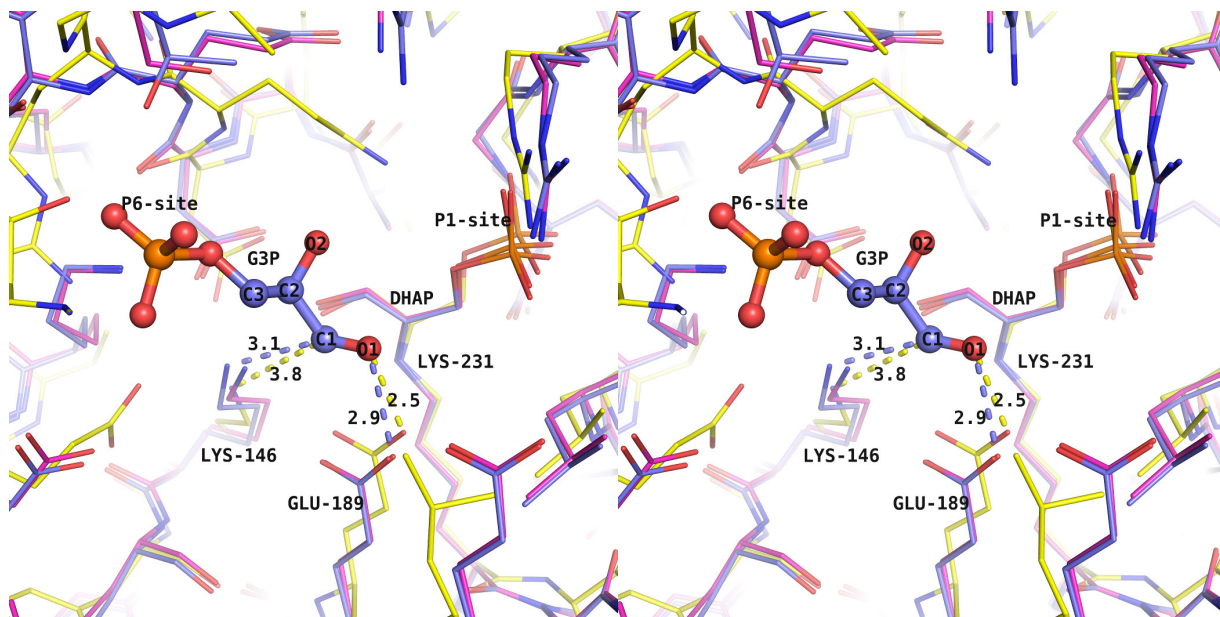
Figure 6-2. Superposition of intermediates from diverse aldolases (stereo view).

Diverse aldolases were superposed by the combinatorial extension algorithm (cealign – PyMol) using the TgALD ternary structure as a reference, which is depicted in *blue*. In *magenta* is illustrated the covalent DHAP intermediate of rabbit muscle aldolase (ALDOA) (PDB ID: 2QUT) which has 57 % sequence identity with TgALD. The *yellow* structure depicts a tagatose-bisphosphate aldolase (TBPA) structure with a covalent DHAP intermediate (PDB ID: 3MHG). Conserved active site residues include: Lys-231 which forms the Schiff-base intermediate; Glu-189, the acid/base responsible for proton exchange during cleavage and condensation; and Lys-146, which forms stabilizing electrostatic interactions. The anchoring phosphate sites are illustrated as the P1- and P6-sites. The TgALD ternary structure (*blue*) is the first FBPA structure showing the binding of G3P prior to condensation. The structure reveals binding of G3P in the *cis*-configuration (describing the positions of O1 and O2 around the C1-C2 bond). The proximity of C1 to Lys-146 (*blue dash* - 3.1Å) precludes proton transfers with Glu-189 in the *cis* orientation (*blue dash* - 2.9Å). The strong resemblance of active site architecture for ALDOA suggests a conserved mechanism for FPBAs. The non-selective TBPA active site is evidenced by its more voluminous active site, such as the deeper position of Lys-146. The *cis*-configuration is productive in TBPA for condensation since the G3P aldehyde can form a short hydrogen bond with Glu-189 (*yellow dash* – 2.5Å) without the steric clash between C1 and Ly-146 amino group (*yellow dash* – 3.8Å). The RMSD of alignments are: 1.143 over 344 residues for TgALD – ALDOA; and 3.837 over 296 residues for TgALD – TBPA.

exception of its endogenous substrate, FBP. The lack of selectivity in TBPA compared to FBP aldolase was in part explained by its larger active site (~ 30% larger than FBP aldolase), which readily accommodates various configurations of G3P that allow catalysis of both 4(*S/R*) epimers. The FBP aldolase active site is more rigid and undergoes large-scale conformational

changes that are marginal in comparison to TBPA (Low-Kam, 2015). Indeed, soaking experiments with substrate revealed G3P bound in the active site, anchored only at the phosphate-loci. The carbon skeleton of G3P pointed towards the exterior of the active site, and it was suggested that initial binding of G3P to the active site follows such a trajectory. Our ternary structure indicates a much tighter binding for G3P, where the frame is aligned next to covalent DHAP. The structural findings predict a stronger binding affinity for substrate in FBP aldolases, consistent with such experimental observations for the hexose FBP, where the affinities (K_m) are ~ 5 μM and ~ 2000 μM respectively for TgALD and TBPA, a near 400 fold difference. Comparison of our ternary structure superposed with TBPA (PDB ID: 3MHG) corroborates the reasoning for lack of specificity at the C4 position. Specifically, TBPA Lys-125 (TgALD Lys-146) is 1.2Å deeper in the active site cleft, and doesn't interfere with G3P C1 (3.8Å) in the *cis*-configuration. In this state, *cis*-G3P forms the anticipated short hydrogen bond (2.5Å) with TBPA Glu-165 (TgALD Glu-189), allowing for catalysis of the 4(*S*) epimer, TBP.

The size of the active site cleft has been invoked to reason the lack of stereoselectivity towards FBP and TBP in other aldolases, including the class II FBP aldolase in *Thermus caldophilus*, whose active site is 25% larger than the selective class II FBPA from E. coli (Lee et al., 2006).

The binding geometry of the G3P also enabled us to make interesting observations regarding stereoselectivity at the C5 position, resolving the question regarding discrimination against the L-enantiomer of G3P. FBP aldolase discriminates L-G3P because of orbital clashes occurring between the O2 hydroxyl and Asp-34 carboxylate. Consequently, this explains the inactivity of FBP aldolases for L-sorbose-bisphosphate (L-SBP), the condensation product of DHAP and L-G3P. We conclude that active site geometry in glycolytic class I FBP aldolases has evolved to suppress a specific stereoisomer by disfavoring their activation to ensure strict stereospecificity in the reaction pathway.

6.1.2 Engineering of aldolase for synthetic biocatalyst applications

Our efforts provide relevant information that can be help with the rational engineering of aldolases for exploitable purposes. Carbon-carbon bond formation is a cornerstone reaction in synthetic organic chemistry (Schmidt et al., 2016). Chief amongst the methods available, the enzymatic aldol addition offers a powerful tool towards the production of pure compounds with controlled stereocenters. Increasingly, because of the prospects of manipulating activity, substrate selectivity, and stability, aldolase-catalyzed routes are finding acceptance among synthetic chemists seeking to develop asymmetric complex, bioactive compounds, such as carbohydrates, amino acids and their analogues (Windle et al., 2014). Extensive knowledge of the precise reaction mechanism arising from structural and biochemical studies, as presented in Chapter 2, are leading the development of novel biocatalysts by rational engineering and *de novo* computational design. Another method for engineering aldolases is directed evolution which can be accomplished without a priori structural or mechanistic knowledge. This approach involves one of two strategies: 1) the enzyme is evolved to accept an unnatural stereoisomer as a substrate; or 2) libraries are created by random or semi-rational mutagenesis (Chica et al., 2005; Giger et al., 2013; Williams et al., 2003). For a more comprehensive coverage of advances in aldolase-mediated biosynthetic applications, the following reviews are recommended: Bednarski et al., 1989; Bolt et al., 2008; Clapés et al., 2010; Clapés and Garrabou, 2011; Fessner, 1998; Williams et al., 2003; Windle et al., 2014; Wong and Whitesides, 1983. The following are brief examples demonstrating the rational engineering approach that is afforded by a better understanding of the aldol addition in aldolases.

Aldolases are classified according to their donor specificity. DHAP-dependent aldolases are highly specific for the donor component, DHAP, but can accept a broad range of aldehyde acceptors as the electrophilic component of the aldol reaction (Bednarski et al., 1989), albeit with variable tolerance (i.e. high K_m) towards bulky acceptors. For example, RhuA (L-rhamnulose-1-phosphate), a DHAP-dependent aldolase can accept aldehydes containing azide or N-Cbz-amine substitutions. Removal of the phosphate group is followed with reduction of the azide or deprotection of N-Cbz group. Intramolecular reductive amination then affords a series of iminocyclitols (Calveras et al., 2007; Whalen and Wong, 2006), attractive drug

candidates for specific inhibition of glycosidases – a key enzyme involved in a variety of metabolic disorders and diseases such as diabetes, infections and cancer (Asano, 2003). A similar strategy was employed in an extensive modeling study on reaction stereoselectivity to prepare structurally diverse polyhydroxylated pyrolidine derivatives, also effective against glycosidase (Calveras et al., 2009). Other cascade reactions make use of FBP aldolase for aldol addition to generate aminocyclitol analogs of valiolamine, a specific inhibitor of intestinal glycosidase (El Blidi et al., 2006). Another example illustrating the rational approach is the case of 2-deoxy-d-ribose 5-phosphate aldolase (DERA), a pyruvate-dependent aldolase. DERA, like class I FBP aldolase, accepts D-glyceraldehyde 3-phosphate in preference to the L-enantiomer. In situations when the G3P C2 substituent is changed from a hydroxyl group to a methyl or methoxyl group this preference is reversed, allowing for the formation of products with new stereochemistries (Liu et al., 2002). Together, these above strategies make use of detailed structural and mechanistic information that are provided by studies like ours. Understanding the binding of aldehydes may yield strategies for increasing affinity towards aldehydes and improving the efficacy of biocatalysts.

6.1.3 Methylglyoxal formation in Aldolase

We also undertook an extensive structural and biochemical investigation of the suspected role of aldolase in methylglyoxal (MGO) production. In the reaction mechanism, the phosphate moiety of covalent DHAP will generate the reactive phenolate of the mobile Tyr-363 through a bridging water molecule, which abstracts the C3 pro(S) proton to generate the reaction enamine that condenses with incoming aldehydes. Preliminary structural data from our laboratory with rabbit muscle aldolase crystals soaked with DHAP indicated the presence of cleaved phosphate oxyanion at the P1-site. Grazi and Trombetta postulated the existence of such a complex, leading to our systematic investigation of the mechanism that produces the intermediate that releases MGO from the active site (Grazi and Trombetta, 1978). This involved soaking native rabbit muscle aldolase crystals with DHAP for incremental time intervals and flash-freezing to trap intermediate states.

A thorough analysis of the high-resolution structures provided a competing account for the appearance of the unexplained density at the P1-site. The developing electron density at the P1-site and lack thereof between DHAP C1-C2 was explained by a mixture of covalent DHAP and water molecules at sites overlapping with DHAP oxygen atoms. Increasing the soaking period of aldolase crystals with DHAP allowed the active sites to become fully populated, evidenced by the increase of refined occupancies for DHAP and concomitant decrease of refined occupancies for water molecules. The subsequent decrease of DHAP population past 60 minutes of soaking is likely a result of active site turnover.

The enzymatic production of MGO by aldolase was also investigated, and called into question the significance of our working hypothesis. We showed that aldolase doesn't produce MGO above levels occurring spontaneously from decomposition of the triose-phosphates, DHAP and G3P. The inherent instability of triose-phosphates was demonstrated by the steady increase of phosphate release measured over several hours. A solution of 10 mM DHAP released P_i at a rate of 40 μM/hour, while G3P produced P_i at a rate of 88 μM/hour. The addition of aldolase to these mixtures had no influence on P_i release, suggesting little implication of aldolase towards enzymatic production of MGO. A solution containing FBP did not yield any phosphate but the addition of aldolase produced phosphate at a rate of 27 μM/hour, indicating that upon hexose cleavage by aldolase, the resulting triose-phosphates are vulnerable to spontaneous decomposition. Direct measurements of MGO with the glyoxalase assay proved to be difficult since quenching methods introduced a fair amount of variability. First, we showed that heat quenching and acid quenching alone introduce significant artefacts. A method combining ionic exchange and acid quenching was the most appropriate for reducing background production of MGO. Using this method, the 30 minutes of incubation were insufficient to observe any difference between aldolase-treated and untreated samples. Since we measured a rate of 27 μM/hour in the phosphate detection assay, it is conceivable that a difference would be observed if a longer incubation period was employed; nevertheless it would be redundant since the latter was shown by phosphate detection.

The observations in our enzymatic assays are consistent with the structural data showing little evidence of phosphate release. MGO production below the detection limits of the assay cannot be ruled out but even if demonstrated is well below the rate of MGO produced spontaneously

from decomposition, calling into question its biological significance. This raises interesting questions regarding the ubiquitous nature of glyoxalases – the MGO detoxifying enzymes – and the role of triose-phosphate instability and MGO in metabolism. It has been suggested that MGO is an inopportune vestige from the past (Kalapos, 2008, 1997). One hypothesis traces MGO to prebiotic evolution where it served as an anaplerotic route for the reductive citric acid cycle. In this route, MGO was generated from trioses, glyceraldehyde and dihydroxyacetone – intermediates of the formose cycle. This binds MGO to early carbohydrate metabolism and extant metabolism. Additionally, MGO synthetase in several lower organisms is postulated to have a physiological role in providing P_i for the second stage of glycolysis when the cells are deficient in P_i (Kalapos, 2008).

6.1.4 Future studies – Mechanism

The aldol addition is a reaction that has defensibly received significant attention over the last few decades. The potential for development of aldolase as a biocatalyst has already been discussed. From a mechanistic perspective, further studies comparing the known DHAP-dependent aldolases (FBPA: D-fructose-1,6-bisphosphate aldolase, RhuA: L-rhamnulose-1-phosphate aldolase, FucA: L-fuculose-1-phosphate aldolase and TBPA: D-tagatose-1,6-bisphosphate aldolase) would provide additional clues for how enzymes have evolved stereoselectivity towards aldehydes. Several crystallographic structures of each of these enzymes are available in structure databases and their structural alignment would be the first step towards formulating hypotheses. FucA has already demonstrated its value for the synthesis of rare sugars (Li et al., 2011a). The stereoselectivity of aldehydes has been investigated in RhuA but the molecular basis of the stereo preference is only speculative (Li et al., 2011b). A structural study in our laboratory has explored this comparison, specifically in D-tagatose-1,6-bisphosphate aldolase, and it was shown that TBPA uses a larger and more flexible active site (Low-Kam, 2015).

Otherwise related to the mechanism, the implication of sub-terminal aldolase residues in modulating the catalytic activity remains unexplained. The crystallographic resolution of rabbit muscle aldolase with C-terminal point mutations, in the presence of substrate or P_i, would clarify

the role of these residues. These mutant structures may reveal details of the importance of certain residues during the transient burrowing of the C-terminus in the active site. A molecular dynamics (MD) simulation probing the entry of the C-terminus into the active site in the presence and absence of substrate would complement the above. MD simulations in our laboratory have been applied to the study of catalytic loop dynamics in class II aldolases (Coinçon, 2010) and would complement a study on C-terminal dynamics in class I aldolases.

Finally, the conclusions drawn from our aldolase-enamine-G3P ternary structure may be corroborated by hybrid QM/MM (quantum mechanics/molecular mechanics), as has been applied to understanding the mechanism in an archaeal aldolase (Hou et al., 2014). Such simulations requires a profound acquaintance with quantum mechanics but could clarify the precise trajectory of G3P *cis-trans* rearrangement, and concerted short hydrogen bond formation during proton donation by Glu-189 and C3-C4 bond formation.

6.2 The aldolase scaffolding activity in apicomplexan parasites

In Chapter 5, we explored aldolase functions unrelated to metabolism – known collectively as moonlighting functions. Specifically, the binding mode of *T. gondii* aldolase (TgALD) to cell surface adhesin partners was investigated. TgALD forms scaffolding interactions between the cytoplasmic region of micronemal adhesin proteins and the parasite actomyosin complex that are crucial for efficient host-cell invasion and parasite dissemination. However, our primary objective of elucidating the structural binding mode of the cytoplasmic C-terminal tails of micronemal protein 2 (MIC2) and apical membrane antigen 1 (AMA1) with TgALD was complicated by unforeseen dependencies on ionic strength, shown by isothermal titration calorimetry assays. The binding energetics determined from this study indicated a mode of binding that is entropically driven. The enthalpy became favourable with truncation of the TgALD C-terminal region – a flexible region catalyzing events in the active site – suggesting that disruption of non-bonding interactions between TgALD C-terminus and active site residues upon binding of adhesin tail contributes towards the unfavourable enthalpy change. Therefore the adhesin C-tails compete for binding near the active site cleft. The gain in entropy from

desolvation of the active site and increase in conformational freedom form the displacement of the docked TgALD C-terminal region compensates for the unfavourable enthalpy change.

The abrogation of adhesin C-tail binding by the addition of salt is nonetheless intriguing. We observed a decrease in binding affinity (K_D) with MIC2t-25 from 6 μM > 12 μM > 17 μM by increasing the Tris buffer (pH 7.4) concentration from 5 mM, 20 mM and 100 mM; this represents an increase in ionic strength of 0.004 < 0.016 < 0.085. The addition of salt (simulate crystallographic buffer conditions) with an ionic strength of 0.3 (100 mM Li_2SO_4) eliminates binding. When Tris (100 mM) is mixed with a lower salt concentration (10 mM $MgCl_2$) for an overall ionic strength of 0.122, binding is also eliminated. We inferred that ionic strengths $\geq$ 0.1 considerably impact binding. This introduced a significant challenge for co-crystallization of TgALD and the adhesin C-tails as ionic strengths in crystallization buffers are generally greater than 0.1, and should to be considered for future structural studies. In our study, a low ionic strength crystallization screen did not yield any co-crystal structures. It also raises questions regarding the relevance of previous *in vitro* studies indicating an interaction between TgALD and adhesins. For example, the interactions between TgALD and MIC2/AMA1 were demonstrated by GST pull-down from cell lysates resuspended in a buffer composed of 50 mM KCl, 20 mM Hepes pH 7.5, 2 mM $MgCl_2$ and 0.2 mM EDTA (Jewett and Sibley, 2003; Shen and Sibley, 2014; Starnes et al., 2006), which has an ionic strength of 0.064 – within the range of binding demonstrated by ITC. Likewise, *in vitro* binding assays, such as F-actin binding assays, are often conducted in lower ionic strengths (0.01 – 0.05 M) in order to enhance potential interactions (Ouporov et al., 1999). The ionic strength dependence of association between aldolase and F-actin is an accepted phenomenon, but appreciable interactions still occur at physiological ionic strengths (0.1 – 0.15 M) (Forlemu et al., 2011). To gain a fuller appreciation of this phenomenon in aldolase-adhesin binding, a systematic investigation is required. The nature of the salts is a variable that equally needs consideration.

Apicomplexan parasites invariably require an actin-based mechanism for host-cell invasion (Drewry and Sibley, 2015) but the importance of aldolase crosslinking activity to cell surface receptors was recently contested when it was shown that TgALD knockout parasites and an ALD mutant deficient in adhesin binding supported normal invasion (Shen and Sibley, 2014). Our results are consistent with this finding. The apparent contradiction requires reconciliation

with studies showing decreased invasion of ALD mutant strains deficient in MIC2t binding (Starnes et al., 2009), or more recent work showing co-localization of ALD and actin with the tight junction of invasive *Plasmodium* merozoites (Riglar et al., 2016). It is conceivable that ALD localizes with the junction during invasion, providing the gliding motor a direct access to energy production during invasion. Also plausible is the implication of other adaptors that contribute to the scaffolding function, including GAPDH that binds to several *Plasmodium* adhesin tails *in vitro* (Pal-Bhowmick et al., 2012). It has also been recently proposed that the interaction between apical proteins and aldolase is regulated by phosphorylation/dephosphorylation events that modulate invasion of *Plasmodium* merozoites into erythrocytes, as shown with phosphorylated adhesin C-domains using biolayer interferometry (Diaz et al., 2016). A role for aldolase in mediating a bridging function may be reconciled to the contesting genetic studies by considering the destabilizing consequences of high concentrations of FBP on membrane bilayers (Ehringer et al., 2002), as anticipated in ALD-depleted parasites. There are indications that FBP is a potent calcium and divalent ion chelator, and high FBP concentrations could chelate the counterbalancing ions that interact with the phospholipid head groups of the lipid bilayer, affecting membrane stability (Ehringer et al., 2002). Disruption of the membrane by FBP accumulation may provoke host-cell invasion by an unknown mechanism. According to this model, the invasive behaviour of ALD-depleted parasites may be an artefact of FBP accumulation. This should be revisited in ALD-depleted models.

Another consideration is the notion of ionic strength as a mechanism for regulating these interactions. Such a mechanism has been proposed for modulating the aldolase-actin interaction, thereby providing a control of the glycolytic flux (Shearwin et al., 1990). We suggest a similar mechanism for uncoupling the aldolase moonlighting and metabolic activities. Local substrate concentrations can also influence the binding equilibrium, as has been proposed for the aldolase-WASP interaction (St-Jean, 2008). A collaborative project with Dariusz Rakus, University of Wroclaw, Poland, exploring a novel class of aldolase inhibitors targeting the aldolase-actin dynamics has investigated the influence of substrate (FBP and DHAP) on the latter in F-actin co-sedimentation assays (article in preparation). Experiments conducted by myself with rabbit muscle aldolase demonstrate that indeed, metabolic substrates promote the dissociation of

aldolase-F-actin, and is thought to be the consequence of competing for binding in the active site. This is in agreement with a study in *Plasmodium* showing a partial disruption of the aldolase-TRAP duplex and F-actin-aldolase-TRAP ternary complex in the presence of compounds that bind to the enzyme active site (Buscaglia et al., 2003).

Macromolecular crowding is another factor that can influence binding equilibria and local solute concentrations (Ellis, 2001). In the case of aldolase-F-actin binding, crowding appears to favour association (Lakatos and Minton, 1991). There is evidence indicating actin and adhesin C-tails bind to the same basic groove in the aldolase active site, suggesting that crowding may also be a factor in the aldolase-adhesin dynamic. Actin-aldolase-adhesin conceivably form a large dissociable dynamic complex with the rest of the cytoskeletal motor beneath the cell surface. We suggest that enzymatic turnover will not disrupt all of these links simultaneously. The localized concentration of substrate/product near the cortical cytoplasm is presumably lower than that required to promote dissociation of the complex, implying that glycolysis is compartmentalized to a different space. In such a case, the ATP required for actin remodeling would be generated outside the cortical space. The large pool of aldolase required to perform its numerous functions reconciles the atypically high aldolase concentrations observed in eukaryotic cells (μM range), largely exceeding the metabolic requirements (Gefflaut et al., 1995). Further studies dealing with the mechanisms of energy conversion in parasites and its relation to gliding motility, invasion and the actin cytoskeleton may clarify these issues.

There is a precedent for aldolase binding to actin as an important process for mediating numerous cellular events. For example, the surface expression of the mammalian insulin-responsive glucose transporter GLUT4 in 3T3L1 adipocytes requires interactions with aldolase (Kao et al., 1999). The C-terminal domain of GLUT4 associates with aldolase, thereby connecting it to the actin cytoskeleton. Disruption of this interaction results in reduced expression of GLUT4. Interestingly, GLUT4 shares a conserved acidic domain and critical tryptophan found in other aldolase-binding partners, including the adhesin C-tails. This apparently simple motif has prompted the search for homologous sequences and has allowed the identification of novel human aldolase binding partners, summarized in Section 1 of the Annex (Buscaglia et al., 2006). Matches were found in a variety of transcription factors, zinc-finger proteins, translation initiating factors, actin regulating proteins, importins, and others.

Several matches tested positive for binding to aldolase in pull-down assays. Needless to state, the presence of the motif and the *in vitro* binding only provide the first steps towards identification of a biological aldolase partner. The aldolase interaction with parasite cell surface adhesins provides a case in point of the challenge in demonstrating *bona fide* biological links. Does aldolase serve as a generalized intermediate scaffold to F-actin? Because aldolase substrates disrupt their interaction, metabolic flux may constitute a regulatory checkpoint for formation of the ternary complexes with F-actin. This would prevent non-productive interactions with aldolase in glycolytic compartments. Further studies are required to clarify the precise role of aldolase in mediating interactions with cellular partners.

6.2.1 Future studies – Moonlighting

First, in continuation of the structural work with TgALD and adhesin C-tails, we should systematically evaluate the ionic strength dependence of this interaction, in addition to other binding partners that successfully co-crystallized with aldolase, such as the rabbit muscle aldolase-WASP interaction or the *Plasmodium* aldolase-TRAP interaction, to assess the specificity of this phenomenon. If indeed the dependency is generalized, then we must continue to speculate reasons for the challenges towards obtaining co-crystals structures. Several hypotheses were offered in Chapter 5, including the crystal packing and occlusion by the ALD C-terminus. The advent of micro-focus technologies and more advanced infrastructures is paving the way for data collection on micro-crystals. This will allow screening and resolution of structures from crystallography conditions that are never successfully optimized during scale-up. If the ionic strength dependency is unique to the TgALD-adhesin interaction, we favor the idea that ionic strength provides a regulatory checkpoint in addition to substrate competition to prevent non-productive interactions.

Defining the players that are important for gliding motility and invasion remains a priority for future study. Genetic studies have questioned the role of several supposedly key players, including aldolase, myosin, and adhesins, suggesting that either 1) there are alternate invasion pathways that do not rely on the actomyosin complex, or 2) that multiple redundancies exist to complement for the deletion of individual genes, or 3) that parasite actomyosin activity is not as

critical as previously thought, and host cell actin may play an important role during invasion (Egarter et al., 2014). Conversely, a recent study in *Plasmodium* validated the aldolase-TRAP interaction as a suitable drug target by proving both that it can be pharmacologically targeted, disrupting the parasite's motility and invasion capabilities (Nemetski et al., 2015). The success of a similar approach in *T. gondii* is uncertain but hopeful.

6.3 Development and optimization of inhibitors for class I aldolase

Finally, the knowledge acquired from structural and mechanistic studies have been indispensable for the design of highly specific aldolase inhibitors. The focus of chapter 3 was the development of high affinity class I aldolase inhibitors for their potential as anti-glycolytic agents. A rational approach stimulated the development of the most potent aldolase inhibitor known, a naphthyl-bisphosphonate (PNAB, 2-phosphate-naphthyl 6-bisphosphonate). This work emanated from a previous collaboration on class I aldolase inhibition with Dr. Casimir Blonski's chemistry group at Université de Paul Sabatier, Toulouse. First, we crystallized a high-resolution structure of rabbit muscle aldolase with the competitive active site inhibitor, naphthyl 2,6-bisphosphate (NA-P$_2$), demonstrating the molecular basis of its inhibitory mechanism. NA-P$_2$ was initially conceived by structural mimicry of FBP, primarily by respecting the intramolecular *trans*-phosphate distance of bound FBP (~ 9Å). The naphthyl moiety, replacing the linear carbon frame was introduced to impart structural rigidity, reducing


NAP2   **PNAB**   **NAB**   **PBB**
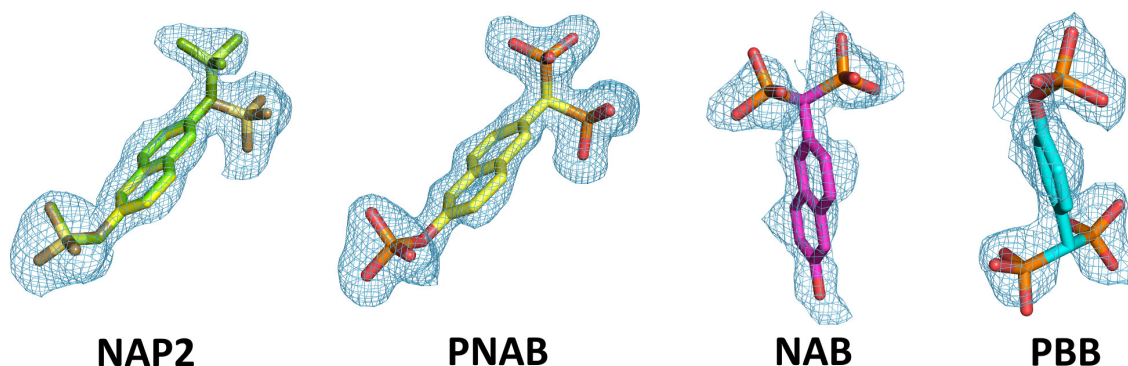
Figure 6-3. Naphthalenic-phosphate and bisphosphonate derivatives as high affinity aldolase inhibitors.

the entropic cost of binding. Indeed, the binding sites of the phosphates in NA-P$_2$ are quasi-isostructural with the phosphate loci in the aldolase-FBP Schiff-base intermediate with a slight nuance at the P1-site. While the P1-phosphate contacts Arg-303 through a stabilizing salt bridge in the aldolase-FBP structure, the NA-P$_2$ phosphate binds in two conformations: a minor conformation (0.35), the so-called *cis*-arrangement (in reference to phosphate positions about the aromatic core) that is analogous to P1-phosphate in FBP; and a major conformation (0.65), *trans*-arrangement, that contacts backbone resides, including Ser-271, Gly-272, Ser-300, and Lys-229 and several ordered water molecules. This structure served as a guide for designing a novel class of aldolase inhibitors, aromatic bisphosphonates. We hypothesized that bisphosphonates would have strong affinities for aldolase, given the added potential for synchronously contacting the *cis* and *trans* loci observed with NA-P$_2$.

We envisaged the synthesis of several bisphosphonates with varied aromatic cores and transannular substitutions. The candidates retained for crystallographic and enzymatic analysis were 2-phosphate-naphthyl 6-bisphosphonate (PNAB), naphthol 6-bisphosphonate (NAB), and 1-phosphate-benzyl-4-bisphosphonate (PBB). We successfully resolved high-resolution structures of the three bisphosphonates with rabbit muscle aldolase. PNAB associates with the active site in the anticipated binding groove, forming a total of eight hydrogen bonds (excluding water molecules) at the P1-site, compared to the five hydrogen bonds observed for NA-P$_2$ in either conformation. The hydrogen bonding network at the P6-phosphate site is analogous to the FBP-iminium intermediate: NA-P$_2$ and PNAB form contacts with Ser-35, Ser-38, and Lys-107. However, NAB and PBB favored unexpected binding modes, neither using the P1-site for fixation of their bisphosphonate moieties. Rather, the naphthalene core of NAB is sandwiched in a hydrophobic groove formed by two arginines (Arg-42 and Arg-303) in the active site. And PBB burrows the bisphosphonate moiety along the lining of basic residues (Lys-107, Lys-146, and Lys-229) at the base of the active site. The curious binding modes of the latter, less potent bisphosphonates demonstrates two important features of active site aldolase inhibitors: 1) the presence of an additional phosphate group that can contact the P6-site (absent with NAB); and 2) the optimal intramolecular distance between the extremity phosphates (shorter with PBB). Inhibition kinetics were realized for each bisphosphonate, revealing a slow-binding mechanism of inhibition for PNAB, dual competitive inhibition by NAB, and competitive inhibition by

PBB. We were surprised by the slow-binding mechanism of PNAB, as slow-binding is typically associated with isomerization reactions or covalent inhibitors, such as HNA-P, a slow-binding tight inhibitor of aldolase that forms a covalent adduct with the active-site residue Lys-107 (Dax et al., 2005). Slow-binding inhibition involves rapid equilibrium formation between enzyme E and inhibitor I, followed by the initial complex EI undergoing a slow and reversible isomerization to a kinetically more stable complex form, EI*. For this kinetic sequence, K_i* represents the overall inhibition constant. Enzyme activity was competitively inhibited by NA-P$_2$ ($K_i = 0.28 \pm 0.03$ μM). However, PNAB exhibited K_i* of 0.038 μM, whereas NAB and PBB had competitive K_i of 13.1/8.7 μM and 41.6 μM. Using the most potent bisphosphonate, PNAB, we were able to demonstrate the potential to limit cell growth in a cancer cell by following the cell viability in treated cells.

We probed several possibilities for the slow-binding mechanism, looking particularly for anomalous conformational changes in the enzyme upon binding. Comparison of native structure with derived structures revealed a backbone conformational change that we speculated as responsible for the slow-binding mechanism. Binding of PNAB requires a backbone shift of >1Å at residues 272-274 that brings the Gly-272 carbonyl to within close hydrogen-bonding distance of the bisphosphonate. A smaller movement incurred upon NA-P$_2$ binding at this site may explain the difference with regards to slow-binding.

We explored other possibilities to explain the slow-binding mechanism of PNAB not presented in Chapter 3. A force field was probed (CHARMM General Force Field) (Vanommeslaeghe et al., 2010) to investigate preferred geometries of aromatic bisphosphonates, notably PNAB, with the premise that slow-binding may be the result of PNAB crossing a high-energy barrier to satisfy the final active site binding mode observed in our crystal structure. However, a 1 ηano second molecular dynamics (MD) simulation conducted with NAMD 2.10 (Phillips et al., 2005) using the CHARMM force field corroborated the binding mode of PNAB in the ALDOA-PNAB structure, suggesting a stable binding geometry. [MD methodology: the molecule was solvated with water molecules (TIP3P) (Jorgensen et al., 1983) in a cubic system (33Å wide) with or without relevant conjugating ions (sodium or lithium). Two independent MD simulations were performed for each system. Atomic coordinates generated by the dynamical simulations were sampled at a frequency of 1 ps for the subsequent analysis using

VMD (Humphrey et al., 1996). The equations of motion were integrated with a 1-fs time step, and bonded, non-bonded short- and non-bonded long-range interactions were calculated every 1 fs. The particle mesh Ewald (PME) method (Darden et al., 1993; Essmann et al., 1995) was used to handle the non-bonded long-range electrostatic interactions. All of the simulations were performed in the NpT ensemble (T = 303.15K; P = 1 atm)]. [The MD simulations were conducted by Benoit Jacques in the Sygusch lab].

The simulation revealed yet another possible reason for the slow-binding mechanism: the strong affinity of bisphosphonates for the conjugating ions Li^+ and Na^+. MD simulations conducted in the presence of Li^+ or Na^+ revealed a tight interaction consisting of a bridging cation between the pair of phosphonate groups. During a 1 ηano second simulation, a cation remained fixed at this position, suggesting that bisphosphonates have a strong affinity for Na^+ and Li^+. Disruption of this interaction upon active site binding may correspond to a slow-binding event. Consistent with this hypothesis is the preliminary finding that in solution (Tris-Acetate buffer, pH 7.5, 50 μM FBP) the presence of Li^+ (50 mM LiCl) appears to delay the slow-binding inhibition of aldolase by PNAB. In the absence of Li^+, the IC50 drops from 15.7 to 9.6 after 30 minutes of pre-incubation but in the presence of Li^+, the IC50 only lowers from 17.8 to 17.1, suggesting that the presence of excess Li^+ has a pseudo-protective effect that impedes the formation of the tight EI* complex. We did not observe a difference in the presence of Na^+ (50 mM NaCl), suggesting that the radius of the cation may play a role in its affinity to the bisphosphonate at the bridging locus. A more comprehensive study involving full progress curves is needed to address this phenomenon.

6.3.1 Future Studies - Inhibition

Our study represents a successful application of rational drug design towards the development of class I aldolase inhibitors. Using this blueprint, we will envisage the addition of functional groups based on the proximity of surrounding residues to produce a library of high-affinity inhibitors that will serve as leads for future studies. The incorporation of a rigid backbone (i.e. naphthalene) is a strategy that should be conserved for future studies, as the smaller loss of entropy upon binding contributes significantly to the potency of the inhibitor.

Another desirable feature is an inhibitor that can recognize both phosphate sites (P1 and P6). An important consideration for the development of biologically active bisphosphonate-based inhibitors is the poor membrane permeation that subsists with phosphate bioisosteres. Several possibilities may be envisioned, such as synthesizing the bisphosphonates as prodrugs, with protective neutralizing esters that allow permeation of the prodrug into the cells (Conway et al., 2006; Krise and Stella, 1996; Li et al., 1998, 1997; Mentel et al., 2011; Schultz, 2003; Subramanian et al., 2010). These are efficiently removed by endogenous esterases which restore the charge and biological activity of the drug. This approach was successfully implemented with a bisphosphonate inhibitor of inositol monophosphatase, where initially, poor membrane permeability was noted, but was rescued by using a tetrapivaloyloxy-methyl ester prodrug that retained biological activity after removal by endogenous esterases (Atack et al., 1994, 1993). Alternatively, caged derivatives are used for carrying photoactivatable groups that prevent biological activity until it is removed by a flash of light (Subramanian et al., 2010).

Other strategies are being pursued by our laboratory to develop our understanding of class I aldolase inhibitors. Notably, we have identified a potent aldolase inhibitor (UM76) from a high throughput screen (HTS) of 130,000 compounds at IRIC (Institute for Research in Immunology and Cancer) with the premise of developing a novel anti-cancer target. Initially UM76 was tested in *T. gondii* for its ability to potentially displace the necessary interaction that occurs between TgALD and the cytoplasmic tails of adhesin molecules that are required for invasion. Preliminary docking experiments placed UM76 distal to the active site and a crystal structure that we collected appeared to indicate that a fragment of UM76 was bound covalently to Lys-231 in the active site but recent controls have demonstrated this to be a false lead. No fragments were identified by MS. Further, additional control datasets revealed a very similar density in the active site (likely DMSO and water). This was also confirmed by doing ITC and enzyme inhibition assays. Nonetheless, these controls helped gather valuable data with respect to the binding mode for UM76 in class I aldolases. ITC data indicates that 2 binding sites (with different affinities) are exploited by UM76, which was confirmed by the mixed inhibition profile that we generated thereafter (Figure 6-4A). We then demonstrated that UM76 exhibits a slow-
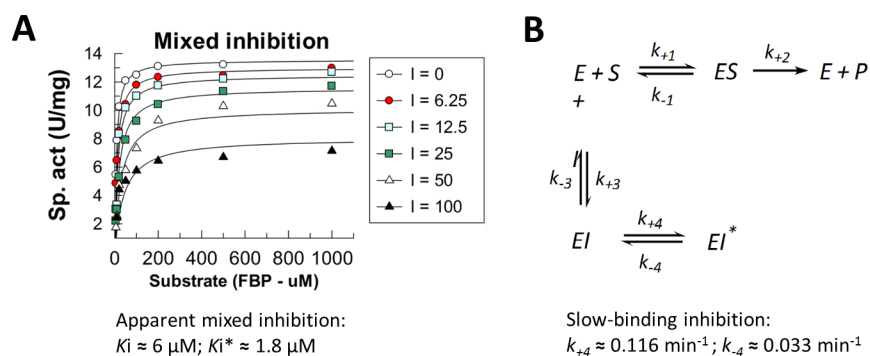
Figure 6-4. Kinetic analysis of aldolase inhibition by UM76 showing apparent mixed inhibition (A) and slow-binding inhibition (B).

binding behaviour (Figure 6-4B). It was also noted that at higher concentrations, UM76 induced aggregation of aldolase, as demonstrated by sodium dodecyl sulfate (SDS) and native gels. The ability of UM76 to interfere with aldolase-actin binding was also explored after findings from our collaborator (Dariuz Rakus – Wroclaw University) lead to this hypothesis. Using an actin-binding assay, whereby a protein of interest is tested for its ability to co-sediment with F-actin, we showed that alone, UM76 does not interfere with aldolase-actin binding but indirectly, by means of its inhibition of the glycolytic metabolon (which consequently leads to increase levels of upstream/downstream metabolites), UM76 causes an increase in FBP which itself can induce dissociation of aldolase-actin binding. This supports binding of UM76 at a site distal from the active site, as shown previously by docking and MS experiments (near Cys-72/Cys-338). Furthermore, disruption of the local glycolytic metabolon would reduce available levels of ATP that are required for actin polymerization and thus motility. Levels of FBP/Triose-phosphates are currently being measured in human cells to assess our hypothesis that FBP levels are significantly higher in cells treated with UM76. The results from this study will be submitted for publication shortly.

We are spearheading another HTS from a library of 10,000 known, biologically active compounds. Preliminary hits have been identified by differential scanning fluorimetry and their inhibition profiles will be tested shortly.

The Warburg effect is a recognized phenomenon that is increasingly studied for its therapeutic potential. The high expression of aldolase in a variety of malignant cancers suggests

aldolase to be a viable therapeutic target. Our efforts are leading the way towards producing the first biological leads targeting class I aldolases.

Chapter 7

Conclusion

Conclusion

The general aim of this thesis project was to provide structural-based answers for mechanistic and moonlighting functions of class I aldolases and provide strategies to inhibit these functions. This glycolytic enzyme continues to draw attention for its ability to form/cleave a carbon-carbon bond, its homo-tetrameric state, its elevated cellular concentration, and for the plethora of putative interactions it establishes with various cellular partners. Our investigation was focalized on crystallographic structural determination as an elementary tool to study the molecular basis of these functions. There is much left to explore, and hopefully the results of our investigation will be insightful for the future of aldolase-related research.

Annex

Section 1. Putative Human Aldolase Binding Partners

Protein Description	Putative Aldolase Binding Motif [a,b]	Accession [c]
Amyloid βA4 precursor protein-binding family A member 3	[143]edpdedsdspewve	O96018
Anaphase promoting complex subunit 4	[745]emdiddeweldessdeeee	Q9UJX5
Bloom's Syndrome Protein	[552]didnfdiddfdddddwed	P54132
Calreticulin precursor	[251]edwdeemdgeweppviqnpe	P27797
Calsequestrin-1	[365]eeledwledvlege	P31415
Carbonic anhydrase-related protein	[16]eedeeeeegvewgyeegve	P35219
Chromatin assembly factor 1 subunit A	[581]dsdeeweeee	Q13111
Coiled-coil domain containing protein 9	[410]edegeenegeedeewedisedeeeeieve egdeee	Q9Y3X0
Cortactin isoform b	[15]ddagaddwetdpdfvndvse	Q96H99
Cyclin H	[310]eeeewtdddlve	P51946
Death-associated protein 1	[35]dtkeekdkddqewe	P51397
DNA ligase III	[71]edltelegweeledneke	P49916
DNA-repair protein complementing XP-C cells	[119]edsneeeeesendweeveelse	Q01831
Eukaryotic translation initiation factor 3 subunit 8	[216]ddededsedseddedwdtgstssdsdseeee	Q99613
Eukaryotic translation initiation factor 5	[196]eeeedddwgedttee	P55010
Harmonin-interacting ankyrin repeat-containing protein	[327]ddlpwdddeveweed	Q8N8V4
Huntingtin-associated protein 1	[575]eegvmeeaelvseetegweevelelde	P54257
Importin-7	[925]edgddedweeddaee	O95373
Importin-8	[923]edeeeedddwdeevleetale	O15397
Leucine-rich repeat-containing protein 17	[410]esfdqdteddewe	Q8N6Y2
Makorin-1	[457]ddeltdsedewd	Q9UHC7
N-WASp	[486]dedededdeedfedddewed	O00401
P53-associated parkin-like cytoplasmic protein	[2461]eaeeeeeddeddvpewqqdefdeeldnd	Q8IWT3
PR-domain zinc finger protein 10	[48]eeedededdedteedeeedgedtdlddwepdp prpfd	Q9NQV6
Prickle-like protein 1	[398]eqetpedpeewadhed	Q96MT3

Protein C12orf2	217dveieeeefwenelqieqene	Q8NHQ8
Protein KIAA0685	604dddedediwedsd	O75170
Rap Guanine nucleotide exchange factor 5	41deededdew	Q92565
RING finger protein 14	462dvdddiwedeved	Q9UBS8
RNA polymerase II elongation factor ELL3	248dlqegedweqededmd	Q9HB65
Serine/threonine-protein kinase Nek3	475deedtdfeeeddnpdwvse	P51956
Serine/Threonine-protein kinase RI01	49engegeiedeeeegydddddwdwde	Q9BRS2
Sorting-nexin 18	149gsdddwddewddsstvade	Q96RF0
Sorting-nexin 9	156gpatgddddwdedwdgpksssc	Q9Y5X1
Splicing factor 4	165dedeeedyeqwle	Q8IWZ8
STE20/SPS1-related proline-alanine-rich protein kinase	380edgdwewsddemde	Q9UEW8
Thyroid hormone receptor-associated protein complex 240 kDa component	248emseekqedmdwedd	Q9UHV7
Tripartite motif protein 26	381edeeegdeeeegeeeeeeeeagygdgydd wetdedees	Q12899
Tripartite motif protein 52	51edeedqneeedeweeeedee	Q96A61
Tuftelin-interacting protein 11	9dgegridddddderenfeitdwd	Q9UBB9
Ubiquitin carboxyl-terminal hydrolase 10	566eeeqeeqgegsedewe	Q14694
Ubiquitin ligase protein RNF8	113enkenaeyeyevteedwe	O76064
WASp	484degedqagdededdewdd	P42768
WASp family member 1 (WAVE-1)	542eysdseddsefdevdwle	Q92558
WASp family member 2 (WAVE-2)	480eysdseddssefdeddwsd	Q9Y6W5
WASp family member 3 (WAVE-3)	485eysdsdddsefdendwsd	Q9UPY6
WD-repeat protein 43	643eeesseeesddeiadkdsednwdedeeese se	Q15061
Zinc finger protein 277	268ddrelldhqeddwsdwee	Q9NRM2
Zinc finger protein 622	195eedseeeeedldgddwedidsdeelecedte amdd	Q969S3
Zinc finger protein Rlf	1779eseekeddfddwe	Q13129

[a] The authors identified the putative aldolase-binding motifs through database searching (http://us.expasy.org/tools/scanprosite) using the algorithm $(X_{(0-2)}\text{-}E/D\text{-}X_{(0-1)})_y\text{-}W\text{-}(X_{(0-1)}\text{-}E/D\text{-}X_{(0-2)})_{8-y}$, where X stands for any amino acid, and E/D means that either D or E are accepted at this position. The identified matches and the flanking sequences in the corresponding proteins were further analyzed to define the putative aldolase-binding motifs. For more detail concerning search criteria, refer to the following citation - Buscaglia et al., 2006.

[b] The relative position of the first residue of each motif on the corresponding protein is indicated.

[c] The accession number for each protein on the UniProt database is indicated.

Bibliography

Adams, P.D., Grosse-Kunstleve, R.W., Hung, L.-W., Ioerger, T.R., McCoy, A.J., Moriarty, N.W., Read, R.J., Sacchettini, J.C., Sauter, N.K., Terwilliger, T.C., 2002. *PHENIX* : building new software for automated crystallographic structure determination. Acta Crystallogr. D Biol. Crystallogr. 58, 1948–1954.

Adelman, R.C., Morse, D.E., Chan, W., Horecker, B.L., 1968. Evidence for a substrate-mediated change in conformation of rabbit muscle aldolase. Arch. Biochem. Biophys. 126, 343–352.

Ali, M., Rellos, P., Cox, T.M., 1998. Hereditary fructose intolerance. J. Med. Genet. 35, 353–365.

Anai, M., Lai, C.Y., Horecker, B.L., 1973. The pyridoxal phosphate-binding site of rabbit muscle aldolase. Arch. Biochem. Biophys. 156, 712–719.

Arnold, H., Nolte, J., Pette, D., 1969. Quantitative and Histochemical Studies on the Desorption and Readsorption of Aldolase in Cross-Striated Muscle. J. Histochem. Cytochem. 17, 314–320.

Arnold, H., Pette, D., 1970. Binding of Aldolase and Triosephosphate Dehydrogenase to F-Actin and Modification of Catalytic Properties of Aldolase. Eur. J. Biochem. 15, 360–366.

Arnold, H., Pette, D., 1968. Binding of Glycolytic Enzymes to Structure Proteins of the Muscle. Eur. J. Biochem. 6, 163–171.

Asano, N., 2003. Glycosidase inhibitors: update and perspectives on practical use. Glycobiology 13, 93R–104R.

Atack, J.R., Cook, S.M., Watt, A.P., Fletcher, S.R., Ragan, C.I., 1993. In Vitro and In Vivo Inhibition of Inositol Monophosphatase by the Bisphosphonate L-690,330. J. Neurochem. 60, 652–658.

Atack, J.R., Prior, A.M., Fletcher, S.R., Quirk, K., McKernan, R., Ragan, C.I., 1994. Effects of L-690,488, a prodrug of the bisphosphonate inositol monophosphatase inhibitor L-690,330, on phosphatidylinositol cycle markers. J. Pharmacol. Exp. Ther. 270, 70–76.

Avigad, G., Englard, S., 1972. The covalent binding of d-fructose 1,6-diphosphate to muscle aldolase. Arch. Biochem. Biophys. 153, 337–346.

Bai, N.J., Pai, M.R., Murthy, P.S., Venkitasubramanian, T.A., 1982. Fructose-bisphosphate aldolases from mycobacteria. Methods Enzymol. 90 Pt E, 241–250.

Bai, N.J., Ramachandra Pai, M., Suryanarayana Murthy, P., Venkitasubramanian, T.A., 1975. Fructose diphosphate aldolase from Mycobacterium smegmatis. Purification and properties. Arch. Biochem. Biophys. 168, 230–234.

B L Horecker, Mehler, and A.H., 1955. Carbohydrate Metabolism. Annu. Rev. Biochem. 24, 207–274.

Baldwin, S.A., Perham, R.N., 1978. Novel kinetic and structural properties of the class-I D-fructose 1,6-bisphosphate aldolase from Escherichia coli (Crookes' strain). Biochem. J. 169, 643–652.

Baranowski, T., Niederland, T.R., 1949. Aldolase activity of myogen A. J. Biol. Chem. 180, 543–551.

Baynes, J.W., Thorpe, S.R., 2000. Glycoxidation and lipoxidation in atherogenesis. Free Radic. Biol. Med. 28, 1708–1716.

Bednarski, M.D., Simon, E.S., Bischofberger, N., Fessner, W.D., Kim, M.J., Lees, W., Saito, T., Waldmann, H., Whitesides, G.M., 1989. Rabbit muscle aldolase as a catalyst in organic synthesis. J. Am. Chem. Soc. 111, 627–635.

Beernink, P.T., Tolan, D.R., 1992. Construction of a high-copy "ATG vector" for expression in Escherichia coli. Protein Expr. Purif. 3, 332–336.

Beisswenger, B.G.K., 2005. Ketosis Leads to Increased Methylglyoxal Production on the Atkins Diet. Ann. N. Y. Acad. Sci. 1043, 201–210.

Beisswenger, P.J., Howell, S.K., O'Dell, R.M., Wood, M.E., Touchette, A.D., Szwergold, B.S., 2001. α-Dicarbonyls Increase in the Postprandial Period and Reflect the Degree of Hyperglycemia. Diabetes Care 24, 726–732.

Benkovic, S.J., Engle, J.L., Mildvan, A.S., 1972. Magnetic resonance studies of the anomeric distribution and manganese binding properties of fructose phosphates. Biochem. Biophys. Res. Commun. 47, 852–858.

Berthiaume, L., Tolan, D.R., Sygusch, J., 1993. Differential usage of the carboxyl-terminal region among aldolase isozymes. J. Biol. Chem. 268, 10826–10835.

Blom, N., Sygusch, J., 1997. Product binding and role of the C-terminal region in class I D-fructose 1,6-bisphosphate aldolase. Nat. Struct. Biol. 4, 36–39.

Blonski, C., De Moissac, D., Périé, J., Sygusch, J., 1997. Inhibition of rabbit muscle aldolase by phosphorylated aromatic compounds. Biochem. J. 323, 71–77.

Blonski, C., Gefflaut, T., Perie, J., 1995. Effects of chirality and substituents at carbon 3 in dihydroxyacetone-phosphate analogues on their binding to Rabbit muscle aldolase. Bioorg. Med. Chem. 3, 1247–1253.

Bloom, B., Topper, Y.J., 1956. Mechanism of Action of Aldolase and Phosphotriose Isomerase. Science 124, 982–983.

Bolt, A., Berry, A., Nelson, A., 2008. Directed evolution of aldolases for exploitation in synthetic organic chemistry. Arch. Biochem. Biophys., Special Issue: Enzymology in Europe 474, 318–330.

Brändén, C.-I., 1991. The TIM barrel—the most frequently occurring folding motif in proteins. Curr. Opin. Struct. Biol. 1, 978–983. A

Brownlee, M., 2005. The Pathobiology of Diabetic Complications A Unifying Mechanism. Diabetes 54, 1615–1625.

Brownlee, M., 2001. Biochemistry and molecular cell biology of diabetic complications. Nature 414, 813–820.

Buchner, E., 1897. Alkoholische Gährung ohne Hefezellen. Berichte Dtsch. Chem. Ges. 30, 117–124.

Buscaglia, C.A., Coppens, I., Hol, W.G.J., Nussenzweig, V., 2003. Sites of Interaction between Aldolase and Thrombospondin-related Anonymous Protein in Plasmodium. Mol. Biol. Cell 14, 4947–4957.

Buscaglia, C.A., Penesetti, D., Tao, M., Nussenzweig, V., 2006. Characterization of an Aldolase-binding Site in the Wiskott-Aldrich Syndrome Protein. J. Biol. Chem. 281, 1324–1331.

Callaway, E., 2015. The revolution will not be crystallized: a new method sweeps through structural biology. Nat. News 525, 172.

Calveras, J., Casas, J., Parella, T., Joglar, J., Clapés, P., 2007. Chemoenzymatic Synthesis and Inhibitory Activities of Hyacinthacines A1 and A2 Stereoisomers. Adv. Synth. Catal. 349, 1661–1666.

Calveras, J., Egido-Gabás, M., Gómez, L., Casas, J., Parella, T., Joglar, J., Bujons, J., Clapés, P., 2009. Dihydroxyacetone Phosphate Aldolase Catalyzed Synthesis of Structurally Diverse Polyhydroxylated Pyrrolidine Derivatives and Evaluation of their Glycosidase Inhibitory Properties. Chem. – Eur. J. 15, 7310–7328.

Calvo, M. n., Bartrons, R., Castaño, E., Perales, J. c., Navarro-Sabaté, A., Manzano, A., 2006. PFKFB3 gene silencing decreases glycolysis, induces cell-cycle delay and inhibits anchorage-independent growth in HeLa cells. FEBS Lett. 580, 3308–3314.

Capodagli, G.C., Sedhom, W.G., Jackson, M., Ahrendt, K.A., Pegan, S.D., 2013. A noncompetitive inhibitor for M. tuberculosis's class IIa fructose 1,6-bisphosphate aldolase. Biochemistry (Mosc.).

Casazza, J.P., Felver, M.E., Veech, R.L., 1984. The metabolism of acetone in rat. J. Biol. Chem. 259, 231–236.

Case, E.M., Cook, R.P., 1931. The occurrence of pyruvic acid and methylglyoxal in muscle metabolism. Biochem. J. 25, 1319–1335.

Cash, D.J., Wilson, I.B., 1966. The Cyanide Adduct of the Aldolase Dihydroxyacetone Phosphate Imine. J. Biol. Chem. 241, 4290–4292.

Chabot, N., Vinatier, V., Gefflaut, T., Baudoin, C., Rodriguez, F., Blonski, C., Hoffmann, P., 2008. Irreversible inhibition of aldolase by a phosphorylated α-dicarbonyl compound. J. Enzyme Inhib. Med. Chem. 23, 21–27.

Chaerkady, R., Harsha, H.C., Nalli, A., Gucek, M., Vivekanandan, P., Akhtar, J., Cole, R.N., Simmers, J., Schulick, R.D., Singh, S., Torbenson, M., Pandey, A., Thuluvath, P.J., 2008. A Quantitative Proteomic Approach for Identification of Potential Biomarkers in Hepatocellular Carcinoma. J. Proteome Res. 7, 4289–4298.

Chan, W.-H., Wu, H.-J., Shiao, N.-H., 2007. Apoptotic signaling in methylglyoxal-treated human osteoblasts involves oxidative stress, c-Jun N-terminal kinase, caspase-3, and p21-activated kinase 2. J. Cell. Biochem. 100, 1056–1069.

Chang, T., Wu, L., 2006. Methylglyoxal, oxidative stress, and hypertension. Can. J. Physiol. Pharmacol. 84, 1229–1238.

Chica, R.A., Doucet, N., Pelletier, J.N., 2005. Semi-rational approaches to engineering enzyme activity: combining the benefits of directed evolution and rational design. Curr. Opin. Biotechnol., Protein technologies and commercial enzymes 16, 378–384.

Chiu, T.H., Feingold, D.S., 1969. L-rhamnulose 1-phosphate aldolase from Escherichia coli. Crystallization and properties. Biochemistry (Mosc.) 8, 98–108.

Choi, K.H., Mazurkie, A.S., Morris, A.J., Utheza, D., Tolan, D.R., Allen, K.N., 1999. Structure of a Fructose-1,6-bis(phosphate) Aldolase Liganded to Its Natural Substrate in a Cleavage-Defective Mutant at 2.3 Å,. Biochemistry (Mosc.) 38, 12655–12664.

Choi, K.H., Shi, J., Hopkins, C.E., Tolan, D.R., Allen, K.N., 2001. Snapshots of Catalysis: the Structure of Fructose-1,6-(bis)phosphate Aldolase Covalently Bound to the Substrate Dihydroxyacetone Phosphate,. Biochemistry (Mosc.) 40, 13868–13875.

Choi, K.H., Tolan, D.R., 2004. Presteady-State Kinetic Evidence for a Ring-Opening Activity in Fructose-1,6-(bis)phosphate Aldolase. J. Am. Chem. Soc. 126, 3402–3403.

Christen, P., Riordan, J.F., 1968. Reaction of an aldolase-substrate intermediate with tetranitromethane. Biochemistry (Mosc.) 7, 1531–1538.

Clapés, P., Fessner, W.-D., Sprenger, G.A., Samland, A.K., 2010. Recent progress in stereoselective synthesis with aldolases. Curr. Opin. Chem. Biol., Biocatalysis and Biotransformation/Bioinorganic Chemistry 14, 154–167.

Clapés, P., Garrabou, X., 2011. Current Trends in Asymmetric Synthesis with Aldolases. Adv. Synth. Catal. 353, 2263–2283.

Clarke, F.M., Masters, C.J., 1975. On the association of glycolytic enzymes with structural proteins of skeletal muscle. Biochim. Biophys. Acta BBA - Gen. Subj. 381, 37–46.

Clarke, F.M., Morton, D.J., 1976. Aldolase binding to actin-containing filaments. Formation of paracrystals. Biochem. J. 159, 797–798.

Clift, F.P., Cook, R.P., 1932. A method of determination of some biologically important aldehydes and ketones, with special reference to pyruvic acid and methylglyoxal. Biochem. J. 26, 1788–1799.

Coinçon, M., 2010. Étude structure-fonction des fructose-1,6-bishosphate aldolases métallo-dépendantes: Mécanisme catalytique et développement d'antimicrobiens. Université de Montréal.

Connett, R.J., 1985. In vivo glycolytic equilibria in dog gracilis muscle. J. Biol. Chem. 260, 3314–3320.

Conway, S.J., Thuring, J.W., Andreu, S., Kvinlaug, B.T., Roderick, H.L., Bootman, M.D., Holmes, A.B., 2006. The Synthesis of Membrane Permeant Derivatives of myo-Inositol 1,4,5-Trisphosphate. Aust. J. Chem. 59, 887–893.

Cooper, R.A., 1984. Metabolism of Methylglyoxal in Microorganisms. Annu. Rev. Microbiol. 38, 49–68.

Cooper, R. a., Anderson, A., 1970. The formation and catabolism of methylglyoxal during glycolysis in Escherichia coli. FEBS Lett. 11, 273–276.

Copley, R.R., Bork, P., 2000. Homology among (βα)8 barrels: implications for the evolution of metabolic pathways1. J. Mol. Biol. 303, 627–641.

Daher, R., Therisod, M., 2010. Highly Selective Inhibitors of Class II Microbial Fructose Bis-phosphate Aldolases. ACS Med. Chem. Lett. 1, 101–104.

Dakin, H.D., Dudley, H.W., 1913. An enzyme concerned with the formation of hydroxy acids from ketonic aldehydes. J. Biol. Chem. 14, 155–157.

Darden, T., York, D., Pedersen, L., 1993. Particle mesh Ewald: An N·log(N) method for Ewald sums in large systems. J. Chem. Phys. 98, 10089–10092.

Dax, C., Coinçon, M., Sygusch, J., Blonski, C., 2005. Hydroxynaphthaldehyde Phosphate Derivatives as Potent Covalent Schiff Base Inhibitors of Fructose-1,6-bisphosphate Aldolase †. Biochemistry (Mosc.) 44, 5430–5443.

Dax, C., Duffieux, F., Chabot, N., Coincon, M., Sygusch, J., Michels, P.A.M., Blonski, C., 2006. Selective Irreversible Inhibition of Fructose 1,6-Bisphosphate Aldolase from Trypanosoma brucei. J. Med. Chem. 49, 1499–1502.

Desai, K.M., Chang, T., Wang, H., Banigesh, A., Dhar, A., Liu, J., Untereiner, A., Wu, L., 2010. Oxidative stress and aging: Is methylglyoxal the hidden enemy? Can. J. Physiol. Pharmacol. 88, 273–284.

Di Iasio, A., Trombetta, G., Grazi, E., 1977. Fructose 1,6-bisphosphate aldolase from liver: The absolute configuration of the intermediate carbinolamine. FEBS Lett. 73, 244–246.

Diaz, S.A., Martin, S.R., Howell, S.A., Grainger, M., Moon, R.W., Green, J.L., Holder, A.A., 2016. The Binding of Plasmodium falciparum Adhesins and Erythrocyte Invasion Proteins to Aldolase Is Enhanced by Phosphorylation. PLoS ONE 11.

Drechsler, E.R., Boyer, P.D., Kowalsky, A.G., 1959. The Catalytic Activity of Carboxypeptidase-degraded Aldolase. J. Biol. Chem. 234, 2627–2634.

Drewry, L.L., Sibley, L.D., 2015. Toxoplasma Actin Is Required for Efficient Host Cell Invasion. mBio 6, e00557-15.

Du, S., Guan, Z., Hao, L., Song, Y., Wang, L., Gong, L., Liu, L., Qi, X., Hou, Z., Shao, S., 2014. Fructose-Bisphosphate Aldolase A Is a Potential Metastasis-Associated Marker of Lung Squamous Cell Carcinoma and Promotes Lung Cell Tumorigenesis and Migration. PLoS ONE 9, e85804.

Dukic-Stefanovic, S., Schinzel, R., Riederer, P., Münch, G., 2001. AGES in brain ageing: AGE-inhibitors as neuroprotective and anti-dementia drugs? Biogerontology 2, 19–34.

Egarter, S., Andenmatten, N., Jackson, A.J., Whitelaw, J.A., Pall, G., Black, J.A., Ferguson, D.J.P., Tardieux, I., Mogilner, A., Meissner, M., 2014. The Toxoplasma Acto-MyoA Motor Complex Is Important but Not Essential for Gliding Motility and Host Cell Invasion. PLoS ONE 9, e91819.

Ehringer, W.D., Su, S., Chiang, B., Stillwell, W., Chien, S., 2002. Destabilizing effects of fructose-1,6-bisphosphate on membrane bilayers. Lipids 37, 885–892.

El Blidi, L., Ahbala, M., Bolte, J., Lemaire, M., 2006. Straightforward chemo-enzymatic synthesis of new aminocyclitols, analogues of valiolamine and their evaluation as glycosidase inhibitors. Tetrahedron Asymmetry 17, 2684–2688.

Ellis, R.J., 2001. Macromolecular crowding: obvious but underappreciated. Trends Biochem. Sci. 26, 597–604.

Essmann, U., Perera, L., Berkowitz, M.L., Darden, T., Lee, H., Pedersen, L.G., 1995. A smooth particle mesh Ewald method. J. Chem. Phys. 103, 8577–8593.

Fantin, V.R., St-Pierre, J., Leder, P., 2006. Attenuation of LDH-A expression uncovers a link between glycolysis, mitochondrial physiology, and tumor maintenance. Cancer Cell 9, 425–434.

Ferroni, E.L., Harper, E.T., Fife, W.K., 1991. Slow reversible inhibition of rabbit muscle aldolase by D-erythrulose 1-phosphate. Biochem. Biophys. Res. Commun. 176, 511–516.

Fessner, W.-D., 1998. Enzyme mediated C☐C bond formation. Curr. Opin. Chem. Biol. 2, 85 –97.

Fischer, E., 1894. Einfluss der Configuration auf die Wirkung der Enzyme. Berichte Dtsch. Chem. Ges. 27, 2985–2993.

Forlemu, N.Y., Njabon, E.N., Carlson, K.L., Schmidt, E.S., Waingeh, V.F., Thomasson, K.A., 2011. Ionic Strength Dependence of F-actin and Glycolytic Enzyme Associations: A Brownian Dynamics Simulations Approach. Proteins 79, 2813–2827.

Fothergill-Gilmore, L.A., Michels, P.A.M., 1993. Evolution of glycolysis. Prog. Biophys. Mol. Biol. 59, 105–235.

Freemont, P.S., Dunbar, B., Fothergill-Gilmore, L.A., 1988. The complete amino acid sequence of human skeletal-muscle fructose-bisphosphate aldolase. Biochem. J. 249, 779–788.

Funasaka, T., Hu, H., Yanagawa, T., Hogan, V., Raz, A., 2007. Down-Regulation of Phosphoglucose Isomerase/Autocrine Motility Factor Results in Mesenchymal-to-Epithelial Transition of Human Lung Fibrosarcoma Cells. Cancer Res. 67, 4236–4243.

G, P., M, T., Ed, W., 1975. Histological examination of the aldolase monomer composition of cells from human kidney and hypernephroid carcinoma. Beitr. Pathol. 156, 266–279.

Gamblin, S.J., Cooper, B., Millar, J.R., Davies, G.J., Littlechild, J.A., Watson, H.C., 1990. The crystal structure of human muscle aldolase at 3.0 A resolution. FEBS Lett. 262, 282–286.

Gefflaut, T., Blonski, C., Périé, J., 1996. Slow reversible inhibitions of rabbit muscle aldolase with substrate analogues: synthesis, enzymatic kinetics and UV difference spectroscopy studies. Bioorg. Med. Chem. 4, 2043–2054.

Gefflaut, T., Blonski, C., Perie, J., Willson, M., 1995. Class I aldolases: Substrate specificity, mechanism, inhibitors and structural aspects. Prog. Biophys. Mol. Biol. 63, 301–340.

Gerstein, M., Levitt, M., 1997. A structural census of the current population of protein sequences. Proc. Natl. Acad. Sci. U. S. A. 94, 11911–11916.

Ghalambor, M.A., Heath, E.C., 1966. The Biosynthesis of Cell Wall Lipopolysaccharide in Escherichia coli V. Purification and Properties of 3-Deoxy-D-Manno-Octulosonate Aldolase. J. Biol. Chem. 241, 3222–3227.

Ghalambor, M.A., Heath, E.C., 1962. The Metabolism of l-Fucose II. THE ENZYMATIC CLEAVAGE OF l-FUCULOSE 1-PHOSPHATE. J. Biol. Chem. 237, 2427–2433.

Giger, L., Caner, S., Obexer, R., Kast, P., Baker, D., Ban, N., Hilvert, D., 2013. Evolution of a designed retro-aldolase leads to complete active site remodeling. Nat. Chem. Biol. 9, 494–498.

Ginsburg, A., Mehler, A.H., 1966. Specific anion binding to fructose diphosphate aldolase from rabbit muscle. Biochemistry (Mosc.) 5, 2623–2634.

Gonzalez, F.J., 1988. The molecular biology of cytochrome P450s. Pharmacol. Rev. 40, 243–288.

Götz, F., Fischer, S., Schleifer, K.-H., 1980. Purification and Characterisation of an Unusually Heat-Stable and Acid/Base-Stable Class I Fructose-1,6-bisphosphate Aldolase from Staphylococcus aureus. Eur. J. Biochem. 108, 295–301.

Gray, G.R., 1971. An examination of D-fructose 1,6-diphosphate and related sugar phosphates by fourier transform 31 P nuclear magnetic resonance spectroscopy. Biochemistry (Mosc.) 10, 4705–4711.

Gray, G.R., Barker, R., 1970. Studies on the substrates of D-fructose 1,6-diphosphate aldolase in solution. Biochemistry (Mosc.) 9, 2454–2462.

Grazi, E., Cheng, T., Horecker, B.L., 1962a. The formation of a stable aldolase-dihydroxyacetone phosphate complex. Biochem. Biophys. Res. Commun. 7, 250–253.

Grazi, E., Rowley, P.T., Cheng, T., Tchola, O., Horecker, B.L., 1962b. The mechanism of action of aldolases. III. Schiff base formation with lysine. Biochem. Biophys. Res. Commun. 9, 38–43.

Grazi, E., Sivieri-Pecorari, C., Gagliano, R., Trombetta, G., 1973. Complexes of fructose diphosphate aldolase with dihydroxyacetone phosphate and dihydroxyacetone sulfate. Biochemistry (Mosc.) 12, 2583–2590.

Grazi, E., Trombetta, G., 1978. A new intermediate of the aldolase reaction, the pyruvaldehyde-aldolase-orthophosphate complex. Biochem. J. 175, 361–365.

Hartman, F.C., Barker, R., 1965. An Exploration of the Active Site of Aldolase Using Structural Analogs of Fructose Diphosphate*. Biochemistry (Mosc.) 4, 1068–1075.

Hartman, F.C., Brown, J.P., 1976. Affinity labeling of a previously undetected essential lysyl residue in class I fructose bisphosphate aldolase. J. Biol. Chem. 251, 3057–3062.

Healy, M.J., Christen, P., 1973. Mechanistic probes for enzymatic reactions. Oxidation-reduction indicators as oxidants of intermediary carbanions (studies with aldolase, aspartate aminotransferase, pyruvate decarboxylase, and 6-phosphogluconate dehydrogenase). Biochemistry (Mosc.) 12, 35–41.

Herbert, D., Gordon, H., Subrahmanyan, V., Green, D.E., 1940. Zymohexase. Biochem. J. 34, 1108–1123.

Hers, H.G., Joassin, G., 1961. [Anomaly of hepatic aldolase in intolerance to fructose]. Enzymol. Biol. Clin. (Basel) 1, 4–14.

Hester, G., Brenner-Holzach, O., Rossi, F.A., Struck-Donatz, M., Winterhalter, K.H., Smit, J.D., Piontek, K., 1991. The crystal structure of fructose-1,6-bisphosphate aldolase from Drosophila melanogaster at 2.5 A resolution. FEBS Lett. 292, 237–242.

Hiratake, J., 2005. Enzyme inhibitors as chemical tools to study enzyme catalysis: rational design, synthesis, and applications. Chem. Rec. 5, 209–228.

Hodel, A., Kim, S.H., Brünger, A.T., 1992. Model bias in macromolecular crystal structures. Acta Crystallogr. A 48, 851–858.

Hopper, D. j., Cooper, R. a., 1971. The regulation of Escherichia coli methylglyoxal synthase; a new control site in glycolysis? FEBS Lett. 13, 213–216.

Hou, Q., Sheng, X., Liu, Y., 2014. QM/MM studies of the mechanism of unusual bifunctional fructose-1,6-bisphosphate aldolase/phosphatase. Phys. Chem. Chem. Phys. 16, 11366–11373.

Howells, R.E., 1985. The modes of action of some anti-protozoal drugs. Parasitology 90, 687–703.

Hsu, P.P., Sabatini, D.M., 2008. Cancer Cell Metabolism: Warburg and Beyond. Cell 134, 703–707.

Humphrey, W., Dalke, A., Schulten, K., 1996. VMD: Visual molecular dynamics. J. Mol. Graph. 14, 33–38.

Ishikita, H., Saito, K., 2014. Proton transfer reactions and hydrogen-bond networks in protein environments. J. R. Soc. Interface 11.

Iyengar, R., Rose, I.A., 1981. Concentration of activated intermediates of the fructose-1,6-bisphosphate aldolase and triosephosphate isomerase reactions. Biochemistry (Mosc.) 20, 1223–1229.

Iyengar, R., Rose, I.A., 1981. Liberation of the triosephosphate isomerase reaction intermediate and its trapping by isomerase, yeast aldolase, and methylglyoxal synthase. Biochemistry (Mosc.) 20, 1229–1235.

Jewett, T.J., Sibley, L.D., 2003. Aldolase forms a bridge between cell surface adhesins and the actin cytoskeleton in apicomplexan parasites. Mol. Cell 11, 885–894.

Jorgensen, W.L., Chandrasekhar, J., Madura, J.D., Impey, R.W., Klein, M.L., 1983. Comparison of simple potential functions for simulating liquid water. J. Chem. Phys. 79, 926–935.

Kalapos, M.P., 2013. Where does plasma methylglyoxal originate from? Diabetes Res. Clin. Pract. 99, 260–271.

Kalapos, M.P., 2008. Methylglyoxal and glucose metabolism: a historical perspective and future avenues for research. Drug Metabol. Drug Interact. 23, 69–91.

Kalapos, M.P., 1999. Methylglyoxal in living organisms: chemistry, biochemistry, toxicology and biological implications. Toxicol. Lett. 110, 145–175.

Kalapos, M.P., 1997. Possible Evolutionary Role of Methylglyoxalase Pathway: Anaplerotic Route for Reductive Citric Acid Cycle of Surface Metabolists. J. Theor. Biol. 188, 201–206.

Kao, A.W., Noda, Y., Johnson, J.H., Pessin, J.E., Saltiel, A.R., 1999. Aldolase mediates the association of F-actin with the insulin-responsive glucose transporter GLUT4. J. Biol. Chem. 274, 17742–17747.

Karkhoff-Schweizer, R., Knull, H.R., 1987. Demonstration of tubulin-glycolytic enzyme interactions using a novel electrophoretic approach. Biochem. Biophys. Res. Commun. 146, 827–831.

Kawahara, K., Tanford, C., 1966. The number of polypeptide chains in rabbit muscle aldolase. Biochemistry (Mosc.) 5, 1578–1584.

Kelley, P.M., Tolan, D.R., 1986. The Complete Amino Acid Sequence for the Anaerobically Induced Aldolase from Maize Derived from cDNA Clones 1. Plant Physiol. 82, 1076–1080.

Kim, J.H., Lee, S., Kim, J.H., Lee, T.G., Hirata, M., Suh, P.-G., Ryu, S.H., 2002. Phospholipase D2 Directly Interacts with Aldolase via Its PH Domain. Biochemistry (Mosc.) 41, 3414–3421.

Kitajima, Y., Takasaki, Y., Takahashi, I., Hori, K., 1990. Construction and properties of active chimeric enzymes between human aldolases A and B. Analysis of molecular regions which determine isozyme-specific functions. J. Biol. Chem. 265, 17493–17498.

Koerner, T.A., Cary, L.W., Bhacca, N.S., Younathan, E.S., 1973. Tautomeric composition of D-fructose phosphates in solution by Fourier transform carbon-13 nuclear magnetic resonance. Biochem. Biophys. Res. Commun. 51, 543–550.

Koppenol, W.H., Bounds, P.L., Dang, C.V., 2011. Otto Warburg's contributions to current concepts of cancer metabolism. Nat. Rev. Cancer 11, 325–337.

Kresge, N., Simoni, R.D., Hill, R.L., 2005. Otto Fritz Meyerhof and the Elucidation of the Glycolytic Pathway. J. Biol. Chem. 280, e3–e3.

Krise, J.P., Stella, V.J., 1996. Prodrugs of phosphates, phosphonates, and phosphinates. Adv. Drug Deliv. Rev., Low Molecular Weight Pro Drugs 19, 287–310.

Kuhla, B., Lüth, H.-J., Haferburg, D., Boeck, K., Arendt, T., Münch, G., 2005. Methylglyoxal, Glyoxal, and Their Detoxification in Alzheimer's Disease. Ann. N. Y. Acad. Sci. 1043, 211–216.

Kuo, D.J., Rose, I.A., 1985. Chemical trapping of complexes of dihydroxyacetone phosphate with muscle fructose-1,6-bisphosphate aldolase. Biochemistry (Mosc.) 24, 3947–3952.

Lai, C.Y., Hoffee, P., Horecker, B.L., 1965. Mechanism of action of aldolases. XII. Primary structure around the substrate binding site of rabbit muscle aldolase. Arch. Biochem. Biophys. 112, 567–579.

Lai, C.Y., Martinez-de Dretz, G., Bacila, M., Marinello, E., Horecker, B.L., 1968. Labeling of the active site of aldolase with glyceraldehyde 3-phosphate and erythrose 4-phosphate. Biochem. Biophys. Res. Commun. 30, 665–672.

Lakatos, S., Minton, A.P., 1991. Interactions between globular proteins and F-actin in isotonic saline solution. J. Biol. Chem. 266, 18707–18713.

Lebherz, H.G., Rutter, W.J., 1973. A Class I (Schiff Base) Fructose Diphosphate Aldolase of Prokaryotic Origin PURIFICATION AND PROPERTIES OF MICROCOCCUS AEROGENES ALDOLASE. J. Biol. Chem. 248, 1650–1659.

Lebherz, H.G., Rutter, W.J., 1969. Distribution of fructose diphosphate aldolase variants in biological systems. Biochemistry (Mosc.) 8, 109–121.

Lee, J.H., Bae, J., Kim, D., Choi, Y., Im, Y.J., Koh, S., Kim, J.S., Kim, M.-K., Kang, G.B., Hong, S.-I., Lee, D.-S., Eom, S.H., 2006. Stereoselectivity of fructose-1,6-bisphosphate aldolase in Thermus caldophilus. Biochem. Biophys. Res. Commun. 347, 616–625.

Lehninger, A.L., Sice, J., Jensen, E.V., 1955. Effect of substrate structure on the aldolase equilibrium. Biochim. Biophys. Acta 17, 285–287.

Leoncini, G., 1979. The role of alpha-ketoaldehydes in biological systems. Ital. J. Biochem. 28, 285–294.

Lew, C.R., Tolan, D.R., 2012. Targeting of Several Glycolytic Enzymes Using RNA Interference Reveals Aldolase Affects Cancer Cell Proliferation through a Non-glycolytic Mechanism. J. Biol. Chem. 287, 42554–42563.

Li, W., Llopis, J., Whitney, M., Zlokarnik, G., Tsien, R.Y., 1998. Cell-permeant caged InsP3 ester shows that Ca2+ spike frequency can optimize gene expression. Nature 392, 936–941.

Li, W., Schultz, C., Llopis, J., Tsien, R.Y., 1997. Membrane-permeant esters of inositol polyphosphates, chemical syntheses and biological applications. Tetrahedron 53, 12017–12040.

Li, Z., Cai, L., Qi, Q., Styslinger, T.J., Zhao, G., Wang, P.G., 2011a. Synthesis of Rare Sugars with L-fuculose-1-phosphate aldolase (FucA) from Thermus thermophilus HB8. Bioorg. Med. Chem. Lett. 21, 5084–5087.

Li, Z., Cai, L., Qi, Q., Wang, P.G., 2011b. Enzymatic synthesis of d-sorbose and d-psicose with aldolase RhaD: Effect of acceptor configuration on enzyme stereoselectivity. Bioorg. Med. Chem. Lett. 21, 7081–7084.

Liu, J., Desai, K., Wang, R., Wu, L., 2012a. Up-regulation of Aldolase A and Methylglyoxal Production in Adipocytes. Br. J. Pharmacol.

Liu, J., DeSantis, G., Wong, C.-H., 2002. Structure-based rationalization of aldolase-catalyzed asymmetric synthesis. Can. J. Chem. 80, 643–645.

Liu, J., Mak, T.C.-P., Banigesh, A., Desai, K., Wang, R., Wu, L., 2012b. Aldolase B Knockdown Prevents High Glucose-Induced Methylglyoxal Overproduction and Cellular Dysfunction in Endothelial Cells. PLoS ONE 7, e41495.

Liu, J., Wang, R., Desai, K., Wu, L., 2011. Upregulation of aldolase B and overproduction of methylglyoxal in vascular tissues from rats with metabolic syndrome. Cardiovasc. Res. 92, 494–503.

London, J., 1974. Variations in the Quaternary Structure of Three Lactic Acid Bacteria Aldolases EVIDENCE FOR THE EXISTENCE OF A CLASS I AND CLASS II ALDOLASE IN LACTOBACILLUS CASEI. J. Biol. Chem. 249, 7977–7983.

Lorentzen, E., Siebers, B., Hensel, R., Pohl, E., 2005. Mechanism of the Schiff Base Forming Fructose-1,6-bisphosphate Aldolase: Structural Analysis of Reaction Intermediates ‡. Biochemistry (Mosc.) 44, 4222–4229.

Low-Kam, C., 2015. La tagatose-1,6-bisphosphate et la fructose-1,6-bisphosphate aldolase de classe I : mécanisme et stéréospécificité. Université de Montréal.

Lundmark, R., Carlsson, S.R., 2004. Regulated Membrane Recruitment of Dynamin-2 Mediated by Sorting Nexin 9. J. Biol. Chem. 279, 42694–42702.

Magnien, A., Le Clef, B., Biellmann, J.F., 1984. Suicide inactivation of fructose-1,6-bisphosphate aldolase. Biochemistry (Mosc.) 23, 6858–6862.

Manchester, K.L., 1995. Louis Pasteur (1822–1895) — chance and the prepared mind. Trends Biotechnol. 13, 511–515.

Marks, G.T., Harris, T.K., Massiah, M.A., Mildvan, A.S., Harrison, D.H.T., 2001. Mechanistic Implications of Methylglyoxal Synthase Complexed with Phosphoglycolohydroxamic Acid As Observed by X-ray Crystallography and NMR Spectroscopy. Biochemistry (Mosc.) 40, 6805–6818.

Marsh, J.J., Lebherz, H.G., 1992. Fructose-bisphosphate aldolases: an evolutionary history. Trends Biochem. Sci. 17, 110–113.

Maughan, D.W., Henkin, J.A., Vigoreaux, J.O., 2005. Concentrations of Glycolytic Enzymes and Other Cytosolic Proteins in the Diffusible Fraction of a Vertebrate Muscle Proteome. Mol. Cell. Proteomics 4, 1541–1549.

Maurady, A., Zdanov, A., de Moissac, D., Beaudry, D., Sygusch, J., 2002. A Conserved Glutamate Residue Exhibits Multifunctional Catalytic Roles in D-Fructose-1,6-bisphosphate Aldolases. J. Biol. Chem. 277, 9474–9483.

McLellan, A.C., Thornalley, P.J., 1989. Glyoxalase activity in human red blood cells fractioned by age. Mech. Ageing Dev. 48, 63–71.

McLellan, A.C., Thornalley, P.J., Benn, J., Sonksen, P.H., 1994. Glyoxalase System in Clinical Diabetes Mellitus and Correlation with Diabetic Complications. Clin. Sci. 87, 21–29.

Mehler, A.H., Bloom, B., 1963. Interaction between Rabbit Muscle Aldolase and Dihydroxyacetone Phosphate. J. Biol. Chem. 238, 105–107.

Mehler, A.H., Cusic, M.E., 1967. Aldolase Reaction with Sugar Diphosphates. Science 155, 1101–1103.

Mentel, M., Laketa, V., Subramanian, D., Gillandt, H., Schultz, C., 2011. Photoactivatable and Cell-Membrane-Permeable Phosphatidylinositol 3,4,5-Trisphosphate. Angew. Chem. Int. Ed. 50, 3811–3814.

Merk, A., Bartesaghi, A., Banerjee, S., Falconieri, V., Rao, P., Davis, M.I., Pragani, R., Boxer, M.B., Earl, L.A., Milne, J.L.S., Subramaniam, S., 2016. Breaking Cryo-EM Resolution Barriers to Facilitate Drug Discovery. Cell 165, 1698–1707.

Meyerhof, O., Junowicz-Kocholaty, R., 1943. The Equilibria of Isomerase and Aldolase, and the Problem of the Phosphorylation of Glyceraldehyde Phosphate. J. Biol. Chem. 149, 71–92.

Meyerhof, O., Lohmann, K., 1934. Über die Enzymatische Gleichgewichtsreaktionen Zwischen Hexosediphosphorsäure und Dioxyacetonphosphorsäure. Biochem Z 273, 413.

Midelfort, C.F., Gupta, R.K., Rose, I.A., 1976. Fructose 1,6-bisphosphate: isomeric composition, kinetics, and substrate specificity for the aldolases. Biochemistry (Mosc.) 15, 2178–2185.

Model, P., Ponticorvo, L., Rittenberg, D., 1968. Catalysis of an oxygen-exchange reaction of fructose 1,6-diphosphate and fructose 1-phosphate with water by rabbit muscle aldolase. Biochemistry (Mosc.) 7, 1339–1347.

Molyneux, D.H., Ashford, R.W., 1983. The biology of Trypanosoma and Leishmania, parasites of man and domestic animals. Taylor and Francis, London.

Morris, A.J., Tolan, D.R., 1994. Lysine-146 of Rabbit Muscle Aldolase Is Essential for Cleavage and Condensation of the C3-C4 Bond of Fructose 1,6-Bis(phosphate). Biochemistry (Mosc.) 33, 12291–12297.

Morris, A.J., Tolan, D.R., 1993. Site-directed mutagenesis identifies aspartate 33 as a previously unidentified critical residue in the catalytic mechanism of rabbit aldolase A. J. Biol. Chem. 268, 1095–1100.

Morrison, J.F., Walsh, C.T., 1988. The Behavior and Significance of Slow-Binding Enzyme Inhibitors, in: Meister, A. (Ed.), Advances in Enzymology and Related Areas of Molecular Biology. John Wiley & Sons, Inc., pp. 201–301.

Morton, D.J., Clarke, F.M., Masters, C.J., 1977. An electron microscope study of the interaction between fructose diphosphate aldolase and actin-containing filaments. J. Cell Biol. 74, 1016–1023.

Munger, C., 2002. Mécanisme enzymatique de la fructose 1,6-bisphosphate aldolase de muscle de lapin: Étude du rôle des sérinés 271 et 300 du site actif. Université de Montréal, Montreal.

Murray, C.J., al., 2015. Global, regional, and national age-sex specific all-cause and cause-specific mortality for 240 causes of death, 1990-2013: a systematic analysis for the Global Burden of Disease Study 2013. Lancet 385, 117–171.

Nagano, N., Orengo, C.A., Thornton, J.M., 2002. One Fold with Many Functions: The Evolutionary Relationships between TIM Barrel Families Based on their Sequences, Structures and Functions. J. Mol. Biol. 321, 741–765.

Nakayama, K., Nakayama, M., Iwabuchi, M., Terawaki, H., Sato, T., Kohno, M., Ito, S., 2008. Plasma &alpha;-Oxoaldehyde Levels in Diabetic and Nondiabetic Chronic Kidney Disease Patients. Am. J. Nephrol. 28, 871–878.

Navarro-Lérida, I., Martínez Moreno, M., Roncal, F., Gavilanes, F., Albar, J.P., Rodríguez-Crespo, I., 2004. Proteomic identification of brain proteins that interact with dynein light chain LC8. PROTEOMICS 4, 339–346.

Nemet, I., Turk, Z., Duvnjak, L., Car, N., Varga-Defterdarović, L., 2005. Humoral methylglyoxal level reflects glycemic fluctuation. Clin. Biochem., LC Mass Spectrometry: Recent Developments in Clinical Chemistry 38, 379–383.

Nemetski, S.M., Cardozo, T.J., Bosch, G., Weltzer, R., O'Malley, K., Ejigiri, I., Kumar, K.A., Buscaglia, C.A., Nussenzweig, V., Sinnis, P., Levitskaya, J., Bosch, J., 2015. Inhibition by stabilization: targeting the Plasmodium falciparum aldolase–TRAP complex. Malar. J. 14.

Neuberg, C., 1913. Weitere Untersuchungen über die biochemische Umwandlung von Methylglyoxal in Milchsäure nebst Bemerkungen über die Entstehung der verschiedenen Milchsäuren in der Natur. Biochem Z 51, 484–508.

Nobelprize.org, 1907. Nobel Media AB 2014. [WWW Document]. URL <http://www.nobelprize.org/nobel_prizes/chemistry/laureates/1907/press.html> (accessed 1.18.16).

Odani, H., Shinzato, T., Matsumoto, Y., Usami, J., Maeda, K., 1999. Increase in Three α,β-Dicarbonyl Compound Levels in Human Uremic Plasma: Specificin VivoDetermination of Intermediates in Advanced Maillard Reaction. Biochem. Biophys. Res. Commun. 256, 89–93.

Opperdoes, F.R., 1987. Compartmentation of Carbohydrate Metabolism in Trypanosomes. Annu. Rev. Microbiol. 41, 127–151.

O'Reilly, G., Clarke, F., 1993. Identification of an actin binding region in aldolase. FEBS Lett. 321, 69–72.

Otwinowski, Z., Minor, W., 1997. [20] Processing of X-ray diffraction data collected in oscillation mode, in: Charles W. Carter, J. (Ed.), Methods in Enzymology, Macromolecular Crystallography Part A. Academic Press, pp. 307–326.

Ouporov, I.V., Knull, H.R., Thomasson, K.A., 1999. Brownian dynamics simulations of interactions between aldolase and G- or F-actin. Biophys. J. 76, 17–27.

Pal-Bhowmick, I., Andersen, J., Srinivasan, P., Narum, D.L., Bosch, J., Miller, L.H., 2012. Binding of Aldolase and Glyceraldehyde-3-Phosphate Dehydrogenase to the Cytoplasmic Tails of Plasmodium falciparum Merozoite Duffy Binding-Like and Reticulocyte Homology Ligands. mBio 3.

Peanasky, R.J., Lardy, H.A., 1958. Bovine Liver Aldolase I. Isolation, crystallization, and some general properties. J. Biol. Chem. 233, 365–370.

Peng, Q., Zhou, Q., Zhou, J., Zhong, D., Pan, F., Liang, H., 2008. Stable RNA interference of hexokinase II gene inhibits human colon cancer LoVo cell growth in vitro and in vivo. Cancer Biol. Ther. 7, 1128–1135.

Penhoet, E., Kochman, M., Valentine, R., Rutter, W.J., 1967. The subunit structure of mammalian fructose diphosphate aldolase. Biochemistry (Mosc.) 6, 2940–2949.

Penhoet, E., Rajkumar, T., Rutter, W.J., 1966. Multiple forms of fructose diphosphate aldolase in mammalian tissues. Proc. Natl. Acad. Sci. U. S. A. 56, 1275–1282.

Phillips, J.C., Braun, R., Wang, W., Gumbart, J., Tajkhorshid, E., Villa, E., Chipot, C., Skeel, R.D., Kalé, L., Schulten, K., 2005. Scalable Molecular Dynamics with NAMD. J. Comput. Chem. 26, 1781–1802.

Phillips, S.A., Thornalley, P.J., 1993. The formation of methylglyoxal from triose phosphates. Investigation using a specific assay for methylglyoxal. Eur. J. Biochem. FEBS 212, 101–105.

Poschmann, G., Sitek, B., Sipos, B., Ulrich, A., Wiese, S., Stephan, C., Warscheid, B., Klöppel, G., Vander Borght, A., Ramaekers, F.C.S., Meyer, H.E., Stühler, K., 2009. Identification of proteomic differences between squamous cell carcinoma of the lung and bronchial epithelium. Mol. Cell. Proteomics MCP 8, 1105–1116.

Pricer, W.E., Horecker, B.L., 1960. Deoxyribose Aldolase from Lactobacillus plantarum. J. Biol. Chem. 235, 1292–1298.

Priotto, G., Kasparian, S., Mutombo, W., Ngouama, D., Ghorashian, S., Arnold, U., Ghabri, S., Baudin, E., Buard, V., Kazadi-Kyanza, S., Ilunga, M., Mutangala, W., Pohlig, G., Schmid, C., Karunakara, U., Torreele, E., Kande, V., 2009. Nifurtimox-eflornithine combination therapy for second-stage African Trypanosoma brucei gambiense trypanosomiasis: a multicentre, randomised, phase III, non-inferiority trial. The Lancet 374, 56–64.

Rae, C., Bubb, W.A., Kuchel, P.W., 1992. Aldolase-catalyzed diketone phosphate formation from oxoaldehydes. NMR studies and metabolic significance. J. Biol. Chem. 267, 9713–9717.

Ray, B.D., Harper, E.T., Fife, W.K., 1983. Carbon-13 NMR evidence of carbinolamine formation at the active site of an imine-forming aldolase. J. Am. Chem. Soc. 105, 3731–3732.

Ray, P.H., Benedict, C.D., 1980. Purification and Characterization of a Specific 3-Deoxy-d-manno-Octulosonate 8-Phosphate Phosphatase from Escherichia coli B. J. Bacteriol. 142, 60–68.

Raychaudhuri, S., Younas, F., Karplus, P.A., Faerman, C.H., Ripoll, D.R., 1997. Backbone makes a significant contribution to the electrostatics of α/β-barrel proteins. Protein Sci. 6, 1849–1857.

Reddy, V.P., Obrenovich, M.E., Atwood, C.S., Perry, G., Smith, M.A., 2002. Involvement of maillard reactions in Alzheimer disease. Neurotox. Res. 4, 191–209.

Rho, J.-H., Roehrl, M.H.A., Wang, J.Y., 2009. Glycoproteomic Analysis of Human Lung Adenocarcinomas Using Glycoarrays and Tandem Mass Spectrometry: Differential Expression and Glycosylation Patterns of Vimentin and Fetuin A Isoforms. Protein J. 28, 148–160.

Richard, J.P., 1993. Mechanism for the formation of methylglyoxal from triosephosphates. Biochem. Soc. Trans. 21, 549–553.

Richard, J.P., 1991. Kinetic parameters for the elimination reaction catalyzed by triosephosphate isomerase and an estimation of the reaction's physiological significance. Biochemistry (Mosc.) 30, 4581–4585.

Richard, J.P., 1985. Reaction of triose phosphate isomerase with L-glyceraldehyde 3-phosphate and triose 1,2-enediol 3-phosphate. Biochemistry (Mosc.) 24, 949–953.

Richard, J.P., 1984. Acid-base catalysis of the elimination and isomerization reactions of triose phosphates. J. Am. Chem. Soc. 106, 4926–4936.

Richards, O.C., Rutter, W.J., 1961. Comparative Properties of Yeast and Muscle Aldolase. J. Biol. Chem. 236, 3185–3192.

Riglar, D.T., Whitehead, L., Cowman, A.F., Rogers, K.L., Baum, J., 2016. Localisation-based imaging of malarial antigens during erythrocyte entry reaffirms a role for AMA1 but not MTRAP in invasion. J Cell Sci 129, 228–242.

Riviere-Alric, I., 1991. Synthèse et étude du mécanisme d'action d'inhibiteurs des enzymes glycolytiques : hexokinase et aldolase. Toulouse 3.

Rose, I.A., O'Connell, E.L., 1969. Studies on the Interaction of Aldolase with Substrate Analogues. J. Biol. Chem. 244, 126–134.

Rose, I.A., O'Connell, E.L., Mehler, A.H., 1965. Mechanism of the Aldolase Reaction. J. Biol. Chem. 240, 1758–1765.

Rose, I.A., Rieder, S.V., 1958. Studies on the Mechanism of the Aldolase Reaction Isotope Exchange Reactions of Muscle and Yeast Aldolase. J. Biol. Chem. 231, 315–329.

Rose, I.A., Rieder, S.V., 1955. THE MECHANISM OF ACTION OF MUSCLE ALDOLASE1. J. Am. Chem. Soc. 77, 5764–5765.

Rose, I.A., Warms, J.V.B., 1985. Complexes of muscle aldolase in equilibrium with fructose 1,6-bisphosphate. Biochemistry (Mosc.) 24, 3952–3957.

Rupp, B., 2009. Biomolecular Crystallography: Principles, Practice, and Application to Structural Biology, 1st ed. Garland Science.

Russell, G.K., Gibbs, M., 1967. Partial purification and characterization of two fructose diphosphate aldolases from Chlamydomonas mundana. Biochim. Biophys. Acta 132, 145–154.

Rutter, W.J., 1964. Evolution of Aldolase. Fed. Proc. 23, 1248–1257.

Rutter, W.J., Groves, W.E., 1964. Coherence and variation in macromolecular Structures in phylogeny, in: Taxonomic Biochemistry and Serology. Ronald Press, New York, pp. 417–434.

Rutter, W.J., Ling, K.H., 1958. The mechanism of action of fructose diphosphate aldolase. Biochim. Biophys. Acta 30, 71–79.

Sawyer, L., Fothergill-Gilmore, L.A., Freemont, P.S., 1988. The predicted secondary structures of class I fructose-bisphosphate aldolases. Biochem. J. 249, 789–793.

Schmidt, N.G., Eger, E., Kroutil, W., 2016. Building Bridges: Biocatalytic C–C-Bond Formation toward Multifunctional Products. ACS Catal. 6, 4286–4311.

Schultz, C., 2003. Prodrugs of biologically active phosphate esters. Bioorg. Med. Chem. 11, 885–898.

Shapiro, S., Enser, M., Pugh, E., Horecker, B.L., 1968. The effect of pyridoxal phosphate on rabbit muscle aldolase. Arch. Biochem. Biophys. 128, 554–562.

Shearwin, K., Nanhua, C., Masters, C., 1990. Interactions between glycolytic enzymes and cytoskeletal structure--the influence of ionic strength and molecular crowding. Biochem. Int. 21, 53–60.

Shen, B., Sibley, L.D., 2014. Toxoplasma aldolase is required for metabolism but dispensable for host-cell invasion. Proc. Natl. Acad. Sci. 201315156.

Siebers, B., Brinkmann, H., Dörr, C., Tjaden, B., Lilie, H., Oost, J. van der, Verhees, C.H., 2001. Archaeal Fructose-1,6-bisphosphate Aldolases Constitute a New Family of Archaeal Type Class I Aldolase. J. Biol. Chem. 276, 28710–28718.

Sigel, P., Pette, D., 1969. Intracellular Localization of Glycogenolytic and Glycolytic Enzymes in White and Red Rabbit Skeletal Muscle a Gel Film Method for Coupled Enzyme Reactions in Histochemistry. J. Histochem. Cytochem. 17, 225–237.

Spolter, P.D., Adelman, R.C., Weinhouse, S., 1965. Distinctive properties of native and carboxypeptidase-treated aldolases of rabbit muscle and liver. J. Biol. Chem. 240, 1327–1337.

Starnes, G.L., Coincon, M., Sygusch, J., Sibley, L.D., 2009. Aldolase Is Essential for Energy Production and Bridging Adhesin-Actin Cytoskeletal Interactions during Parasite Invasion of Host Cells. Cell Host Microbe 5, 353–364.

Starnes, G.L., Jewett, T.J., Carruthers, V.B., Sibley, L.D., 2006. Two Separate, Conserved Acidic Amino Acid Domains within the Toxoplasma gondii MIC2 Cytoplasmic Tail Are Required for Parasite Survival. J. Biol. Chem. 281, 30745–30754.

Steele, R.H., White, A.G.C., Pierce, W.A., 1954. The fermentation of galactose by streptococcus pyogenes. J. Bacteriol. 67, 86–89.

St-Jean, M., 2008. Multifonctionnalité de l'aldolase glycolytique : mécanisnle catalytique et interaction avec un peptide de la protéine du syndrome Wiskott-Aldrich. Université de Montréal.

St-Jean, M., Izard, T., Sygusch, J., 2007. A Hydrophobic Pocket in the Active Site of Glycolytic Aldolase Mediates Interactions with Wiskott-Aldrich Syndrome Protein. J. Biol. Chem. 282, 14309–14315.

St-Jean, M., Lafrance-Vanasse, J., Liotard, B., Sygusch, J., 2005. High resolution reaction intermediates of rabbit muscle fructose-1,6-bisphosphate aldolase: substrate cleavage and induced fit. J. Biol. Chem. 280, 27262–27270.

St-Jean, M., Sygusch, J., 2007. Stereospecific Proton Transfer by a Mobile Catalyst in Mammalian Fructose-1,6-bisphosphate Aldolase. J. Biol. Chem. 282, 31028–31037.

Strapazon, E., Steck, T.L., 1976. Binding of rabbit muscle aldolase to band 3, the predominant polypeptide of the human erythrocyte membrane. Biochemistry (Mosc.) 15, 1421–1424.

Stribling, D., Perham, R.N., 1973. Purification and characterization of two fructose diphosphate aldolases from Escherichia coli (Crookes' strain). Biochem. J. 131, 833–841.

Subramanian, D., Laketa, V., Müller, R., Tischer, C., Zarbakhsh, S., Pepperkok, R., Schultz, C., 2010. Activation of membrane-permeant caged PtdIns(3)P induces endosomal fusion in cells. Nat. Chem. Biol. 6, 324–326.

Suh, B., Barker, R., 1971. Fluorescence studies of the binding of alkyl and aryl phosphates to rat muscle aldolase. J. Biol. Chem. 246, 7041–7050.

Swenson, C.A., Barker, R., 1971. Proportion of keto and aldehydo forms in solutions of sugars and sugar phosphates. Biochemistry (Mosc.) 10, 3151–3154.

Sygusch, J., Beaudry, D., Allaire, M., 1987. Molecular architecture of rabbit skeletal muscle aldolase at 2.7-A resolution. Proc. Natl. Acad. Sci. U. S. A. 84, 7846–7850.

Taylor, J.F., Green, A.A., Cori, G.T., 1948. Crystalline Aldolase. J. Biol. Chem. 173, 591–604.

Terwilliger, T.C., Grosse-Kunstleve, R.W., Afonine, P.V., Moriarty, N.W., Adams, P.D., Read, R.J., Zwart, P.H., Hung, L.-W., 2008. Iterative-build OMIT maps: map improvement by iterative model building and refinement without model bias. Acta Crystallogr. D Biol. Crystallogr. 64, 515–524.

Thomson, G.J., Howlett, G.J., Ashcroft, A.E., Berry, A., 1998. The dhnA gene of Escherichia coli encodes a class I fructose bisphosphate aldolase. Biochem. J. 331, 437–445.

Thornalley, P.J., 1993. The glyoxalase system in health and disease. Mol. Aspects Med. 14, 287–371.

Thornalley, P.J., 1990. The glyoxalase system: new developments towards functional characterization of a metabolic pathway fundamental to biological life. Biochem. J. 269, 1–11.

Thornalley, P.J., 1988. Modification of the glyoxalase system in human red blood cells by glucose in vitro. Biochem. J. 254, 751–755.

Thornalley, P.J., Hooper, N.I., Jennings, P.E., Florkowski, C.M., Jones, A.F., Lunec, J., Barnett, A.H., 1989. The human red blood cell glyoxalase system in diabetes mellitus. Diabetes Res. Clin. Pract. 7, 115–120.

Tolan, D.R., Amsden, A.B., Putney, S.D., Urdea, M.S., Penhoet, E.E., 1984. The complete nucleotide sequence for rabbit muscle aldolase A messenger RNA. J. Biol. Chem. 259, 1127–1131.

Topper, Y.J., Mehler, A.H., Bloom, B., 1957. Spectrophotometric Evidence for Formation of a Dihydroxyacetone Phosphate-Aldolase Complex. Science 126, 1287–1287.

Tung, T.C., Ling, K.H., Byrne, W.L., Lardy, H.A., 1954. Substrate specificity of muscle aldolase. Biochim. Biophys. Acta 14, 488–494.

Vander Heiden, M.G., 2011. Targeting cancer metabolism: a therapeutic window opens. Nat. Rev. Drug Discov. 10, 671–684.

Vander Heiden, M.G.V., Cantley, L.C., Thompson, C.B., 2009. Understanding the Warburg Effect: The Metabolic Requirements of Cell Proliferation. Science 324, 1029–1033.

Vanommeslaeghe, K., Hatcher, E., Acharya, C., Kundu, S., Zhong, S., Shim, J., Darian, E., Guvench, O., Lopes, P., Vorobyov, I., MacKerell, A.D., 2010. CHARMM General Force Field (CGenFF): A force field for drug-like molecules compatible with the CHARMM all-atom additive biological force fields. J. Comput. Chem. 31, 671–690.

Veech, R.L., Raijman, L., Dalziel, K., Krebs, H.A., 1969. Disequilibrium in the triose phosphate isomerase system in rat liver. Biochem. J. 115, 837–842.

Verlinde, C.L.M.J., Hannaert, V., Blonski, C., Willson, M., Périé, J.J., Fothergill-Gilmore, L.A., Opperdoes, F.R., Gelb, M.H., Hol, W.G.J., Michels, P.A.M., 2001. Glycolysis as a target for the design of new anti-trypanosome drugs. Drug Resist. Updat. 4, 50–65.

Volker, K.W., Knull, H.R., 1997. A Glycolytic Enzyme Binding Domain on Tubulin. Arch. Biochem. Biophys. 338, 237–243.

Volker, K.W., Reinitz, C.A., Knull, H.R., 1995. Glycolytic enzymes and assembly of microtubule networks. Comp. Biochem. Physiol. B Biochem. Mol. Biol. 112, 503–514.

Walsh, J.L., Keith, T.J., Knull, H.R., 1989. Glycolytic enzyme interactions with tubulin and microtubules. Biochim. Biophys. Acta BBA - Protein Struct. Mol. Enzymol. 999, 64–70.

Wang, J., Morris, A.J., Tolan, D.R., Pagliaro, L., 1996. The Molecular Nature of the F-actin Binding Activity of Aldolase Revealed with Site-directed Mutants. J. Biol. Chem. 271, 6861–6865.

Warburg, O., 1956. On the Origin of Cancer Cells. Science 123, 309–314.

Warburg, O., Christian, W., 1943. Isolierung und Kristallisierung des Garungsfermentes Zymohexase. Biochem Z 314, 149–176.

Warburg, O., Wind, F., Negelein, E., 1927. The Metabolism of Tumors in the Body. J. Gen. Physiol. 8, 519–530.

Weissbach, A., Hurwitz, J., 1959. The Formation of 2-Keto-3-deoxyheptonic Acid in Extracts of Escherichia coli B I. Identification. J. Biol. Chem. 234, 705–709.

Whalen, L.J., Wong, C.-H., 2006. Enzymes in organic synthesis: Aldolase-mediated synthesis of iminocyclitols and novel heterocycles. Aldrichimica Acta 39, 63–71.

Whitesides, G.M., Wong, C.-H., 1985. Enzymes as Catalysts in Synthetic Organic Chemistry [New Synthetic Methods (53)]. Angew. Chem. Int. Ed. Engl. 24, 617–638.

WHO | Trypanosomiasis, human African (sleeping sickness), 2016.

Wierenga, R.K., 2001. The TIM-barrel fold: a versatile framework for efficient enzymes. FEBS Lett. 492, 193–198.

Wilde, J., Hunt, W., Hupe, D.J., 1977. An inhibitor for aldolase. J. Am. Chem. Soc. 99, 8319.

Williams, G.J., Domann, S., Nelson, A., Berry, A., 2003. Modifying the stereochemistry of an enzyme-catalyzed reaction by directed evolution. Proc. Natl. Acad. Sci. 100, 3143–3148.

Windle, C.L., Müller, M., Nelson, A., Berry, A., 2014. Engineering aldolases as biocatalysts. Curr. Opin. Chem. Biol., Biocatalysis and biotransformation. Bioinorganic chemistry 19, 25–33.

Wong, C.H., Whitesides, G.M., 1983. Synthesis of sugars by aldolase-catalyzed condensation reactions. J. Org. Chem. 48, 3199–3205.

Wood, W.A., Boyer, P.D., 1970. The Enzymes. Academic Press, New York, p. 281.

Wu, G., Fang, Y.-Z., Yang, S., Lupton, J.R., Turner, N.D., 2004. Glutathione Metabolism and Its Implications for Health. J. Nutr. 134, 489–492.

Yankeelov, J.A., Mitchell, C.D., Crawford, T.H., 1968. A simple trimerization of 2,3-butanedione yielding a selective reagent for the modification of arginine in proteins. J. Am. Chem. Soc. 90, 1664–1666.

Yarar, D., To, W., Abo, A., Welch, M.D., 1999. The Wiskott–Aldrich syndrome protein directs actin-based motility by stimulating actin nucleation with the Arp2/3 complex. Curr. Biol. 9, 555–558.

Yu, P.H., 2001. Involvement of cerebrovascular semicarbazide-sensitive amine oxidase in the pathogenesis of Alzheimer's disease and vascular dementia. Med. Hypotheses 57, 175–179.

Yu, P.H., Wright, S., Fan, E.H., Lun, Z.-R., Gubisne-Harberle, D., 2003. Physiological and pathological implications of semicarbazide-sensitive amine oxidase. Biochim. Biophys. Acta BBA - Proteins Proteomics, 3rd International Symposium on Vitamin B6, PQQ, Carbonyl Catalysis and Quinoproteins 1647, 193–199.